Technische Universität München
Fakultät für Elektrotechnik und Informationstechnik
Lehrstuhl für Elektrische Energiespeichertechnik

Structural dynamics and vibration durability of lithium-ion cells

Philipp Berg (M.Sc.)

Vollständiger Abdruck der von der Fakultät für Elektrotechnik und Informationstechnik der Technischen Universität München zur Erlangung des akademischen Grades eines

Doktor-Ingenieurs (Dr.-Ing.)

genehmigten Dissertation.

Vorsitzender:	Prof. Dr.-Ing. Rolf Witzmann	
Prüfer der Dissertation:	1.	Prof. Dr.-Ing. Andreas Jossen
	2.	Prof. Dr.-Ing. Michael F. Zäh

Die Dissertation wurde am 22.06.2020 bei der Technischen Universität München eingereicht und durch die Fakultät für Elektrotechnik und Informationstechnik am 11.03.2021 angenommen.

Vorwort und Danksagung

Die vorliegende Dissertation „Structural dynamics and vibration durability of lithium-ion cells" entstand während meiner Tätigkeit als wissenschaftlicher Mitarbeiter am Lehrstuhl für Elektrische Energiespeichertechnik der Technischen Universität München in der Zeit von Dezember 2013 bis September 2019. Dem Lehrstuhlinhaber, Prof. Dr.-Ing. Andreas Jossen möchte ich für die außerordentlich gute Zusammenarbeit, zahlreichen Denkanstöße und umfassende Unterstützung während meiner Zeit am Lehrstuhl danken. Ich bedanke mich des Weiteren bei Prof. Dr.-Ing. Michael F. Zäh für die Erstellung des Zweitgutachtens.

Weiterhin gilt mein Dank allen Lehrstuhlkollegen und insbesondere dem Team Batteriesysteme für die Zusammenarbeit, tolle Zeit am Lehrstuhl, zahlreiche Forschungsrunden, Büro-Nachbarschaften, Stammtische, Obstrunden und mehr. Namentlich hervorgehoben seien hier meine Bürokollegin Elisabeth Kolp sowie Markus Hofmann, Marco Steinhardt, Jonas Soellner, Martin Brand und Simon Schuster, die meinen Weg besonders mitgeprägt haben.

Ein spezieller Dank gilt außerdem unserer Assistentin Carolin Nierwetberg und unseren Technikern Jens Dietrich und Korbinian Schmidt ohne deren fortwährende Unterstützung bei Prüfaufbauten und gute Ideen vieles schwerer oder gar unmöglich gewesen wäre.

Ebenso bedanken möchte ich mich bei allen meinen ehemaligen Studenten für die Zusammenarbeit und ihren Beitrag zu meiner Forschung. Ein großes Dankeschön geht des Weiteren an alle Co-Autoren meiner Publikationen für die tolle Zusammenarbeit.

In diesem Sinne möchte ich mich auch bei allen Kollegen des Projekts ReViSEDBatt für die angenehme Zusammenarbeit, die gemeinsame Forschung und die spannenden Projekttreffen bedanken.

Ein lurchiges Dankeschön geht des Weiteren an meine alten Wegbegleiter aus Karlsruher Studientagen, die während Bachelor und Master mitgeholfen haben die Grundvoraussetzungen für diese Arbeit zu legen. Des Weiteren möchte ich meinem Mentor Jan-Philipp Schmidt für die freundschaftliche Begleitung meiner Arbeit und mutmachenden Worte danken.

Mein abschließender riesiger Dank gilt meiner Familie und meiner Lebensgefährtin Natascha Borshch ohne deren Liebe und Unterstützung dieses Projekt nicht möglich gewesen wäre und auf die ich immer zählen konnte. Diese Arbeit ist Ihnen und insbesondere meiner Mutter Monika Berg gewidmet.

Kurzfassung

Lithium-Ionen-Batterien sind eine der Schlüsseltechnologien für eine emissionsfreie und nachhaltige Zukunft, da die Nutzung erneuerbarer Energien die Elektrifizierung vieler tragbarer und mobiler Anwendungen erfordert. Ein Fehler einer Lithium-Ionen-Batterie, insbesondere in sicherheitskritischen Anwendungen, wie dem Automobil oder in der Luftfahrt, kann verheerende Konsequenzen haben und muss daher verhindert werden. Zudem ist eine lange Lebensdauer essentiell, um kostspielige Austauschvorgänge der Batterien zu vermeiden.

Vibrationen sind eine der Umweltbedingungen, die Lithium-Ionen-Batterien während ihrer Lebensdauer standhalten müssen und stehen im Mittelpunkt dieser Arbeit. Die Arbeit konzentriert sich auf die Zell-Ebene und betrachtet alle drei populären Zellformate, die da wären, zylindrische Zellen, Pouch-Zellen und prismatische Zellen.

Die Gefährdungsabschätzung zeigt, dass Feldfehler von Lithium-Ionen-Zellen oder -Batterien in Verbindung mit Vibrationen nur aufgrund unzureichender Verpackungen und dem damit verbundenen Erzeugen externer Kurzschlüsse und entsprechender negativer Effekte aufgetreten sind. Gleichzeitig haben viele Feldfehler unbekannte Ursachen, die im Nachhinein nicht geklärt werden können. Zusätzlich gilt, dass eine beschleunigte Alterung oder reduzierte Lebensdauer aufgrund von Vibrationen möglicherweise verborgen oder vermischt mit anderen Alterungseffekten geschehen kann.

Die Haupt-Forschungsfrage dieser Arbeit ist daher, welche Fehlermechanismen mit entsprechenden Zuständen und Effekten durch Vibrationen in einer Lithium-Ionen-Zelle ausgelöst werden können. Diese Hauptfrage wird begleitet von verschiedenen Nebenfragen. Eine dieser Fragen ist, wie diese Fehler durch die Konditionen der Zelle, wie zum Beispiel Ladezustand, Gesundheitszustand oder Temperatur und vom inneren Design der Zelle selbst, beeinflusst werden. Der Einfluss der Vibration selbst, zum Beispiel über die Frequenzanteile oder Amplituden, werden ebenfalls berücksichtigt. Der Fokus liegt hierbei auf nichtlinearen Effekten und deren Einfluss auf Vibrationsuntersuchungen, Vibrationstests und Langlebigkeit.

Da die frei verfügbare Literatur im Feld von Vibrationen teilweise widersprüchlich ist, beinhaltet diese Arbeit die grundlegende Frage, „wie“ eine Lithium-Ionen-Zelle vibriert. Dies wird erreicht durch die Anwendung des Konzepts der experimentellen Modalanalyse sowie eines selbstentwickelten Prüfstands, um die Strukturdynamik von Pouch-Zellen und prismatischen Zellen, zu charakterisieren. Signifikant nichtlineares Verhalten und ein starker Einfluss von Randbedingungen durch Wechselwirkungen mit dem Zellgehäuse werden gezeigt. Dies führt zu vollkommen unterschiedlichen Sensitivitäten zum Ladezustand für Pouch-Zellen und prismatische Zellen. Basierend auf der Charakterisierung, wird ein Vorgehen zum Aufbau von Finite-Elemente-

Modellen vorgeschlagen und beispielhaft für Lithium-Ionen-Pouchzellen dargestellt. Diese Studie beinhaltet eine Analyse der Sensitivitäten von elastischen Parametern auf die Strukturantwort.

Neben der Charakterisierung und Modellierung, zeigt eine vergleichende Studie zur Langzeithaltbarkeit mit einer großen Auswahl verschiedener zylindrischer 18650-Zellen, eine Bewegung des inneren Mittelstabs als kritischsten Fehlermechanismus für zylindrische Zellen. Dies ermöglicht die Ableitung von Empfehlungen für das innere Design dieser Zellen.

Abstract

Lithium-ion batteries are one of the key technologies for an emission-free and sustainable future since the usage of renewable energy requires the electrification of many portable or mobile applications. Failure of a lithium-ion battery, especially in safety-critical automotive or aeronautic applications, can have catastrophic consequences and must be prevented. In addition, a long lifetime is crucial to avoid costly replacements.

Vibrations are one of the environmental conditions that lithium-ion batteries must endure during their lifetime and are the focus of this thesis. The thesis concentrates on the cell level, including all three popular cell formats, namely cylindrical cells, pouch cells and prismatic cells.

Risk assessment reveals that field-failures of lithium-ion cells or batteries in connection with vibrations occurred only due to improper packaging, causing external short circuits with respective negative effects. At the same time, many field failures have an unclear underlying cause, which cannot be identified afterwards. In addition, accelerated aging or reduced lifetime due to vibration is probably hidden by or mixed with other aging effects.

The main research question of this thesis is, therefore, which failure mechanisms with respective failure modes and effects can be caused by vibrations in a lithium-ion cell. This main question is accompanied by several side questions. One of them is how these failures are influenced by the cell's conditions, such as state of charge, state of health or temperature and the inner design of the cell itself. The influence of the properties of vibration such as frequency content or amplitude is also considered with a focus on nonlinear effects and their implications on vibration investigation, testing, and durability.

Since the available literature in the field of vibration is sometimes contradictory, this thesis includes the fundamental question "how" a lithium-ion cell vibrates. This question is answered using the concept of experimental modal analysis and a self-developed test bench to characterize the structural dynamics of pouch cells and prismatic cells. Significant nonlinear behavior and the strong influence of the boundary conditions through interdependencies with the cell housing are found. This causes completely different sensitivity to the state of charge for pouch cells and prismatic cells. On the basis of the characterization, an approach to creating finite element models is proposed and exemplarily presented for lithium-ion pouch cells. This study includes an analysis of the sensitivities of the structural response to the elasticity parameters.

Besides characterization and modeling, a comparative durability study with a wide range of 18650 cells shows the movement of the inner mandrel as the most critical failure mechanism for the cylindrical cells. This provides the opportunity to derive recommendations for the inner cell design.

List of publications

Peer-Reviewed Journal Contributions (Lead-Author)

I P. Berg, M. Spielbauer, M. Tillinger, M. Merkel, M. Schoenfuss, O. Bohlen, A. Jossen, Durability of lithium-ion 18650 cells under random vibration load with respect to the inner cell design, Journal of Energy Storage 31 (2020) 101499. https://doi.org/10.1016/j.est.2020.101499.

II P. Berg, J. Soellner, M. Herrmann, A. Jossen, Structural dynamics of lithium-ion cells - part II: Investigation of large-format prismatic cells and method evaluation, Journal of Energy Storage 28 (2020) 101246. https://doi.org/10.1016/j.est.2020.101246.

III P. Berg, J. Soellner, A. Jossen, Structural dynamics of lithium-ion cells - Part I: Method, test bench validation and investigation of lithium-ion pouch cells, Journal of Energy Storage 26 (2019) 100916. https://doi.org/10.1016/j.est.2019.100916.

Peer-Reviewed Journal Contributions (Co-Author)

I M. Spielbauer, P. Berg, M. Ringat, O. Bohlen, A. Jossen, Experimental study of the impedance behavior of 18650 lithium-ion battery cells under deforming mechanical abuse, Journal of Energy Storage 26 (2019) 101039. https://doi.org/10.1016/j.est.2019.101039.

II M.J. Brand, E.I. Kolp, P. Berg, T. Bach, P. Schmidt, A. Jossen, Electrical resistances of soldered battery cell connections, Journal of Energy Storage 12 (2017) 45–54. https://doi.org/10.1016/j.est.2017.03.019.

III M.J. Brand, P. Berg, E.I. Kolp, T. Bach, P. Schmidt, A. Jossen, Detachable electrical connection of battery cells by press contacts, Journal of Energy Storage 8 (2016) 69–77. https://doi.org/10.1016/j.est.2016.09.011.

IV S.F. Schuster, M.J. Brand, P. Berg, M. Gleissenberger, A. Jossen, Lithium-ion cell-to-cell variation during battery electric vehicle operation, Journal of Power Sources 297 (2015) 242–251. https://doi.org/10.1016/j.jpowsour.2015.08.001.

Conference contributions

I P. Berg, M. Tillinger, A. Jossen, The Impact of Automotive Random Vibrations on 18650 Lithium-Ion Cells, in: Advanced Battery Power / Kraftwerk Batterie 2019, Aachen, Germany, 2019.

II P. Berg, M. Merkel, A. Jossen, Increasing Safety and Lifetime of Lithium-Ion Batteries by Understanding the Impact of Vibrations and Resonances, in: Battery Safety 2018, Arlington, VA, USA, 2018.

III P. Berg, J. Soellner, A. Jossen, Risk of Vibrations and Resonances for Lithium-Ion Batteries - A new experimental and simulative characterization method, in: Advanced Battery Power / Kraftwerk Batterie 2018, Muenster, Germany, 2018.

IV P. Berg, A. Jossen, Investigation of the Applicability of Batteries for Aeronautical Applications - A Quantitative Reliability Approach, in: Advanced Battery Power / Kraftwerk Batterie 2017, Aachen, Germany, 2017.

V P. Berg, P. Schmitz, M.J. Brand, M.F. Zaeh, A. Jossen, Lithium-ion battery safety during laser welding for battery system production, in: Advanced Battery Power / Kraftwerk Batterie 2016, Muenster, Germany, 2016.

VI P. Berg, A. Jossen, Integration of Batteries into Aeronautic Applications - Challenges and Opportunities, in: Electric & Hybrid Aerospace Technology Symposium 2015, Bremen, Germany, 2015.

VII P. Berg, A. Jossen, Sustainable Transport - Technology and Status, in: JSPS Symposium, Tokyo, Japan, 2015.

VIII P. Berg, S.F. Schuster, M.J. Brand, M. Gleissenberger, A. Jossen, Trend of Lithium-ion cell-to-cell variation during Battery Electric Vehicle operation, in: European Electric Vehicle Congress (EEVC) 2015, Brussels, Belgium, 2015.

Contents

List of abbreviations

AEA	all electric airplane
BEV	battery electric vehicle
BMS	battery management system
BSI	British Standards Institution
CC	constant current
CCCV	constant current constant voltage
CID	current interrupt device
CPSC	Consumer Product Safety Commission
CT	computed tomography
DIN	Deutsches Institut für Normung e.V.
DMC	dimethyl carbonate
DOE	design of experiment
DOF	degree of freedom
DP	driving point
DPM	driving point measurements
DRT	distribution of relaxation times
EIS	electrochemical impedance spectroscopy
EMA	experimental modal analysis
EV	electric vehicle
FAA	Federal Aviation Administration
FDS	fatigue damage spectrum
FEM	finite element model
FIT	failure in time
FMEA	failure mode and effect analysis
FMMEA	failure mode, mechanism and effect analysis
FMMECA	failure mode, mechanism, effect and cause analysis
FRF	frequency response functions
FTA	fault tree analysis
HCF	high cycle fatigue
HEV	hybrid electric vehicle
ICE	internal combustion engine
IEC	International Electrotechnical Commission
IEPE	integrated electronics piezo electric
ISC	internal short circuit

ISO	International Organization for Standardization
LCC	life-cycle costs
LCF	low cycle fatigue
LiPo	lithium-polymer
MD	machine direction
MDOF	multi degree of freedom
MEA	more electric aircraft
MSC	micro short circuit
NCA	nickel cobalt aluminum oxide
NHTSA	National Highway Traffic Safety Administration
NiCd	nickel-cadmium
NiMH	nickel-metal hydride
NMC	nickel manganese cobalt oxide
ODS	operational deflection shape
PDF	probability density function
PROM	parametric reduced order model
PSD	power spectral density
QEIS	quick electrochemical impedance spectroscopy
RMS	root mean square
SAE	Society of Automotive Engineers
SC	short circuit
SDOF	single degree of freedom
SNR	signal-to-noise ratio
SOC	state of charge
SOH	state of health
SPEIS	single point electrochemical impedance spectroscopy
SRS	shock response spectrum
TPM	transfer point measurement
UAV	unmanned aerial vehicle
UNECE	United Nations Economic Commission for Europe
WMG/MBK	Warwick Manufacturing Group/Millbrook Proving Ground
WP	work package

List of symbols

A	A-factor	-
$A(f)$	Fourier transformation of $a(t)$	(e.g.) N
$a(t)$	Excitation signal for FRF calculation, e.g., force	(e.g.) N
A_0	Area (initial)	m^2
acc	Acceleration	g
acc_{RMS}	Root mean square acceleration	g
$B(f)$	Fourier transformation of $b(t)$	(e.g.) m/s^2
$b(t)$	Response signal for FRF calculation, e.g., acceleration	(e.g.) m/s^2
c	Damping constant	kg/s
C	Damping matrix	kg/s
c_0	Critical damping coefficient	kg/s
cf	Crest factor	-
c_k	Stiffness proportional damping coefficient (same as β)	s
c_m	Mass proportional damping coefficient (same as α)	1/s
E	Young's modulus or Elastic modulus	MPa
E_x	Elastic modulus in direction x	MPa
E_y	Elastic modulus in direction y	MPa
E_z	Elastic modulus in direction z	MPa
F	Force	N
f	Frequency	Hz
F_{max}	Maximum force	N
f_{nat}	Natural frequency	Hz
$f_{nat,ANSYS,n}$	Natural frequency of mode n calculated in ANSYS	Hz
$f_{nat,n}$	Natural frequency of mode n	Hz
f_r	Resonance frequency	Hz
FRF	Frequency response function	$m\ s^{-2}\ N^{-1}$
g	Standard gravity (~9.81 m/s^2)	-
G	Shear modulus	MPa
G_{AA}	Auto-correlation of $A(f)$	N^2
G_{AB}	Cross-correlation of $A(f)$ and $B(f)$	$N\ m\ s^{-2}$
G_{BA}	Cross-correlation of $B(f)$ and $A(f)$	$N\ m\ s^{-2}$
G_{BB}	Auto-correlation of $B(f)$	$m^2\ s^{-4}$
G_{xy}	Shear modulus in plane xy	MPa
G_{xz}	Shear modulus in plane xz	MPa
G_{yz}	Shear modulus in plane yz	MPa

$H1(f)$	Estimator for calculation of the frequency response function (FRF)	m s^{-2} N^{-1}
$H2(f)$	Estimator for calculation of the frequency response function (FRF)	m s^{-2} N^{-1}
H_{ij}	Frequency response function for DOFs i and j	m s^{-2} N^{-1}
$\underline{I}(\omega)$	Complex current	A
I_{ampl}	Current amplitude	A
i	DOF index for FRF	-
j	DOF index for FRF	-
k	Stiffness	kg m^{-1} s^{-2}
K	Stiffness matrix	kg m^{-1} s^{-2}
k_{fail}	Number of failed devices in recall analysis	-
l	Length	m
m	Mass	kg
M	Mass matrix	kg
N	Total number of modes	-
n	Number of a mode	-
N_{cyc}	Number of cycles in S-N curve (Woehler curve)	-
n_{sold}	Number of sold items/devices in recall analysis	-
PSD	Power spectral density	g^2 Hz^{-1}
Q	Q-factor	-
r	Angular frequency normalized by natural angular frequency ω_{nat}	-
R	Stress ratio or cycle coefficient	-
R_{CT}	Charge transfer resistance	Ω
R_i	Ohmic resistance	Ω
r_p	Normalized peak frequency	-
t	Time	s
T	Temperature	°C
$\underline{U}(\omega)$	Complex voltage	V
U_{ampl}	Voltage amplitude	V
$x(t)$	Generalized time signal	-
x_{RMS}	Root mean square value of generalized time signal	-
z	Relative displacement	m
$\dot{z}$	Derivation of z (velocity)	m/s
$\ddot{z}$	Derivation of $\dot{z}$ (acceleration)	m/s^2
$\underline{Z}(\omega)$	Complex impedance	Ω
α	Mass proportional damping coefficient (same as c_m)	1/s
β	Stiffness proportional damping coefficient (same as c_k)	s
$\gamma^2(f)$	Coherence	-
Δf	Frequency spacing	Hz
Δl	Extension of an original length l	m
$\Delta\varphi$	Phase difference	°
$\varepsilon_{f,n}$	Relative deviation of natural frequency values from measurement and ANSYS for mode n	%

ε_n	Tensile or normal strain	-
ε_t	Relative strain in the plane of the cross-section	-
ε_x	Extension along the longitudinal direction (equal to normal strain ε_n)	-
ε_y	Transversal reduction during strain	-
$\varepsilon_{\zeta,n}$	Absolute deviation of damping ratio values from measurement and ANSYS for mode *n*	%
ζ	Damping ratio	%
ζ_n	Damping ratio of mode *n*	%
λ_n	Complex eigenvalue or modal frequency of the n^{th} mode	rad/s
μ	Kurtosis	-
ν	Poisson's ratio	-
ν_{xy}	Poisson's ratio in plane *xy*	-
ν_{xz}	Poisson's ratio in plane *xz*	-
ν_{yz}	Poisson's ratio in plane *yz*	-
ϱ	Density	g/cm³
σ	Normal stress	MPa
σ_a	Alternating stress amplitude of cyclic stress	MPa
σ_D	Fatigue limit	MPa
σ_{max}	Largest algebraic value for the cyclic stress	MPa
σ_{mean}	Mean stress	MPa
σ_{min}	Smallest algebraic value for the cyclic stress	MPa
σ_p	Proportional stress limit	MPa
σ_u	Ultimate tensile strength	MPa
σ_y	Yield stress	MPa
τ	Shear stress	MPa
Φ	Modal matrix	-
ϕ^n	Normalized mode shape of mode *n*	-
ω	Angular frequency	rad/s
ω_1	First half-power bandwidth angular frequency	rad/s
ω_2	Second half-power bandwidth angular frequency	rad/s
ω_{nat}	Natural angular frequency	rad/s
$\omega_{nat,n}$	Natural angular frequency of mode *n*	rad/s
ω_r	Angular resonance frequency	rad/s

1 Introduction

Lithium-ion batteries are gaining importance with an increasing pace in many portable or mobile applications such as cellphones, notebooks, power tools, electric bikes and scooters, hybrid electric vehicles (HEV) and battery electric vehicles (BEV). This is due to their high specific energy, long cycle life and high efficiency [1].

The importance of lithium-ion batteries is reflected in numbers. In 2018, for example, seven billion cellphones and two million electric vehicles were in operation [2]. Additional accelerated replacement of existing technologies with more efficient and cleaner technologies is required to achieve a sufficient reduction in greenhouse gas emissions to meet the targets of the Paris agreement [3].

The success of this technological revolution strongly depends on the success of the lithium-ion batteries since the battery is a major factor in terms of cost, lifetime and safety considerations [1]. Nowadays, lithium-ion batteries are even being incorporated into aeronautical technologies such as more electric airplanes (MEA) or all electric airplanes (AEA) [4], helicopters [5] or unmanned aerial vehicles (UAV) [6] to improve the ecological footprint of air transportation [7]. At the same time, the aeronautics industry has very high requirements regarding reliability and safety. Because of the severity of the consequences of an accident, a catastrophic failure, for example, must occur less than once in 10^9 operational hours, also called a maximum of 1 failure in time (FIT) [8].

In contrast, several highly publicized incidents involving fire and explosion of lithium-ion batteries [9–17] still raise doubts regarding the applicability of lithium-ion batteries for safety critical applications. In addition, while the aging of lithium-ion batteries is less harmful than are safety critical issues, a long lifetime is important to achieve consumer acceptance and to reduce life-cycle costs (LCC).

To ensure the safe operation and long-life operation of the lithium-ion battery and to accelerate the required introduction of sustainable technology, a deep understanding of the different failure modes and the underlying failure mechanisms is of utmost importance. A good understanding will make it possible to improve the design, production and operation of batteries or cells. Additionally, it is of high interest if and how these failures can be prevented, detected, diagnosed, or predicted.

1.1 Motivation

In all mobile or portable applications, the lithium-ion battery and its cells must endure different mechanical loads. These loads can be categorized as abnormal abuse loads and normal loading conditions, which occur during the lifetime of a battery. Fig. 1 depicts these loads.

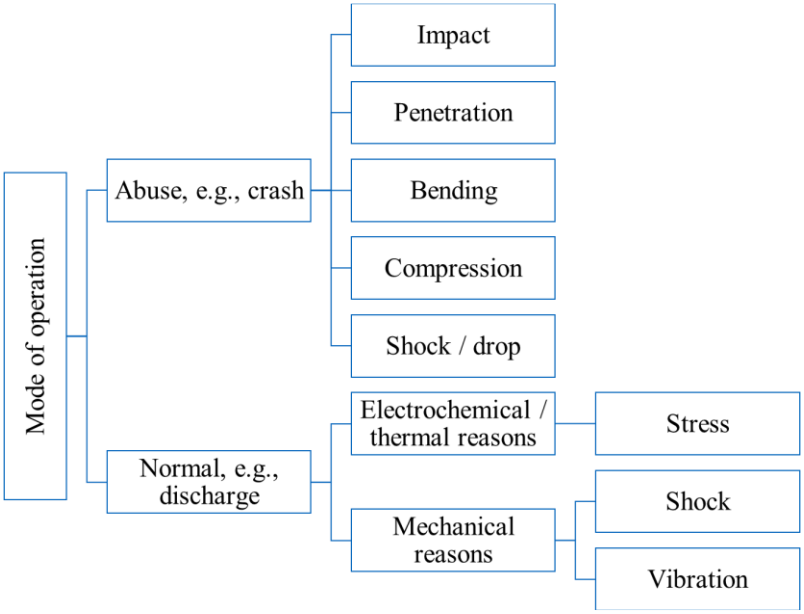

Fig. 1: Categorization of different mechanical impacts on lithium-ion cells and batteries

Regarding the first category, “abuse”, possible loads are, for example, impact, penetration, bending, compression, or shock. These loads can occur in case of the crash of an electric vehicle or electric bike or the dropping of a portable device during handling. This category also includes a huge share of the existing and available literature in the field of mechanical loads because of the importance of lithium-ion battery safety [18–49].

Another mechanical load that has to be endured by lithium-ion batteries during operation is a quasi-static stress which occurs during operation because of the intercalation-induced swelling [50–67] or thermal swelling [52,53,68,69] of the lithium-ion cells. In addition, externally applied bracing and the corresponding stress are investigated with regard to the impact on performance or aging of the constrained lithium-ion cells [54,61,70–78].

Vibrations can occur during operation for several reasons. These reasons are, for example, rough street surfaces in the case of electric vehicles, electric bikes, scooters or other road-based transportation devices or the vibration of a cordless power tool, e.g., a drill hammer. Other applications as ships, railways, airplanes, helicopters or others also pose requirements regarding vibration durability [79]. Shock loads can occur, for example, due to driving over curbsides or potholes in case of electric mobility or in the application of hammering cordless tools. The available but limited literature regarding vibration and shocks of lithium-ion cells is introduced in Section 3.2 in more detail.

This thesis aims to improve the understanding of vibrations and their impact on lithium-ion cells of different geometries with respect to safety and lifetime.

1.2 Framework

This thesis was developed mostly in the framework of the ReViSEDBatt cooperation project (Duration from 15.09.2017 – 14.09.2020, funded by the German Federal Ministry for Economic Affairs under grant number 03ETE004B for the sub-project of the Technical University of Munich [80]. The term ReViSEDBatt is the acronym for "**Re**sonances, **Vi**brations, **S**hocks, **E**xternal Mechanical Forces and **D**etection Methods for Lithium-Ion-**Batt**eries". These terms show that the ReViSEDBatt project is focused on the second branch of Fig. 1, dealing with the load conditions occurring during operation. Fig. 2 depicts the structure of the project.

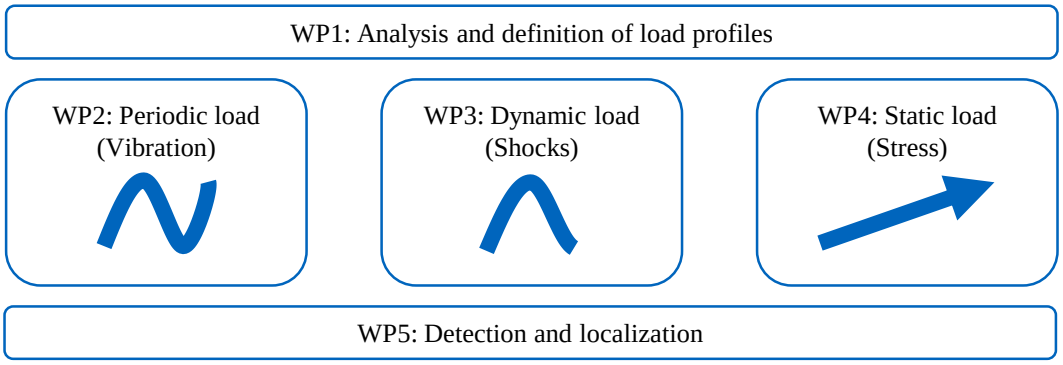

Fig. 2: Structure of the ReViSEDBatt project with the respective scientific work packages (WP)

The scope of the project is separated into five work packages (WP). The Institute of Electrical Energy Storage Technology and hence, the author of this thesis, participated in WP1 (load profiles), WP2 (vibrations), and WP5 (detection and localization). The other two, WP3 and WP4, concentrate on the other two loads, namely shocks in WP3 and stress due to bracing and swelling in WP4. The investigations are done on different levels, namely for cells, contact units, sensors, and modules, which incorporate the single components.

The purpose of ReViSEDBatt is to improve the aging and safety characteristics with respect to the described mechanical loads. This can be achieved through better cell and pack design, improved production processes, better testing procedures and better operational strategies. Other options are improved online diagnostics and detection methods to avoid or at least to detect or to predict critical conditions prior to a severe failure.

1.3 Purpose

The investigation of the possible slow and hidden degradation or of the sudden spontaneous failure of lithium-ion cells and its underlying failure mechanism caused by vibration is the focus of this thesis. The state of the art in Chapter 3 shows that the available knowledge about the influence or impact of vibrations was limited at the beginning of this thesis.

To understand if vibrations can cause any safety critical state of the lithium-ion cell or if aging of the cells might be accelerated, methods of theoretical risk assessment, load profile testing, mechanical, optical, and electrical characterization as well as finite element model (FEM) simulation are applied on lithium-ion cells of different size and shape.

The several different industries that participate in ReViSEDBatt, deal with a wide range of applications, for example, cordless systems, trains, forklifts and vehicles with different installation spaces, performance requirements and environmental conditions [81]. Therefore, all three popular cell formats, namely cylindrical cells, pouch bag cells and prismatic cells, are included in this thesis. For each respective investigation, the best choice out of these three formats was based on cell availability, relevance, state of the scientific knowledge, risk assessment and applicability to the investigation.

As a starting point, the scientific literature about the impact of vibrations on lithium-ion cells and packs, a wide range of failure reports, including battery related recalls, governmental investigations of incidents and other publicly available reports are revised for mechanically induced failure in general and for vibration induced failure in particular. In general, literature from other mechanical loads according to Fig. 1 is also considered in this thesis, because literature specifically dealing with vibration of lithium-ion cells is not available in sufficient depth and detail. In addition to the real-world incident analysis, a theoretical risk assessment with focus on mechanical loads is made with a failure mode, mechanism, and effect analysis (FMMEA). The procedure is explained in [82,83]. The FMMEA provides an overview of possible failure modes and mechanisms. The relevant research objectives are derived from these theoretical investigations.

Experimental durability tests based on load profiles are applied, exemplarily for the cylindrical 18650 cell type, to bridge my own research with the available scientific literature. It is also done to investigate the influence of vibrations on lithium-ion cells in an application-oriented approach as well as to investigate the significance of the inner cell design to derive cell design rules for high vibration durability.

At the same time, it must be recognized that testing all possible vibration profiles for all possible cells requires an enormous testing effort and is, therefore, often limited to a pass-or-fail criterion. It is at the same time limited in effectiveness in gaining knowledge about failure mechanism as well as in learning about sensitivities and influencing parameters such as cell design, state of charge (SOC) or the effect of nonlinear characteristics.

Therefore, one focus of this thesis is to understand the structural dynamics of lithium-ion cells. Structural dynamics describe the response of a structure to an excitation or, rather “how” the lithium-ion cell vibrates. Lithium-ion cells are very complex structures composed of many porous layers filled with electrolyte in different shapes and with different boundary conditions due to different cell housings or module designs. As the cell is charged or discharged, the mechanical behavior or structural dynamics further changes. Therefore, mechanical characterization methods are applied to understand the sensitivities to SOC, state of health (SOH), temperature, as well as nonlinear stiffness and damping. This characterization is done for all cell types, but is included only for both pouch cells and prismatic cells, since cylindrical 18650 cells are more difficult to investigate due to their small and stiff geometry.

The obtained data are used to build FE models, exemplarily included for the pouch cell in this thesis. Such FE models can be used for simulations after proper parameterization. They can provide better

insights into the inner cell or into unmeasurable or difficult to measurable quantities, such as the cell's internal stresses, which can determine possible fatigue of materials or components inside the cell.

The main research purpose of this thesis is to identify failure mechanisms caused by vibrations and to validate their occurrence, impact, and severity with respect to both safety and aging in a structural approach. In addition, the sensitivities to the cell design and parameters as SOC, SOH or temperature as well as different excitation types and levels with regard to nonlinear response are investigated in terms of structural dynamics.

If failure mechanisms are properly understood, recommendations regarding cell or pack design, the acceleration of tests and the detection or prediction of vibration-induced failures can be derived. While this chapter is meant to provide a quick overview, the more detailed and explicit research questions for this thesis are introduced in Section 3.5, based on the deduced state of the art.

1.4 Outline

Fig. 3 illustrates the structure of this thesis. Each chapter has its own focus on theory, experiments, or simulations. This reflects the chosen scientific approach to understand the vibration behavior of lithium-ion cells from the very beginning rather than doing mostly application-related durability and qualification testing.

Chapter 2 provides all the required fundamentals about the cells under investigation, the experiments and the applied methods and procedures. At the beginning, the theory behind vibrations and durability testing and all methods of characterization are introduced. This includes mechanical characterization using experimental modal analysis (EMA), electrical characterization using capacity check-ups and electrochemical impedance spectroscopy (EIS) and optical non-destructive characterization using computed tomography (CT). In addition, the fundamentals and underlying principles for the FEM approach, such as a short introduction of elasticity and fatigue, are given.

Chapter 3 provides a literature review to present the state of the scientific knowledge in the field of vibrations for lithium-ion batteries at the beginning of this thesis. While this thesis is dedicated to understanding the impact on the cell level, the literature review is not limited and includes pack and system investigations. Besides durability testing, investigations regarding application-related load profile determination, the applicability of testing standards of different organizations and the determination of structural dynamics, both experimentally and FEM based, are introduced. At the end of Chapter 3, the first conclusion of this thesis is given, summarizing insufficiently examined research questions in the field of this thesis. The objectives for this thesis are derived on this basis.

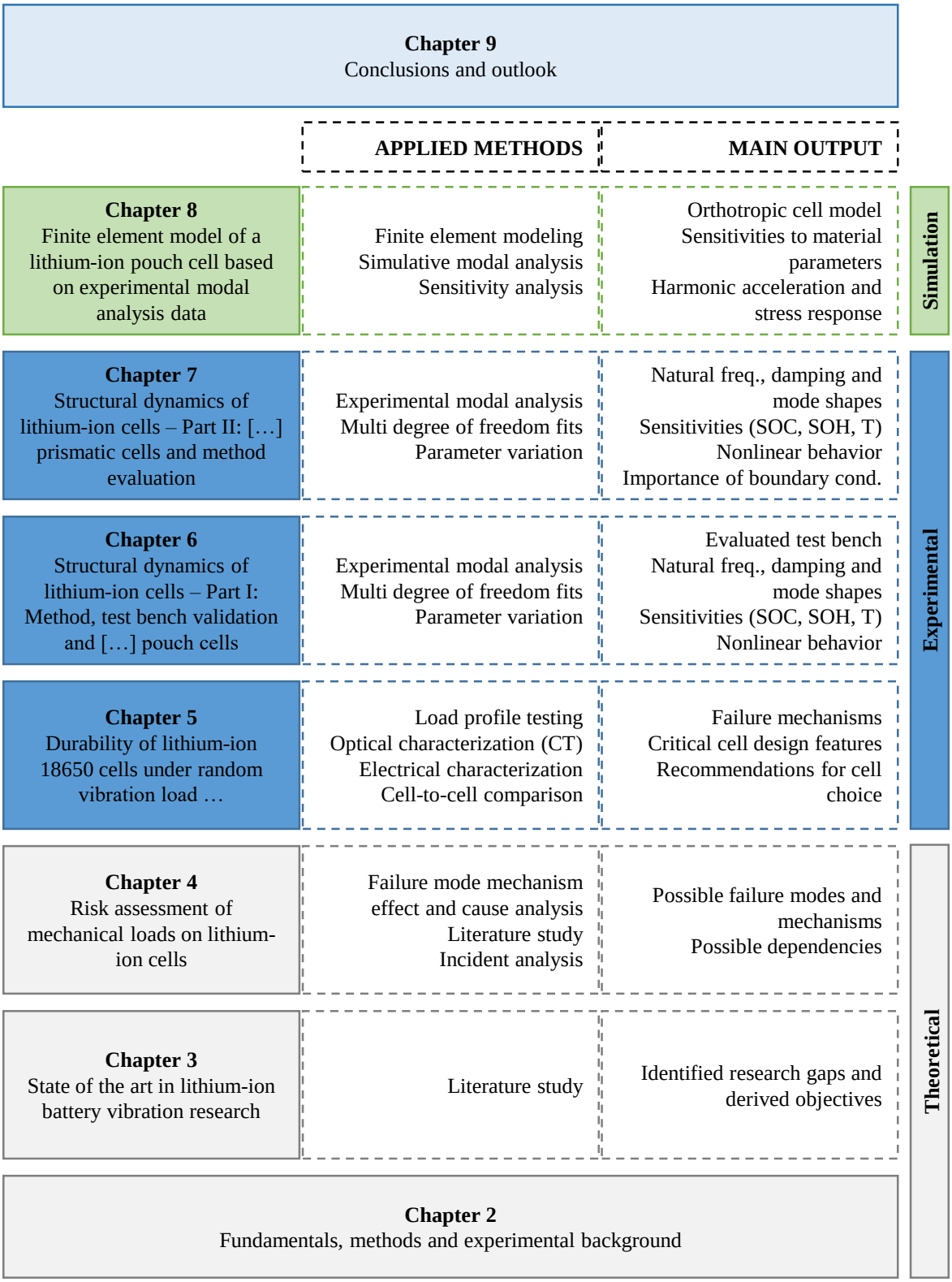

Fig. 3: Structure of this thesis

Chapter 4 is the first part of the overall risk assessment for vibration loading on lithium-ion cells. Public incidents associated with lithium-ion batteries are examined for mechanical causes. Secondly, based on the academic literature about the safety and reliability of lithium-ion batteries a failure mode, mechanism, effect, and cause analysis (FMMECA) is performed to identify possible failure

mechanisms, which are reconsidered in the following chapters as a guideline for the design of experiments (DOE). At the end of Chapter 4, a short summary is given to introduce the following investigations.

Chapter 5 is the bridge to the existing research in literature, which is mostly concentrated on 18650 cells and automotive random vibration. Therefore, the publication presented in Chapter 5 investigates random automotive vibration as well. In addition to the state of the art, this publication includes an inner cell design study and comparison of 18650 cells and an investigation of the influence of cyclic aging on vibration durability. Recommendations for the cell design regarding random vibration durability are given at the close of Chapter 5 and the respective journal publication [84].

The Chapters 6 and 7 describe the use of EMA to identify the structural dynamics of lithium-ion cells and are both presented as parts of a series of papers. Part I of the series is presented in Chapter 6 and introduces the test bench, which was especially designed for this investigation and during this thesis. In addition, the EMA method and the results of the investigations for a consumer pouch cell are presented. The pouch cell is characterized by means of natural frequencies, damping ratios and the respective mode shapes. These parameters are investigated with respect to their sensitivities from SOC, SOH, aging history, temperature, and excitation level.

In Chapter 7, the second part of the series of papers investigating the structural dynamics of lithium-ion cells is presented. In this paper, a large-format prismatic cell with a nominal capacity of 94 Ah for BEV application is investigated using EMA. Again, the sensitivities to SOC, different aging conditions, temperature and excitation level are presented. The findings are compared with the results from the pouch cell in Chapter 6, revealing the importance of interfaces and boundary conditions. At the end of this paper, the applicability of the EMA for lithium-ion cell research is evaluated, based on my experiences and results.

Chapter 8 presents the possible use of data that can be obtained through EMA. The findings and results from the characterization of a lithium-ion pouch cell in Chapter 6 are applied to the design of a first FE model of the respective cell. The parameterization of the model reveals several sensitivities and enables the parameterization of several elastic parameters of an orthotropic model. It is also shown that for the full optimization of an orthotropic model and to obtain, for example, reliable stress responses, the measured frequency response functions (FRF) must be used directly in combination with the harmonic response toolbox in the FEM software for further model optimization. If this is successful, it would be an important step in investigating if the high-cycle fatigue (HCF) of an inner cell component, such as the separator or the electrodes, can be caused by vibration.

Chapter 9 closes with a short conclusion for each of the objectives of this thesis and gives some recommendations where to put focus in future research in this field.

2 Fundamentals, methods, and experimental background

This chapter presents the background information required to understand the conducted experiments and investigations. The focus is on the methods that have been used throughout this thesis and their respective characteristics. This includes the theoretical methods for risk assessment in Section 2.1, the durability testing and the required definitions (Section 2.2) as well as the several experimental characterization methods in the mechanical (Section 2.3), electrical (Section 2.4) and optical (Section 2.5) domain. The information about the cells under investigation (Section 2.6) and the test bench (Section 2.7) which was developed for the majority of the presented investigations, gives the experimental framework, while Section 2.8 concludes this chapter with the fundamentals for the simulative part of this thesis.

2.1 Risk assessment method

Numerous methods exist for the theoretical evaluation and assessment of risk, reliability or safety [8,85–87]. The development of these methods has been driven by the high requirements for safety and reliability, e.g., of civil airborne systems [8], aerospace systems [88] or nuclear power plants [87].

In this work, the method of failure mode and effect analysis (FMEA) [8,83,85,87] is chosen because of its simplicity. FMEA uses a simple table to make a collection of the possible failure modes and effects. FMEA usually contains further information, such as the failure cause [89].

The advantage of FMEA is its general simplicity due to the simple tabular depiction. A disadvantage of the FMEA method is that logical failure sequences and complex interdependencies cannot be easily described. FMEA tables also have limitations in properly displaying combined failure modes in case of complex systems [90]. Especially for complex systems, many possibilities exist to describe the system in FMEA. The definition and distinction of failure mode, mechanism, cause, and effect often becomes confused depending on the level (e.g., cell, module, pack for batteries) and the depth of the analysis. Therefore, the respective terms must always carefully defined for each analysis, which is done in the following, based on [85].

Birolini describes failure mode as the symptom by which the failure is observed [85]. In the case of a lithium-ion cell in this work, the possible failure modes are “open”, “short” and “wear out”. Especially in case of an analysis on the module level including battery management system (BMS) and connectors, more failure modes such as “intermittent contact” or “parameter shifts” [8] can be included.

The failure cause can be intrinsic due to weaknesses or extrinsic, e.g., due to misuse or mishandling [85]. In this work, the most relevant failure cause is extrinsic in terms of mechanical loads, especially vibrations.

The effect of a failure depends on the level of analysis, as the effect can be the cause for further failures on another level [85]. The effect is of subordinated importance in this work, but could be, for example, a heat build-up in a cell because of a short circuit (SC).

The highest importance in this thesis is given to the failure mechanism that describes the physical, chemical or other process of the failure [85]. Understanding the failure mechanism for the vibration-caused failure of lithium-ion cells can help improve or accelerate vibration testing, improve the cell or pack design, identify methods for diagnostic and avoid critical loads in the application by suitable countermeasures.

Therefore, throughout this thesis, the term FMMEA is used to highlight the importance of the failure mechanism. The FMMEA is used to capture the assumptions and observations made in the literature in a structured manner in Chapter 4.

2.2 Vibration and durability testing

Vibration durability testing is a common practice in the industry to evaluate the durability of a specific component under vibration load. These tests are also part of many regulations and standards [91,92].

Durability tests are usually performed under laboratory conditions to ensure up front that the device under test does not fail in later operation and consumer usage at different stages of product life. It is important to achieve a sufficient representation of the real-world load in a reasonable testing duration. [93]

Subsection 2.2.1 provides a brief introduction to the simplest mechanical model and the required definitions for an understanding of the following fundamentals and methods. Secondly, a brief introduction of different kinds of vibrations and how they can be characterized is given in Subsection 2.2.2. Subsection 2.2.3 briefly introduces specific profiles with respect to different applications, and Subsection 2.2.4 offers an overview of the concept of combined loads, which have been designed during this thesis.

2.2.1 Important definitions for mechanical systems

To understand the impact of vibrations on an item or a structure, it is helpful to establish a model concept that can describe the structure as a mathematical system. The terms introduced here are especially valuable for understanding the methods for the mechanical characterization in Section 2.3.

The simplest representation of a mechanical system is the so-called single degree of freedom (SDOF) system. This system consists of one perfect mass (perfectly rigid and non-dissipative of energy), a perfect stiffness element (massless and perfectly elastic) and a perfect damping element (massless and perfectly rigid). This system is, furthermore, only allowed to move in one direction and is constrained in all other directions. In an unconstrained condition, this system would have three

degrees of freedom (DOF) to define its point in space. A real solid indeed has six DOF in general, three translational and three rotational (the three rotational DOF do not apply just to a concentrated and perfect mass). Real world structures are of course not perfect in terms of the definition above and are much more complex than the SDOF model. These real structures exhibit continuously distributed masses as well as stiffness and damping elements, which are coupled, instead of being separated. If a system is deformable, it has an infinite number of DOF. [79]

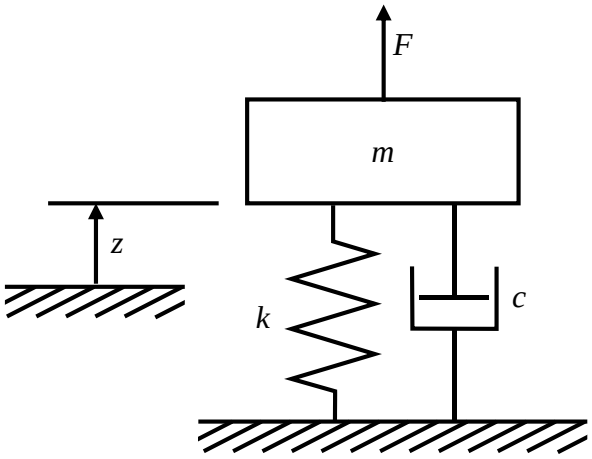

Fig. 4: Schematic depiction of an SDOF system with stiffness k, damping c, mass m and a relative displacement z due to the external force F, adapted from [79]

Since this causes an infinite number of elements, it is often both interesting and required to simplify the structure into a lumped parameter system, finding a good compromise between accuracy and computational effort. This is called a multi degree of freedom (MDOF) model. Exploitation of these models shows that the lumped parameter model vibrates in certain ways, which are called modes. Each of these modes has its characteristic movement, called mode shape and occurs at its respective natural frequency. If the system is excited, the response at any point on the structure is a combination of the corresponding mode shapes of all excited frequencies. If the system or structure can be assumed as linear, the principle of superposition can be used. [79]

For the sake of simplicity, further explanations are made for the simple SDOF system. The SDOF system is also of interest because it is often used to evaluate or compare the severity of different vibrations or shocks. The underlying assumption is that, if a vibration A causes a higher relative displacement response for an SDOF system than a vibration B, that vibration A is more severe for a complex structure with several DOF, too. [79]

This principle is the basis for methods such as the fatigue damage spectrum (FDS) [94] and the shock response spectrum (SRS) [95], which both are based on the assumed response of an SDOF system and the comparison of relative displacement responses named above.

An SDOF system which is excited by a force can be described according to Eq. (1) and Fig. 4, adapted from [79]. Here m is the mass, c is the damping constant and k describes stiffness. The value z is the resulting relative displacement of the mass to the support due to the exciting force F with its derivatives velocity $\dot{z}$ and acceleration $\ddot{z}$.

$$m\ddot{z} + c\dot{z} + kz = F \tag{1}$$

With some conversions and calculations, an equation for the natural frequency f_{nat} or natural angular frequency ω_{nat} in case of an undamped system and the damping ratio ζ for a damped system can be obtained according to the Eq. (2) and (3). [79,93]

$$\omega_{nat} = 2\pi f_{nat} = \sqrt{\frac{k}{m}} \tag{2}$$

$$\zeta = \frac{c}{c_0} = \frac{c}{2m\omega_{nat}} = \frac{c}{2\sqrt{km}} \tag{3}$$

The term c_0 is here the critical damping coefficient, which is the minimum of c, where the movement is non-oscillatory [79].

The natural frequency f_{nat} is similar, but not identical to the resonance frequency f_r for lightly damped systems. In case of an undamped system ($\zeta = 0$), f_{nat} is equal to f_r, according to Eq. (4), adapted from [93].

$$\omega_r = \sqrt{1 - 2\zeta^2}\,\omega_{nat} \tag{4}$$

Eq. (4) applies for the FRF, which is calculated from displacement response and force excitation, while the angular resonance frequency ω_r in the case of an acceleration response can be calculated according to Eq. (5) [93]. Further information on the various definition of an FRF are given in Subsection 2.3.1.

$$\omega_r = \frac{1}{\sqrt{1-2\zeta^2}}\,\omega_{nat} \tag{5}$$

From Eq. (4) and Eq. (5), it becomes apparent that for a small damping ratio, e.g., $\zeta \leq 0.1$ (10%), the deviation of resonance frequency and natural frequency is below 1.01%.

For lightly damped systems, the half power bandwidth method can be applied for calculation of the *Q*-factor. The *Q*-factor defines the sharpness of the resonant peak and is defined by Eq. (6) and (7). ω_1 and ω_2 are the frequency values with an amplification of $1/\sqrt{2}$ (-3 dB) of the peak value and are named half-power points. [93]

$$Q = \frac{\omega_{nat}}{\Delta\omega} = \frac{1}{2\zeta} \tag{6}$$

$$\Delta\omega = \omega_2 - \omega_1 \tag{7}$$

Since only a brief overview without detailed derivations of all quantities can be given in this thesis, the interested reader is referred to [79,93].

Natural frequencies and damping ratios are the major characteristics to be obtained through EMA and shall be the key take-away of this subsection.

2.2.2 Sine and random vibration profiles and required definitions

Devices, components, or structures must endure different kind of vibrations in different applications. These vibrations can be classified as different kinds of vibrations, which are [79]:

- sinusoidal vibration (single sine or multi sine)
- swept sine vibration
- random vibration
- a combination of the preceding vibrations, e.g.
    - sine on random
    - swept sine on random

In real-world conditions, sine loads can occur, e.g., due to the rotational movement of helicopter rotor blades or ship propellers. In addition, sine loads are popular for laboratory investigations due to the deterministic nature of the signal and the simple mathematical treatment, easy cycle counting etc. Furthermore, sine sweeps are common practice for the identification of resonance frequencies. During a sine sweep, the frequency is varied in a linear or logarithmic manner. The sine excitation of the respective resonance frequencies is also popular for stress-endurance tests because resonance excitation can impose severe stress into a structure or device. [79]

Single sine, multi-sine or sine sweep vibration can be described in both time and frequency domain. For the description in the frequency domain, the spectral representation is the common presentation with each single sine appearing as a single peak with its respective amplitude at its frequency value. [79]

Regarding real-world applications, random profiles reflect the real environment often better than do sines or sine sweeps and are often used for durability testing. In addition, each resonance can be excited simultaneously. [96]

Random vibrations, represented as wideband noise with Gaussian distribution, occur in automotive applications and in other land-based means of transport as railways due to the irregularities of the road surface or the rail tracks [79,96].

Random vibrations have a stochastic instead of a deterministic nature and are usually depicted using power spectral density (PSD) plots. The application of spectra is not useful for random vibration, because the amplitudes of the spectra would differ, depending of the frequency spacing Δf. [96]

The PSD normalizes the respective value, e.g., any measured acceleration *acc* and its respective root mean square (RMS) value acc_{RMS} according to Eq. (8) and makes the representation independent of the chosen frequency spacing. [96]

$$PSD(acc) = \frac{{acc_{RMS}}^2}{\Delta f} \tag{8}$$

The PSD representation of different random profiles can be compared with respect to frequency content as well as load level in terms of power spectral density. The overall RMS level of the vibration can be obtained through the area below the PSD curve. For the full description of a random profile, other important parameters, such as the load duration are required. Random vibrations have further

stochastic characteristics. The instantaneous probability distribution of the signal can differ for identical PSD. [96]

In the simplest case, the probability distribution follows a Gaussian (normal) distribution, but the analysis of load profiles in the ReViSEDBatt project showed that this is not always the case in real world-applications and, more specifically, are not valid for cordless power tools.

These deviations from the normal distribution can be described by the parameters of skewness and kurtosis. In the following, kurtosis μ is discussed since it is assumed to have an impact on fatigue damage. Kurtosis μ describes the distribution of the peak values. A value of $\mu = 3$ indicates a normal distribution. A value of $\mu < 3$ indicates a truncated signal or the existence of sinusoidal components, while a kurtosis $\mu > 3$ indicates the presence of more peaks of high value than in the normal case. [96]

Fig. 5 depicts an example with two different random vibrations profiles that exhibit the same PSD in Fig. 5b and have the same overall RMS level of 1.2 g_{RMS}, but different kurtosis values of 3 and 7. This represents a normal distribution and a distribution with more pronounced peaks of higher amplitude.

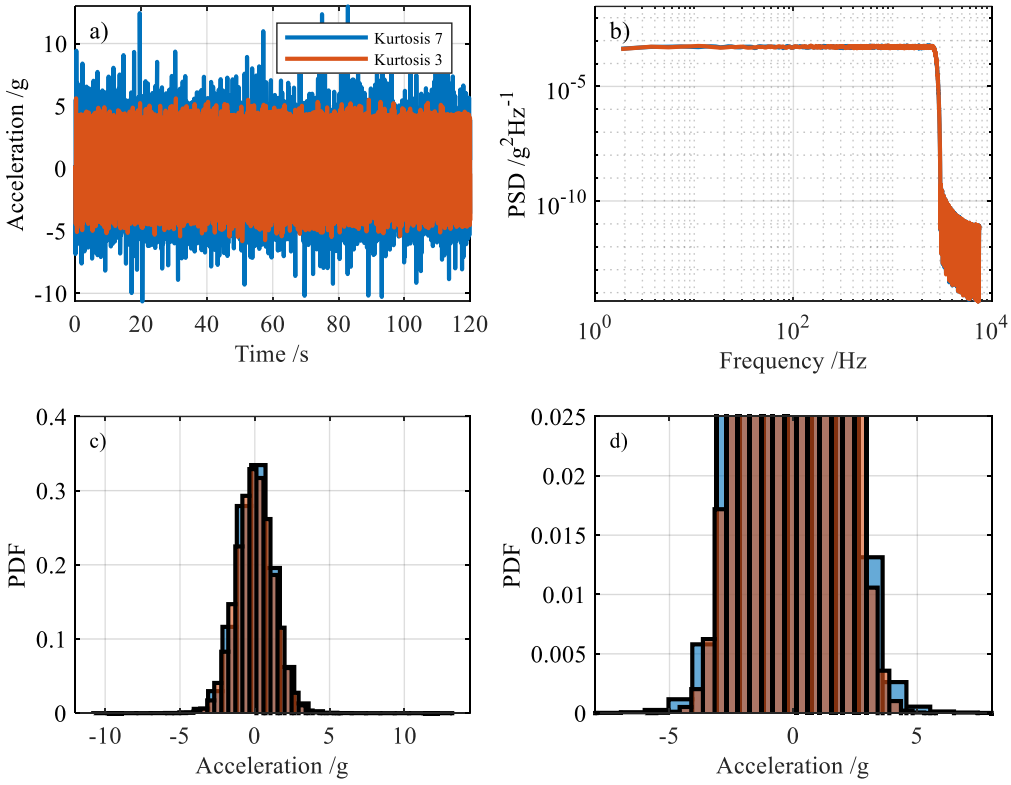

Fig. 5: Exemplary comparison of two random profiles with identical RMS value and identical PSD, but different kurtosis of $\mu = 3$ and $\mu = 7$; a) time domain representation of the signals, b) power spectral density (PSD) representation, c) probability density function (PDF) of the acceleration amplitudes with zoomed view in d). The PSD spectra were calculated using the vibration data toolbox from [97].

The time domain representation in Fig. 5a shows more significant peaks for the signal with a kurtosis of 7, which is also visible in the histogram of the probability density function (PDF) in Fig. 5c and the zoom in Fig. 5d. Both show a higher probability of peaks with higher amplitudes for the signal

with a kurtosis of 7. Therefore, kurtosis is an important value to consider in vibration durability testing as the higher probability of higher amplitudes usually causes the profile to be more severe.

Another important and corresponding value is the crest factor *cf*, which describes the ratio between the largest peak in the signals and the RMS value of the signal according to Eq. (9) for a generalized signal $x(t)$. Taking the two signals from Fig. 5 into account, the respective crest factors would be $cf_{\mu 3} = 4.85$ and $cf_{\mu 7} = 10.8$ (calculated with the toolbox from [97]). Besides its impact on durability testing, the crest factor is of high importance for mechanical characterization with respect to nonlinearity (see Chapter 6 and 7). [96]

$$cf = \frac{\max\left(|x(t)|\right)}{x_{RMS}} \tag{9}$$

Further, very detailed information about vibrations and shocks, their properties, related fatigue and more can be obtained from the book series of Lalanne [79,94–96,98] and from De Silva et al. [93].

2.2.3 Application-specific vibration profiles

In the ReViSEDBatt project the following applications are considered:

- Automotive
- Logistics, e.g., forklifts
- Railway transportation
- Cordless tools

Automotive vibrations are investigated in this thesis due to their importance in the scientific literature. The vibrations in logistics probably do not differ extensively from the automotive application because both are ground-based means of transportation.

No self-measured load profiles from the ReViSEDBatt project were available at the time of this thesis for the first three applications. Therefore, the vibration profiles used in available scientific literature, which are based on testing standards and regulations, were taken as the basis for the durability testing in Chapter 5. This also offers the advantage of better comparability to the results of other researchers.

Load profiles for the battery packs of cordless tools were available at the time of this thesis for different tools (e.g., rotary hammers, fastening tools, saws) and different states of operation. Accelerometers were placed on the surface of the battery pack during load profile recording. The clarification of transmissibility from pack to cell level was an on-going topic to the time of this thesis. Hence, no cell tests with load profiles measured on cordless tools could be included in this thesis and are part of future research. Nevertheless, a brief analysis of the power tool load profiles revealed higher acceleration amplitudes and a wider frequency range as well as higher share of the signal power at higher frequencies in the PSD representation in comparison to automotive application.

2.2.4 Combination of vibrations and other loads

Damage scenarios that are more complex include the combination of different loads and abuse conditions. These might be drops prior to a certain amount of vibrations (e.g., during transport or during handling of a power tool) or safety-critical events, e.g., an overcharge condition, after a

damage of the current interrupt device (CID) with potentially reduced functionality of the CID [99] to name only two examples.

In the course of this thesis, the combination of drops and vibrations was investigated in a pre-study as part of the master thesis from Christian Schenk [100] based on the idea from and under supervision of the author of this thesis. For these investigations, cylindrical cells of the type Molicel IHR18650A and A123 18650M1A were pre-loaded with several drops through a 2 m long downpipe in axial orientation. After leaving the downpipe, the cells dropped on a solid plate with the negative pole downside. These drops were performed by Markus Spielbauer at the University of Applied Sciences in Munich during a joint project to investigate combined loads on lithium-ion 18650 cells. An overview of the results is given in Appendix A.1.

Further studies with a wider range of different 18650 cells and variations, such as the number of drops, vibration amplitude, etc., are an on-going topic while this thesis is written.

2.3 Mechanical characterization methods

The method for the mechanical characterization in this thesis is called EMA. Detailed background information on EMA is available in [93,101–103].

Through the course of EMA, a mechanical system can be described by its natural frequencies, modal damping ratios and mode shape vectors. This information can be used to obtain an "experimental model," which can be applied for the purpose of system analysis, fault detection and diagnosis, design, and control. Modal analysis enables the engineer to identify the extent and location of severe vibration. The results of mechanical characterization through modal analysis, namely natural frequencies and *Q*-factors (the reciprocal of the damping ratio) are further required to understand the stresses, e.g., due to a shock, and the subsequent damage or fatigue. [93]

Besides the natural frequencies and *Q*-factors or damping ratios, modal analysis can reveal mode shapes. Mode shapes are the characteristic displacements that occur in the case of the excitation of a natural frequency. The knowledge of mode shapes might deliver valuable information, e.g., about displacement of inner components and subsequent stress localizations.

Experimental and simulative modal analyses based on FEM are combined in this thesis. The direct measurement of in-situ stress in a structure is generally difficult [104] and no method to measure it for a lithium-ion cell could be identified. Therefore, the FEM approach can give further insights and is introduced in Section 2.8 together with a general introduction of the required knowledge in terms of elasticity, stress, and fatigue.

During EMA, several FRF are measured. FRF, which is initially and briefly introduced in Subsection 2.2.1 is further explained in Subsection 2.3.1. Subsection 2.3.2 introduces the procedure of the EMA.

2.3.1 Frequency response functions

Various definitions of FRF exist depending on the various possible excitation and response signals. While a very detailed derivation of all possible variations is given in [79], the main representations

are summarized here. Table 1 provides an overview of some of the most common frequency-response functions according to [93]. The normalized frequency r is defined according to Eq. (10) with the natural angular frequency ω_{nat}. The value r_p in Table 1 is, according to this definition, the normalized peak or resonance frequency.

$$r = \frac{\omega}{\omega_{nat}} \tag{10}$$

*Table 1: FRFs for different combinations of response and excitation in the case of a simple oscillator or SDOF system. *In case of transmissibility, the FRF is the same for both force (force/force) and motion transmissibility (e.g., acceleration/acceleration). Information in this table is reproduced from* [93].

Response / Excitation	**Normalized FRF**	**Normalized peak frequency r_p**	**Normalized peak magnitude**
Displacement / Force	$\frac{1}{(1-r^2)+2j\zeta r}$	$\sqrt{1-2\zeta^2}$	$\frac{1}{2\zeta\sqrt{1-2\zeta^2}}$
Velocity / Force	$\frac{jr}{(1-r^2)+2j\zeta r}$	1	$\frac{1}{2\zeta}$
Acceleration / Force	$\frac{-r^2}{(1-r^2)+2j\zeta r}$	$\frac{1}{\sqrt{1-2\zeta^2}}$	$\frac{1}{2\zeta\sqrt{1-\zeta^2}}$
Transmissibility*	$\frac{1+2j\zeta r}{(1-r^2)+2j\zeta r}$	$\frac{\sqrt{\sqrt{1+8\zeta^2}-1}}{2\zeta}$	$\sqrt{1+\frac{1}{4\zeta^2}}$ (For small ζ)

FRF with acceleration response and force excitation (also called accelerance [105]) is the common method for experimental modal analysis because there are no velocity or displacement transducers available [105]. Nevertheless, these variations can be easily calculated through integration of the acceleration response. With the known mathematical FRF representations in mind, Subsection 2.3.2 gives the procedure for the experimental determination of the FRF by EMA. It must be added that the equations from Table 1 describe the mathematical model, also called modal model in [102]. They can be linked with the actual measurements, called the response model in [102], through a fitting procedure, which is also introduced in Subsection 2.3.2.

2.3.2 Experimental modal analysis

EMA [93,101,103] is a powerful tool to describe structural dynamics, including resonance frequencies, structural damping and the mode shapes of the structure under test. For the explanation of these terms, please refer to Subsection 2.2.1. Fig. 6 gives a schematic depiction of the procedure. A set of responses is obtained through EMA in the first step. A modal model can be constructed through a fitting procedure. These two steps define the main body of two included peer-review journal publications in the Chapters 6 and 7 for pouch and prismatic cells, respectively. The third step, to develop a spatial model based on results from the EMA, is the scope of Chapter 8 in this thesis, exemplarily shown for pouch cells.

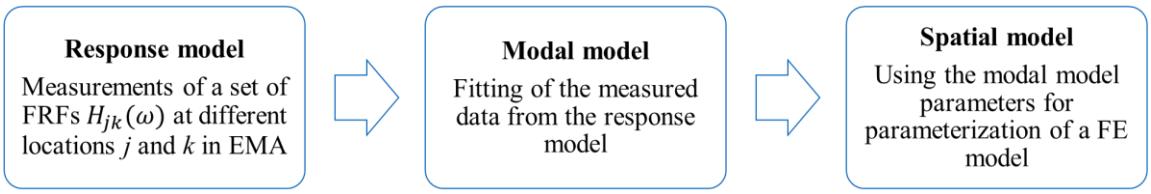

Fig. 6: Schematic depiction of the procedure to obtain a modal model and an FE-based spatial model of a structure based on the EMA, adapted from [102]

Fig. 7 shows the procedure to obtain a FRF during modal analysis, based on the explanations in [102] and own measurements. A structure (in this case a simple aluminum block) is excited by a signal $a(t)$ and a response $b(t)$ is measured. The signals $a(t)$ and $b(t)$ can be of a different kind, as introduced in the preceding Subsection 2.3.1. In this work, $a(t)$ is the force excitation and $b(t)$ is the acceleration response. The excitation is performed with burst random (random excitation with time period of zero excitation at the end) due to advantageous linearization and leakage minimization as it is explained in Chapter 6 and in [106]. The signals in time domain $a(t)$ and $b(t)$ are transformed into the frequency domain $A(f)$ and $B(f)$ with the frequency f in the second step (second column in Fig. 7).

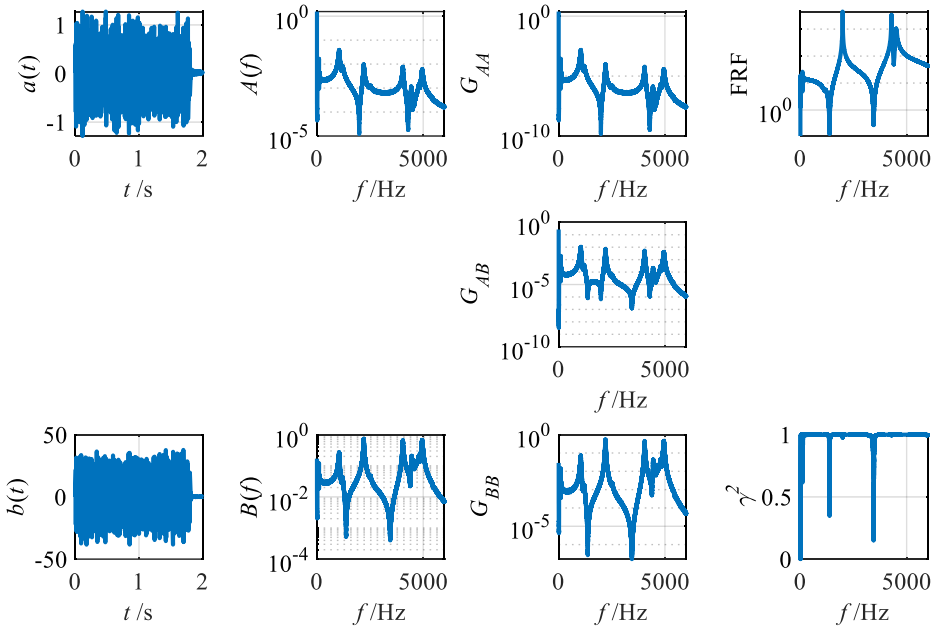

Fig. 7: Procedure for FRF estimation based on time domain burst random measurements, reproduced from [102]

In the case of random excitation, the measurement must be repeated for several times to increase the signal-to-noise-ratio (SNR) through averaging. Complex quantities cannot be averaged directly since varying phases can cause the signal to be averaged to zero. Therefore, the autocorrelation G_{AA} and G_{BB} and cross-correlation G_{AB} or G_{BA} are calculated as depicted in the third column of Fig. 7. Based on auto-correlation and cross-correlation, both FRF and coherence $\gamma^2(f)$ can be calculated as depicted in the fourth column of Fig. 7. [102]

For the FRF calculation, various estimators are available in literature. The two most usual estimators *H1* and *H2* are given in the Eq. (11) and (12). The right estimator must be chosen depending on if noise at the input or at the output is more dominant. The estimator *H1* is recommended in the case of noise at the output, while the estimator *H2* is recommended in the case of noise at the input. [102]

$$H1(f) = \frac{G_{AB}(f)}{G_{AA}(f)} \tag{11}$$

$$H2(f) = \frac{G_{BB}(f)}{G_{BA}(f)} \tag{12}$$

Bilosova recommends the use of the *H2* estimator in case of shaker excitation, since the excitation signal becomes noisy in the vicinity of resonances, especially for lightly damped structures, because the structure behaves like a short circuit at a resonance [102].

In this thesis, a comparison of *H1* and *H2* showing no differences or advantageous results for *H2*. Therefore, *H1* is used throughout this thesis. This deviation from theoretically expected behavior can be due to the complex structure of the cell with high damping ratio or the usage of an accelerometer with low sensitivity due to weight constraints. This can reduce the SNR of the response signal, which supports the choice of the *H1* estimator.

Coherence $\gamma^2(f)$ is a useful quantity to evaluate the quality of the results [102,107]. Nevertheless, coherence has its limitations and must be used carefully, especially if nonlinear structures and sine excitations are combined [106]. The respective limitations of the coherence value are discussed in Chapter 6 with regard to the complex pouch cell characterization. Coherence is calculated by Eq. (13) [102].

$$\gamma^2(f) = \frac{|G_{AB}(f)|^2}{G_{AA}(f) \times G_{BB}(f)} \tag{13}$$

Values close to 1 indicate measurements of high quality, while lower values indicate different kind of possible measurement errors, e.g., noise at input or output or system nonlinearities. [102]

The procedure explained in Fig. 7 is used to obtain the response model from Fig. 6. If the structure is excited at several positions *k* and the response is measured at several positions *j*, a set of FRFs $H_{jk}(\omega)$ is obtained. With a sufficient and correctly chosen set of locations, the characteristic mode shapes for each natural frequency can be revealed. [103]

The preceding sections introduced an SDOF system because it is the easiest representation. Nevertheless, usual real-world systems must be described as an MDOF system.

EMA is a linear method and, therefore, the principle of superposition applies, the MDOF system can be represented as the sum of a linear combination of several FRFs of SDOF systems. The measurable FRF H_{ij} with positions *i* and *j* and the different modes *n*, assuming a total number of modes *N*, is given by Eq. (14) in the modal space. [107]

$$H_{ij}(\omega) = \sum_{n=1}^{N} H_{ij}^{n}(\omega) = \sum_{n=1}^{N} \frac{\phi_i^n \times \phi_j^n}{{\lambda_n}^2 - \omega^2} \tag{14}$$

λ_n is the complex eigenvalue or modal frequency of the n^{th} mode. Φ^n is the normalized mode shape vector of the n^{th} mode (equal to the n^{th} column in the modal matrix [Φ]). The value ω is the angular frequency. The FRF of a system can also be represented by its poles and residues [102,107].

With Eq. (14) or any other representation of a modal model, a fitting algorithm can be used to adjust the modal parameters to the experimental results from the response model. Several algorithms for both SDOF and MDOF systems and different characteristics (e.g., light or strong damping) are available in the m+p Analyzer software [108]. Further information on the used fitting algorithm is always given at the respective location for each investigation in Chapter 6 and Chapter 7 and the respective publications [109,110].

2.4 Electrical characterization methods

The electrical characterization is used for evaluation of possible damage of the lithium-ion cells caused by the applied vibrations or load conditions. The EIS and the capacity checkup are used to examine the two most important and common performance parameters impedance and capacity and are introduced in the Subsections 2.4.1 and 2.4.2.

2.4.1 Electrochemical impedance spectroscopy

EIS is a popular method for characterizing lithium-ion cells. During EIS, the cell is excited with a sinusoidal current or voltage of small amplitude around its equilibrium and the respective response is measured. By varying the excitation frequency, the frequency-dependent complex impedance $\underline{Z}(\omega)$ can be calculated according to Eq. (15) with the complex voltage $\underline{U}(\omega)$ and current $\underline{I}(\omega)$. [111,112]

$$\underline{Z}(\omega) = \frac{\underline{U}(\omega)}{\underline{I}(\omega)} = \frac{U_{ampl}}{I_{ampl}} \mathrm{e}^{\mathrm{j}\Delta\varphi} \tag{15}$$

U_{ampl} and I_{ampl} are the respective amplitudes of both voltage and current. $\Delta\varphi$ is the phase difference between the two signals. Because EIS is a method for linear, time-invariant, and causal systems, care must be taken to use a small excitation to avoid nonlinear responses. In addition, measurement duration must kept small enough to avoid time-variance, e.g., due to aging, during measurement. Measurements at very low frequencies can also change the SOC of the cell during one half-sinusoidal excitation and, therefore, violate the condition of time-invariance. Therefore, the minimum measurable frequency value for the EIS of a lithium-ion cell is limited. [113,114]

In this thesis, galvanostatic EIS (current excitation) is used with current amplitudes in a range from 50-150 mA, depending on the impedance of the respective cell to ensure linearity and to achieve a sufficient SNR. The advantage of galvanostatic EIS is that the current is well defined and, therefore, the maximum amount of charge and the respective ΔSOC can be calculated.

EIS is often used directly or in combination with methods such as the distribution of relaxation times (DRT) to investigate different loss processes inside the lithium-ion cell, to attribute them to the respective electrodes [114–116] and to investigate aging [117,118].

In this thesis, EIS is used to extract characteristic values that can be easily compared before and after vibration testing. These values are ohmic resistance R_i and charge transfer resistance R_{CT} and can be

found in Fig. 8. The value R_i is defined as the intersection of the impedance curve with the real axis, while the R_{CT} is given by the diameter of the half circle. This half circle includes possible influences due to passive layers [119], which cannot always be resolved in the spectra because of similar time constants and are, therefore, included in R_{CT} for the sake of simplicity. Interpolation between two nearest neighbors is used to estimate R_i and R_{CT} as precisely as possible.

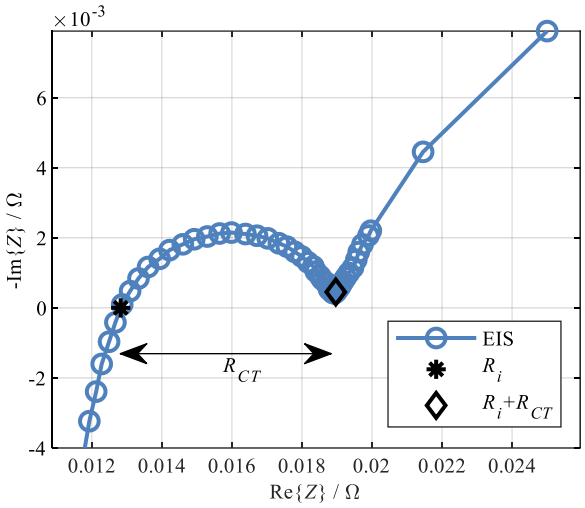

Fig. 8: Exemplary EIS in a Nyquist plot representation with the two characteristic values ohmic resistance R_i and charge transfer resistance R_{CT}, based on the definitions in [119]

While EIS delivers valuable information, there are some shortcomings. One shortcoming is that processes with similar time constants overlap in the spectrum and are hard to resolve, e.g., if anode and cathode shares must be distinguished [115]. The second shortcoming, which is especially important in this thesis, is that due to the large surface area of lithium-ion electrodes, small disturbances, and damage such as a local short circuit, a decontamination, or local cracks and delamination are difficult to detect. These local disturbances are only small factors in a virtual parallel circuit and often have a negligible influence on the measurable EIS. This phenomenon was also observed in another publication, which is not included in this thesis. Local loading of 18650 cells with a nail caused no changes in EIS before the first occurrence of an internal short circuit (ISC), while a large area compression caused an increase in ohmic resistance [120].

Therefore, the capability of EIS as a method for damage or failure detection is limited. Nevertheless, there are not many alternatives readily available. For this reason, EIS is a very common method for failure detection and condition monitoring [121,122] and is also applied in this thesis for failure detection and cell monitoring.

Several different EIS variations have been developed and are used. These are full-scale EIS to characterize a cell with high accuracy (see Fig. 8), and also a Single-Point EIS (SPEIS) and Quick EIS (QEIS, with 10 frequency values and no averaging). SPEIS and QEIS are the tools of choice for online monitoring during vibration testing at the test bench due to the very fast acquisition time.

2.4.2 Capacity and voltage discharge curve

In addition to EIS, the capacity of the lithium-ion cell is measured. Since this measurement usually takes several hours, depending on the chosen C-rate, this method is not suitable for online monitoring purposes. Therefore, it can be used only during pre- and post-vibration check-ups.

To estimate capacity, the constant current constant voltage (CCCV) charge and discharge procedure is used. Respective charge and discharge rates as well as termination criteria are given in detail in the respective section for each investigation in this thesis.

In addition to the comparison of estimated constant current (CC) discharge capacities C_{CC} or CCCV discharge capacities C_{CCCV} through charge integration, the voltage curves can be directly compared in pre- and post-vibration testing.

2.5 Optical characterization by computed tomography

Visual X-ray computed tomography has become a valuable tool in lithium-ion battery research [120,123–127]. The optical resolution provides detailed information about local deformations, displacements, local short circuits, delamination, wrinkles, buckles, cracks, or ruptures and is, thus, a very useful addition to the application of EIS with its aforementioned shortcomings in Subsection 2.4.1. Fig. 9 depicts an example of the detection of jelly roll failures or damage inside the cell, in this case caused by cyclic aging.

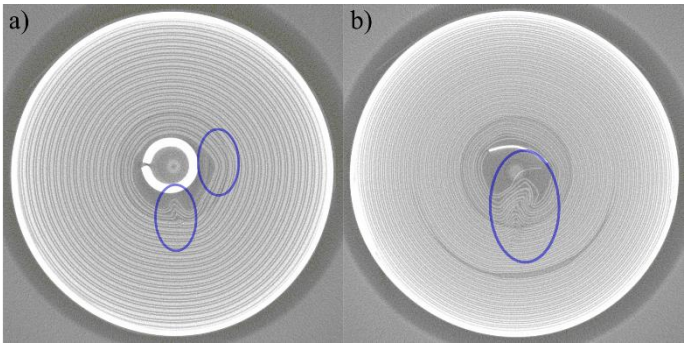

Fig. 9: CT depictions of cycled a) Molicel IHR18650A and b) Samsung INR18650-25R showing jelly roll deformations (blue ellipses) caused by cyclic aging.

In this work, a Phoenix nanotom s research|edition by GE (General Electric, USA), located at the University of Applied Sciences Munich, was used to investigate the vibrated cells for any displacements, cracks, ruptures, or other damage inside the cell that might be undetectable in the electrical signals. Optical characterization with this device is geometrically limited to cylindrical 18650 cells.

In addition, a wide range of new and undamaged 18650 cells was investigated for comparison of the inner cell designs (e.g., regarding mandrel, jelly roll fitting, spacer design, or tab welding) and to identify potential candidate cells for specific investigations. Mechanical design is assumed to be one of the most important factors for vibration durability of lithium-ion cells.

An example of such a pre-selection of cells with different inner cell designs which was used in Chapter 5 and the respective publication, is given in Fig. 10, incorporating different mandrels, layer thicknesses, jelly roll fittings, and spacer designs.

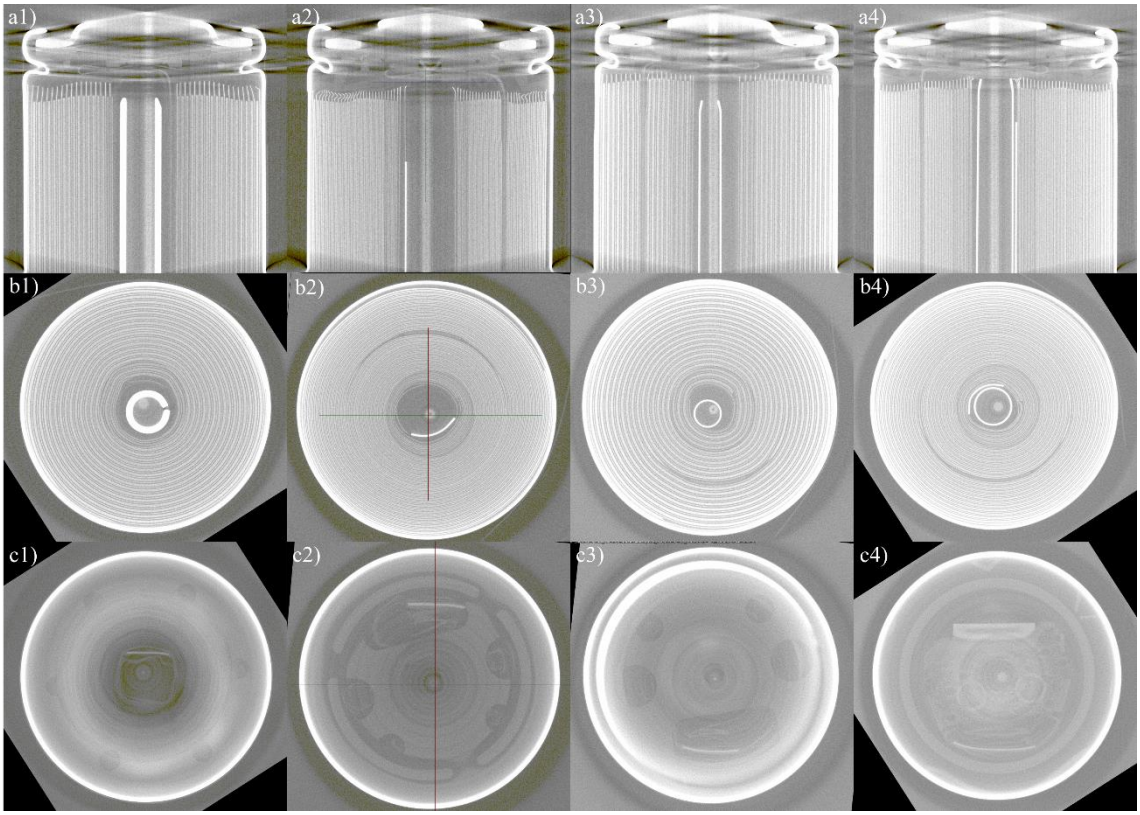

Fig. 10: Exemplary selection of four different 18650 cells (Column 1: Molicel IHR18650A, 2: Samsung INR18650-25R, 3: Samsung INR18650-35E and 4: Sony US18650 VTC5) with their different designs e.g., regarding the inner mandrel (row a and b) and the spacers below the positive tab (row c)

2.6 Lithium-ion cells under examination

Lithium-ion cells exist mainly in three different variations:

- Cylindrical hard-case cells (mostly of the type 18650 and of recently developed types, such as 21700)
- Pouch-bag cells
- Prismatic hard-case cells

All three cell formats were tested in this work, because each cell format has its importance for a specific application. In addition, some cell types are more suitable for specific experiments including characterization or durability testing.

In the case of cylindrical cells, 18650 cells were chosen because they offer a wide range of manufacturers and products with different characteristics and inner designs. Eighteen different commercially available 18650 cells are introduced and investigated in Chapter 5 and the respective publication [84]. A CT-device can be used to evaluate vibration durability with respect to the inner cell design.

Pouch-bag cells were used for the development of the test bench for EMA and are a good choice for the investigation of electrode stack fatigue due to their soft casing and few outer constraints. In this thesis, the Kokam SLPB356495 with 2.1 Ah was chosen. An advantage of this cell is that cells with identical geometry (length and width), but more z-folded layers are also produced (Kokam SLPB546495 with 3.3 Ah and Kokam SLPB776495 with 5.4 Ah). This offers flexibility if some variation is required, for example, to validate material parameters obtained in a FEM simulation by variation of the cell thickness.

For the prismatic hard-case cells, a 94 Ah large format cell is used. Prismatic cells are especially interesting in this work, because they are assumed to be less rigidly constrained, compared, e.g., to, cylindrical cells, with their tight packaging [128,129]. Therefore, prismatic cells are a good candidate to investigate possible failure behavior in case of periodic movement of inner components, e.g., of the electrode windings and the resulting stress on the respective welding spots, where the electrodes are joined with the outer tabs of the cell.

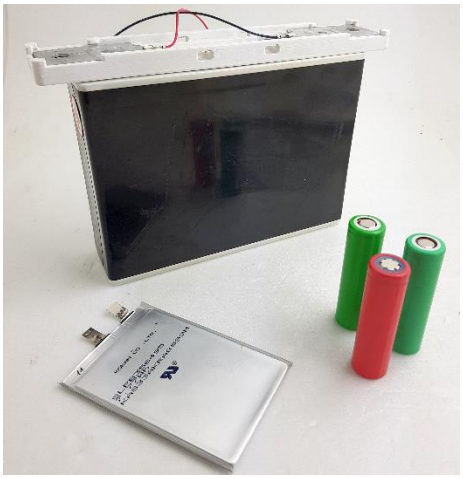

Fig. 11: Cell types under investigation in this thesis: The large format prismatic cell with a connector unit on top (black cell), investigated in Chapter 7, the consumer pouch cell Kokam SLPB356495, investigated in Chapter 6, and exemplary 18650 cylindrical cells, investigated in Chapter 5

2.7 Test bench developed for experimental investigations

A test bench was developed to perform the required investigations. Fig. 12 depicts the test bench.

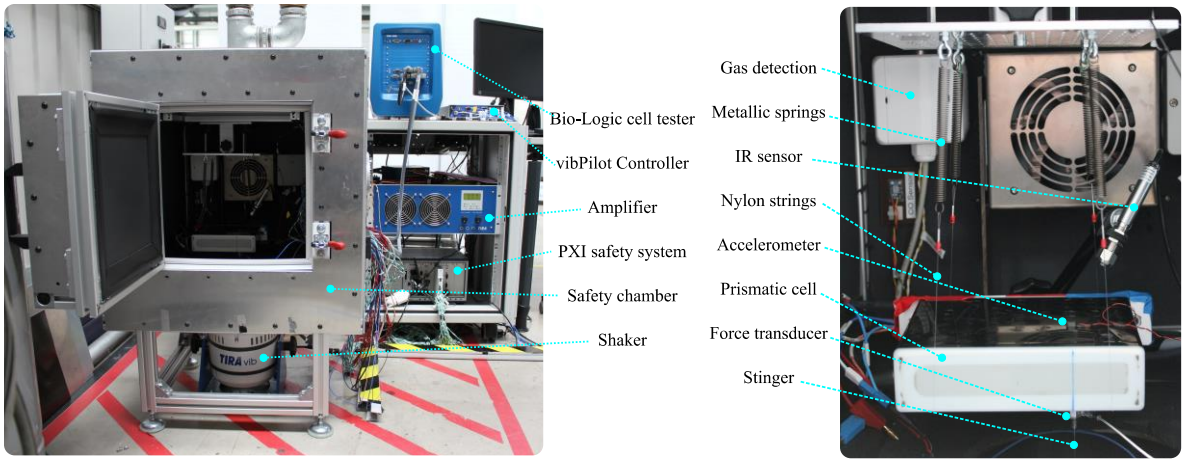

Fig. 12: Test bench for the investigation of vibration durability and the mechanical characterization of lithium-ion cells

The main components of the test bench are a custom-made safety and temperature chamber made from stainless steel with gas drainage, a *TIRA S 51140* shaker (TIRA GmbH, Germany), a BAA 100 amplifier (TIRA GmbH, Germany) for shaker drive and an eight-channel *m+p vibPilot* vibration controller and dynamic signal analyzer (m+p international, Germany) with integrated electronics piezo electric (IEPE) sensor conditioning.

Acceleration and force measurements are performed using only IEPE (called ICP® in the case of PCB Piezotronics Inc., USA) accelerometers and force transducers with voltage output due to their simple and stable operation in comparison to sensors which work in charge mode. The exact sensor descriptions are always given at the respective place for each investigation in this thesis.

To ensure safe operation and testing and to enable the test bench for online diagnostic of the lithium-ion cells under test, several monitoring capabilities were included. Therefore, a webcam (non-visible in Fig. 12) allows the direct observation of the cell under test. Temperature can be tracked both contactlessly using the *optris CS LT* infrared sensor (optris GmbH, Germany) or using up to 13 thermocouples of the type K. The generation or accumulation of harmful gases inside the test chamber due to cell opening, thermal cell reaction or others, can be monitored with two gas sens*ors: Fuehlersysteme eNet CO-A/A and the Adafruit MiCS5524 CO, Alcohol and VOC Gas Sensor B.* Furthermore, 12 channels for voltage monitoring are available. Thermocouple-based temperature monitoring, voltage monitoring and gas monitoring are managed with a *PXI* system (National Instruments, USA) and self-programmed monitoring software using *LabView* (National Instruments, USA). This software allows graph-based and numerical observation of the values, logging, and the activation of safety limits with an automatic shutdown of the shaker in case of values out of bounds.

While the aforementioned monitoring capabilities are mostly established for safety reasons, a Bio-Logic VSP-300 (Bio-Logic Science Instruments, France) with impedance measurement capability and 10 A booster is included in the test bench for SOC adjustment, voltage monitoring, capacity

checks and both offline- and online-EIS measurements (QEIS or SPEIS) according to the described procedures in Subsection 2.4.1.

The test bench can be used for both mechanical characterization using EMA (theory in Subsection 2.3.2, application in Chapter 6 and 7) and transmissibility, as well as for load profile testing (theory in Section 2.2, application in Chapter 5). Therefore, the shaker armature is extended into the safety chamber with an aluminum extension and a rubber membrane to seal the chamber. This extension can be equipped with various devices for the different investigations. In addition, an adjustable suspension (adjustable in 3 dimensions) was designed to support cells under test and to achieve the free-free condition. For characterizations with EMA in this work, a thin stinger of 1.5 mm diameter made from stainless steel was found to be valid. This stinger is, therefore, used for the presented investigations. The stinger is connected with the shaker by clamping and hosts the force transducer on its top. If correctly designed, the stinger offers high rigidity in the vertical dimension for the transmission of the shaker force, while it is flexible in all other dimensions to allow free movement of the structure under test in each of its respective mode shapes [130]. Together with a sufficiently soft and linear suspension, the cells under test in this work can be approximately decoupled from shaker-stinger-structure interaction and gravimetric forces. Regarding suspension, only metallic springs with spring constants, which ensure safe operation in the linear elastic range, worked well for the characterization of lithium-ion cells. Rubber bands, which are proposed in literature [103], do not provide sufficient long-term stability, reproducibility and linearity. Fig. 13 gives another view on the setup with both springs and stinger clearly visible.

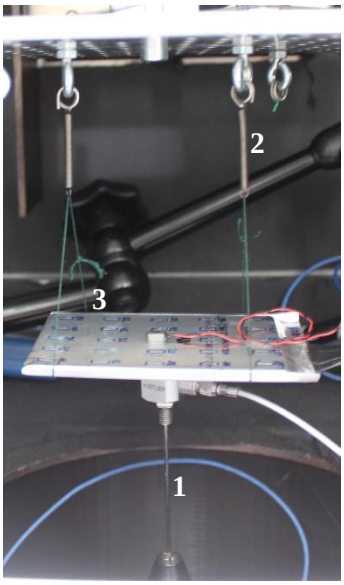

Fig. 13: Zoomed view on a lithium-ion pouch cell (marked with a 3) under test, depicting the support with metallic springs (2) and the stinger (1) to achieve the free-free condition

Two software packages are available for shaker control and post-processing of the measurement data: the *m+p Analyzer* (m+p international GmbH, Germany) and the *VibControl* package (m+p international GmbH, Germany). The first is used for characterization measurements; the latter is used for both load profile testing and characterization (in case of sine sweep testing).

2.8 Mechanical simulation

The main aim of this thesis is to reveal possible failure mechanisms and their sensitivities to, e.g., cell type and design, the internal parameters as SOC or SOH and external parameters such as temperature as well as to the properties of the vibration profile. Subsection 2.8.1 introduces the concept of fatigue as a possible failure mechanism. Since stress in the material is one of the driving factors for fatigue and cannot be measured directly, FEM simulations are applied in this thesis. Subsection 2.8.2 gives an overview of the model characteristics and the required parameter settings.

2.8.1 Elastic parameters, stress-strain relationship, and fatigue

In the elastic phase of the material of a structure, it is assumed that the strain at a specific point of the structure is proportional to the elastic force acting at this point. This law is called Hooke's law and is valid only for very small strains. The relationship according to Hooke's law is defined according to Eq. (16) for the normal stress σ and Eq. (17) for the shear stress τ. [94]

$$\sigma = E\,\varepsilon_n \tag{16}$$

$$\tau = E\,\varepsilon_t \tag{17}$$

E is the elastic modulus or Young's modulus. ε_n is the tensile strain parallel to the axis of the part and ε_t is the relative strain in the plane of the cross-section. Tensile strain ε_n is defined according to Eq. (18) with the original length l and Δl being its extension. [94]

$$\varepsilon_n = \frac{\Delta l}{l} \tag{18}$$

Stress is the force F per area (here A_0) and is represented by Eq. (19). [94]

$$\sigma = \frac{F}{A_0} \tag{19}$$

If the force on a tensile specimen is progressively increased and the elongation of the specimen is measured, the engineering stress-strain curve, depicted in Fig. 14 is obtained.

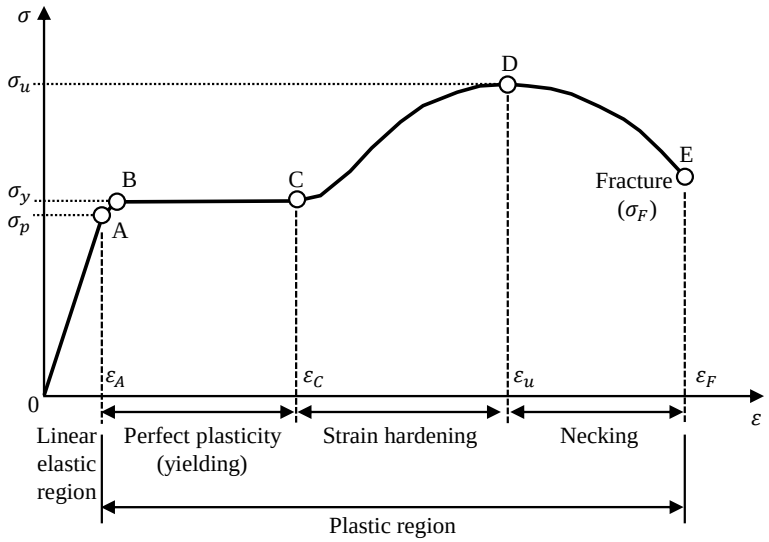

Fig. 14: Engineering stress-strain curve for a ductile material, reproduced from [94]

In the linear region (0-A), up to the proportional limit σ_p, elongation is perfectly elastic without any residual strain after unloading. The slope of the linear stress-strain curve in this region equals the elastic modulus. This region is smaller than the proportions in Fig. 14 imply. From B to C, the specimen has significant stretching without a noticeable increase in force. Yield stress σ_y marks the transition to this area. From C to D, strain hardening occurs with a much slower elongation than in the elastic region. Ultimate tensile strength σ_u is the ratio of the maximum force $F_{\max}$ for the sample and the initial area A_0 according to Eq. (20). [94]

$$\sigma_u = \frac{F_{\max}}{A_0} \tag{20}$$

The engineering stress-strain diagram can be directly calculated from the load-displacement curve and the initial area A_0, while the true and instant cross-sectional area must be measured for the true stress-true strain diagram. Therefore, true stress is always higher than engineering stress, since the effective area decreases with increased tensile force. [94]

The stress-strain diagram introduced from Fig. 14 is of course an idealized depiction and does not represent each material, because, for example, brittle and ductile materials show different curves. While the explanation above is for tensile forces, the same procedure applies for compressive forces. Compressive and tensile behaviors are not necessarily identical. In addition, these curves are measured with very slow variation of force. The materials have a different behavior when loaded dynamically. [94]

Besides Young's modulus and shear modulus, Poisson's ratio ν is another required parameter for FEM based modal analysis and subsequent investigation of vibration. While loaded with a tensile stress, the specimen undergoes two types of strain. At first, an extension ε_x, along its longitudinal axis, which is equal to the normal strain ε_n from Eq. (18) and a transversal reduction ε_y.

The relationship of these two types of strain is defined with Poisson's ratio v according to Eq. (21). [94]

$$\varepsilon_y = -v\varepsilon_x \tag{21}$$

For polycrystalline solids, v is approximately 0.33 [131]. In general, failure due to mechanical loads, e.g., due to a shock, can occur due to two mechanisms. On the first hand, the stress exceeds the threshold of the material or component causing instant failure, e.g., in case of a stress higher than ultimate stress σ_u. On the second hand, a failure can occur due to a repetition of the load, which causes the damage to accumulate. This second mechanism is called fatigue. [94,95]

The effect of fatigue is especially interesting for this thesis, as it is a classical means of vibration-caused damage. Vibration causes stress conditions, which repeat themselves many times. At the same time, it is more complex, because fatigue strongly depends on localized stress concentrations. [94]

Fatigue can be investigated in terms of a so-called SN-curve. S represents the stress and N the number of cycles to failure. Other terms are the Woehler's curve or endurance curve. Fig. 15 depicts an exemplary SN-curve.

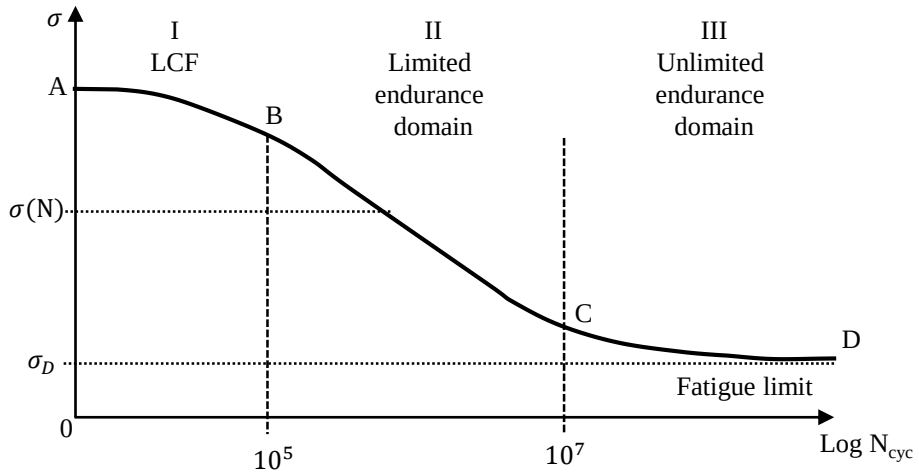

Fig. 15: Exemplary SN-curve with low cycle fatigue (LCF) domain, limited endurance domain or high-cycle fatigue (HCF) and unlimited endurance domain, reproduced from [94]

This curve consists of three regions. Region I represents the low cycle fatigue (LCF) domain with stresses higher than the yield stress, causing plastic deformation. This zone is irrelevant for this thesis and the investigated vibrations. In the zone of limited endurance (region II), fatigue occurs without measurable plastic deformation. Beyond point C in region III, the SN-curve tends towards the fatigue limit σ_D. Stress levels below σ_D never cause fatigue. Point D, therefore, represents infinite life. Again, this curve is an idealized representation and depends on the material, in example, not every material has a limit for infinite life. Due to variations, the SN-curve is usually measured with several specimen for each stress level to obtain a statistical representation. [94]

Fatigue further depends on a wide range of parameters, e.g., the type of dynamic stress (e.g., periodic, random, or transitory), frequency, cycle coefficient, or stress ratio R in Eq. (22) or the A-factor according to Eq. (23). The A-factor gives the ratio of the alternating stress amplitude σ_a to mean stress

σ_{mean}. σ_{min} and σ_{max} are the smallest and largest algebraic values for the cyclic stress. With these parameters, the influence of mean stress as well as superimposed cyclic stress can be considered. [94]

$$R = \frac{\sigma_{\text{min}}}{\sigma_{\text{max}}} \tag{22}$$

$$A = \frac{\sigma_a}{\sigma_{\text{mean}}} = \frac{\sigma_{\text{max}} - \sigma_{\text{mean}}}{\sigma_{\text{mean}}} \tag{23}$$

Of course, the overview given in this thesis is far from exhaustive, but is sufficient to understand the approach for the investigation of the possible fatigue behavior of lithium-ion cells. The interested reader can find a very detailed introduction to the topic of fatigue in [94], which also served as the main source for this subsection.

2.8.2 Finite element simulation

Fatigue is a classical failure mechanism under repetitive loading, which vibrations happen to be, and is often related to stress or to localized stress concentrations [94]. Since stress inside a lithium-ion cell under vibration is an unmeasurable quantity, FE models are the method of choice in this thesis.

The models were designed and investigated in ANSYS, a FEM software, in various versions (17.2-19.2). Toolboxes for modal analysis, harmonic response, and direct optimization from ANSYS are used.

The materials used in the simulation are all treated as linearly elastic for the sake of simplicity. The required parameters in ANSYS are density ϱ, elastic modulus E and Poisson's ratio v in the case of isotropic materials. Shear modulus G is automatically calculated from E and v in the case of isotropy. Besides isotropic materials, orthotropic materials, which have different properties according to their orthotropic axes, are used in this thesis. Instead of the three elastic parameters E, G and v, nine parameters E_x, E_y, E_z, G_{xy}, G_{xz}, G_{yz} and v_{xy}, v_{xz} and v_{yz} are required in case of orthotropic materials with respect to the three orthogonal axes x, y, and z and the three planes xy, yz and xz.

As a starting point, a parameter study based on available literature was done to find suitable parameters for the first model. A sample of relevant values for material parameters of lithium-ion cells is given at the beginning of Chapter 8. These material parameters must be optimized both manually and automatically to fit the results for the modal analysis in ANSYS with the results of the MDOF fit after EMA in this work (results from Chapter 6 and Chapter 7).

During this optimization, material parameters are changed in such a manner that the natural frequencies from measurement and simulation fit to each other for each respective mode shape. Of course, this must be done with respect to the obtained mode shapes so that similar natural frequencies of equal modes are compared. In a second step, the harmonic response of the model and the simulative FRF is calculated, which can be compared with the FRF measurement.

Damping is defined in ANSYS according to the definition of Rayleigh damping. In the case of Rayleigh damping, the damping is assumed to be proportional. The modal damping ratio ζ_n for mode n, which is introduced in Subsection 2.2.1, is then represented by Eq. (24), adapted from [93], with natural angular frequencies $\omega_{nat,n}$ for mode n and the Rayleigh terms c_m (also often called α) and c_k (also often called β).

$$\zeta_n = \frac{1}{2}\left(\frac{c_m}{\omega_{nat,n}} + c_k\omega_{nat,n}\right) = \frac{1}{2}\left(\frac{\alpha}{\omega_{nat,n}} + \beta\omega_{nat,n}\right) \quad (24)$$

In this mathematical expression c_m or α is proportional to the mass matrix of the spatial model of the structure and c_k or β is proportional to the stiffness matrix, given the following expression for the damping matrix C of an MDOF system in the spatial representation according to Eq. (25). [93]

$$\mathrm{C} = c_m\mathrm{M} + c_k\mathrm{K} \quad (25)$$

M is the mass matrix and K is the stiffness matrix, as in the system description in Eq. (1) in Subsection 2.2.1. The matrix-based spatial resolution applies to a system with multiple DOF instead of only SDOF as it is the case in Eq. (1).

3 State-of-the-art in lithium-ion battery vibration research

This chapter gives an introduction of the state of the art in related research. The investigations in this thesis are based upon it. Section 3.1 introduces several publications dealing with the comparison of different industry vibration testing standards from, e.g., governmental organizations with each other or with self-measured load profiles. Section 3.2 provides an overview of all available experimental studies investigating the impact of vibrations by load experiments. Section 3.3 introduces some publications which used EMA or simulative modal analysis to investigate lithium-ion cells or packs. Section 3.4 summarizes the results, especially regarding the limitations of current scientific knowledge. These results are used to derive the final research questions in Section 3.5, which motivate the chosen approaches.

3.1 Investigations of vibration testing standards and regulations for lithium-ion cells

Vibration testing is part of many standards and regulations. Standards are voluntary documents drafted by non-governmental organizations. A few examples of these organizations are the International Electrotechnical Commission (IEC), the International Organization for Standardization (ISO) and the Society of Automotive Engineers (SAE) on the international level as well as national organizations such as the Deutsche Institut für Normung e.V. (DIN), or the British Standards Institution (BSI). [92]

In contrast, regulations have the force of law and are, for example, issued by the United Nations Economic Commission for Europe (UNECE) or the National Highway Traffic Safety Administration (NHTSA) [92]. Detailed lists of different organizations and their standards and regulations are available in [91,92,132] for the interested reader.

While each testing standard or regulation usually contains a lot of different safety tests [92,132], this short overview is limited to the topic of vibration. Hooper identified 23 vibration testing procedures for electric vehicle (EV) application in his dissertation, many of which reference each other [133]. Hence, he identified 9 different vibration load profiles in total [133].

Several researchers compared or investigated the different vibration tests with respect to their differences and shortcomings [92] and their fatigue damage potential by application of FDS [134] and evaluated their usefulness with respect to safety during transportation [135]. In addition, they compared the standards for automotive application in an electric vehicle with self-measured vibration load profiles on EVs and vehicles with internal combustion engines (ICE) [136,137] or recommended a self-devised random profile for testing EV-batteries [138]. The next paragraphs discuss these publications.

A comparison of safety testing standards revealed significant differences in among the required tests in, for example, test duration, SOC during testing, amplitude or ambient temperature to name only a few [92,137]. For example, according to IEC 62660-2 cells have to be tested at 100% SOC for BEV and 80% SOC for HEV, while FreedomCAR manuals and recommendations according to SAE J2380 recommend testing at 100%, 60% and 20% SOC [137]. Only one of the testing standards, ISO 12405, requires vibration testing at different ambient temperature conditions [92]. Ruiz et al., therefore, question whether the testing conditions have been sufficiently developed and validated if there is such a wide variance [92].

Among the comparisons, there are also differences, e.g., the SAE J2380 is categorized as a test procedure on the cell-, module- and pack level in [92], while it is listed only for the module and pack level in [137]. Referring to the norm itself, the SAE J2380 is meant only for testing modules and packs [139]. At the same time, this profile with a maximum frequency of 190 Hz is the most tested vibration profile on cell level in the scientific literature as is shown in Section 3.2. Small devices like cells usually have their critical frequencies in a higher frequency range above the 190 Hz [137]. Therefore, standards such as IEC62660-2, which are usually designed for the testing of electronic devices, contain frequencies up to 2000 Hz [92,137,138]. Testing cells under these load conditions could cause other damage compared to the published results (see Section 3.2 for the respective literature overview).

Hooper et al. performed their own vibration measurements on both EV and ICE vehicles. They measured significant vibration outside the frequency range of SAE J2380 (random) standard, with frequencies up to 800 Hz for some vehicles [136]. In addition, their emulated and compressed profile to achieve identical testing time and identical frequency range as in SAE J2380 (random) resulted in a lower PSD level compared to the SAE J2380 (random) [136]. There were also significant differences among the measurements at different vehicles [136].

Without going into detail, these examples are sufficient to show that there are significant differences regarding the requirements and recommendations between the standards and regulations[92,134,137], in between measurements selected by different researchers and for different vehicles [136–138] and of course between standards and measurements [136–138]. Therefore, relying on only one standard or regulation might give a false sense of safety or it may be that all tests are too harsh.

3.2 Impact of vibrations on the durability of lithium-ion cells and packs

In the literature, vibration testing and simulation for lithium-ion cells and packs were performed mostly for qualification testing or the development of qualification testing procedures for aviation [140], space applications [141–144], telecommunications [145], electric buses [146], electric vehicles [147–149], or heavy duty vehicles [150] or for safety in general [151]. As the descriptive term “qualification” already indicates, these publications do not include a detailed investigation of possible failure mechanisms, especially not on the cell level, but are more concentrated on a pass-or-fail evaluation. Moreover, failures such as broken battery fixing brackets [148] are out of the scope of this thesis. Other publications, such as [141,151] do not provide indispensable information such as, for example, the duration of their vibration tests.

Therefore, the aforementioned publications have been reviewed but are not taken into further detailed consideration, as they cannot contribute to the goal of this thesis to increase the general understanding of the influence of vibrations on lithium-ion cells.

More detailed investigations have been done by Hooper et al. [152–155] and Zhang et al. [156]. They tested the durability of 18650 cells of nickel manganese cobalt oxide (NMC) and nickel cobalt aluminum oxide (NCA) chemistry under the load of electric vehicle random vibration according to the SAE J2380 (random) testing standard and a self-made vibration profile called Warwick Manufacturing Group/Millbrook Proving Ground (WMG/MBK) by single-axis shaker testing [152,153,156] and multi-axis shaker table testing [155] and found divergent results.

Not further specified 18650 NCA cells did not show significant degradation for either shaker configuration [153,155], while for NMC cells of the type Samsung ICR18650-22F significant degradation was reported. The most significant change was reported for inner resistance [152]. Some cells which were reported to show a strong increase in resistance, e.g., one cell with an increase of the internal resistance by 254%, showed no change in capacity [152]. Therefore, no reproducible correlation between capacity decrease and resistance increase could be identified. This implies that further research into the underlying physics of failure or failure mechanism is needed. Four cells (three vibrated cells and one reference cell) taken from [152] were further analyzed by X-ray photoelectron spectroscopy. It was proposed that vibration damaged the passive layers on the negative electrode. This was reported to cause subsequent layer rebuilding with other chemical compositions and hence increased ionic resistance, causing an increased ohmic resistance value [154]. Zhang et al. tested 32 18650 cells under random load according to SAE J2380 to obtain a statistical conclusion. They observed a degradation with decreasing capacity mean and increasing spread [156], but it is also possible that other reasons for the observed behavior existed.

18650 cells were also tested under different sine loads, but no load duration was reported and the data for, e.g., capacity show a very wide spread in between the tests so that no reliable conclusion can be taken from this (e.g., 2.584 Ah before vibration, 2.375 Ah after vibration with 5 Hz and 2.493 Ah after all vibration). [157]

Brand et al. tested 18650 cells (1.95 Ah) and Pouch cells (0.7 Ah) with an SOC of 50%. They used sine vibration and shock profile testing according to the recommendations UN 38.3 T3 and T4 as well as a self-designed long-term sine sweep profile with 1.5 mm constant displacement in a frequency range between 4 Hz and 20 Hz, which ran for 186 days. The same 18650 cell is also tested in Chapter 5 of this thesis. The pouch cells in in-plane and out-of-plane orientation, all 18650 cells vibrated in radial direction and the 18650 cells tested with the UN 38.3 sine profile did not show any degradation. The cells, which were shocked in the axial direction, were found to have a damaged current interrupt device (CID) due to mandrel displacement inside the jelly roll, while impedance and capacity remained constant. The long-term test with vibration in an axial orientation caused local short circuits inside the cell accompanied by a drop in capacity, an increase in resistance and a partly melted separator identified by computed tomography and post-mortem analysis. In addition, it was shown that the inner mandrel can cause damage in the negative current collector tab, which connects the jelly roll with the can. [99]

3.3 Structural dynamics identification of lithium-ion cells and packs

EMA has been used by several researchers for structural response analysis of pouch cells [158–161] and prismatic cell packs [162].

Choi et al. [158] made the first attempt to investigate the structural dynamics of lithium-ion pouch cells for one SOC by experimental modal analysis with impact testing and shaker testing, but neither gave any values for damping nor obtained any mode shapes. Additionally, support conditions during impact testing are unclear and during shaker testing, no free-free condition existed.

Hooper et al. investigated several pouch cells of one type at different SOC by impact testing. They reported no sensitivity of the structural response in terms of stiffness and attributed differences in cell-to-cell variation. They further reported damping values and mode shapes. [160]

Popp et al. also used EMA for the analysis of 25 Ah NMC lithium-ion pouch cells. They used a miniature shaker in combination with an impedance head. This shaker-sensor-combination was placed upside down on the cell to measure the driving point (DP) FRF. Structural dynamics were then captured for different SOC, two SOH (one new and one cycled cell under test) and temperature. They reported sensitivity of the response for both SOC and temperature. [159,161]

Volk et al. performed experimental modal analysis on 14 cell packs composed of 16 prismatic hard-case 26 Ah lithium-ion cells with different SOC and different SOH and investigated the first two bending modes. The variations of the resonance frequencies did not reveal a statistically significant dependence on either SOC or SOH and were assumed to be due to cell-to-cell variations because of production tolerances. [162]

Hong et al. used simulative modal analysis by application of FE models on the pack level. The numerical model consists of 20 stacked nominally identical pouch cells. For this pack, an FE model and a parametric reduced order model (PROM) were built. With the PROM, computationally efficient Monte-Carlo calculations were performed to investigate the effect of parameter variations. The influence of pre-stress and cell-to-cell variation was investigated. They found increased stress and stress localization in the case of cell-to-cell variation as well as dependence on pre-stress. While a model-to-model comparison between FEM and PROM was performed, no measurements have been taken or used for parameterization or validation so far. [163]

Nam et al. built an FEM and a PROM model of a lithium-ion battery pack composed of prismatic lithium-ion cells. They considered the effects of SOC, aging and cell-to-cell variations. The model was built to improve the structural design, to avoid local stress concentration and to identify suitable locations for battery monitoring based on the batteries' structural response. Again, the model is based on literature values, not on parameterized or validated by measurements. Unfortunately, they propose modes with natural frequencies of 3000 Hz and higher for the structural monitoring, which is out of the relevant frequency range for EV applications, as presented in Section 3.1. [164]

3.4 Conclusions and identified gaps in current research

In the previous Sections 3.1-3.3, a short summary of the available literature in the field of lithium-ion battery research with respect to vibration is given. This Section 3.4 aims to consolidate the findings from the three separate sections to identify existing gaps and to derive a direction for the research in this thesis.

In Section 3.1, publications that reviewed and investigated testing standards or regulations or performed load profile measurements have been collected. This collection revealed several findings, shortcomings, and gaps:

1. The available research about vibration load profiles is focused on EV profiles due to the importance of electric mobility [92,134,136–138,165]. Other applications, such as power tools were not considered in detail with respect to their vibration characteristics in the available scientific literature.
2. There are significant variances in both standards and regulations, as well as in measured load profiles [92,134,136–138]. While for qualification testing in the industry, the appropriate choice about future application must be made to obtain valid results, a scientific investigation should rather concentrate on identifying the underlying failure mechanisms and sensitivities in order to reveal universal and assignable results. Otherwise, there is the risk that the results tend to be valid for only a very specific case.
3. The different requirements regarding SOC or temperature during testing [92,134], indicate a need to understand the influence of these parameters on vibration behavior, fatigue, damage etc.
4. Methods such as FDS and SRS are used to compare different load profiles [134,138], while the validity or applicability of these approaches for lithium-ion cells and batteries has never been proven.

If the investigations of cell durability under vibration loads briefly reviewed in Section 3.2 are considered as well, the following findings can be added:

5. None of the available publications that investigate vibration durability and were introduced in Section 3.2 includes a theoretical risk assessment regarding vibration-caused failure for lithium-ion cells prior to the tests.
6. Applications other than EV, e.g., space applications, have been tested, but due to the limitations of these publications given in Section 3.2 all but two of the additionally considered publications [99,157] concentrated on EV application [152,153,155,156]. The vibration durability of lithium-ion cells, e.g., in power tool applications, has not been investigated in the scientific literature.
7. The standard according to SAE J2380 (random) is the most common in the available literature about automotive vibration testing on the cell level [152–156], because it is defined as being representative for a 100,000 mile vehicle life [152]. At the same time, it has been stated that this profile might not be representative for real load conditions [136,138] and that small components, such as 18650 cells have their critical frequencies in a higher frequency

range [137]. It is hence unproven if cell level testing according to SAE J2380 is valid or if another profile should be applied.

8. With regard to finding 7, it would be interesting to measure vibrational load profiles not only somewhere on the battery pack [136] or other locations such as trunk or center [134], but also inside the battery to understand transmissibility from outer vibrations to the inner parts of the battery pack, in particular to the cell.
9. Testing the durability of cells under automotive random load according to SAE J2380 revealed varying results for different cells under the same test conditions with significant degradation of the cells in [152] and no degradation of the cells in [153]. In [154], the same group, which performed both durability tests, attributes the observed degradation to vibration-induced surface layer generation on the negative electrode. If this is true, the question remains why the cells in [153], which also have a graphite anode, did not show the same degradation. A detailed look into the different cells and their inner design, e.g., into the jelly roll design would be required. Surface layer destruction and reconstruction could be favored when relative movement of the electrode layers is possible.
10. With regard to finding 9, none of the publications testing durability for automotive random profiles [152,153,155,156] considered the inner cell design.
11. In addition, the vibration durability of electrically pre-aged cells has not yet been investigated. This is interesting, because the lithium-ion cells inside an electric vehicle and in every other application age during their lifetime and therefore undergo some of the vibration in an aged condition.
12. A fully proven failure mechanism (moving mandrel) with subsequent failure mode (e.g., ISC) caused by vibration, was shown by Brand et al. [99]. They showed that vibration has the general potential to cause local short circuits and subsequent critical failure in a lithium-ion cell under certain circumstances and revealed the root cause due to a specific cell design with a loose mandrel inside the jelly roll. The limitation here is that failure was obtained after more than 120 days of testing time, which might be far from real load conditions and impossible to reproduce in a cost and time-driven environment.
13. The findings by Brand et al. [99] are limited to one cell and the respective cell design. The investigation of other cell designs is, therefore, of high interest.
14. The long testing time to failure in [99] and the “result-less” testing in [153,155,156] without clear failure mechanisms give rise to the need for a holistic approach to the vibration durability testing of lithium-ion cells. Otherwise, testing all possible variations (SOC, temperature, SOH, excitation type, excitation amplitude etc.) produces a far too large test matrix.
15. The failure mechanism of a loose mandrel striking up and down [99] is the only clearly proven possible failure mechanism and at the same time is not a classic case of fatigue, which supports the concerns that methods such as FDS are not valid methods to describe lithium-ion cell vibration durability or to compare load profiles (see finding 4).
16. While some investigations regarding the vibration durability of 18650 cells are available [99,141,151–157], the available information regarding the vibration durability of lithium-ion pouch cells [99,144,166] or prismatic cells [145] is very limited.

17. All cell failures proven or probably due to vibrations have been recognized at a certain point in time during a check-up procedure [99,152]. Therefore, it is unclear if failure appears in a creeping manner or instantaneously and if it can be detected or even predicted.

This long list of shortcomings and gaps requires a holistic approach for investigating the influence of vibrations. One step is the application of modal analysis, as it provides the most general description of structural dynamics and therefore the structural behavior of the lithium-ion cells. As mentioned in Section 3.3, some investigations have been made with the following identified gaps:

18. Lithium-ion cells are complex structures with many components and interfaces. This structure is very likely to behave nonlinearly. As modal analysis is a linear technique, test benches and the obtained results should be carefully evaluated to ensure proper validity of the results. This has not been done for cell level testing up to now [158–161]. In addition, no one has systematically investigated nonlinear effects in the structural dynamics of lithium-ion cells.
19. The literature discusses the application of EMA on the cell level [158–161] and the pack level [162]. Modal analysis based on FEM is available on the pack level for both pouch [163] and prismatic cells [164]. These two FEM-based investigations did not use experimental data for parameterization or validation. Only in one case, investigating the design of structural batteries, were the advantages of experiments and simulations combined by Galos et al. [167].
20. As far as the author knows, no FE model to describe structural dynamics or vibration response of a single lithium-ion cell is yet available.

The approach chosen in this thesis is motivated by these numerous shortcomings in the available scientific knowledge.

3.5 Derived research questions and objectives

The investigation of the available literature regarding lithium-ion cell vibration durability revealed several shortcomings and limitations. Since the list is very exhaustive, this section breaks it down into fewer and wider objectives, which provide the framework for this thesis.

The main and most important research question or objective of this thesis is the following:

Objective 1: Which failure mechanisms in lithium-ion cells can be caused by vibrations?

The focus of this thesis is to identify the underlying failure mechanisms with vibration as the cause for different cell types without limitation to one specific loading condition or specific cell design. At the beginning of this thesis, only one single failure mechanism (moving mandrel inside an 18650 cell [99]) had been proven, given all the listed limitations in Section 3.4 (see identified limitations 12, 13, 14, 15, 16 and 17). To understand the failure mechanism can help improve or accelerate vibration testing, improve the cell or pack design for durability, identify diagnostic methods for or prevent critical loads in application by suitable countermeasures.

The theoretical risk assessment in Chapter 4, including a field failure study, is the first step to reveal the potential failure mechanisms (addressing limitation 5), which are subsequently investigated throughout this thesis. Therefore, load testing in Chapter 5 with the consideration of different cell

designs (with regard to the limitations 9 and 10) and different SOC and SOH (see limitation 11) as well as the characterizations in Chapter 6 and Chapter 7 are used.

Characterization can reveal sensitivities, e.g., from SOC or SOH, and in the best case can be used to identify the criticality of different states of the battery cells without testing at each state, which is related to the limitations 3 and 14.

In addition, the characterization results are the foundation for the FE model of a lithium-ion pouch cell in Chapter 8, addressing the limitations 19 and 20 regarding the availability of a valid and experimentally parameterized FE model of a lithium-ion cell for the investigation of vibration. This model was built because it can give further insights, for example, into inner-cell stress states, which is mandatory to investigate fatigue as one of the possible failure mechanisms.

From the description above, it becomes obvious that this central question is related to the further objectives which are based on objective 1 or are required to fulfill the tasks related to objective 1:

Objective 2: Which failure modes are associated with the failure mechanisms in lithium-ion cells caused by vibrations?

Besides the underlying failure mechanisms, failure modes are of high interest. Answering this question will reveal if, for example, accelerated aging (or more generally wear out) can be caused by vibrations besides safety critical events as a short circuit. Failure mechanisms with non-safety critical effects, but accelerated aging, are even more difficult to identify, since the aging must be isolated from other aging mechanisms. This objective is also related to limitation 17 regarding the instantaneous or creeping characteristic of a vibration-caused failure.

Objective 3: What influence does the (inner) cell design and other common parameters or conditions such as SOC, SOH and temperature have on a lithium-ion cell's vibration durability and structural response?

This objective is related to limitations 2 and 3 with regard to the differences in standards and to limitations 9, 10, 11, 13, and 14 with regard to vibration durability. The topic is addressed in Chapters 5, 6 and 7. In Chapter 5, 18 different 18650 cells are compared with respect to their vibration durability under consideration of different inner cell designs and with respect to variations in SOC and SOH. In Chapters 6 and 7, the significance of these parameters for the vibrational behavior of lithium-ion cells is investigated through EMA to reveal the dependence of the structural response on the different parameters.

Objective 4: Is it possible to compare or accelerate vibration durability tests for lithium-ion cells, e.g., by the application of methods such as FDS with a focus on failure mechanisms and nonlinear behavior?

This objective is related to limitations 4, 7, 12, 14, 15 and 18. Since the application of FDS assumes classical fatigue-based failure and test acceleration is usually accomplished by an increase of the load amplitude, both the failure mechanism and the degree of nonlinearity in the structural response must be understood. This is investigated through the application of EMA in Chapters 6 and 7.

Objective 5: What potential lies in the application of EMA as a characterization method in lithium-ion cell research at all?

EMA has been chosen for this thesis as the basic method to understand what happens inside a lithium-ion cell during vibration and to enable the design of FE models for a combined experimental-simulative approach on the cell level (see limitations 19 and 20). It is also used to identify sensitivities from cell parameters, ambient conditions or boundary conditions (see limitations 2, 3 or 18). At the same time, it is a comparably new method in the field of lithium-ion cell research and therefore it is evaluated with respect to its potential for any application in research, online monitoring etc.

Limitations 1, and 6 regarding applications other than EV and limitation 8 regarding the transmissibility from pack to cell level are not covered in this thesis in sufficient depth to be included as an objective.

4 Risk assessment for mechanical loads on lithium-ion cells

In this chapter, a theoretical investigation of the risk of vibrations for lithium-ion cells is given. At first, an analysis is performed to investigate safety-critical incidents caused by lithium-ion batteries in Section 4.1. It must be said that vibrations can also cause increased degradation without becoming safety critical. Section 4.2 collects and summarizes the findings of various reliability-investigating publications in the form of an FMMECA with a focus on mechanically induced failures. Section 4.3 relates this to the state of the art, which is introduced in Chapter 3. Based on these findings, Section 4.4 gives a conclusion about possible failure mechanisms from a theoretical perspective (see identified limitation 5 on page 35). The results are used to adjust the focus in the subsequent experimental investigations.

4.1 Analysis of lithium-ion cell related incidents

Due to the novelty of lithium-ion batteries and the severity of failures owing to the high-energy content and the difficulties of stopping a failure in progress [15,168,169], incidents associated with lithium-ion batteries attract high public awareness, although the probability of failure is quite low [165]. Besides the high risk for people and surrounding objects in case of battery failure leading to thermal runaway with fire and explosion [11,15] and the evolution of toxic gases [170–172], such failures can cause reputational and economic damage. To give an example, the incidents with the Samsung Note 7 and the costly product recall of millions of devices reduced Samsung's mobile division profits by 98% and by 30% for the whole company [173].

Several sources are reviewed below to find out how many incidents have been triggered due to mechanical causes in general and due to vibrations in particular. At first, the website of the US Consumer Product Safety Commission (CPSC), www.cpsc.gov, is used to identify and analyze similar events that initiated a product recall. In addition, several researchers investigated and collected incidents associated with lithium ion batteries [9–17,174]. Thirdly, a collection of 238 airport incidents in the period from May 1994 until December 2018 by the US Federal Aviation Administration (FAA) [175] is reviewed for incidents associated with mechanical loads. Only the incidents caused by mechanical loads are extracted from these three resources and then included in this thesis. The wider focus comprising all mechanical loads was chosen to collect more ideas and to be able to derive relations from static and dynamic loads, for example.

The recall study comprised 155 battery related product recalls between 1997 and 2016. The initial collection was done by Constanze Kranner in her bachelor thesis under the supervision of the author of this thesis [176]. This data collection has been used, updated, and newly analyzed.

Several recalls collected in [176] are excluded here due to the following reasons (number of neglected recalls in brackets):

- products with unknown battery cell chemistry (lithium-ion cell or not) (53)
- products with nickel-metal hydride (NiMH) or nickel-cadmium battery (NiCd) (11)
- products with primary lithium, alkaline, lead acid or other battery technologies (15)
- products with reported sales number lower than 10,000 units (59)
- products with counterfeit batteries (2)

After this data cleanup, 48 recalls associated with lithium-ion and lithium-polymer (LiPo) batteries remained. An overview over these recalls is available in Appendix A.3. These add up to a total reported sales number n_{sold} of 18,375,210 of all these items and $k_{fail} = 718$ failed devices ($k_{fail}/n_{sold} = 0.0039\%$).

The analysis of the product categories in Fig. 16a shows that most recalls pertained to laptops followed by consumer electronic devices, such as cell phones, DVD players etc., battery packs and toys. One recall is known for hoverboards (Mobility), for screw drivers (Others) and bicycle lights (Lights). The numbers of sold and failed items for each category are provided in Table 2.

Fig. 16b depicts the failure modes by which the devices failed. It is obvious that in most cases (28 in total) the failure mode is unknown. Identified failure modes are in the order of their frequency: short circuits (SC) - including internal short circuit (ISC) and external short circuit (ESC), cell defects, overcharge failures and others.

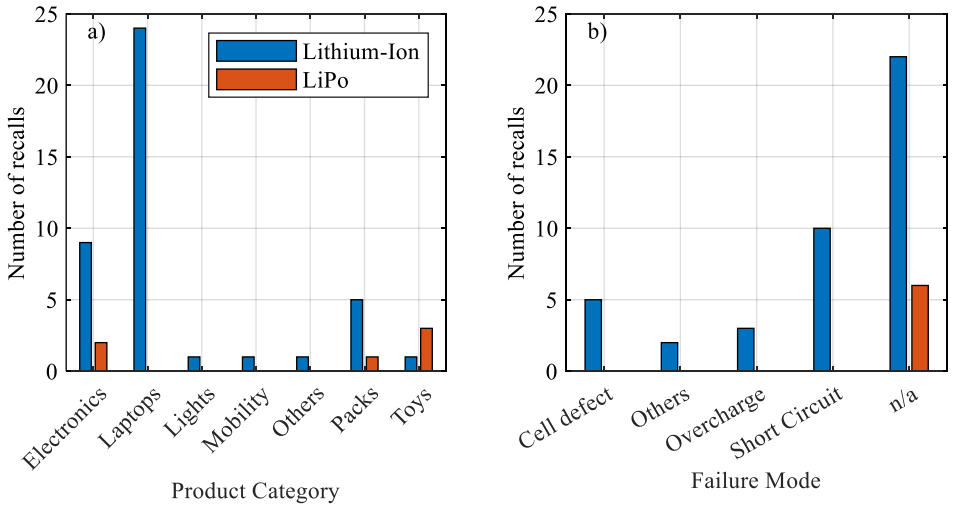

Fig. 16: Analysis of lithium-ion battery related recalls with respect to a) product category and b) failure mode

Table 2: List of all product categories in the investigated recalls with the respective numbers for each product category

Product category	**Number of recalls**	**Number of sold items n_{sold}**	**Number of failed items k_{fail}**	**k_{fail}/n_{sold}**
Laptops	24	11,751,200	265	0.0023%
Consumer electronics	11	4,791,200	205	0.0043%
Battery packs	6	264,710	71	0.0268%
Toys	4	1,007,000	72	0.0071%
Mobility (hoverboards)	1	501,000	99	0.0198%
Others (screw drivers)	1	42,000	3	0.0071%
Lights (bicycle lights)	1	18,100	3	0.0166%
Sum	**48**	**18,375,210**	**718**	**0.0039%**

The information obtained from the recalls has numerous limitations:

- Unknown beginning of operation, known as left censoring [177,178].
- Unknown time of failure, known as interval censoring [177,178].
- Truncation of data, also called suspended or right censored data, as most devices are removed from operation before failure at the date of recall [178].
- Unknown operational conditions such as temperature, shocks, vibrations etc.
- Unrepresentative sample, as recalls only contain defective devices, e.g., Note 7 is not representative for all Samsung smartphones with 1.9 million recalled Note 7 [179] in contrast to 292.3 million Samsung smartphone shipped worldwide in 2018 [180].
- Many of the recalls relate to low-quality products. This can be seen in sales numbers. Out of all recalls, 59 recalls (equals 38%) were excluded from the analysis as each of the recalled products was sold less than 10,000 times.
- For most of the recalls, failure modes are unknown (see Fig. 16b); underlying failure causes are even less known.
- Many of the recalls and failures occurred due to failures in the BMS and periphery and not due to a cell failure [165].

The Samsung Note 7 incident is an exception that can be used to obtain valuable information because Samsung made a significant effort to analyze the root cause of the failure. The investigation revealed two failure causes: First, the battery cell did not fit into the compartment and therefore the negative electrode was deflected. Secondly, high welding burrs and insufficient insulation caused penetration of the separator. Both errors caused an ISC and the cells subsequently went into thermal runaway. [14]

Incidents associated with lithium-ion batteries have been also collected in several scientific publications [9–17,174] and from governmental agencies, e.g., the FAA [175].

Several incidents occurred due to a combination of vibration during transportation and improper packaging in cargo [175]. These incidents were excluded from the analysis because the root failure cause was not vibration, but improper packaging and subsequent external short circuit [17,91]. Proper packaging is out of the scope of this thesis. 23 of 238 (approx. 10%) incidents collected in air

transportation were caused by mechanical impacts, mostly because cells or devices were dropped, penetrated or crushed during handling or after sliding in an airplane seat. [175]

Several field failures of EVs were also reported with mechanical impacts as the identified failure cause. For example, in June 2011, a fire occurred in a Chevrolet Volt EV three weeks after a crash test [15,174,181]. Investigations revealed that the impact of the crash caused the cooling system of the battery pack to leak, the subsequent external short circuit caused fire in the vehicle after some delay [9,15]. Some Tesla Model S vehicles caught fire because of direct impact of sharp metallic objects or a tow hitch with subsequent short circuit [15,174,182].

Table 3 summarizes all identified incidents with a mechanical cause in the style of a failure mode, effect, and cause analysis (FMECA). If not otherwise mentioned, the batteries in the table are always lithium-ion batteries. The incident itself, date and failure effect are taken from the references directly. The failure causes are possible assignments made by the author of this thesis because the failure cause cannot always be clearly identified. For example, being wedged in an airplane seat can cause penetration, bending and compression. Hence, for most of the incidents several failure causes are listed, while only one of them might have caused the failure. Vibration, the focus of this thesis, was not identified as a failure cause. While not explicitly mentioned for each accident, a short circuit failure mode can be assumed for each of the incidents in Table 3, since the reported failure effects – heat, smoke and fire – are common reactions after a short circuit of lithium-ion batteries [15].

Table 3: List of collected incidents with different mechanical causes (Drop, Penetration, Compression, Bending or Vibration) and the subsequent failure mode Short Circuit (SC) and effects, (not necessarily mentioned in the respective references, and marked with possible)*

Incident / *Item*	**Date**	**Possible failure cause(s)***	**Possible failure mode***	**Reported failure effect**	**Ref.**
Battery was dropped in flight	2009/09/09	D	SC	Fire	[175]
Chevrolet Volt EV caught fire three weeks after crash test (cooling system was damaged and caused subsequent short circuit)	2011/06/--	P, C	SC	Fire	[9,15,174]
Electronic reading device became wedged when airplane seat was moved to upright position	2011/10/10	C, P, B	SC	Smoke and fire	[175]
BYD E6 taxi was rear-ended and caught fire	2012/06/--	C, P, B	SC	Fire	[182]
Tesla Model S caught fire due to direct impact of sharp metallic object	2013/10/01	P	SC	Fire	[15,174]
Laptop was damaged by a dolly	2013/10/02	C, P	SC	Fire	[175]
Tesla Model S crashed at high speed	2013/10/18	C, P, B	SC	-	[174]
Tesla Model S struck a tow hitch	2013/11/06	P	SC	-	[174]
Cell phone wedged into airplanes seat mechanism	2016/05/15	C, P, B	SC	Smoke	[175]
Several Samsung Note 7 caught fire and were recalled	2016/10/--	B, P	SC	Fire	[14]
iPhone 7 became wedged in airplane seat was moved to upright position	2017/01/15	C, P, B	SC	Smoke	[175]
Batteries were inadvertently dragged by a dolly	2017/04/13	C, P	SC	Expl.	[175]
13 boxes of laptops were bumped causing one box to fall to the ground	2017/05/02	D	SC	Heat, smoke	[175]
iPad was crushed against motorized airplane seat	2017/06/22	D, C, P, B	SC	Fire	[175]
Package with iPhones fell out of container and was run over	2017/10/04	C, P	SC	Fire	[175]
iPhone was crushed when airplane seat was electronically reclined	2017/12/16	C, P, B	SC	Fire	[175]
Laptop smoked and became hot after being dropped	2018/01/03	D	SC	Smoke	[175]
Samsung cell phone smoked after being punctured by the sort system	2018/02/14	P	SC	Smoke	[175]
iPhone became wedged in airplane seat and started to smoke	2018/03/12	C, P, B	SC	Smoke	[175]
iPad became wedged in airplane seat and started to smoke	2018/04/07	C, P, B	SC	Heat, smoke	[175]
A package of *Li-metal 3.9 V batteries* fell, was run over, and caught fire	2018/06/08	D, C, P	SC	Fire	[175]
Batteries were punctured during sort process	2018/07/10	P	SC	Smoke	[175]
Battery power pack was crushed when business seat was reclined during cabin cleaning	2018/07/23	C, P, B	SC	Fire	[175]
6 Ah Battery smoked after it was run over by a tug	2018/07/25	C, P	SC	Smoke, smolder	[175]
Laptop smoked after being crushed during transit	2018/08/28	C	SC	Smoke	[175]
1 of 180 boxes of *used cell phones* was punctured by a forklift (10 phones damaged)	2018/08/29	P	SC	Smoke, fire	[175]
Spare batteries were punctured by a forklift	2018/11/02	P	SC	Smoke	[175]
1 of 22 dropped *spare batteries* smokes	2018/11/09	D	SC	Smoke	[175]

The detailed investigation of field failures revealed no incident that was proven to be caused by vibration. At the same time, it must be said that vibration failures usually occur after some time of damage accumulation [99] and therefore can be hardly correlated with a specific event. In addition, the recall analysis also revealed that many incidents have unclear failure reasons. Last but not least, an incident evaluation is always limited to safety-critical events. Therefore, for example, no conclusion about possible consequences of accelerated aging due to vibration can be drawn.

4.2 Failure mode mechanism effect and cause analysis

Available reviews and theoretical risk assessments are considered in this section. It is not a review of all available publications on each specific topic. The findings of this section are linked and cross-checked with the vibration-related literature, which is introduced in the Sections 3.1-3.4, in the following Section 4.3.

Several researchers used common reliability evaluation methods such as FMEA [85] or fault tree analysis (FTA) [87,88] to investigate lithium-ion battery safety and reliability.

Bubbico et al. used FMEA to obtain a hazard identification based on manufacturing defects, electrical, mechanical and thermal abuse and aging [183]. Hendricks et al. performed an FMMEA to provide insight into the most critical failures as a basis for the physics of failure modelling and improvement of test standards [184]. Li et al. performed an FMEA for the failure analysis of lithium iron phosphate batteries, but did not include mechanical effects [185]. Schlasza et al. made a brief review of aging mechanisms in lithium-ion batteries with an FMEA [186]. A risk identification by Soares et al. investigated all the risks from production to operation and maintenance and identified vibrations, noise, mobile or rotary components, shock, compression, sharp or cutting objects and metal projection as mechanical risks [187].

Held et al. used FTA and showed that a safe cell does not entail a safe battery automatically [188]. Arora et al. reviewed mechanical design and strategic placement for EV battery packs [189] and used a robust design methodology to identify critical technical requirements for modularity [190]. They found the thermal management system and packaging architecture to be the two most important parameters [190]. They also compared the structural characteristics of different types of battery cells and identified the pouch cell as the weakest cell type due to possible delamination, poor compressive force endurance and high local stress [190]. Qi et al. investigated lithium-ion battery safety by FTA coupled with rheology mutation theory [182]. Kong et al. presented a method based on residual charging capacity to detect micro short circuits (MSC) and expected severe vibration to be a possible cause for MSC development [16].

The failures related to mechanical loads, which are described in the named literature above, are summarized as a failure FMMECA for mechanically induced failures in Table 4. The identified failure modes are open circuit, short circuit and wear out. This can be further broken down, for example, into local and global short circuit, but at this point, the chosen distinction is sufficient.

According to these findings, the failure mode “open” (high resistance) can occur due to solder failure and has been also associated with vibrations as one of several possible failure causes [190].

For the safety critical case of short circuit with the subsequent potential of thermal runaway the same causes penetration, shock, drop, crash, compression, or impact as in the incident analysis in Table 3 can be found. Bending was not found as a failure cause in the investigated literature. Vibration is named as a possible cause for MSC initiation [16].

Wear out failure has been associated with mechanical stress due to intercalation, causing particle fracture or separator pore clogging. Arora et al. also assumed that vibration could cause cell wear out due to continuous vibration, resonances or shocks [189,190]. Other reported failure mechanisms are electrode delamination and electrolyte leakage.

Table 4: FMMECA of lithium-ion cell and module failure due to mechanical loads based on a literature survey (added by author and not originally from reference)*

Failure Mode	Failure Mechanism	Failure Cause	Possible effects*	Ref.
Open	Solder cracking at the terminals	Vibration, thermal or mechanical fatigue	Circuit disconnect	[184,190]
Short	Hole in separator, electrodes in contact	Crushing of the cell, load on the cell	Thermal runaway, toxic exposure, capacity loss and power fade	[166,184,189]
Short	Micro short circuit through dendrites piercing separator	Vibration	Thermal runaway, toxic exposure	[16]
Short	Penetration by sharp or cutting objects	Penetration	Thermal runaway, toxic exposure	[187]
Short	Shock against a heavy object or drop	Shock, drop, impact	Thermal runaway, toxic exposure	[187]
Wear out	Anode particle fracture	Mechanical stress due to intercalation	Capacity loss and power fade	[183,184,186,190]
Wear out	Casing failure, electrolyte leakage	Mechanical stress, shock, vibration, resonances	Capacity loss and power fade, toxic exposure	[91,183,187,190]
Wear out	Cathode particle fracture	Mechanical stress due to intercalation	Capacity loss and power fade	[183,184,190]
Wear out	Closing of multilayer separator pores	Mechanical stress	Capacity loss and power fade	[76,183]
Wear out	Electrode delamination	Shock or continuous vibration, resonances	Capacity loss and power fade	[189,190]

4.3 Comparison with the state of the art in vibration research

In the preceding Sections 4.1 and 4.2, the risks associated with mechanical loads are investigated by incident analysis and a risk assessment based on a FMMECA is performed.

The analysis of incidents did not yield very helpful information to understand the impact of vibrations. Possible reasons are that vibrations never caused an in-field failure or that vibration just never could be identified as the root cause, because failure occurred in a hidden manner over a period of time.

Nevertheless, welding burrs and electrode deflections as reported for the Samsung Note 7 recall [14] could be interesting for vibration research as well.

The risk assessment in Section 4.2 identified vibration as a possible failure cause according to some published studies. Vibration-caused failure can be found and attributed to all three failure modes – open, short and wear out – according to the reviewed publications.

If limited to vibrations, the failure mode “open” was associated with the failure mechanism solder cracking. The failure mode “short” was to a pierced separator by dendrites. In case of “wear out”, electrode delamination was assumed to be a possible failure caused by vibration, while particle cracking was attributed only to mechanical stress due to intercalation. In addition, electrolyte leakage and casing failure were reported as possible failure mechanisms (for respective references see Table 4).

With regard to vibrations, Brand et al. revealed local short circuits due to damage through the moving mandrel [77], which could not be found in any of the several risk assessments. In addition, the local short circuit caused decreased capacity and increased resistance, but not a full short circuit with the failure mode “short”. This shows the possible complexity of the various failure scenarios. Hooper et al. found increased resistance in 18650 cells after vibration [152], and Somerville et al. [154] attributed this to extended passive layer generation, while the risk assessment identified electrode delamination as a possible failure mechanism without experimental proof [189,190].

4.4 Conclusions of the theoretical risk assessment

The preceding investigations made it obvious that very few generally accepted and reproducible investigations regarding vibration failure of lithium-ion cells exist.

Therefore, Chapters 3 and 4 are used as a source together with our own considerations to create a summary of possible failure mechanisms for lithium-ion batteries due to vibrations. These are linked to the experimental and simulative investigations in the following sections. Fig. 17 depicts the overview of possible combinations of cell components, failure mechanisms and failure modes.

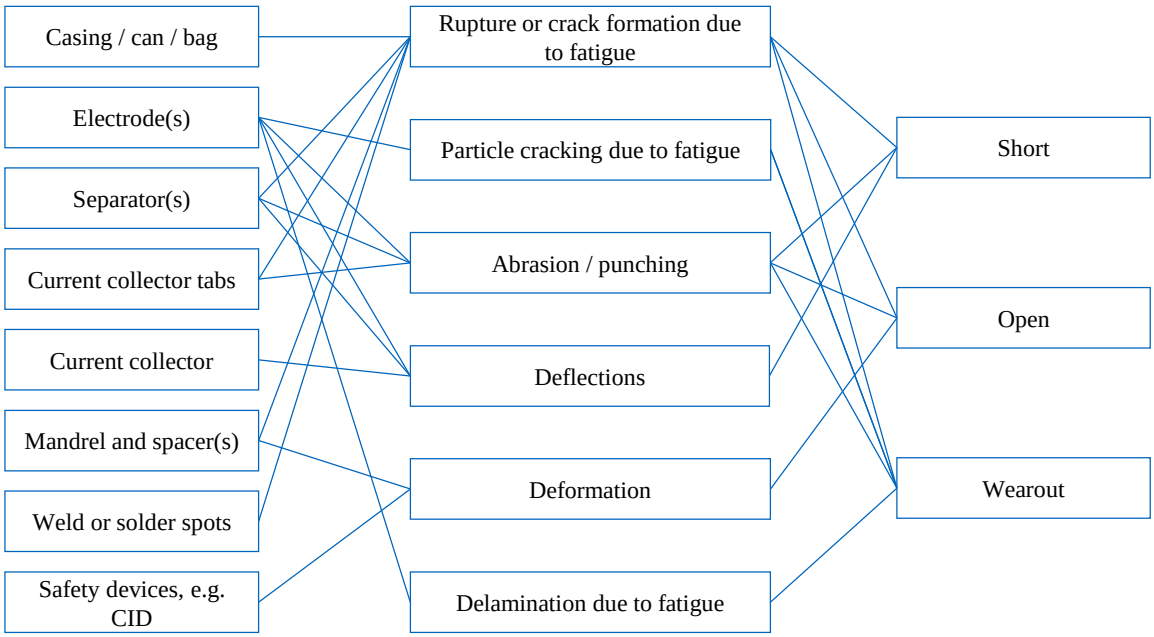

Fig. 17: Possible combinations of damageable cell components (left), failure mechanisms (middle) and failure modes (right)

In the first column of Fig. 17, the various possible components of a lithium-ion cell are listed. Of course, not each component pertains to each cell type, since, for example, pouch cells do not have an inner mandrel. In the second column various possible failure mechanisms based on our own considerations and the investigated literature in the preceding chapters are given. The third column depicts the three failure modes open, short and wear out. The connecting lines show possible failure combinations. In the following, the mechanisms are further explained and linked with the respective investigations that are included in this thesis.

Loose components inside a cell can pose a risk to vibration durability. Brand et al. showed this when they detected a moving mandrel damaging the cylindrical cells inside [99]. The failure mechanism due to this moving mandrel can be, e.g., **abrasion** or **rupture** of current collector tabs and separator layers in the region of the mandrel. Since this has been demonstrated for only one type of 18650 cells, in this thesis an analysis with 18 different 18650 cells is presented in Chapter 5 to investigate the sensitivity of vibration durability to the cell design and to answer the question whether other things can happen, such as layer-to-layer displacements in the jelly roll or electrode stack. These could result in **abrasion** at the location of welding burrs inside the jelly roll or **electrode deflections** at the upper or lower end of the jelly roll.

Since it is assumed that the jelly rolls in a prismatic cell are less tightly constrained than in a cylindrical cell [128,129], a large format prismatic cell is characterized regarding their structural dynamics in Chapter 7. The revealed dynamics can also give a hint whether the displacement of the jelly rolls in this type of cell can cause a failure due to insufficiently constrained components. Possible failure mechanisms could be, for example, **abrasion** between jelly rolls and cell casing, **cracks or rupture** of the current collector foils or the welding connections between current collector foils and cell terminals due to fatigue. The results of such durability tests are likely to depend on several parameters, e.g., the SOC of the cell and the respective electrode swelling, the SOH, the temperature,

or the outer constraints due to external bracing. The first step in this research topic, therefore, is the characterization of the structural dynamics of large-format prismatic cells in Chapter 7.

Fatigue is mentioned in the preceding paragraph as a possible failure mechanism for the welding spots inside a cell when significant displacement occurs. It is, in general, an interesting question if vibration can cause any stress or strain related **HCF** in a lithium-ion cell, e.g., of the electrodes and the respective electrode material, the separator, the current collector tabs or the welding spots of the current collector tabs inside the cell. **Fatigue** is one of the most common failure mechanisms in case of vibrations in general [154] and is worth considering in lithium-ion cell research. Answering this question and understanding the dynamic behavior of the cells and its components can also provide valuable knowledge, e.g., to understand if methods as FDS can be applied. **Fatigue**-related failure mechanisms are also the most prominent ones in Fig. 17 with the theoretical possibility of causing all three different failure modes short, open and wear out in a wide range of different variations.

A possible **HCF** of electrodes and separators is investigated with pouch cells in this thesis, since they impose the least constraints on these components for all cell types. Therefore, a characterization such as the one described for prismatic cells is also made for pouch cells in Chapter 6. The results are used for model parameterization in Chapter 8 to calculate stress and strain levels. Subsequent experiments might clarify if, for example, **electrode delamination**, **particle cracking** or damages, such as holes in the separator due to **fatigue rupture** are relevant mechanisms for vibration failure. Another possible failure mechanism could be **HCF** of the casing, which can result in casing failure or electrolyte leakage.

The investigations and results of Chapters 5-7 have been published in peer-reviewed scientific journals and are included in this thesis as they have been published. Each chapter and its respective publication are given with an additional summary prior to the publication itself. These summaries provide the motivation and idea behind each work based on the identified research questions together with the essential results and the contribution of each author of the respective publication.

5 Durability of lithium-ion 18650 cells under a random vibration load with respect to the inner cell design

In the following, the first of the core-publications [84] of this thesis is briefly introduced.

Introduction and motivation

This chapter and the respective publication [84] build the bridge to the existing research, as it combines the successful methods EIS (2.4.1) and CT (2.5) from [99] and the majority of vibration-related publications, which investigated the impact of automotive vibration load conditions on lithium-ion cells [133,152–156,191]. This method provides the best possibility for identifying possible failure mechanisms. The motivation was also to clarify the unclear origin of the reported degradation in [152] (see also Section 3.2 for a detailed literature review). In addition, the impact of different inner cell designs as well as previous cyclic aging on vibration durability is investigated in this chapter. To understand the impact of different inner cell designs, 18 different commercially available cells are investigated and tested in detail. An upscaled load profile was derived to increase the probability of failure. The 18650 cell format is chosen because it is both the most investigated cell type in literature regarding vibration durability and the cell format with the highest commercial availability. This availability offers a wide range of various cell designs for the comparison.

Addressed objectives

This approach addresses multiple objectives that are introduced in Section 3.5. The upscaled profile and the varying cell designs combined with EIS- and CT-analysis can help to identify various failure mechanisms (Objective 1) and failure modes (Objective 2). The variation of the inner cell design and the two parameters SOC and SOH addresses Objective 3 (influencing factors).

Key results

None of the tested cells showed significant electrical performance degradation due to vibration. Post-vibration CT of cells tested with the upscaled profile revealed mechanically damaged negative current collector tabs inside two cell types due to a loose mandrel, similar to the observations in [99]. The cells with damaged current collector tabs are the cells with the lowest ratio of mandrel diameter to inner jelly roll diameter, emphasizing the importance of the inner cell design for vibration durability. In case of applications with high vibration loads, the use of a tightly packed cell without an inner mandrel or with a mandrel, but with a high diameter-ratio is recommended. Additionally, ultrasonic welding of tab and can with a wide welding area prevented high ohmic (open) or intermittent failure of the cell. Such failure modes could occur if a complete rupture of the connection between tab and can would occur.

The tests based on the automotive vibration profile according to SAE J2380 showed no damage at all in electrical and optical check-ups in contrast to the results from Hooper et al. [152].

Both SOC and SOH revealed no influence on vibration durability, but it must be stated that this has not been sufficiently tested for the upscaled load profile. A negative impact of vibration levels that occur in automotive applications, could not be found. The upscaled profile has shown to be useful to reveal the influence of the inner cell design on the vibration durability.

Results with regard to the objectives

This publication proved damage of the current collector tab due to a moving mandrel to be the most important and most likely failure mechanism in an 18650 cell regarding Objective 1 (failure mechanisms). No failure mode regarding Objective 2 occurred, since the cells were still fully functional. With a smaller welding area an "open" or maybe an "intermittent" failure might occur. A "short" failure might occur if a particle of the damaged current collector tab could find its way into the jelly roll layers, posing a threat to pierce the separator. Regarding Objective 3 (influencing factors) a dependency on the inner cell design could be found, namely a critical limit of the ratio of mandrel diameter to inner jelly roll diameter.

Outlook

The upscaled profile has shown to be useful to reveal failure mechanisms and dependencies on the inner cell design. This can be transferred to other kinds of applications, e.g., power tools. Power tools are especially interesting, since in this application cells are loaded in various orientations. This can increase the risk of an ISC due to metallic particles. It would also be interesting to investigate cyclically pre-aged cells with the upscaled profile to evaluate the effect of aging-induced jelly roll deformations [192–194] on vibration durability, but since for example, no layer-to-layer displacement occurred, it is likely that the cells would show similar durability.

Contributions

The author of this thesis is responsible for the overall research idea of this publication and the definition of the methodology as well as the overarching research goals, which also define the framework of this thesis. He is also responsible for the design of experiment, the discussion and evaluation of all measurements results including the CT scans, and the test bench for the SAE J2380 testing, as well as the funding acquisition and the project administration of the ReViSEDBatt project at the Institute for Electrical Energy Storage Technology. The author of this thesis wrote the complete manuscript of this publication including the creation of all the figures.

Matthias Merkel performed the experiments for the SAE J2380 testing with uncycled cells during his bachelor thesis [195]. Maik Schoenfuss performed the experiments for the SAE J2380 testing with pre-cycled cells during his bachelor thesis [196]. Michael Tillinger performed the experiments for the upscaled testing and was responsible for the second test bench as part of his master thesis at the TUEV Sued Battery Testing GmbH [197]. Markus Spielbauer performed the CT measurements. Andreas Jossen supervised the work, was involved in the research conceptualization and in the discussion of the results. All co-authors did proof-read of this publication.

Durability of lithium-ion 18650 cells under random vibration load with respect to the inner cell design

Philipp Berg, Markus Spielbauer, Michael Tillinger, Matthias Merkel, Maik Schoenfuss, Oliver Bohlen, Andreas Jossen

Journal of Energy Storage 31 (2020) 101499

Permanent weblink: https://doi.org/10.1016/j.est.2020.101499

Journal of Energy Storage 31 (2020) 101499

Contents lists available at ScienceDirect

Journal of Energy Storage

journal homepage: www.elsevier.com/locate/est

Durability of lithium-ion 18650 cells under random vibration load with respect to the inner cell design

Philipp Berg[a,*], Markus Spielbauer[a,b], Michael Tillinger[c], Matthias Merkel[a], Maik Schoenfuss[a], Oliver Bohlen[b], Andreas Jossen[a]

[a] Technical University of Munich (TUM), Institute for Electrical Energy Storage Technology, Arcisstrasse 21, 80333 Munich, Germany
[b] University of Applied Sciences Munich, Lothstrasse 64, 80335 Munich, Germany
[c] TUEV Sued Battery Testing GmbH, Daimlerstrasse 15, 85748 Garching, Germany

ARTICLE INFO

Keywords:
lithium-ion battery
Random vibration
Vibration durability
Mechanical strength
Noise vibration harshness
Computed tomography

ABSTRACT

Lithium-ion batteries undergo random vibrations in automotive applications, for example due to rough road surfaces. So far, no investigation based on random vibration has considered the influence of the inner cell design and the influence of cyclic aging on vibration durability. Therefore, in this study, 18 different 18650 cell types from seven different manufacturers are tested, using two random vibration load profiles. The applied vibration profiles are the random profile according to the standard SAE J2380 and another upscaled, more severe profile. The SAE J2380 test is carried out using both new and electrically pre-cycled cells. All cell types are analyzed by computed tomography in terms of their inner design with a focus on inner mandrel, spacer and tab design. The performance of the cells is checked in terms of capacity, electrochemical impedance spectroscopy and post-vibration computed tomography. None of the cells shows significant electrical performance degradation due to the vibration. Post-vibration computed tomography reveals mechanically damaged negative current collector tabs inside of two cell types due to a loose mandrel in the case of the upscaled profile. These cell types have the lowest ratio of mandrel diameter to inner jelly roll diameter, emphasizing the importance of the inner cell design for vibration durability.

1. Introduction

The growing awareness of global warming and its consequences increase the importance of technological developments towards a sustainable future. One major required technological change is the transformation from combustion-driven to electrified vehicles [1]. The key component for the success of battery electric vehicles (BEV) or hybrid electric vehicles (HEV) is the traction battery, because it mainly determines price, lifetime and safety [2]. The failure of the battery in an electric vehicle can cause severe damage by fire, explosion and the evolution of toxic gases [3,4]. Therefore, great effort is spent in terms of both research [5,6] and standardized safety testing [7].

One of the several stress factors that batteries and the cells inside the battery have to withstand is the vibration during operation, e.g., due to rough street surfaces. Some publications have already investigated the impact of vibrations by means of experimental testing. Vibration durability was investigated on lithium-ion battery pack level for the application in aerospace [8,9], electric buses [10], electric vehicles [11,12] and heavy-duty vehicles [13]. These publications do not focus in detail on the cell level and also did not report any cell failure. Two publications are available regarding other cell formats. Tsujikawa et al. tested prismatic lithium-ion cells according to UN 38.3 and did not report any damage, but investigated only the open circuit voltage and the integrity of the casing [14]. Wang et al. investigated pouch cells regarding vibration durability for space applications under vacuum conditions and reported a stable configuration with stable voltage and current and therefore no cell failure [15].

Before the various publications regarding vibration durability testing of lithium-ion 18650 cells are presented a short glance is given on different common safety testing standards and regulations. These are important since the major part of the publications, including the present one, is based on the respective standards and regulations. Several researchers compared the different testing requirements regarding parameters, such as frequency content, amplitude, duration, cell condition, severity etc. [7,16–19]. Out of the wide range of standards, the standard SAE J2380 from SAE

Abbreviations: ABS, Acrylnitril-Butadien-Styrol; BEV, Battery electric vehicle; BOL, Begin of life; CID, Current interrupt device; CC, Constant current; CV, Constant voltage; CT, Computed tomography; CTS, Cell test system; EIS, Electrochemical impedance spectroscopy; HEV, Hybrid electric vehicle; NMC, Nickel manganese cobalt oxide, PSD, Power spectral density; RMS, Root mean square; SOC, State of charge; SOH, State of health

* Corresponding author.
E-mail address: philipp.berg@tum.de (P. Berg).

https://doi.org/10.1016/j.est.2020.101499
Received 4 February 2020; Received in revised form 27 March 2020; Accepted 26 April 2020
Available online 04 July 2020
2352-152X/

International [20] (equal to the random test defined in the FreedomCAR abuse test manual [21]) is the most-often tested one in literature, mostly by Hooper et al. [22–24] and Zhang et al. [25]. Hooper et al. chose this standard because it is assumed to be equal to 100,000 miles of vehicle life. They reported significant degradation of the tested lithium-ion 18650 cells due to vibration, with up to 257.82% increase of internal resistance after performing single-axis shaker testing. The tested Samsung ICR18650-22F cells with Nickel Manganese Cobalt Oxide (NMC) cathode and graphite anode were tested with two different vibration profiles: The SAE J2380 and an emulated profile called Warwick Manufacturing Group/Millbrook Proving Ground (WMG/MBK) [22]. The second profile WMG/MBK is based on vehicle vibration measurements by the same research group and also reported to be representative of 100,000 miles of vehicle life [17,19].

Table 1 shows a small extract of the test results from [22], which are especially interesting for our research in this publication. The three presented cells are of interest, because they have been tested according to SAE J2380, in the same orientation on a single-axis shaker and with the same state of charge (SOC) as a part of the tested cells in the present publication. The two cells with an SOC of 25% (cell 10) and 50% (cell 13) showed an increase of the ohmic resistance R_i (intersection of the Nyquist curve with the real axis), given as ΔR_i. The capacity has not been influenced for cell 10 with 25% SOC. Cell 13 showed a capacity decrease ΔC of -1.79%. Unfortunately, for cell 16, only capacity values could be reported due to cell issues [22]. At the same time, cell 16 is the cell with the worst capacity degradation ΔC of all 24 cells (18 test cells and 6 reference cells) that have been reported in [22]. In general, the results in [22] show no linear correlation with a determination coefficient R^2 of only 4.35% between ΔC and ΔR_i. This uncorrelated effect of vibration on the different battery performance parameters further promotes the need to understand vibration-based failure mechanisms and effects in detail.

The other two studies of the same group for other 18650 cells did not reveal a comparable impact of vibrations on the lithium-ion cell performance in terms of, e.g., capacity and inner resistance, no matter if tested using a single-axis shaker [23] or a multi-axis shaker [24].

Zhang et al. tested 32 18650 cells of the same type with random load according to SAE J2380 to obtain a statistical conclusion and observed a degradation with decreasing capacity mean and increasing spread of the capacity values [25].

It is not completely clear that vibrations are the cause for the observed degradation in [25], since no non-vibrated reference cells have been included in the study. Other aging effects could also cause the degradation. Electrochemical aging effects can cause an increased parameter spread, too [26, 27]. The same group tested 18650 cells under different sine loads. The load duration is not given and, e.g., the reported values for capacity show a spread in between the tests. For example, the capacity of 2.584 Ah before vibration is reported to decrease to 2.375 Ah after vibration with 5 Hz and to partly recover to 2.493 Ah after all vibration loads. [28]

Brand et al. tested 18650 cells and pouch cells on a single-axis shaker using sine vibration and shock profile tests based on the testing standard UN 38.3 and a self-designed long-term sine sweep profile of 186 days duration. All test cells were tested at a SOC of 50%. The 18650 cells shocked in the axial direction revealed a damaged current interrupt device (CID) due to mandrel displacement inside the jelly roll, whereas the electrochemical impedance spectroscopy (EIS) and capacity check-ups did not indicate any damage. The long-term test caused local short circuits inside the axially oriented cells with partly melted separator. This has been revealed through computed tomography (CT) measurements and post-mortem analysis. The damaged cells also showed a capacity drop and a rise in ohmic resistance during EIS. The axial direction was the most severe because the moving inner mandrel was identified as the critical failure mechanism. Cells oriented in the radial direction revealed no damage in terms of capacity, resistance or CT images. [29]

Chapin et al. also used CT to investigate the effect of vibrations on 18650 cells and did not report about any cell failure [30]. Kim et al. investigated a range of different 18650 cells and did not find a negative impact of vibrations or shocks for space qualification on the tested lithium-ion cells. The results are difficult to take into consideration since for example the duration for the random vibration is missing. [31]

Therefore, to date only few researchers have published vibration-studies of lithium-ion cells with the application of CT to identify possible inner-cell failures. None of these studies used automotive random vibration profiles. At the same time, CT has shown to be very useful in the vibration studies by Brand et al., because it was capable to reveal damages, which were hidden in the electrical signal [29]. The precise 3D measurement of structures using X-ray CT allows to detect damages very precisely with high local resolution, which has been demonstrated several times [29,32–35]. The local resolution of CT allows to identify damages, which do not directly cause a change in capacity, impedance or other electrical parameters. Such failures can be, but are not limited to, the presence of conductive particles, which not yet caused an internal short circuit, damaged CIDs which are not completely deactivated [29], damaged current collectors, which still can carry the respective current, but could fail later, and others.

Since safety and lifetime is especially important in the field of electric mobility, automotive random vibration is the most tested kind of vibration in scientific literature, as presented. It is hence reasonable to combine automotive vibration testing with the method of CT for the damage detection for the first time. Brand et al. tested one kind of 18650 cells with one kind of pouch cells and considered the inner cell designs [29]. Hooper et al. tested two different kinds of 18650 cells across several publications [22–24], but without consideration of the inner cell design. Therefore, a study, which investigates a higher number of different 18650 cell types and which uses CT to take cell-to-cell differences in the cell design into account is missing yet. In addition, no one so far has reported on the impact of vibrations on aged lithium-ion cells. Lithium-ion cells can show significant deformations in the jelly roll due to cyclic aging [36–39]. The electrodes itself have been also reported to show changes in their mechanical stability [40]. The structural stability and vibration durability of the lithium-ion cells and their active components might therefore change throughout the lifetime of the cells. The aforementioned aspects are addressed in this publication, taking the effects of different inner cell designs and different state of health into account using vibration testing with capacity estimation, EIS and CT analysis for failure identification. It is arguable that vibration conditions change if a cell is installed and packed in a battery module or pack. Nevertheless, to achieve the highest possible safety, it is inevitable to understand every possible failure mechanism inside the cell before all additional effects due to the pack design are investigated.

Table 1
Selected results from [22] for comparison. Three Samsung ICR18650-22F were tested according to SAE J2380 using the same assumed orientation (axial axis of the cell equal to the yaw axis of the vehicle) at three different SOC levels. Strongly increased ohmic resistance for cell 10 and 13 and strongly decreased capacity for cell 16 is reported (*no data available due to cell issues according to [22]).

Cell [22]	SOC	ΔR_i/%	ΔR_{CT}/%	ΔC/%
10	25%	+89.00	+21.16	0.00
13	50%	+82.61	+24.68	-1.79
16	75%	-*	-*	-12.22

2. Experimental

In this section, all required background information is given. The focus is on the vibration load profiles in Section 2.1, the cells under tests and their differences in the inner cell design in Section 2.2, the applied test benches in Section 2.3 and the electrical and optical check-up procedure in Section 2.4.

2.1. Automotive random vibration load profiles

The first chosen load profile is designed according to the standard SAE J2380, because it is the most common in literature [22–25,41]. This test is performed with both uncycled and pre-cycled cells. Pre-cycled cells are cycled down to a state of health (SOH) of approx. 75%-85% (more detailed information is given in Section 2.2 and in the Appendix in Table A.1). To achieve comparability, the SOC levels are adjusted according to [22] and therefore differ from the SOC level given in the SAE standard itself. The SAE J2380 vibration profile, which is referenced by SAE J2929, can be used for cell, module, and pack level testing according to Ruiz et al. [7]. Another random profile out of the standard IEC 62660-2 is included in this study for comparison, while not being tested, since this profile is meant for testing on cell level [7].

Fig. 1 depicts the two mentioned profiles, SAE J2380 and IEC 62660-2, in comparison with an own upscaled profile. This additional upscaled profile is defined to increase the probability of failure, since high durability of the cells was expected prior to the tests. The upscaled profile has the widest frequency range and a higher power spectral density (PSD) level for all frequencies than both mentioned random vibration testing standards, as depicted in Fig. 1a. Consequently, the root mean square (RMS) level a_{RMS} of the vibration is the highest, as given in Fig. 1b. Fig. 1c depicts that the upscaled test is also the test with the longest duration (240 h). The upscaled profile is oriented on the general PSD shape of automotive random vibrations. It is furthermore designed to use the full potential of the vibration exciter. While this upscaled profile might not perfectly match real loads, it is designed here to detect weak cell designs and the respective failure mechanisms. There are also other applications, such as off-road or construction vehicles, which probably have to withstand higher vibration levels.

2.2. Investigated lithium-ion 18650 cells and their inner cell designs

Four different cell types with different inner cell designs are chosen for SAE J2380 testing and 17 different cell types are chosen for the upscaled profile. Detailed information for the different cells under test is given in Table 2. In addition, different levels of SOC and SOH are compared for the SAE J2380 testing. In the case of SAE J2380 testing, six electrically uncycled and six pre-cycled cells (electrically aged cells) are tested for each cell type. Each set of six cells is divided into three cells for vibration testing and three reference cells. For the uncycled cells, three different SOC levels (25%, 50%, and 75%) similar to [22] are chosen. The SOC could have an influence on vibration durability due to the swelling of the jelly roll in the course of the intercalation of lithium [43]. In the case of the pre-cycled cells, only one SOC of 50% is chosen for all six cells. This is done to take increased cell-to-cell variation due to aging [26,27,44] into account. In the case of the upscaled profile, during the first round with a testing duration of 120 h, the cells are taken from storage as they were (SOC equal or below 50% SOC). For the second round of another 120 h, the SOC was adjusted to 0% SOC.

Fig. 2 depicts the four cell types chosen for SAE J2380 testing in the new condition in both axial and radial cross-sections of the 3D CT-measurement at different positions. This gives a good introduction into exemplary differences in the inner cell design of commercially available lithium-ion 18650 cells. An 18650 cells always consists of its housing, called can, which is joint and sealed with the positive terminal (top cap including the CID) at the end of the cell manufacturing, and the so called jelly roll. The jelly roll itself is the rolled stack of the negative electrode (anode), the separator and the positive electrode (cathode). The whole jelly roll is wetted with electrolyte to ensure ionic conductivity. The current collectors of the anode and cathode can be coated with different thicknesses. Cells, which are designed for higher currents such as the Samsung INR18650-25R (Fig. 2d–f) and the Sony US18650 VTC5 (Fig. 2j–l) have thinner coatings, while the high-energy cells with lower power capability such as Molicel IHR18650A (Fig. 2a–c) and Samsung INR18650-35E (Fig. 2g–i) have thicker coatings.

Current collector tabs electrically connect the cathode with the positive terminal and the anode with the negative terminal (the cell can itself) through welding. The current collector tabs can be located close to the can, in the middle of the jelly roll or in the center of the cell. The locations and number of tabs can vary from cell type to cell type. Figs. A.1 and A.2 in the Appendix categorize all 18 cell types in this work regarding the cathode and anode tab locations and the respective numbers of tabs. Some 18650 cell types contain an inner mandrel in the center of the cell. This also applies for three out of four cells in Fig. 2. Only the Samsung INR18650-25R in Fig. 2d–f has no mandrel. These inner mandrels are in focus of this study, because the mandrel has been the most critical component in [29], causing damage in the jelly roll and of the negative current collector tab. This also explains the choice of these four cell types for the SAE J2380 testing. They include cell designs (from left to right in Fig. 2)

- with a thick and therefore heavy mandrel (Molicel IHR18650A),
- without a mandrel (Samsung INR18650-25R),
- with a thin mandrel with a much smaller diameter than the inner circle of the jelly roll (Samsung INR18650-35E),
- with a thin mandrel but a tighter fit of the mandrel in the empty space of the jelly roll (Sony US18650 VTC5).

Other important design aspects are the fitting of the jelly roll in the

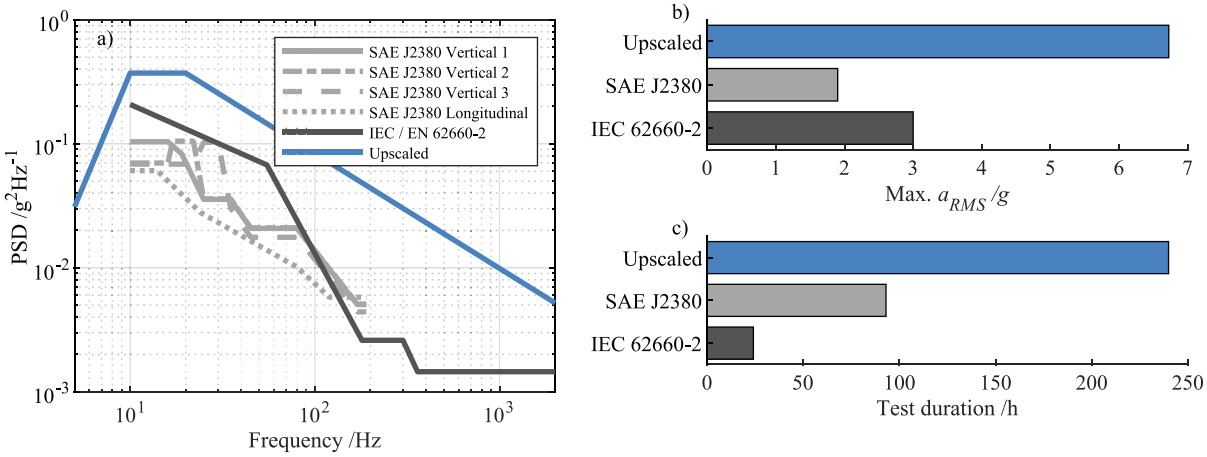

Fig. 1. Comparison of the most common vibration testing standards and the load profiles used in this paper by means of a) power spectral density (PSD), b) maximum RMS acceleration a_{RMS} and c) test duration. The SAE J2380 standard gives four different profiles, which have to be tested subsequently: three for the vertical axis, one for the two longitudinal axes of the vehicle. Profile data is taken from [7,16–18,21,42].

Table 2
List of all investigated 18650 cells in this work with their nominal capacity C_{nom}, cut-off voltages U_{min} and U_{max}, a distinction if an inner mandrel exists, if they have been electrically Cycled or Uncycled and in which experiment they have been applied (J2380 or upscaled). Application is indicated as Test cell (indicated by a T) or Reference cell (indicated by an R) together with the number of applied cells n for each experiment.

Cell type ID	Manufact.	Cell type	C_{nom}/ Ah	U_{min}/ V	U_{max}/ V	Mandrel (Yes/No)	Cycled / Uncycled	n_{cells} J2380	n_{cells} Upscaled
1	A123	APR18650M1A	1.10	2.00	3.60	Yes	U	-	1T
2	LG	18650HE2	2.50	2.50	4.20	No	U	-	1T
3	LG	18650HG2	3.00	2.50	4.20	No	U	-	1T
4	LG	INR18650MJ1	3.50	2.50	4.20	No	U	-	1T
5	Molicel	IHR18650A	1.95	3.00	4.20	Yes	U/C	6T/6R	1T
6	Molicel	IHR18650C	2.05	2.00	4.20	No	U	-	1T
7	Panasonic	NCR18650B	3.35	2.50	4.20	Yes	U	-	1T
8	Panasonic	NCR18650E	2.25	2.00	4.20	Yes	U	-	1T
9	Panasonic	NCR18650PF	2.70	2.50	4.20	Yes	U	-	1T
10	Panasonic	UR18650RX	1.95	2.50	4.20	No	U	-	1T
11	Samsung	ICR18650-22FM	2.20	3.00	4.20	Yes	U	-	1T
12	Samsung	INR18650-25R	2.50	2.50	4.20	No	U/C	6T/6R	1T
13	Samsung	INR18650-30Q	3.00	2.50	4.20	No	U	-	1T
14	Samsung	INR18650-35E	3.35	2.65	4.20	Yes	U/C	6T/6R	1T
15	Sanyo	UR18650E	2.05	2.75	4.20	Yes	U	-	1T
16	Sony	US18650V2	2.10	2.50	4.20	Yes	U	-	1T
17	Sony	US18650VTC4	2.10	2.50	4.20	Yes	U	-	1T
18	Sony	US18650VTC5	2.55	2.50	4.20	Yes	U/C	6T/6R	-

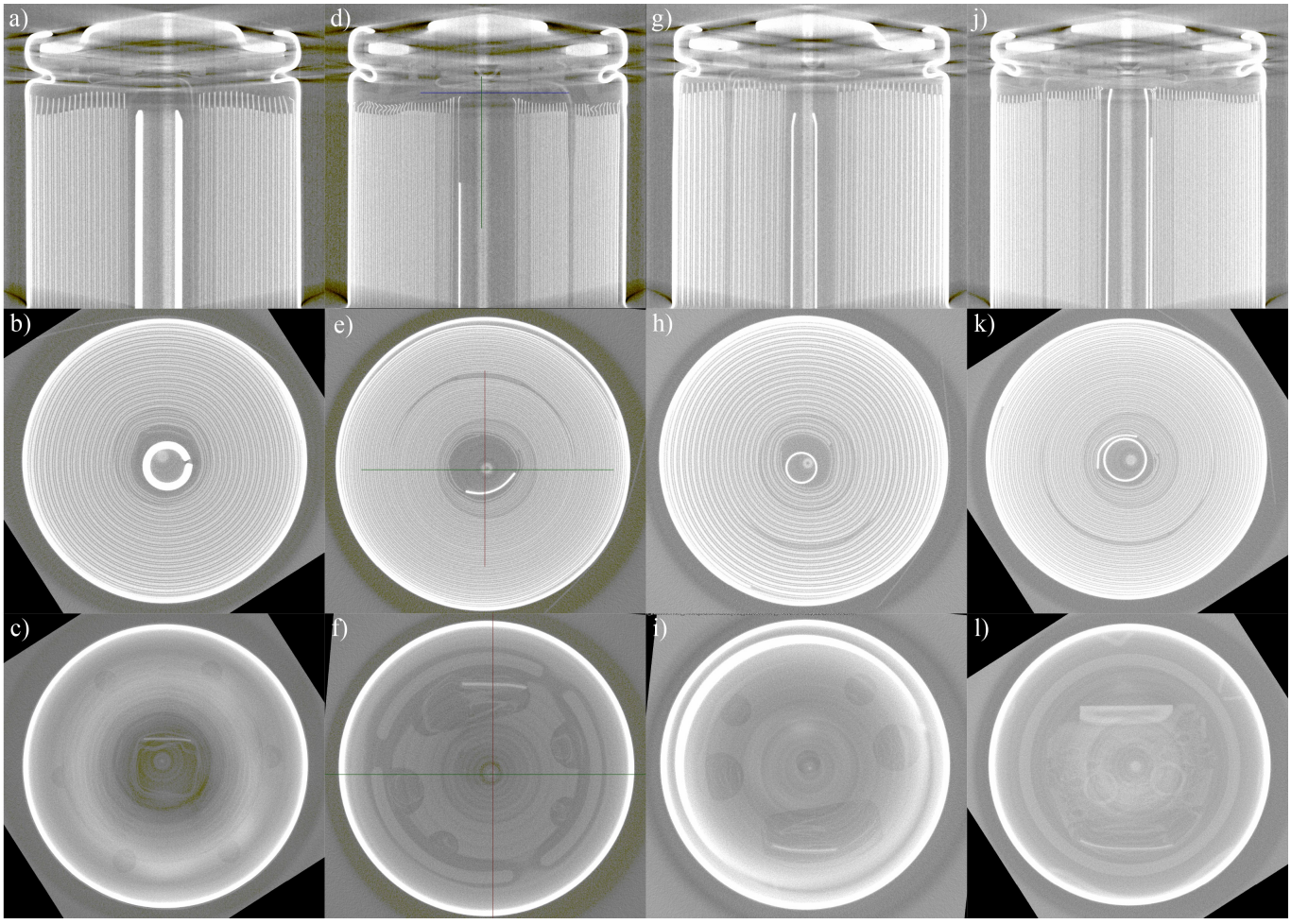

Fig. 2. CT visualization of the four different cell types Molicel IHR18650A (column 1, a-c), Samsung INR18650-25R (column 2, d-f), Samsung INR18650-35E (column 3, g-i) and Sony US18650 VTC5 (column 4, j-l). These cell types are applied for SAE J2380 testing. Row a) depicts axial cross-sections with a side view on the positive tab of each cell, row b) depicts radial cross-sections of the jelly roll and the mandrel while row c) depicts the spacer below the positive terminal of the cells. In the case of Samsung 25R (d-f) the thin lines indicate the cross-sections, the blue line in d) therefore shows the position of the spacer, which is depicted in f). Similar depictions are given for all investigated cell types in the supplementary material of the electronic version of this article. (For interpretation of the references to color in this figure legend, the reader is referred to the web version of this article.)

can, the spacers that keep the jelly roll in its place as well as the current collector tabs and their welding to the can or the top cap. The spacers, which pose a barrier between the jelly roll and the positive terminal for isolation are depicted in the lower row of Fig. 2 (c,f,i,l). Again differences exist, e.g. a more rigid spacer in case of the Samsung INR18650-25R in Fig. 2f, compared to the spacer of the Molicel IHR18650A in Fig. 2c. Similar images such as in Fig. 2 are also given for the other cells as supplementary material in the electronic version of this publication.

The motivation for testing the vibration durability of pre-aged cells is based on three assumptions. At first, the cells are cycled in operation and therefore throughout the lifetime of an electric vehicle. Hence, part of the vibration has to be endured by cycled and aged cells. At second, lithium-ion cells and their components can undergo significant changes in mechanical stability [40] and in the shape of the jelly roll windings in the course of aging [36–39]. At third, in standardized testing, the cells are usually tested at begin of life (BOL), therefore the knowledge regarding the influence of vibrations on aged cells is limited. Exemplary radial cross-sections of the jelly roll of pre-aged cells, which have been tested in this study, are given in Fig. 3. All four cell types show jelly roll deformations, most prominently in the Samsung INR18650-25R in Fig. 3b due to the absence of an inner mandrel and an asymmetry caused by the cathode current collector in the jelly roll. It is of high interest, if for example the strong deformations in Fig. 3b due to the absence of a mandrel or the combination of jelly roll deformations with a mandrel, e.g. in Fig. 3c can be harmful. The aging was made only as preparation for the vibration test and is not itself in focus. Therefore, aging relevant information, especially the charge and discharge protocols, the SOH and the number of full cycles are given in the Appendix in Table A.1.

2.3. Applied vibration test benches

Two different test benches are applied in this paper, which are both depicted in Fig. 4.

The SAE J2380 testing is done with a TIRA S51140 311 N (RMS) force exciter (TIRA GmbH, Germany) with a frequency range between 2 and

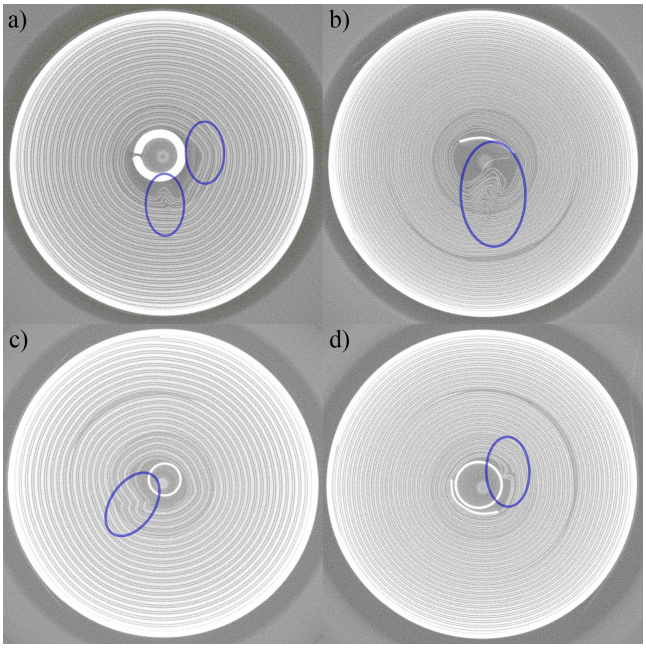

Fig. 3. Exemplary CT depictions of the jelly rolls of a) cycled Molicel IHR18650A (MoliA T4), b) cycled Samsung INR18650-25R (Sam25R T4), c) cycled Samsung INR18650-35E (Sam35E T6), d) cycled Sony US18650VTC5 (SonyVTC5 T4). All cells show jelly roll deformations especially in case of the Samsung INR18650-25R due to non-existing inner mandrel (specific cell names given in brackets for reference to Table A.1).

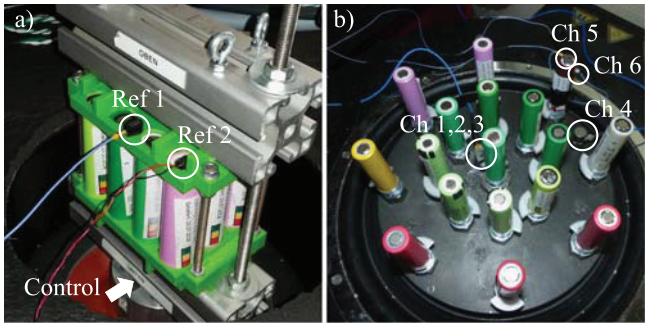

Fig. 4. Depiction of the two vibration test benches used in this study: a) test bench for SAE J2380 testing with a 3D printed cell holder (green ABS). The holder can be clamped in all three axes between two aluminum profiles with control sensor hidden in the aluminum cylinder below the lower aluminum profile and two reference sensors [1] and [2] on top of the module and on one cell. Depicted is the axial orientation of the cells, which are used to apply the vertical profiles of SAE J2380. Part b) shows the test bench for the upscaled testing with cells glued on screws which are directly screwed into the shaker too achieve maximum rigid connection as required for testing up to 2000 Hz. (For interpretation of the references to color in this figure legend, the reader is referred to the web version of this article.)

6500 Hz. The shaker is controlled by an eight-channel m+p vibPilot (m+p international GmbH, Germany) and is driven by an amplifier BAA 1000 (TIRA GmbH, Germany). The shaker is placed underneath a self-made temperature-controlled safety chamber with a gas detection and gas evacuation system. The shaker is extended into the chamber with a membrane-sealed aluminum extension. In the middle of the aluminum extension, the control sensor PCB 355M102 (PCB Piezotronics Inc., USA) is lowered into the extension in the center of the shaker armature. The PCB 355M102 has a sensitivity of 10 mV/g and a measurement range of ± 500 g pk. The 12 cells are placed into a 3D-printed cell holder with steel threaded rods to achieve rigidity. The 3D print material is acrylnitril-butadien-styrol (ABS). The cell holder itself is braced between two aluminum profiles that are connected with rigid M10 threaded rods. The setup is depicted in Fig. 4a. Vibration of the cells and the cell holder can be measured with two lightweight accelerometers to ensure that the vibration of the cells follows the defined profile and is not distorted by resonances or other disturbances in the measurement setup. One of the reference accelerometers is a PCB 352A73 (PCB Piezotronics Inc., USA) with a sensitivity of 100 mV/g, a ± 50 g pk measurement range and a weight of 0.8 grams ([1] in Fig. 4a). The other one is a PCB 352A24NC (PCB Piezotronics Inc., USA) with a sensitivity of 5 mV/g, ± 1000 g pk measurement range and a weight of 0.3 grams ([2] in Fig. 4a). All SAE J2380 tests are performed at a controlled temperature of 25 °C.

This setup for SAE J2380 could be validated up to 200 Hz. This is sufficient for SAE J2380, but insufficient for higher frequencies as required for the upscaled profile. Therefore, another test bench, depicted in Fig. 4b, is applied for the upscaled profile with an RMS SW-2-1240APP 10 kN (RMS) shaker in a climate-controlled laboratory environment of approx. 23 °C and a usable frequency range of 5-3000 Hz. To achieve rigid connection without any resonances in the fixture up to 2000 Hz, the cells are glued with two-component adhesive (WEKEM Fluessigmetall) on M10 steel screws with a smoothed surface and a thin 3D-printed isolation layer in between. The screws are directly screwed in the shaker armature thread holes, which are usually used to attach a head extender. The shaker is controlled by a triaxial PCB TLD339A36 (PCB Piezotronics Inc., USA) with a sensitivity of 10 mV/g and ± 500 g pk measurement range. These three channels (Ch) are Ch 1, Ch 2 and Ch 3 in Fig. 4b with Ch 3 used as control channel. The transmissibility to the cells is checked using the accelerometers PCB 352A25 (PCB Piezotronics Inc., USA) with a sensitivity of 2.5 mV/g, ± 2000 g pk measurement range and a weight of 0.6 grams (Ch 5 and Ch 6 in Fig. 4b). For some measurements, an additional single axis accelerometer PCB 353B03 (PCB Piezotronics Inc., USA) with a

sensitivity of 10 mV/g and a ± 500 g pk measurement range is glued onto the shaker armature (Ch 4 in Fig. 4b). This setup can be only used to apply vibration in the axial direction in the case of a single axis shaker. This orientation is chosen for the upscaled test, based on the literature. The axial direction is the most severe according to [29]. In [22], the six cells which were reported to show more than 200% rise in ohmic resistance R_i include two cells of each possible orientation which the cell can have in the vehicle (two times Z:Z, two times Z:X, two times Z:Y according to the nomenclature in [22]). Concluding these two studies, the chosen axial orientation can be assumed as the worst case. Other orientations can be investigated in follow-up studies.

2.4. Electrical and optical check-up procedures, measurement setups and cell aging

Fig. 5 depicts the check-up procedures for a) SAE J2380 testing and b) upscaled profile testing. The procedures differ because the tests have been performed at different locations with different available equipment.

2.4.1. Electrical check-ups and electrical cell aging for the SAE J2380 tests

In the case of SAE J2380 testing, capacity checks with constant current-constant voltage (CC-CV) discharge with a C-rate of 1C are applied. Termination criteria are the lower cut-off voltage U_{min} of the cells according to Table 2 for the constant current (CC) phase and a C-rate criterion of C/20 to terminate the constant voltage (CV) phase. After this capacity check, the cell is charged to an SOC of 50% of the current capacity and allowed to relax for at least 24 h. The EIS results would be otherwise influenced by long-term equalization effects [45]. After relaxation, EIS at the SOC of 50% is performed. Subsequently, part of the cells is adjusted to SOC levels of 25% or 75% by CC charge or CC discharge with ampere-hour (Ah) counting. This procedure is carried out prior to the vibration tests and repeated after each 1/3 of the entire SAE J2380 profile until 100% of the profile (approx. 93 h). The capacity checks and SOC adjustments are performed with a BaSyTec Cell Test System (CTS) (BaSyTec GmbH, Germany), the EIS measurements are done with a Bio-Logic Potentiostat VMP3 (Bio-Logic Science Instruments, France) galvanostatically in climate chambers with a controlled temperature of 25 °C. The maximum measured frequency is 50 kHz or 500 kHz. The minimum frequency is 10 mHz. The current amplitudes must be chosen with respect to the cells and the SOH. For the new and uncycled cells, the amplitudes are

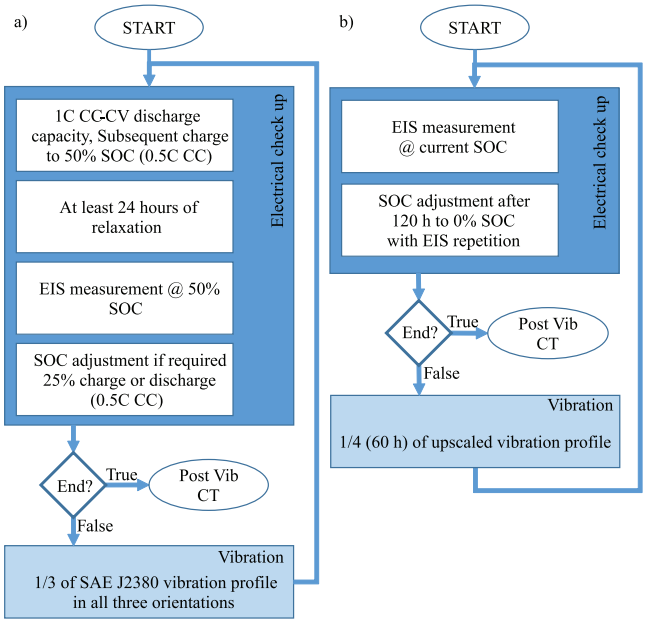

Fig. 5. Schematic flow-charts for testing according to a) SAE J2380 and b) upscaled load profile.

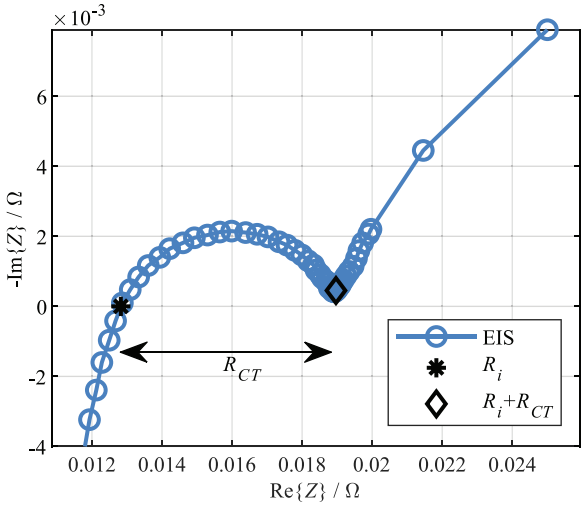

Fig. 6. Exemplary EIS with the characteristic values for degradation identification: the ohmic resistance R_i, which represents the intersection with the real axis and the charge transfer resistance R_{CT}, which represents the diameter of the half circle.

50 mA in the case of the Molicel IHR18650A, 100 mA in the case of the Sony US18650VTC5 and 150 mA in the case of the Samsung INR18650-25R and the Samsung INR18650-35E. For the pre-cycled cells, an amplitude of 50 mA is sufficient for all cells because of the increased impedance due to the aging. The cycling of the pre-aged half of the cells is also executed with the BaSyTec CTS (BaSyTec GmbH, Germany) at a controlled temperature of 25 °C inside a climate chamber according to the protocols given in Table A.1 in the Appendix.

2.4.2. Electrical check-ups for the upscaled tests

For the upscaled test, the procedure had to be simplified due to limited available testing capacities. Therefore, capacity checks before and in between the vibration load profiles have been omitted because the current state of scientific knowledge indicates that the value of the ohmic resistance is the most sensitive indicator for vibration-caused cell failure [22,29]. The EIS measurements at time steps of 60 h each and the SOC adjustment after half of the entire test duration are done with a Bio-Logic VSP and VMP-3 20 Ampere boosters (Bio-Logic Science Instruments, France). The EIS measurements have been performed galavanostatically with a current amplitude of 100 mA for each cell and otherwise similar procedures as given for SAE J2380. The tests are performed in a climate-controlled room of approx. 23 °C with a maximum variation of ±2 °C. After the entire experiment has been conducted according to Fig. 5b (Post-Vib), additional capacity checks on the vibrated cells are done using a BaSyTec CTS (BaSyTec GmbH, Germany) at 25 °C in a climate chamber. Capacity checks are performed with the same procedure and termination criteria as introduced for the SAE J2380 tests. These capacity tests have been additionally performed using reference cells of the same age, taken from permanent storage. The results of this comparison are given in the Appendix in Fig. A.3 because they are outside of the initially planned procedure.

2.4.3. Evaluation of electrochemical impedance spectroscopy results

Fig. 6 presents the methodology to evaluate the EIS. The ohmic resistance R_i and the charge transfer resistance R_{CT} are used according to [46,47] for both tests. For the sake of simplicity, R_i is defined as the cross-section of the impedance curve with the real axis in the Nyquist representation and R_{CT} is defined as the diameter of the half circle extending from R_i to the minimum which marks the transition to the diffusion [46]. The value R_{CT} therefore also includes impedance shares due to passive layers on the surface of the electrodes. This simplification is chosen for better and easier comparison.

Measuring the inductance (high frequency part of the EIS) of the

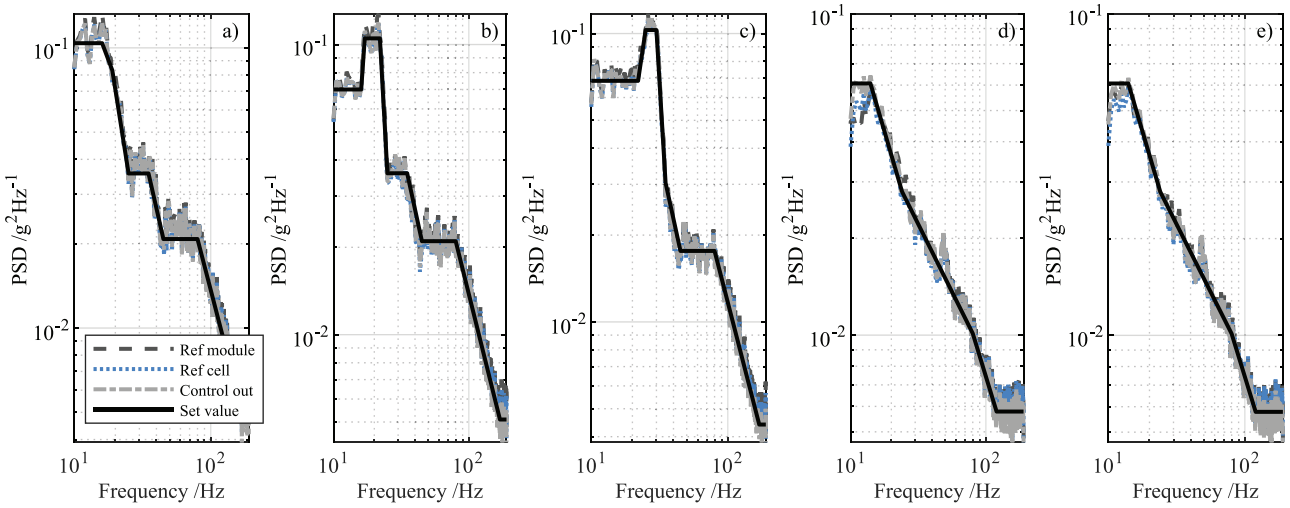

Fig. 7. Results of the test bench validation, depicted are the five different combinations of cell orientation and load profile: a) - c) Vertical 1-3 of SAE J2380 for axial load direction of the cell, d) Longitudinal profile of SAE J2380 for one radial direction (x) and e) Longitudinal profile of SAE J2380 for the other radial direction (y).

cells would be another interesting option, since the high-frequency impedance is also significantly influenced by, e.g., the cell geometry [48] or the tab positions [49]. Therefore, changes such as displacements of the jelly roll, layer-to-layer displacements might become visible as a change in the inductance of the cell and could therefore be an interesting option for the detection of mechanical damages. Unfortunately measuring the inductance of a lithium-ion cell requires sophisticated measurement setups, since the inductivity of the measurement cables can alter the results [50]. Therefore this parameter cannot be taken into account in this study.

2.4.4. Computed tomography measurements

After the vibration tests are completed, every cell is post-checked with a CT investigation for hidden failure or damage inside the cell. The applied CT device is a GE phoenix nanotom s (General Electrics, USA) with a maximum voltage of 180 kV and a maximum power of 15 kW. Each cell has to be scanned twice due to constraints regarding the resolution. Therefore, the upper and the lower part are scanned separately to achieve 3D measurements of sufficient quality. While pre- and post-vibration CT investigation of all cells would be ideal for a detailed comparison of any displacements or damages, this was not possible for all cells due to limited availability of the CT.

The software myVGL 3.25 is used to investigate and analyze the CT measurements. The software can be used to extract different views and for example to measure distances in the recordings.

3. Results and discussion

In the following, the results of the performed experiments are given. Section 3.1 presents the results of the test bench validation for SAE J2380 testing and Section 3.2 gives the respective results according to the electrical check-ups for the SAE J2380 tests. The Sections 3.3 and 3.4 provide the same for the upscaled tests. Section 3.5 discusses all the results and recommendations with respect to the CT analysis.

3.1. Results of the test bench validation for SAE J2380 tests

For the SAE J2380 tests, the assumption is made that the cells are built upright into the electric vehicle battery. Therefore, the axial direction of the cell is equal to the vertical axis of the vehicle. This orientation is chosen because it is the most usual as it offers the simplest design to connect cells in serial and in parallel and to fit the respective modules into the floor of the vehicle. Therefore, the vibration levels for the three profiles Vertical 1, Vertical 2 and Vertical 3 according to SAE J2380 are applied to the cells in an upright position as depicted in Fig. 4a. For the two longitudinal profiles, the cell holder is turned respectively. It must be ensured that the cells undergo the correct vibration level according to SAE J2380. Fig. 7 depicts exemplarily the random profiles for the five possible combinations of load profile and cell orientation. These are the vertical profiles 1-3 for the axial orientation and the longitudinal profile for both radial orientations to account for vibrations along the tilting axis and the pitch axis of the vehicle. In this case, the cell reference sensor (Ref cell) is placed on one of the Samsung INR18650-35E cells. Good correlation of the measured signals from the module (Ref module) and cell reference (Ref cell) accelerometers with the applied control level (Control out) and the required load level (Set value) according to SAE J2380 are visible. Therefore, the cell holder and the complete measurement setup is sufficiently rigid in order to transfer the vibration to each cell in the required frequency range.

3.2. Results of the SAE J2380 tests for new and cycled cells

The cells that underwent random vibrations according to SAE J2380 have been checked at four points in time: prior and post-test as well at intermediate points of 1/3 and 2/3 fulfillment of the entire test duration. Fig. 8 depicts the results of the four check-ups (percentage of SAE J2380 on the horizontal axis) in terms of CC-CV capacity C in the sub-plots a), d), g), j), in terms of R_i in the sub-plots b), e), h), k) and in terms of R_{CT} in the sub-plots c) f) i) l). Each row of sub-plots gives the results for one of the four cell types, which have been introduced in Fig. 2 and Table 2. Both uncycled (blue lines) and cycled cells (dark gray lines) are plotted in the same figures using both test (solid lines) and reference cells (scattered lines).

Most of the cells have been measured with four-point clamping devices, whereas the uncycled reference cells (blue scattered lines) have been connected with spot-welded Hilumin stripes. Therefore, the four-point measurement of the welded cells shows an additional contact resistance. This is the reason, why the uncycled reference cells tend to have a higher internal resistance R_i, e.g., in Fig. 8e and Fig. 8k. Some formation processes for the new cells of the Samsung INR18650-35E type are visible in Fig. 8i with decreasing R_{CT}. No differences between respective test and reference cells can be observed. Therefore, no influence of vibrations according to SAE J2380 on both new and pre-aged 18650 cells of four different designs exist in this study. For a closer look, the results are also given in tabular depiction in the Appendix in Table A.2–Table A.4 for each of the three performance parameters, ordered from worst to best.

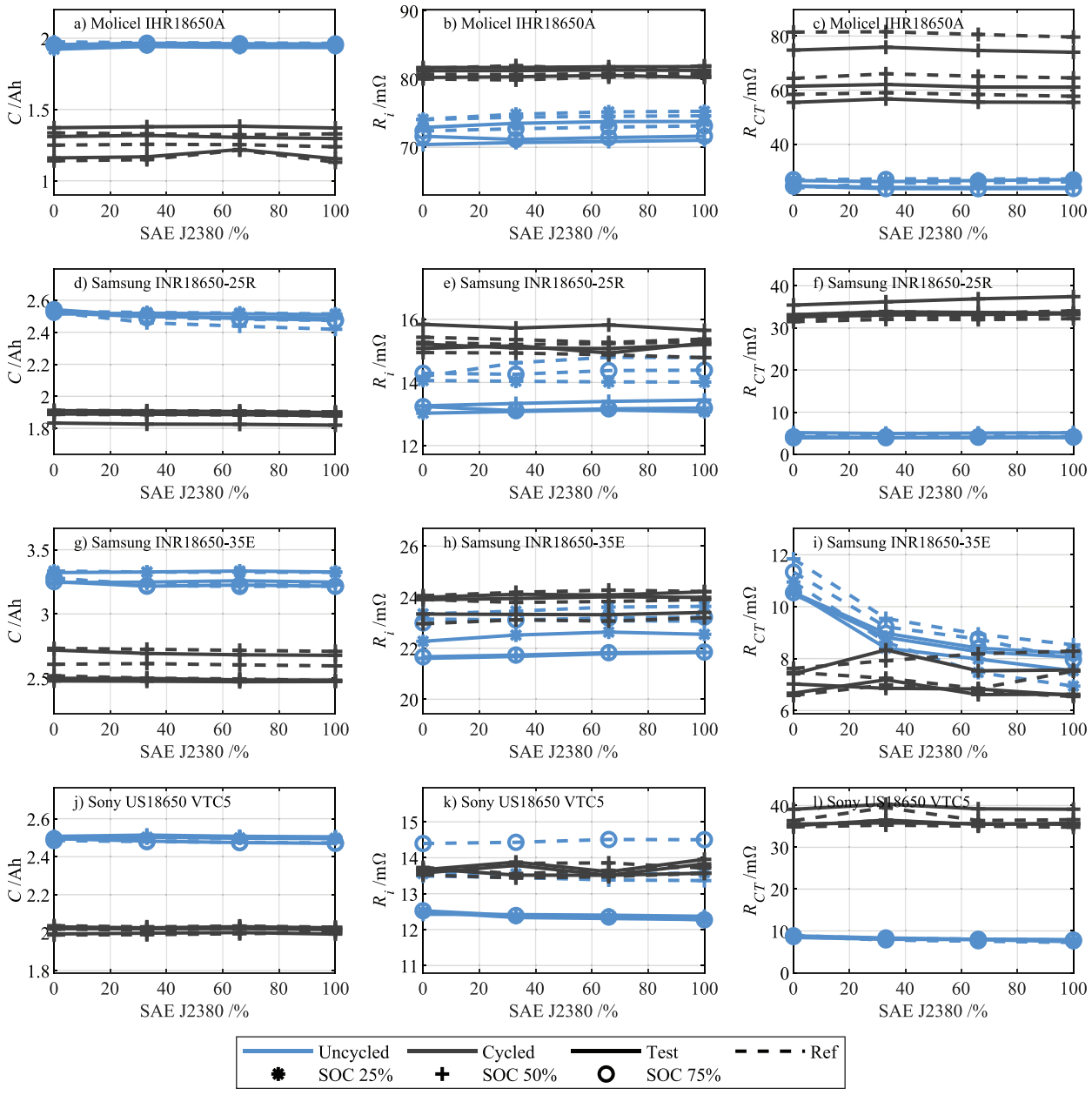

Fig. 8. Results (capacity C, R_i and R_{CT}) of the SAE J2380 tests for all four cell types Molicel IHR18650 A in a) c), Samsung INR18650-25R in d)-f), Samsung INR18650-35E in g)-i) and Sony US18650VTC5 in j)-l) with cycled and uncycled cells. No significant differences between tested cells and reference cells is visible for any cell type and any SOH.

3.3. Results of the test bench validation for upscaled tests

In this section, the vibration transmissibility of the screw connection for the second setup according to Fig. 4b is validated. Fig. 9 depicts the random upscaled profile (Set value) and the measured values at the shaker itself (Control out), the positive terminal (Ch 5 – 18650 top) and the can (Ch 6 – 18650 can) of the exemplary 18650 cell. The vibration is transmitted reliably to the top of the 18650 cell with some perpendicular movement of the cell can. The perpendicular movement is visible in channel 6 (Ch 6). The PSD level of the perpendicular movement is very low in comparison to the PSD level in excitation direction and therefore a reproducible stress for the cell under test can be expected. Therefore the second test bench is validated for tests in the required frequency range up to 2000 Hz.

3.4. Results of the upscaled tests for new cells

For the investigation according to the upscaled profile, ohmic resistance R_i and charge transfer resistance R_{CT} are depicted in Fig. 10 in logarithmic scale. The broken line at 120 h is due to the change of the SOC level at this point in time. Therefore, the values from 0–120 h and from 120–240 h shall be investigated separately. The results from Fig. 10 are also given in the Appendix in Table A.5 and Table A.6. None of the cells shows a rise in ohmic resistance R_i in Fig. 10a. Small visible variations can be explained by uncertainties regarding the ambient temperatures during the check-ups. Charge transfer resistance R_{CT} in Fig. 10b shows stronger variation, but still these variations can be attributed to temperature variations or relaxation and homogenization effects, which are especially slow at low SOC [45]. Not for each cell, the R_{CT} is depicted in Fig. 10b), because the EIS is distorted for some cells at SOC of 0% and a reliable determination of R_{CT} is difficult. Nevertheless, for these cells, the EIS itself

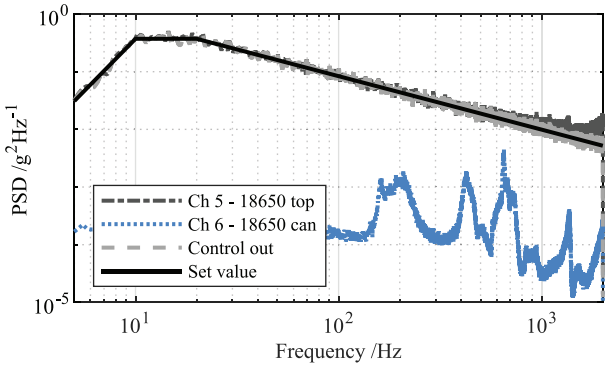

Fig. 9. Validation of the second test bench for the upscaled profile. Two sensors on one exemplary cell according to Fig. 4b are used to validate sufficient transmissibility of the base excitation to the cell. A very good correlation exists with only small exaltation close to 2000 Hz due to a resonance above 2000 Hz in the vertical direction.

was checked in its entirety for homogeneity and none of the cells showed significantly changed EIS from one check-up step to the next one because of the vibration. Again, also for the upscaled profile, no negative influence on the electrical performance of lithium-ion 18650 cell can be seen for random automotive vibrations, no matter which cell manufacturer, type, inner cell design or SOC level is investigated.

3.5. Results from post-vibration CT analysis

To understand the influence of the inner cell design, post-vibration CT is applied and the results are given for SAE J2380 in Section 3.5.1 and for the upscaled tests in Section 3.5.2. Section 3.5.3 discusses the results with regard to a cell-to-cell comparison and Section 3.5.4 provides recommendations regarding cell choice if severe vibration is to be expected.

3.5.1. CT analysis of the SAE J2380 test cells

For the cells, which have been tested according to SAE J2380, no signs or indications of any possible damage caused by the vibration are visible in the CT images. In case of the cycled cells, even pre-vibration CT recordings of the upper half of the cells are available and the cells have been checked for any displacement of the mandrel, the jelly roll or deformations of the CID, as it was observed in [29]. The acceleration profile of SAE J2380 has not caused any displacement, shifts or deformation in the case of the four investigated cell types.

3.5.2. CT analysis of the upscaled test cells

In the case of the upscaled testing, damaged current collector tabs at the negative pole, similar to the findings in [29] occurred for two cells. Fig. 11 shows the respective results. This has been achieved after a much shorter testing time (240 h in comparison to approx. 120 days) and for other cell types. In [29] the tested cell is a Molicel IHR18650A, which is also included in this study. In the present publication, the Molicel IHR18650A under test does not show any damage for both tested vibration profiles. Instead, the failure mechanism of a damaged current collector tab on the negative side can be observed for the Samsung INR18650-35E and the Samsung ICR18650-22FM.

A common characteristic of these three cell types is an inner mandrel inside the cell. In the case of the Samsung INR18650-35E, which has been tested with the upscaled profile, the inner mandrel is completely loose after vibration testing. This can be observed, because the mandrel falls down to the lower tab, depending on which orientation the cell has in the CT during CT examination. The imprints in the negative tab of both cells well correlate with the diameters of each mandrel, as illustrated in Fig. 11. In comparison, the six Samsung INR18650-35E, which have been tested according to SAE J2380, both new and pre-cycled, did not show the same failure mechanism, as mentioned in Section 3.5.1. This is probably because of too low vibration excitation.

The damage to the tab and therefore the connection of the jelly roll with the can did not cause increased resistance of the cell. This is assumed to be due to the ultrasonic welding of the tab over a wide area, visible as small black dots in Fig. 11a and Fig. 11b. In the case of a small resistance welding spot in the center position, the cells might have failed with a completely disconnected negative tab or an intermittent contact and respectively increased impedance. An increased impedance could also subsequently lead to thermal issues with respective safety risks. In the depicted case in Fig. 11, the connectivity is still sufficiently high. Therefore, concerning vibration durability, it is recommended to avoid small spot-welding of the negative tab.

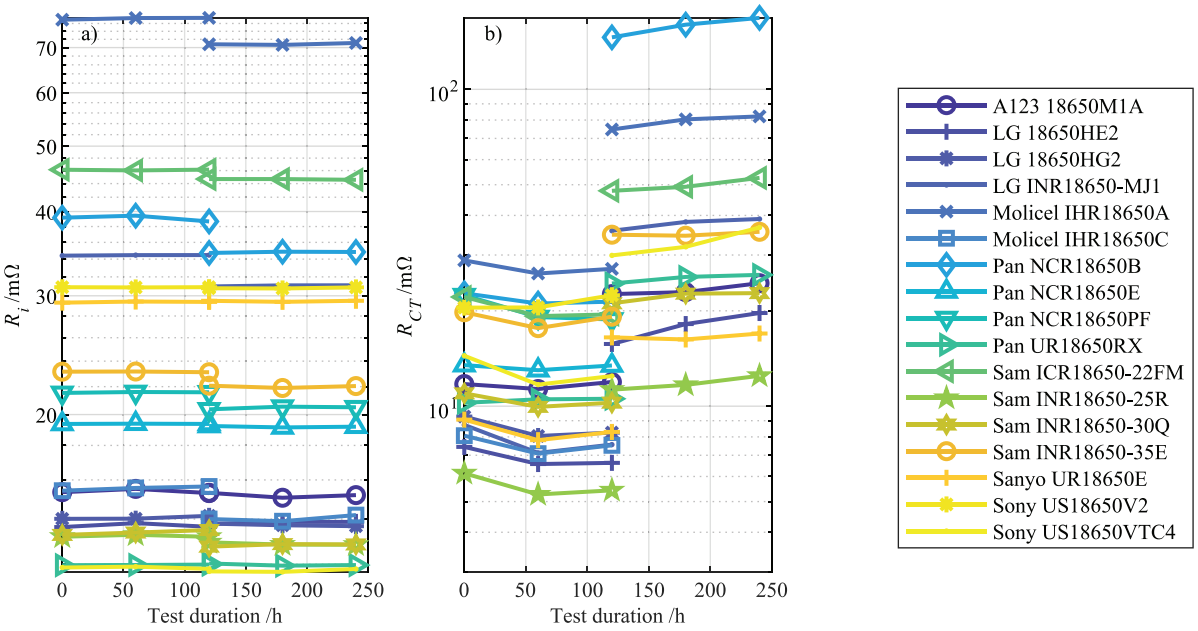

Fig. 10. Values of a) the ohmic resistance R_i and b) the charge transfer resistance R_{CT} for the two sections of different SOC levels during testing from 0–120 h and from 120–240 h. The change of the SOC is the reason for the break at 120 h with a step in the resistance values.

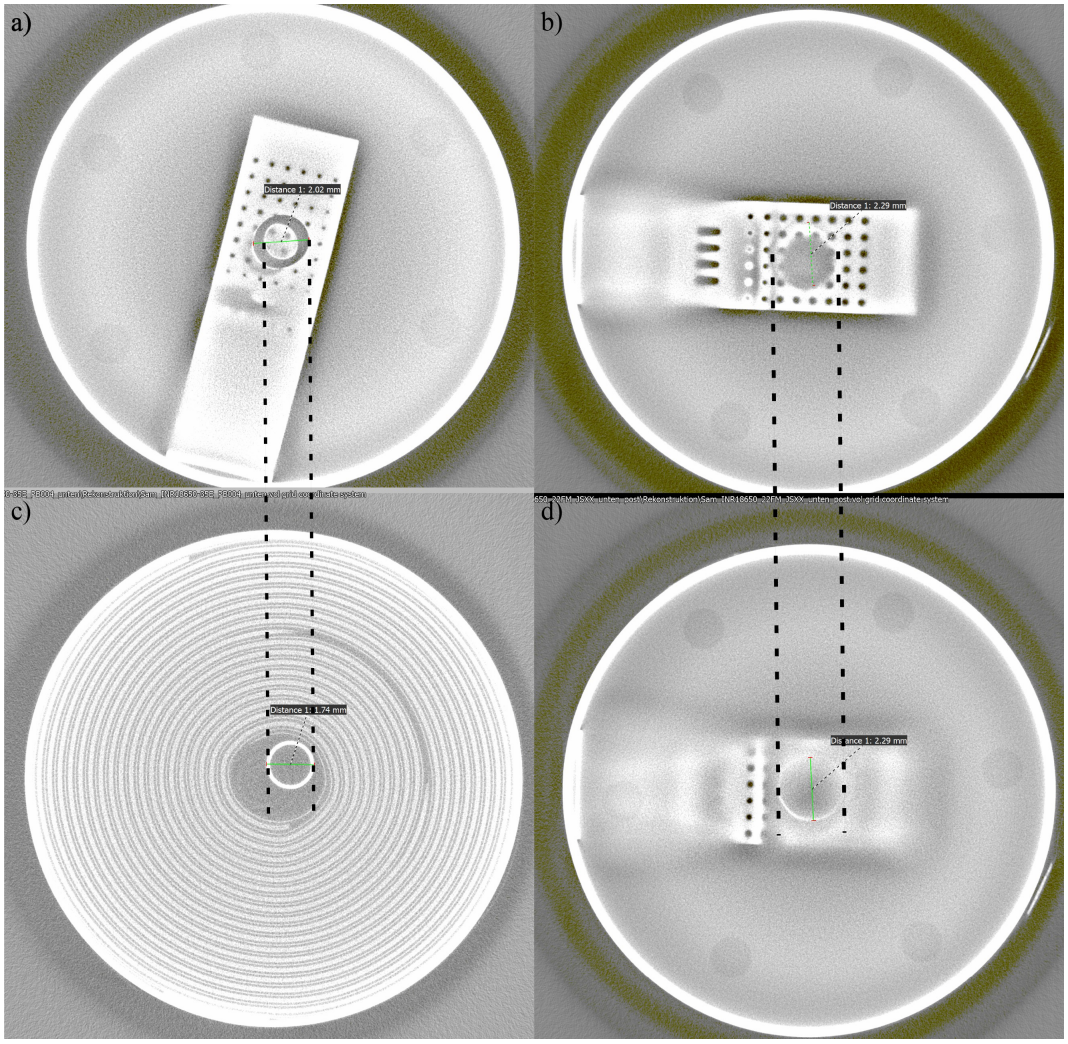

Fig. 11. Depictions of the negative tab of the a) Samsung INR18650-35E and b) Samsung ICR18650-22F together with respective cross-sections showing the top of the inner mandrel in c) and d) The scattered black lines are in parallel for each cell and show the correlation of the hole or imprint in the negative cell and the diameter of the moving mandrel. Cross-section depictions in c) and d) are made on the tip of the mandrel most closely to the respective tab.

3.5.3. Implications of the inner cell design by cell-to-cell comparison

In the following, a detailed look into the importance of the inner cell design on vibration durability is given by a cell-to-cell comparison with respect to the fitting of the inner mandrel.

The Samsung ICR18650-22FM is the successor of the Samsung ICR18650-22F, which has been tested by Hooper et al. in [22]. Three of these cells are introduced exemplarily in Table 1 in the Introduction in Section 1 with strong degradation, becoming visible as increased ohmic resistance R_i. This degradation in [22], would fit well to the failure mechanism of a tab failure caused by the mandrel, as it is described and shown in this work. It is therefore interesting to compare the two cells Samsung ICR18650-22FM and Samsung ICR18650-22F with each other. Fig. 12 depicts this comparison. Only two Samsung ICR18650-22F cells were available, because this cell type is already discontinued. These two cells could not be used for the present experiments, because they have been tested in other vibration experiments in the past and were hence already pre-stressed. Nevertheless, they can be used for comparison by CT. CT analysis of both 22F and 22FM cells reveals a different inner mandrel as the most significant change in the cell. The mandrel of the 22FM has a greater diameter compared with the 22F cell.

Both cells have similar ultrasonic welding areas for the negative tab at the bottom of the can. All investigations in this work are based on the available cells. The cells have the same type designation (ICR18650-22F) and are of similar color as the Samsung ICR18650-22F in Fig. 1 from Hooper et al. [22]. Nevertheless, a possibility remains, that the cells are not completely identical in terms of their inner design.

If an established cell manufacturer changes the diameter of the mandrel in the course of the evolution of a cell type, this could be motivated by a mechanical weakness in the initial design. Therefore, a detailed look at the different mandrel diameters and their incorporation into the different cells is given. All cells in this paper with an inner mandrel, which have been tested with the upscaled load profile are analyzed regarding the outer diameter of the mandrel $d_{Mandrel}$ and the inner diameter of the jelly roll $d_{JR,inner}$. The inner diameter of the jelly roll has been measured three times in different orientations, using the CT recordings and the software myVGL 3.25, and subsequently averaged according to Eq. (1).

$$d_{JR,inner} = \frac{1}{3}\sum_{i=1}^{3} d_{JR,inner,i} \tag{1}$$

This is done to obtain reliable results for $d_{JR,inner}$, since the jelly rolls do not have a perfect circular shape because of, e.g., current collector tabs and the spiral winding.

The ratio r_d of the two diameters is calculated according to Eq. (2).

$$r_d = \frac{d_{Mandrel}}{d_{JR,inner}} \tag{2}$$

A low ratio r_d means that the mandrel has more space and therefore

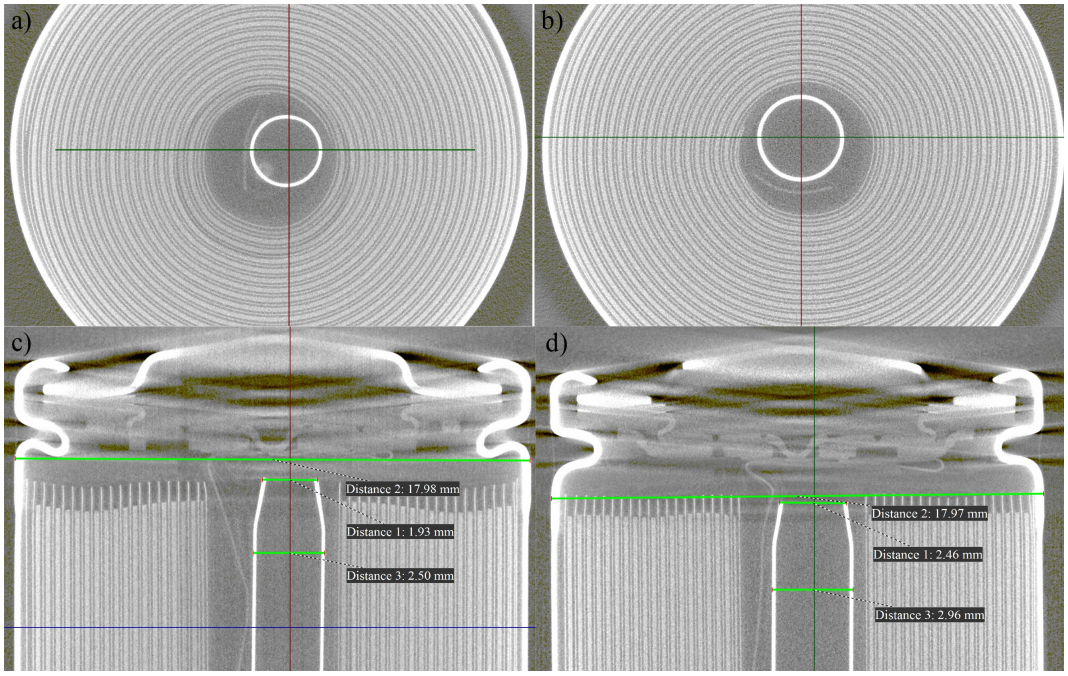

Fig. 12. Comparison of the Samsung ICR18650-22F depicted in a) and c), which has been tested in [22] and its successor Samsung ICR18650-22FM depicted in b) and d), which is tested in this work with the differences in mandrel diameter (Distance 2 = cell diameter, Distance 1 = mandrel diameter at the top, Distance 3 = mandrel diameter).

Table 3
Mandrel diameters $d_{Mandrel}$ and inner jelly roll diameters $d_{JR,inner}$ with the ratio r_d according to Eq. (2). The cells, which showed the possible failure mechanism of a damaged anode tab due to a moving mandrel, are the cells with the lowest ratio of the two diameters.

Cell type ID	Manufact.	Cell type	$d_{Mandrel}$/ mm	$d_{JR,inner}$/ mm	r_d	Observations
CT14	Samsung	INR18650-35E	1.98	3.40	0.58	Damaged anode tabs in this work
CT11	Samsung	ICR18650-22FM	2.97	4.65	0.64	Damaged anode tabs in this work
CT5	Molicel	IHR18650A	3.05	4.61	0.66	Damaged anode tabs in [29]
CT9	Panasonic	NCR18650PF	2.47	3.65	0.68	No damage
CT8	Panasonic	NCR18650E	2.47	3.56	0.69	No damage
CT7	Panasonic	NCR18650B	2.47	3.50	0.71	No damage
CT15	Sanyo	UR18650E	2.84	4.00	0.71	No damage
CT16	Sony	US18650V2	2.79	3.83	0.73	No damage
CT17	Sony	US18650VTC4	2.78	3.79	0.73	No damage
CT1	A123	APR18650M1A	3.27	4.00	0.82	No damage

a higher potential to move and cause damage. The results of the cell-to-cell comparison are given in Table 3 in ascending order of the ratio r_d. The two cell types Samsung INR18650-35E and Samsung ICR18650-22FM show damage to the tab of the negative electrode due to a moving mandrel. These cell types are the cells with the lowest ratios r_d of 0.58 and 0.64. The Molicel IHR18650A, which shows the same failure mechanism in [29], is third in the list with a diameter ratio r_d of 0.66. The available Samsung ICR18650-22F and hence the cell type tested by Hooper et al. [22], has an even lower ratio with an r_d of 0.55 ($d_{Mandrel}$ = 2.51 mm, $d_{JR,inner}$ = 4.6 mm).

All cells which are found to cause a rise of ohmic resistance and / or a damaged anode tab are the cells with the lowest ratio r_d. Therefore, with respect to vibration durability, a low ratio r_d shall be avoided. The effect of the revealed failure mechanism would be a rise in ohmic resistance or an intermittent contact in case of insufficient welding. This fits well with the observed degradation in [22] with increased ohmic resistance and strong cell-to-cell variation of this resistance (38.09%-257.82% [22]). The two Samsung ICR18650-22F, tested for vibration durability by our group, but out of the scope of this publication with other load conditions, have been checked using CT, EIS and capacity. No degradation for EIS or capacity occurred. In contrast, the CT depiction in the Appendix in Fig. A.4 shows a significantly damaged anode current collector tab, where one-half of the tab is nearly disconnected from the other half. This gives a strong optical visualization of possible harmful effects if the ratio of mandrel diameter and inner jelly roll diameter is chosen too small. At the same time, the depiction of the jelly roll inner diameter (red circle), reveals that the mandrel cannot reach the complete welding area. This means that the reason for the increased resistance in [22] cannot be completely clarified yet.

Nevertheless, in summary, it can be stated that the fitting of the mandrel in the jelly roll and the respective diameter ratio is critical for the failure mechanism of negative tab damage due to a moving mandrel. The second critical design aspect is the welding area of the respective tab, since a bigger welding area can cause the cell to be still functional, while the cell tabs are partly damaged. There seems to be also a certain threshold in terms of e.g. vibration amplitude or duration, above which the respective failure mechanisms can happen, since the imprints or cut-outs were not visible in the Samsung INR 35-E, which have been tested with the less severe load profile SAE J2380. The exact conditions under which the respective failure mechanisms occur can be investigated in future studies which higher numbers of similar cells and varying load conditions. Possible risks arising from the observed failure mechanism are discussed in the next Section 3.5.4.

3.5.4. Assessment of possible risks for safety and reliability and corresponding measures

The vibration durability of lithium-ion 18650 cells is investigated with two different vibration profiles in this work. The tests according to SAE J2380 revealed no harmful or severe impact of vibration on the tested cells. The failure mechanism of tab damage due to a moving mandrel and its correlation to the mandrel-jelly roll-diameter ratio is revealed in this work by application of the upscaled profile, which has shown to be useful to reveal critical design aspects. This failure can occur if the mandrel has too much space and is insufficiently constrained and if the welding area of the negative tab is not large enough. This failure mechanism can cause failure modes such as “open” (high ohmic), “intermittent” or “short” (low ohmic) depending on the respective occurring effects. This is discussed in more detail in the following paragraphs.

The first possible effect of this failure is a high ohmic disconnection or intermittent contact. This reduces the reliability on cell level without being safety-critical. It can also have effects on pack level if one or several cells have this failure.

The effects of such a failure on a battery pack level depend on the pack configuration, for example the serial and parallel connection. If not handled properly, it can significantly reduce pack performance, e.g. in a serial connection, since the cell with the poorest condition determines the performance of the pack [51]. In parallel connection, it can cause negative effects due to cell inconsistency with respective problems, e.g., an inhomogeneous current distribution or thermal distribution [52,53].

Another effect of tab cuts due to a moving mandrel is the possible creation of small conductive particles inside the cell, which can cause an internal short circuit. In the case of an upright cell with the positive pole up above and the negative pole at the bottom, the risk might be negligible, because the particles would have to move upwards and cross the spacer and the supernatant separator layers. Inversely, if the cell is mounted the other way around and the mandrel still causes the same damage, small particles might find their way in between the jelly roll layers. Still, the separator layers and the spacers pose a barrier, but a valid statement about the probability of this event cannot be given without further investigation. There are also possible applications, as e.g. power tools, for which the tool and its battery pack is used in wide variety of orientations.

The applied upscaled vibration profile is more severe than what is assumed or expected for a realistic automotive environment. At the same time, it is obvious that in other applications, e.g., for rough off-road conditions, power tools or others, higher vibration levels can occur, compared to conventional road vehicles. In such a case, the inner cell design, as well as the orientation of the cell, have to be considered to ensure reliability and safety. According to the findings in this work, a choice of a cell with stable and rigid spacers and without an inner mandrel is beneficial for the safety of the lithium-ion battery with regard to vibration durability. If a mandrel is required for any reason, e.g. to avoid strong jelly roll deformation in the course of cyclic aging, care should be taken to ensure a low ratio r_d for sufficient fixation of the mandrel. In addition, wide area ultrasonic welding of the negative tab to the can is favorable in contrast to resistance spot-welding.

4. Conclusion

In this work, the impact of random vibration, which can occur for example in automotive applications, is investigated using a wide range of 18650 cells under test. 18 different cell types were investigated with CT regarding their inner cell design parameters. These are, for example, the existence and design of the inner mandrel or the design of the spacers between the jelly roll endings and the respective cell tabs. Two different vibration profiles are used. Tests according to SAE J2380, which shall be representative of 100,000 miles of driving, did not reveal any damages. In contrast, tests with an upscaled profile revealed inner damage to the negative tabs in two cell types because of a loose and moving mandrel. This mandrel caused imprints and cutouts on the negative tab. Because of ultrasonic welding of the tab to the cell can with a sufficiently large welding area, the cells were still fully functional without electrical degradation.

The results show that for possible current or future applications with more severe vibration environment, the inner cell design of the cell and the orientation of the cell shall be considered. While the inner mandrel can be helpful to prevent significant jelly roll deformation due to the cyclic aging, it seems to be at the same time the riskiest component inside an 18650 cell in the case of vibration loading. Resulting cutouts can cause conductive particles, which can increase the risk of an internal short circuit due to particle decontamination. If the inner cell design is taken into account with respect to the expected vibration load during the application, 18650 cells from qualified manufacturers of the current state-of-the art are likely to endure the expected vibration. The choice of cells, which have been proven beforehand, as very durable against severe vibration, for the construction of a battery pack, eliminates certain risks for critical failures, such as an internal short circuit, during pack testing or application. This is of high importance due to the high damage resulting from a pack failure. Vibrations from automotive applications. While the vibration severity in automotive applications is of little harm for the investigated 18650 lithium-ion cells, the sensitivity of vibration durability to the inner cell design, can become very important in the future, with respect to other more severe applications, such as military, helicopters, off-road vehicles, agricultural and construction vehicles, or cordless tools.

Future research should investigate if the contamination due to tab cutouts is likely to cause any safety critical situation and under which circumstances, e.g. varying cell orientations, these situations occur. The studies should be repeated with a higher number of cells with the respective designs to derive dependencies such as to the vibration amplitude in more details. It is furthermore of high interest to investigate the vibration durability on pack level and to evaluate the transferability of the given results.

CRediT authorship contribution statement

Philipp Berg: Conceptualization, Data curation, Formal analysis, Funding acquisition, Methodology, Project administration, Resources, Supervision, Validation, Visualization, Writing - original draft. **Markus Spielbauer:** Investigation, Writing - review & editing. **Michael Tillinger:** Investigation, Resources, Validation, Writing - review & editing. **Matthias Merkel:** Investigation, Validation, Writing - review & editing. **Maik Schoenfuss:** Investigation, Validation, Writing - review & editing. **Oliver Bohlen:** Conceptualization, Writing - review & editing. **Andreas Jossen:** Conceptualization, Writing - review & editing.

Declaration of Competing Interest

The authors declare that they have no known competing financial interests or personal relationships that could have appeared to influence the work reported in this paper.

Acknowledgments

This work was supported by the German Federal Ministry for Economic Affairs and Energy (BMWi) [03ETE004B]. Funding by the German Federal Ministry for Economic Affairs and Energy (BMWi) and the management of the project ReViSEDBatt by the Project Management Juelich (PTJ) are gratefully acknowledged. We also want to thank Martin Knieling from TUEV SUED Battery Testing GmbH and the Institute for Machine Tools and Industrial Management (*iwb*) for their support. The authors also want to thank Prof. Dr. Gregor Feiertag for supporting this project by granting access to the computed tomography device. Philipp Berg also wants to thank Jan Philipp Schmidt for his mentorship.

Supplementary materials

Supplementary material associated with this article can be found, in the online version, at doi:10.1016/j.est.2020.101499.

Appendix

Fig. A.1, Fig. A.2

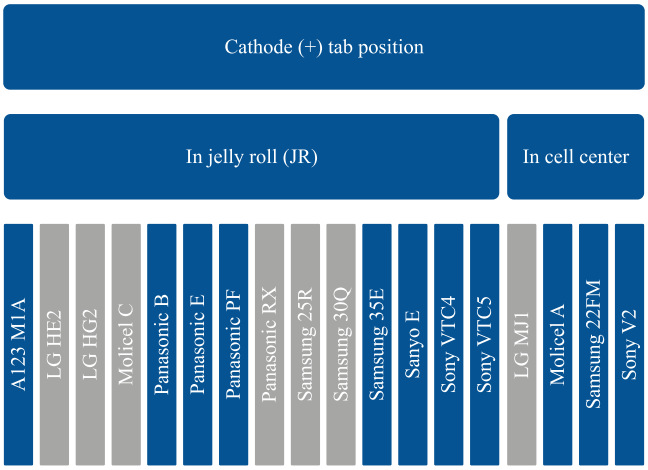

Fig. A.1. Locations of the cathode tabs inside the different cells, cells with a gray background are cells without inner mandrel, cells with a blue background have an inner mandrel.

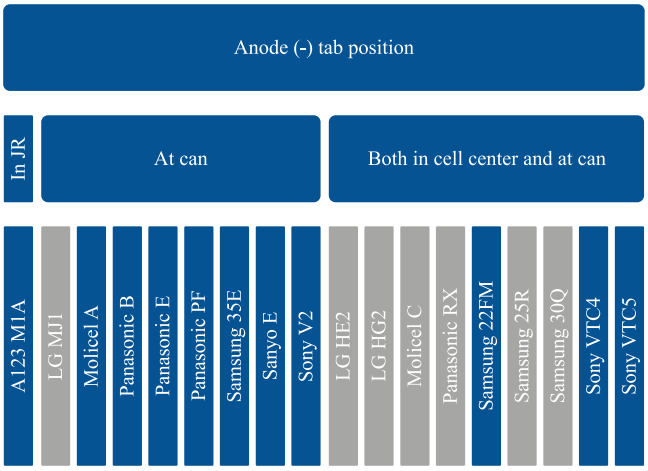

Fig. A.2. Locations of the anode tabs inside the different cells, cells with a gray background are cells without inner mandrel, cells with a blue background have an inner mandrel. Several cells exhibit two anode tabs. In this case, there is always one in the center of the cell and one at the can.

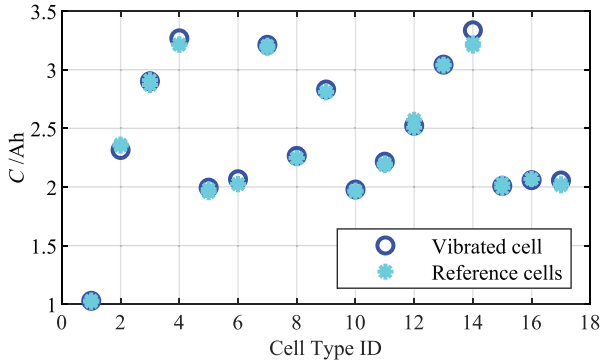

Fig. A.3. Comparison of the CC-CV capacity *C* of the cells vibrated with the upscaled profile and two reference cells of each type, which have been kept in permanent storage throughout the tests. The cell type ID on the horizontal axis refers to Table 2.

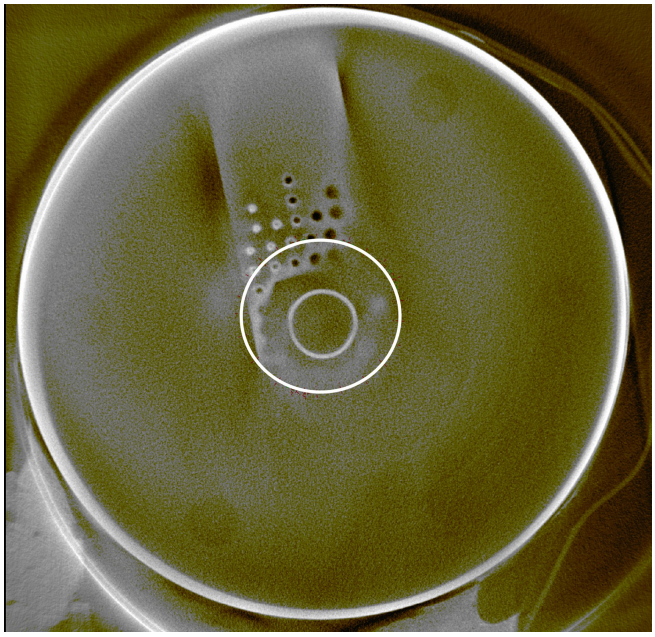

Fig. A.4. Depiction of a Samsung ICR18650-22F, tested in another test with another load showing significant degradation of the current collector tab for the negative electrode. Nevertheless, the cell is still functioning due to the remaining welding spots. The white circle marks the inner diameter of the jelly roll and therefore the possible space for the mandrel to move.

Table A.1
Overview of the pre-cycled cells and the respective charge and discharge protocols, the number of cycles (Check-ups neglected), remaining capacity C from post-aging check-up and the nominal state of health SOH_{nom} in relation to the nominal capacity $C_{nom.}$ (cells with an * have been cycled with half of the current for both charge and discharge in the first 382 cycles, then the current was increased to the mentioned values to increase the speed of aging). The aging took place in a climate chamber with a controlled temperature of 25 °C.

Cell	Charge protocol	Discharge protocol	Cycles	C /Ah	SOH_{nom} /%
MoliA T4	0.5C CC / 4.2V CV (C/10)	1C CC / 3V CV (C/10)	497	1.60	82.2
MoliA R4	0.5C CC / 4.2V CV (C/10)	1C CC / 3V CV (C/10)	281	1.65	84.6
MoliA R5	0.5C CC / 4.2V CV (C/10)	1C CC / 3V CV (C/10)	402	1.64	84.2
MoliA T5	0.5C CC / 4.2V CV (C/10)	1C CC / 3V CV (C/10)	423	1.64	84.1
MoliA T6	0.5C CC / 4.2V CV (C/10)	1C CC / 3V CV (C/10)	512	1.59	81.3
MoliA R6	0.5C CC / 4.2V CV (C/10)	1C CC / 3V CV (C/10)	556	1.58	81.2
Sam25R T4	1C CC / 4.2V CV (C/10)	2C CC / 2.5V CV (C/10)	323	1.87	74.6
Sam25R R4	1C CC / 4.2V CV (C/10)	2C CC / 2.5V CV (C/10)	325	1.94	77.7
Sam25R T5	1C CC / 4.2V CV (C/10)	2C CC / 2.5V CV (C/10)	326	1.94	77.4
Sam25R T6	1C CC / 4.2V CV (C/10)	2C CC / 2.5V CV (C/10)	325	1.95	78.1
Sam25R R5	1C CC / 4.2V CV (C/10)	2C CC / 2.5V CV (C/10)	325	1.95	78.1
Sam25R R6	1C CC / 4.2V CV (C/10)	2C CC / 2.5V CV (C/10)	325	1.93	77.2
Sam35E T4	0.5C CC / 4.2V CV (C/10)	1C CC / 2.65V CV (C/10)	164	2.84	84.8
Sam35E T5	0.5C CC / 4.2V CV (C/10)	1C CC / 2.65V CV (C/10)	155	2.61	78.0
Sam35E T6	0.5C CC / 4.2V CV (C/10)	1C CC / 2.65V CV (C/10)	155	2.63	78.4
Sam35E R4	0.5C CC / 4.2V CV (C/10)	1C CC / 2.65V CV (C/10)	154	2.72	81.2
Sam35E R5	0.5C CC / 4.2V CV (C/10)	1C CC / 2.65V CV (C/10)	176	2.83	84.6
Sam35E R6	0.5C CC / 4.2V CV (C/10)	1C CC / 2.65V CV (C/10)	155	2.64	78.8
SonyVTC5 T4*	1C CC / 4.2V CV (C/10)	2C CC / 2.5V CV (C/10)	969	2.16	84.8
SonyVTC5 R4*	1C CC / 4.2V CV (C/10)	2C CC / 2.5V CV (C/10)	969	2.16	84.6
SonyVTC5 T5*	1C CC / 4.2V CV (C/10)	2C CC / 2.5V CV (C/10)	969	2.17	85.0
SonyVTC5 R5*	1C CC / 4.2V CV (C/10)	2C CC / 2.5V CV (C/10)	968	2.17	85.1
SonyVTC5 T6*	1C CC / 4.2V CV (C/10)	2C CC / 2.5V CV (C/10)	964	2.16	84.6
SonyVTC5 R6*	1C CC / 4.2V CV (C/10)	2C CC / 2.5V CV (C/10)	963	2.16	84.6

Table A.2
Evolution of ohmic resistance values at each check-up step for SAE J2380 testing, ordered according to the change of the ohmic resistance ΔR_i. No significant difference in reference cells (R) and test cells (T) can be observed.

Cell ID	Status	Purp.	SOC/%	R_i (0%)/mΩ	R_i (33%)/mΩ	R_i (66%)/mΩ	R_i (100%)/mΩ	ΔR_i/%
Sam25R R2	Uncycled	Ref	50	14.19	14.62	14.80	14.79	4.24%
SonyVTC5 T4	Cycled	Test	50	13.67	13.88	13.61	13.96	2.11%
SonyVTC5 T6	Cycled	Test	50	13.58	13.79	13.51	13.83	1.88%
MoliA R1	Uncycled	Ref	25	74.11	74.85	75.19	75.27	1.57%
Sam25R T2	Uncycled	Test	50	13.26	13.33	13.40	13.44	1.39%
Sam35E R1	Uncycled	Ref	25	23.35	23.45	23.61	23.64	1.26%
Sam35E T1	Uncycled	Test	25	22.27	22.52	22.63	22.55	1.23%
MoliA T1	Uncycled	Test	25	72.91	73.51	73.77	73.79	1.20%
Sam35E T2	Uncycled	Test	50	21.60	21.68	21.78	21.84	1.09%
Sam25R T5	Cycled	Test	50	15.08	15.17	14.93	15.24	1.09%
Sam35E R5	Cycled	Ref	50	22.96	23.11	23.06	23.20	1.02%
MoliA R3	Uncycled	Ref	75	72.40	72.71	72.96	73.14	1.02%
Sam35E R3	Uncycled	Ref	75	22.99	23.11	23.18	23.22	0.98%
MoliA T2	Uncycled	Test	50	70.40	70.69	70.84	71.04	0.91%
Sam35E T5	Cycled	Test	50	23.99	24.11	24.09	24.21	0.90%
Sam35E T3	Uncycled	Test	75	21.67	21.73	21.83	21.85	0.86%
MoliA R2	Uncycled	Ref	50	74.05	74.41	74.53	74.61	0.77%
SonyVTC5 R3	Uncycled	Ref	75	14.40	14.43	14.51	14.50	0.73%
Sam35E R6	Cycled	Ref	50	24.06	24.19	24.28	24.22	0.69%
Sam25R R3	Uncycled	Ref	75	14.29	14.26	14.38	14.39	0.69%
MoliA R5	Cycled	Ref	50	81.55	81.96	81.40	81.93	0.47%
SonyVTC5 R4	Cycled	Ref	50	13.65	13.84	13.86	13.71	0.46%
MoliA R4	Cycled	Ref	50	80.01	79.86	80.29	80.38	0.46%
Sam35E T6	Cycled	Test	50	23.90	23.95	24.02	23.99	0.38%
Sam25R T1	Uncycled	Test	25	13.03	13.08	13.13	13.07	0.36%
SonyVTC5 R6	Cycled	Ref	50	13.52	13.44	13.47	13.57	0.32%
Sam35E T4	Cycled	Test	50	23.34	23.33	23.31	23.40	0.27%
SonyVTC5 R5	Cycled	Ref	50	13.73	13.56	13.65	13.76	0.22%
Sam25R R4	Cycled	Ref	50	15.27	15.20	15.23	15.30	0.17%
MoliA T5	Cycled	Test	50	81.69	81.70	81.80	81.82	0.16%
SonyVTC5 R1	Uncycled	Ref	25	13.56	13.55	13.54	13.58	0.15%
MoliA R6	Cycled	Ref	50	80.72	80.65	80.79	80.78	0.08%
MoliA T6	Cycled	Test	50	81.21	81.24	81.32	81.25	0.05%
MoliA T3	Uncycled	Test	75	71.62	71.15	71.42	71.63	0.01%
MoliA T4	Cycled	Test	50	80.23	80.34	80.54	80.23	0.00%
Sam35E R4	Cycled	Ref	50	23.91	23.79	23.83	23.91	-0.02%
Sam25R T6	Cycled	Test	50	15.21	15.09	15.08	15.20	-0.08%
Sam25R T3	Uncycled	Test	75	13.24	13.10	13.16	13.19	-0.34%
Sam35E R2	Uncycled	Ref	50	23.14	23.11	23.08	23.06	-0.35%
Sam25R R1	Uncycled	Ref	25	14.06	14.04	14.02	14.01	-0.36%
Sam25R R6	Cycled	Ref	50	15.43	15.36	15.27	15.38	-0.37%
SonyVTC5 T2	Uncycled	Test	50	12.43	12.42	12.40	12.37	-0.46%
SonyVTC5 T5	Cycled	Test	50	13.70	13.52	13.51	13.57	-0.93%
SonyVTC5 R2	Uncycled	Ref	50	13.49	13.45	13.38	13.36	-0.95%
Sam25R R5	Cycled	Ref	50	14.95	14.93	14.88	14.79	-1.08%
Sam25R T4	Cycled	Test	50	15.84	15.72	15.82	15.65	-1.20%
SonyVTC5 T1	Uncycled	Test	25	12.49	12.34	12.31	12.28	-1.69%
SonyVTC5 T3	Uncycled	Test	75	12.52	12.39	12.35	12.27	-2.01%

Table A.3
Evolution of R_{CT} values at each check-up step for SAE J2380 testing, ordered according to the change of the charge transfer resistance ΔR_{CT}. No significant difference in reference cells (R) and test cells (T) can be observed. Fresh uncycled Samsung 35 cells and Sony VTC 5 cells show some kind of formation process with decreasing R_{CT} throughout the first cycles, no matter if they have been vibration test cells or reference cells.

Cell ID	Status	Purp.	SOC/%	R_{CT} (0%)/mΩ	R_{CT} (33%)/mΩ	R_{CT} (66%)/mΩ	R_{CT} (100%)/mΩ	ΔR_{CT}/%
Sam25R R2	Uncycled	Ref	50	4.56	5.00	4.91	5.14	12.77%
MoliA R1	Uncycled	Ref	25	23.72	25.56	25.74	26.09	10.00%
Sam35E R5	Cycled	Ref	50	7.62	7.92	8.19	8.29	8.76%
Sam25R T4	Cycled	Test	50	35.42	36.18	36.90	37.42	5.64%
Sam25R T3	Uncycled	Test	75	3.91	3.94	4.06	4.08	4.50%
Sam25R R5	Cycled	Ref	50	32.11	32.90	32.51	33.12	3.14%
Sam25R R6	Cycled	Ref	50	33.04	33.90	33.54	34.05	3.05%
Sam25R R4	Cycled	Ref	50	31.48	32.02	31.97	32.19	2.25%
Sam25R T6	Cycled	Test	50	32.61	33.06	33.18	33.33	2.20%
MoliA R2	Uncycled	Ref	50	26.61	27.22	27.14	27.17	2.11%
Sam35E T4	Cycled	Test	50	7.41	8.33	7.53	7.56	2.00%
SonyVTC5 T5	Cycled	Test	50	35.18	36.50	35.48	35.76	1.66%
SonyVTC5 R5	Cycled	Ref	50	35.18	36.49	35.25	35.64	1.32%
MoliA T1	Uncycled	Test	25	26.55	26.17	26.57	26.88	1.23%
Sam25R T5	Cycled	Test	50	33.14	33.82	33.67	33.54	1.23%
SonyVTC5 R4	Cycled	Ref	50	36.38	39.50	36.41	36.61	0.63%

(*continued on next page*)

Table A.3 (*continued*)

Cell ID	Status	Purp.	SOC/%	R_{CT} (0%)/mΩ	R_{CT} (33%)/mΩ	R_{CT} (66%)/mΩ	R_{CT} (100%)/mΩ	ΔR_{CT}/%
Sam35E R6	Cycled	Ref	50	7.47	7.24	6.85	7.52	0.59%
MoliA R6	Cycled	Ref	50	64.35	66.04	65.14	64.51	0.25%
Sam25R R3	Uncycled	Ref	75	4.15	4.16	4.12	4.15	0.05%
SonyVTC5 T4	Cycled	Test	50	39.10	40.31	39.21	39.11	0.04%
MoliA T6	Cycled	Test	50	55.48	56.76	55.57	55.49	0.01%
SonyVTC5 R6	Cycled	Ref	50	34.89	35.30	35.06	34.82	-0.21%
MoliA R3	Uncycled	Ref	75	26.88	26.95	26.38	26.83	-0.21%
SonyVTC5 T6	Cycled	Test	50	35.58	35.84	35.66	35.49	-0.25%
MoliA T4	Cycled	Test	50	61.44	62.10	61.15	61.11	-0.55%
Sam35E R4	Cycled	Ref	50	6.58	6.99	6.73	6.54	-0.62%
Sam35E T6	Cycled	Test	50	6.67	7.18	6.61	6.63	-0.64%
Sam25R T2	Uncycled	Test	50	5.14	4.93	5.04	5.09	-0.87%
MoliA T5	Cycled	Test	50	74.81	75.87	74.66	74.02	-1.06%
MoliA R4	Cycled	Ref	50	58.42	59.04	58.39	57.73	-1.18%
MoliA R5	Cycled	Ref	50	81.46	81.58	80.59	79.62	-2.25%
MoliA T2	Uncycled	Test	50	24.61	24.03	24.00	24.03	-2.34%
MoliA T3	Uncycled	Test	75	24.49	23.59	23.55	23.63	-3.49%
Sam25R T1	Uncycled	Test	25	4.18	3.93	3.92	3.96	-5.22%
Sam25R R1	Uncycled	Ref	25	4.31	4.12	4.11	4.08	-5.31%
Sam35E T5	Cycled	Test	50	7.02	6.85	6.83	6.58	-6.23%
SonyVTC5 T2	Uncycled	Test	50	8.73	8.08	8.00	7.90	-9.53%
SonyVTC5 T3	Uncycled	Test	75	8.83	8.31	7.99	7.82	-11.44%
SonyVTC5 R3	Uncycled	Ref	75	8.65	7.86	7.66	7.65	-11.57%
SonyVTC5 T1	Uncycled	Test	25	8.43	8.01	7.93	7.42	-11.94%
SonyVTC5 R2	Uncycled	Ref	50	8.87	8.19	8.06	7.80	-12.07%
SonyVTC5 R1	Uncycled	Ref	25	8.80	7.82	7.54	7.23	-17.80%
Sam35E T3	Uncycled	Test	75	10.54	8.97	8.40	8.21	-22.14%
Sam35E T2	Uncycled	Test	50	10.48	8.82	8.26	8.05	-23.15%
Sam35E R2	Uncycled	Ref	50	11.84	9.55	8.94	8.53	-27.96%
Sam35E T1	Uncycled	Test	25	10.58	8.40	7.98	7.53	-28.79%
Sam35E R3	Uncycled	Ref	75	11.33	9.22	8.75	7.96	-29.76%
Sam35E R1	Uncycled	Ref	25	10.95	8.63	7.46	6.94	-36.63%

Table A.4
Evolution of CC-CV-capacity (C) values at each check-up step for SAE J2380 testing, ordered according to the capacity change ΔC. Test cells (T) show similar or even better capacity values then the reference cells [®]. This indicates little criticality of the applied vibration stress.

Cell ID	Status	Purp.	SOC/%	C (0%)/Ah	C (33%)/Ah	C (66%)/Ah	C (100%)/Ah	ΔC/%
Sam25R R2	Uncycled	Ref	50	2.52	2.46	2.44	2.42	−4.21%
Sam25R T3	Uncycled	Test	75	2.54	2.50	2.49	2.48	−2.58%
Sam25R R3	Uncycled	Ref	75	2.53	2.49	2.48	2.47	−2.08%
Sam35E R3	Uncycled	Ref	75	3.28	3.22	3.21	3.22	−2.03%
Sam35E T4	Cycled	Test	50	2.84	2.82	2.80	2.80	−1.51%
Sam35E R2	Uncycled	Ref	50	3.27	3.24	3.23	3.23	−1.39%
Sam25R T2	Uncycled	Test	50	2.52	2.50	2.49	2.49	−1.24%
Sam35E T3	Uncycled	Test	75	3.25	3.22	3.22	3.22	−1.08%
Sam35E R6	Cycled	Ref	50	2.64	2.63	2.62	2.61	−1.04%
SonyVTC5 T3	Uncycled	Test	75	2.50	2.48	2.47	2.47	−0.99%
Sam25R T4	Cycled	Test	50	1.87	1.86	1.86	1.85	−0.90%
Sam35E R5	Cycled	Ref	50	2.83	2.82	2.81	2.81	−0.87%
MoliA R1	Uncycled	Ref	25	1.97	1.95	1.96	1.96	−0.73%
Sam25R T6	Cycled	Test	50	1.95	1.95	1.95	1.94	−0.68%
Sam25R T5	Cycled	Test	50	1.94	1.93	1.93	1.92	−0.67%
Sam25R R5	Cycled	Ref	50	1.95	1.95	1.95	1.94	−0.67%
Sam25R R1	Uncycled	Ref	25	2.53	2.52	2.52	2.51	−0.66%
Sam25R R6	Cycled	Ref	50	1.93	1.93	1.92	1.92	−0.66%
MoliA T6	Cycled	Test	50	1.59	1.58	1.58	1.57	−0.66%
Sam25R R4	Cycled	Ref	50	1.94	1.94	1.94	1.93	−0.66%
MoliA R4	Cycled	Ref	50	1.65	1.65	1.64	1.64	−0.64%
MoliA R6	Cycled	Ref	50	1.58	1.58	1.58	1.57	−0.61%
MoliA T4	Cycled	Test	50	1.60	1.60	1.60	1.59	−0.59%
MoliA R2	Uncycled	Ref	50	1.97	1.97	1.97	1.96	−0.54%
SonyVTC5 R3	Uncycled	Ref	75	2.49	2.48	2.48	2.47	−0.51%
SonyVTC5 R4	Cycled	Ref	50	2.16	2.15	2.15	2.15	−0.51%
SonyVTC5 T4	Cycled	Test	50	2.16	2.16	2.16	2.15	−0.48%
SonyVTC5 T5	Cycled	Test	50	2.17	2.16	2.16	2.16	−0.48%
SonyVTC5 R5	Cycled	Ref	50	2.17	2.16	2.16	2.16	−0.46%
SonyVTC5 T6	Cycled	Test	50	2.16	2.15	2.15	2.15	−0.43%
Sam35E T6	Cycled	Test	50	2.63	2.62	2.62	2.62	−0.39%
MoliA R5	Cycled	Ref	50	1.64	1.64	1.64	1.64	−0.37%
SonyVTC5 R6	Cycled	Ref	50	2.16	2.15	2.15	2.15	−0.36%
Sam35E R4	Cycled	Ref	50	2.72	2.72	2.71	2.71	−0.33%
Sam35E R1	Uncycled	Ref	25	3.33	3.33	3.32	3.32	−0.30%

(*continued on next page*)

Table A.4 (*continued*)

Cell ID	Status	Purp.	SOC/%	*C* (0%)/Ah	*C* (33%)/Ah	*C* (66%)/Ah	*C* (100%)/Ah	Δ*C*/%
MoliA T5	Cycled	Test	50	1.64	1.64	1.64	1.63	−0.30%
SonyVTC5 R2	Uncycled	Ref	50	2.51	2.50	2.50	2.50	−0.28%
MoliA R3	Uncycled	Ref	75	1.95	1.95	1.95	1.95	−0.26%
SonyVTC5 R1	Uncycled	Ref	25	2.50	2.50	2.50	2.50	−0.20%
Sam25R T1	Uncycled	Test	25	2.51	2.52	2.52	2.51	−0.13%
Sam35E T5	Cycled	Test	50	2.61	2.61	2.61	2.61	−0.11%
SonyVTC5 T2	Uncycled	Test	50	2.51	2.51	2.51	2.50	−0.10%
Sam35E T2	Uncycled	Test	50	3.24	3.25	3.26	3.25	0.10%
SonyVTC5 T1	Uncycled	Test	25	2.49	2.50	2.50	2.50	0.12%
Sam35E T1	Uncycled	Test	25	3.32	3.33	3.33	3.33	0.14%
MoliA T3	Uncycled	Test	75	1.96	1.97	1.96	1.96	0.25%
MoliA T2	Uncycled	Test	50	1.93	1.95	1.94	1.94	0.43%
MoliA T1	Uncycled	Test	25	1.92	1.94	1.94	1.93	0.61%

Table A.5
Values of ohmic resistance R_i throughout the upscaled testing. Superscript [1] indicates tests at higher SOC, Superscript [2] indicates tests at 0% SOC. The presented values are equal to the results depicted in Fig. 10.

Cell ID	R_i (0h)/ mΩ[1]	R_i (60 h)/ mΩ[1]	R_i (120 h)/ mΩ[1]	R_i (120 h)/ mΩ[2]	R_i (180 h)/ mΩ[2]	R_i (240 h)/ mΩ[2]
A123 18650M1A	15.34	15.52	15.30	15.31	15.06	15.19
LG 18650HE2	13.62	13.81	13.63	13.77	13.86	13.87
LG 18650HG2	14.01	14.02	14.15	13.78	13.71	13.66
LG INR18650-MJ1	34.40	34.47	34.47	30.97	31.09	31.09
Molicel IHR18650A	76.98	77.43	77.47	70.79	70.64	71.11
Molicel IHR18650C	15.42	15.57	15.65	14.00	13.90	14.19
Pan NCR18650B	39.17	39.44	38.67	34.72	34.87	34.84
Pan NCR18650E	19.37	19.39	19.37	19.23	19.14	19.19
Pan NCR18650PF	21.53	21.60	21.58	20.36	20.55	20.50
Pan UR18650RX	11.96	11.97	11.98	12.03	11.94	11.96
Samsung ICR18650-22FM	46.13	46.02	46.15	44.69	44.68	44.57
Samsung INR18650-25R	13.18	13.27	13.17	12.93	12.83	12.83
Samsung INR18650-30Q	13.26	13.37	13.49	12.74	12.85	12.84
Samsung INR18650-35E	23.15	23.17	23.11	22.07	21.90	22.04
Sanyo UR18650E	29.30	29.42	29.38	29.49	29.39	29.49
Sony US18650V2	30.89	30.87	30.89	30.78	30.76	30.87
Sony US18650VTC4	11.86	11.90	11.81	11.71	11.69	11.81

Table A.6
Values of charge transfer resistance R_{CT} throughout the upscaled testing. Superscript [1] indicates tests at higher SOC, Superscript [2] indicates tests at 0% SOC. The latter three columns do not contain any values for a few cells, because at 0% SOC the shape of the EIS changes in such a manner that no reliable singular value for the R_{CT} can be obtained. The shape of the EIS showed no significant change and therefore no damage is assumed.

Cell ID	R_{CT} (0 h)/ mΩ[1]	R_{CT} (60 h)/ mΩ[1]	R_{CT} (120 h)/ mΩ[1]	R_{CT} (120 h)/ mΩ[2]	R_{CT} (180 h)/ mΩ[2]	R_{CT} (240 h)/ mΩ[2]
A123 18650M1A	11.75	11.33	11.92	22.58	22.91	24.45
LG 18650HE2	7.44	6.57	6.62	15.71	18.16	19.68
LG 18650HG2	9.28	8.05	8.25	–	–	–
LG INR18650-MJ1	8.73	7.12	7.56	35.79	38.16	38.97
Molicel IHR18650A	28.85	26.23	27.13	74.70	80.39	82.15
Molicel IHR18650C	8.07	7.08	7.52	–	–	–
Pan NCR18650B	22.72	21.09	21.37	145.92	160.00	168.08
Pan NCR18650E	13.48	12.99	13.44	–	–	–
Pan NCR18650PF	22.40	19.11	18.78	–	–	–
Pan UR18650RX	10.25	10.51	10.55	24.39	25.58	25.97
Samsung ICR18650-22FM	22.11	19.24	19.49	47.84	49.25	52.55
Samsung INR18650-25R	6.14	5.26	5.42	11.28	11.67	12.47
Samsung INR18650-30Q	10.98	9.95	10.26	21.12	22.65	22.74
Samsung INR18650-35E	19.79	17.63	19.16	34.77	34.51	35.51
Sanyo UR18650E	9.07	7.81	8.29	16.49	16.24	16.96
Sony US18650V2	20.47	20.50	22.40	–	–	–
Sony US18650VTC4	14.43	11.70	12.45	29.91	31.84	36.64

References

[1] IEA - International Energy Agency, Global EV Outlook2018.
[2] B. Scrosati, J. Garche, Lithium batteries: status, prospects and future, J. Power Sources 195 (2010) 2419–2430, https://doi.org/10.1016/j.jpowsour.2009.11.048 .
[3] C. Mikolajczak, M. Kahn, K. White, Lithium-Ion Batteries Hazard and Use Assessment, Springer, New York, 2012.
[4] Q. Wang, P. Ping, X. Zhao, G. Chu, J. Sun, C. Chen, Thermal runaway caused fire and explosion of lithium ion battery, J. Power Sources 208 (2012) 210–224, https://doi.org/10.1016/j.jpowsour.2012.02.038 .
[5] S. Abada, G. Marlair, A. Lecocq, M. Petit, V. Sauvant-Moynot, F. Huet, Safety focused modeling of lithium-ion batteries: a review, J. Power Sources 306 (2016) 178–192, https://doi.org/10.1016/j.jpowsour.2015.11.100 .

[6] J. Zhu, T. Wierzbicki, W. Li, A review of safety-focused mechanical modeling of commercial lithium-ion batteries, J. Power Sources 378 (2018) 153–168, https://doi.org/10.1016/j.jpowsour.2017.12.034 .

[7] V. Ruiz, A. Pfrang, A. Kriston, N. Omar, P. van den Bossche, L. Boon-Brett, A review of international abuse testing standards and regulations for lithium ion batteries in electric and hybrid electric vehicles, Renew. Sustain. Energy Rev. 81 (2018) 1427–1452, https://doi.org/10.1016/j.rser.2017.05.195 .

[8] M.G. Darvish, Vibration and functional tests on a new designed battery pack of a micro-satellite, Eng. Solid Mech. (2018) 129–134, https://doi.org/10.5267/j.esm.2018.3.001 10.5267/j.esm.

[9] C.-O. Yoon, P.-Y. Lee, M. Jang, K. Yoo, J. Kim, Comparison of internal parameters varied by environmental tests between high-power series/parallel battery packs with different shapes, J. Ind. Eng. Chem. 71 (2019) 260–269, https://doi.org/10.1016/j.jiec.2018.11.034 .

[10] L. Shuyan, C. Yan, J. Fachao, Z. Jianzhu, W. Guoye, Research on the finite element analysis and failure strengthening test of electric bus quick-change battery box, 2015 8th International Conference on Intelligent Computation Technology and Automation (ICICTA), Nanchang, China, IEEE, 2015, pp. 771–775.

[11] Y. Choi, D. Jung, K. Ham, S. Bae, A study on the accelerated vibration endurance tests for battery fixing bracket in electrically driven vehicles, Procedia Eng. 10 (2011) 851–856, https://doi.org/10.1016/j.proeng.2011.04.140 .

[12] J.-K. Lee, J.-S. Yeo, M.-C. Jang, J.-M. Yoon, D.M. Kang, Mechanical durability and electrical durability of an aluminium-laminated lithium-ion polymer battery pack for a hybrid electric vehicle, Proc. Inst. Mech. Eng. Part D 224 (2010) 765–773, https://doi.org/10.1243/09544070JAUTO1388 .

[13] P. Svens, Methods for Testing and Analyzing Lithium-Ion Battery Cells Intended for Heavy-Duty Hybrid Electric Vehicles, Chemical Science and Engineering, KTH Royal Institute of Technology, Stockholm, 2014 Doctoral thesis.

[14] T. Tsujikawa, K. Yabuta, M. Arakawa, K. Hayashi, Safety of large-capacity lithium-ion battery and evaluation of battery system for telecommunications, J. Power Sources 244 (2013) 11–16, https://doi.org/10.1016/j.jpowsour.2013.01.155 .

[15] X. Wang, M. Kato, H. Naito, C. Yamada, G. Segami, K. Kibe, A feasibility study of commercial laminated lithium-ion polymer cells for space applications, J. Electrochem. Soc. 153 (2006) A89, https://doi.org/10.1149/1.2131825 .

[16] J. Frodelius Lang, G. Kjell, Comparing vibration measurements in an electric vehicle with standard vibration requirements for Li-ion batteries using power spectral density analysis, Int. J. Electric Hybrid Veh. 7 (2015), https://doi.org/10.1504/IJEHV.2015.071640 .

[17] J.M. Hooper, J. Marco, Characterising the in-vehicle vibration inputs to the high voltage battery of an electric vehicle, J. Power Sources 245 (2014) 510–519, https://doi.org/10.1016/j.jpowsour.2013.06.150 .

[18] G. Kjell, J.F. Lang, Comparing different vibration tests proposed for li-ion batteries with vibration measurement in an electric vehicle, 2013 World Electric Vehicle Symposium and Exhibition (EVS27), Barcelona, Spain, IEEE, 2013, pp. 1–11.

[19] J. Marco, J.M. Hooper, Defining a representative vibration durability test for electric vehicle (EV) rechargeable energy storage systems (RESS), Electric Vehicle Symposium (EVS 29), Montréal, Québec, 2016, pp. 1–12.

[20] Battery Standards Testing Committee, Vibration Testing of Electric Vehicle Batteries, SAE International, 400 Commonwealth Drive, Warrendale, PA, United States.

[21] D.H. Doughty, C.C. Crafts, FreedomCAR: Electrical Energy Storage System Abuse Test Manual for Electric and Hybrid Electric Vehicle Applications, Albuquerque, New Mexico 87185 and Livermore, California 9455, 2006.

[22] J. Hooper, J. Marco, G. Chouchelamane, C. Lyness, Vibration durability testing of nickel manganese cobalt oxide (NMC) lithium-ion 18,650 battery cells, Energies 9 (2016) 52, https://doi.org/10.3390/en9010052 .

[23] J. Hooper, J. Marco, G. Chouchelamane, C. Lyness, J. Taylor, Vibration durability testing of nickel cobalt aluminum oxide (NCA) lithium-ion 18650 battery cells, Energies 9 (2016) 281, https://doi.org/10.3390/en9040281 .

[24] J.M. Hooper, J. Marco, G.H. Chouchelamane, J.S. Chevalier, D. Williams, Multi-axis vibration durability testing of lithium ion 18650 NCA cylindrical cells, J. Energy Storage 15 (2018) 103–123, https://doi.org/10.1016/j.est.2017.11.006 .

[25] L. Zhang, Z. Ning, H. Peng, Z. Mu, C. Sun, Effects of vibration on the electrical performance of lithium-ion cells based on mathematical statistics, Appl. Sci. 7 (2017) 802, https://doi.org/10.3390/app7080802 .

[26] T. Baumhöfer, M. Brühl, S. Rothgang, D.U. Sauer, Production caused variation in capacity aging trend and correlation to initial cell performance, J. Power Sources 247 (2014) 332–338, https://doi.org/10.1016/j.jpowsour.2013.08.108 .

[27] S.F. Schuster, M.J. Brand, P. Berg, M. Gleissenberger, A. Jossen, Lithium-ion cell-to-cell variation during battery electric vehicle operation, J. Power Sources 297 (2015) 242–251, https://doi.org/10.1016/j.jpowsour.2015.08.001 .

[28] L. Zhang, Z. Mu, X. Gao, Coupling analysis and performance study of commercial 18650 lithium-ion batteries under conditions of temperature and vibration, Energies 11 (2018) 2856, https://doi.org/10.3390/en11102856 .

[29] M.J. Brand, S.F. Schuster, T. Bach, E. Fleder, M. Stelz, S. Gläser, J. Müller, G. Sextl, A. Jossen, Effects of vibrations and shocks on lithium-ion cells, J. Power Sources 288 (2015) 62–69, https://doi.org/10.1016/j.jpowsour.2015.04.107 .

[30] T.J. Chapin, A. Wu, C. Wang, Study of Aging Effects on Safety of 18650-type LiCoOx Cells, 2011.

[31] J. Kim, W. Na, S. Lee, M. Jang, C. Lim, Cell failure evaluations under environmental and safety tests of multiple 18650 li-ion NCA and NMC cells for space cell's qualification estabilishment, 2018 IEEE Energy Conversion Congress and Exposition (ECCE), Portland, OR, USA, IEEE, 2018, pp. 2033–2038.

[32] D.P. Finegan, Dissertation, London, 2016.

[33] V. Yufit, P. Shearing, R.W. Hamilton, P.D. Lee, M. Wu, N.P. Brandon, Investigation of lithium-ion polymer battery cell failure using X-ray computed tomography, Electrochem. Commun. 13 (2011) 608–610, https://doi.org/10.1016/j.elecom.2011.03.022 .

[34] J. Lamb, C.J. Orendorff, Evaluation of mechanical abuse techniques in lithium ion batteries, J. Power Sources 247 (2014) 189–196, https://doi.org/10.1016/j.jpowsour.2013.08.066 .

[35] M. Spielbauer, P. Berg, M. Ringat, O. Bohlen, A. Jossen, Experimental study of the impedance behavior of 18650 lithium-ion battery cells under deforming mechanical abuse, J. Energy Storage 26 (2019) 101039, , https://doi.org/10.1016/j.est.2019.101039 .

[36] X. Fleury, M.H. Noh, S. Geniès, P.X. Thivel, C. Lefrou, Y. Bultel, Fast-charging of lithium iron phosphate battery with ohmic-drop compensation method: ageing study, J. Energy Storage 16 (2018) 21–36, https://doi.org/10.1016/j.est.2017.12.015 .

[37] A.S. Mussa, G. Lindbergh, M. Klett, P. Gudmundson, P. Svens, R.W. Lindström, Inhomogeneous active layer contact loss in a cycled prismatic lithium-ion cell caused by the jelly-roll curvature, J. Energy Storage 20 (2018) 213–217, https://doi.org/10.1016/j.est.2018.09.012 .

[38] A. Pfrang, A. Kersys, A. Kriston, D.U. Sauer, C. Rahe, S. Käbitz, E. Figgemeier, Long-term cycling induced jelly roll deformation in commercial 18650 cells, J. Power Sources 392 (2018) 168–175, https://doi.org/10.1016/j.jpowsour.2018.03.065 .

[39] T. Waldmann, S. Gorse, T. Samtleben, G. Schneider, V. Knoblauch, M. Wohlfahrt-Mehrens, A mechanical aging mechanism in lithium-ion batteries, J. Electrochem. Soc. 161 (2014) A1742–A1747, https://doi.org/10.1149/2.1001410jes .

[40] C. Dai, Z. Wang, K. Liu, X. Zhu, X. Liao, X. Chen, Y. Pan, Effects of cycle times and C-rate on mechanical properties of copper foil and adhesive strength of electrodes in commercial LiCoO2 LIBs, Eng. Fail. Anal. 101 (2019) 193–205, https://doi.org/10.1016/j.engfailanal.2019.03.015 .

[41] L. Somerville, J. Hooper, J. Marco, A. McGordon, C. Lyness, M. Walker, P. Jennings, Impact of vibration on the surface film of lithium-ion cells, Energies 10 (2017) 741, https://doi.org/10.3390/en10060741 .

[42] J.M. Hooper, Dissertation, Warwick, 2017.

[43] S.P.V. Nadimpalli, V.A. Sethuraman, D.P. Abraham, A.F. Bower, P.R. Guduru, Stress evolution in lithium-ion composite electrodes during electrochemical cycling and resulting internal pressures on the cell casing, J. Electrochem. Soc. 162 (2015) A2656–A2663, https://doi.org/10.1149/2.0341514jes .

[44] S. Paul, C. Diegelmann, H. Kabza, W. Tillmetz, Analysis of ageing inhomogeneities in lithium-ion battery systems, J. Power Sources 239 (2013) 642–650, https://doi.org/10.1016/j.jpowsour.2013.01.068 .

[45] F.M. Kindermann, A. Noel, S.V. Erhard, A. Jossen, Long-term equalization effects in li-ion batteries due to local state of charge inhomogeneities and their impact on impedance measurements, Electrochim. Acta 185 (2015) 107–116, https://doi.org/10.1016/j.electacta.2015.10.108 .

[46] S.F. Schuster, T. Bach, E. Fleder, J. Müller, M. Brand, G. Sextl, A. Jossen, Nonlinear aging characteristics of lithium-ion cells under different operational conditions, J. Energy Storage 1 (2015) 44–53, https://doi.org/10.1016/j.est.2015.05.003 .

[47] A. Jossen, Fundamentals of battery dynamics, J. Power Sources 154 (2006) 530–538, https://doi.org/10.1016/j.jpowsour.2005.10.041 .

[48] S. Klink, E. Madej, E. Ventosa, A. Lindner, W. Schuhmann, F. La Mantia, The importance of cell geometry for electrochemical impedance spectroscopy in three-electrode lithium ion battery test cells, Electrochem. Commun. 22 (2012) 120–123, https://doi.org/10.1016/j.elecom.2012.06.010 .

[49] S. Schindler, Diskrete elektrochemische Modellierung und experimentelle Identifikation von Lithium-Ionen-Zellen basierend auf Halbzellpotentialen, Universität Bayreuth, Bayreuth, 2018.

[50] J.P. Schmidt, Verfahren zur Charakterisierung und Modellierung von Lithium-Ionen Zellen, Verfahren zur Charakterisierung und Modellierung von Lithium-Ionen Zellen25 (2013).

[51] K.-C. Chiu, C.-H. Lin, S.-F. Yeh, Y.-H. Lin, C.-S. Huang, K.-C. Chen, Cycle life analysis of series connected lithium-ion batteries with temperature difference, J. Power Sources 263 (2014) 75–84, https://doi.org/10.1016/j.jpowsour.2014.04.034 .

[52] Study of the characteristics of battery packs in electric vehicles with parallel-connected lithium-ion battery cells, in: X. Gong, R. Xiong, C.C. Mi (Eds.), 2014 IEEE Applied Power Electronics Conference and Exposition - APEC 2014, 2014.

[53] M.J. Brand, M.H. Hofmann, M. Steinhardt, S.F. Schuster, A. Jossen, Current distribution within parallel-connected battery cells, J. Power Sources 334 (2016) 202–212, https://doi.org/10.1016/j.jpowsour.2016.10.010 .

6 Structural dynamics of lithium-ion cells – Part I: Method, test bench validation and investigation of lithium-ion pouch cells

In the following, the second of the core-publications [109] is briefly introduced.

Introduction and motivation

This chapter and the respective publication [109] are the first in the field of mechanical characterization to use the EMA method (2.3.2). If the structural dynamics of a lithium-ion cell are well known and can be reliably measured, this allows to understand "how" the cells vibrate and what happens during vibration. It further theoretically supports the use of variations in structural response as a damage indicator in health monitoring or diagnosis. The obtained data can be further used to build FE models, which is done in Chapter 8. The model is based on the data from the publication in this chapter and the respective publication [109]. Fully validated models can provide an insight, for example, into internal stresses, stress distributions and worst-case load conditions in the future. This allows DOE of a maximum-stress-experiment. This experiment can be used to investigate if HCF of electrodes or separators can occur in the case of repetitive loading. The proposed procedure is depicted in Fig. 18. Therefore, in this chapter and in [109], the new test bench (also introduced in Section 2.7) is presented and validated. The test bench design differs significantly from the proposed setups in the literature for EMA on cell level. Choi et al. made the first attempt with impact testing and shaker testing with fixed boundary conditions [158]. Hooper et al. also used impact testing [160]. Popp et al. used a miniature shaker and an impedance head upside down for a single-location measurement [161]. In this work, a shaker-based setup is developed to enable an MDOF approach with minimized influencing boundary conditions.

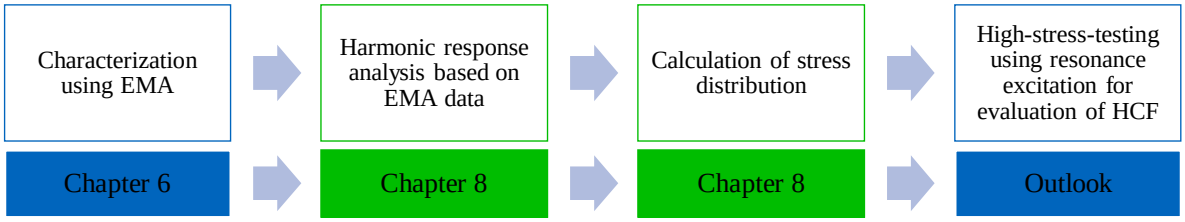

Fig. 18: Description of the approach designed in this thesis to investigate fatigue behavior (HCF). Blue color indicates experimental work, green color indicates FEM simulations.

Addressed objectives

This chapter addresses Objective 1 (failure mechanisms) indirectly since it is a characterization method, which does not directly induce a failure mechanism. Nevertheless, it is the preparation for the investigation of HCF according to the approach described in Fig. 18. Objective 3 (influencing factors) is in the center of this chapter. A detailed sensitivity study with variation of SOC, temperature

and SOH is included. In addition, the nonlinear behavior is investigated using varying excitation levels, which is the basis for the answer to the questions given in Objective 4 (methods).

Key results

In this publication, a new test bench is designed and successfully validated. With that test bench, the structural dynamics of the investigated lithium-ion pouch cells can be identified in terms of natural frequencies, damping ratios and mode shapes. The test bench allows investigation of all cell types and formats with a controlled temperature in the range of approx. 17-34 °C and various measurement possibilities (force, acceleration, voltage, temperature, EIS). The tested unconstrained pouch cells show a strong sensitivity of their structural dynamics to temperature and SOH, while the influence of SOC variation is negligible. Increased temperature causes the cells to soften, while increased aging causes hardening. Both stiffness and damping ratios change in a nonlinear manner.

Results with regard to the objectives

The most relevant parameters for a lithium-ion cell SOC, SOH and temperature are tested regarding the sensitivity of the structural response to each of these parameters. This reveals the importance of temperature and SOH in the case of an unconstrained pouch cell with respect to Objective 3 (influencing factors). The cells showed significant nonlinear behavior even in the case of low excitation forces, making the application of, for example, FDS as a tool for comparison or the reduction of test duration questionable – related to Objective 4 (methods). The obtained data set can be used to further evaluate the question of fatigue regarding Objective 1 (failure mechanisms).

Outlook

Investigations regarding the outlook of this chapter are partly already included in this thesis. The importance of boundary conditions on the structural response can be investigated by comparison with the results of other cells and cell types. With this understanding, the EMA method can be evaluated regarding their usefulness. This addresses Objective 5 (EMA potentials) and is further presented in Chapter 7. The applicability of the data for the parameterization of an FE model is presented in Chapter 8. The results of the FE model can be then used to design experiments for the evaluation of HCF and to gain more insights regarding Objective 1 (failure mechanisms) and Objective 2 (failure modes).

Contributions

The conceptualization of the idea of using EMA for mechanical characterization of lithium-ion cells was initiated, developed, and evaluated by the author of this thesis. He also formulated the overarching research goals and aims and defined the methodology. The author made the DOE and was responsible for the test bench design, conceptualization, construction, and validation as well as the funding acquisition and the project administration of the ReViSEDBatt project at the Institute for Electrical Energy Storage Technology. The author of this thesis was further responsible for analysis and validation of the results. The author of this thesis wrote the complete manuscript for this publication.

Jonas Soellner performed most of the experiments at the test bench and the subsequent MDOF fits according to the DOE by the author of this thesis. Furthermore, he visualized the data in the figures of this publication according to the ideas and instructions of the author of this thesis. Andreas Jossen supervised the work, was involved in the research conceptualization and in the discussion of the results. All co-authors did proof-read of this publication.

Structural dynamics of lithium-ion cells – Part I: Method, test bench validation and investigation of lithium-ion pouch cells

Philipp Berg, Jonas Soellner, Andreas Jossen

Journal of Energy Storage 26 (2019) 100916

Permanent weblink: https://doi.org/10.1016/j.est.2019.100916

Journal of Energy Storage 26 (2019) 100916

Contents lists available at ScienceDirect

Journal of Energy Storage

journal homepage: www.elsevier.com/locate/est

Structural dynamics of lithium-ion cells – Part I: Method, test bench validation and investigation of lithium-ion pouch cells

Philipp Berg*, Jonas Soellner, Andreas Jossen

Technical University of Munich (TUM), Institute for Electrical Energy Storage Technology, Arcisstrasse 21, 80333 Munich, Germany

ARTICLE INFO

Keywords:
Lithium-ion cell
Experimental modal analysis
Vibration
Structural dynamics
Vibration durability
NVH

ABSTRACT

The failure mechanisms that govern the durability of lithium-ion cells under vibration loading are inadequately investigated. It is inevitable for effective durability testing to understand what might determine damage and fatigue. Experimental modal analysis is used to unveil the structural dynamics of lithium-ion pouch cells in terms of natural frequencies, damping ratios, and mode shapes. A test bench for free-free testing has been developed and validated and is presented in this work. Sensitivities from cell parameters such as state of charge, state of health and temperature and from excitation amplitude are revealed. Strong sensitivity of the structural response from excitation amplitude due to nonlinear softening and nonlinear damping was found. Significant softening for increasing temperature with a linear regime, most probably due to changes in the visco-elasticity of the separator, was also observed, while the state of charge showed minor sensitivity. In contrast, cyclic aging caused strongly increased stiffness of the cells. The results can be used for finite element model building to accompany vibration durability research with simulations, to define which parameter sensitivities might determine the level of fatigue during vibration testing and to test the impact of high dynamic stress on lithium-ion pouch cells through resonance excitation.

1. Introduction

Lithium-ion batteries with high performance characteristics are one of the enablers for new environmentally-friendly technologies with better efficiency and lower emissions such as for example battery electric vehicles (BEV), hybrid electric vehicles (HEV) [1] or even electrified airplanes [2]. Furthermore, they are an important and widely used component for power tools, notebooks, smartphones and other portable applications [3]. This is due to their high specific energy, long lifetime, low self-discharge and high-energy efficiency [4]. Despite these many advantages, unfortunately, several incidents with lithium-ion batteries still raise concerns regarding their safety [5–10]. Safety-critical incidents can have catastrophic consequences with rupture, fire, and explosion [5,9,11–13] and the emission of toxic gases [14,15]. Additionally, aging is a critical concern for lithium-ion batteries as a low lifetime increases cost and decreases customer satisfaction.

Besides electrical and thermal conditions in both operation and abuse [5], mechanical loads are present in the applications named above. This work introduces different mechanical loadings and identifies unanswered research questions to motivate the concept of experimental modal analysis (EMA).

The mechanical loads on lithium-ion batteries can be roughly categorized such as follows:

Firstly, abuse loads, usually appearing as a single event with a short duration as for example shock, compression, indentation or bending, e.g. in case of an accident with an electric vehicle or a drop of a power tool or smartphone. Numerous publications are available for this category due to the importance of crash safety for the rise of electric mobility. The research is dedicated to building models for safety investigations [16–18], understanding the deformation characteristics or strain and stress [19–21], describing the short circuit initiation [20,22–24], or identifying the formation and growth of cracks [25] to name only a few research topics and an exemplary set of publications. For a wider overview, the reader is referred to the available reviews

Abbreviations: BEV, battery electric vehicle; CC, constant current; CC-CV, constant current-constant voltage; CID, current interrupt device; CT, computer tomography; DOF, degree of freedom; DPM, driving point measurement; EMA, experimental modal analysis; FEM, finite element model; FRF, frequency response function; HEV, hybrid electric vehicle; IR, infrared; LSCF, least square complex frequency; LSE, least square error; MD, machine direction; MDOF, multi degree of freedom; MIF, mode indicator function; NMC, nickel manganese cobalt; RMS, root mean square; SDOF, single degree of freedom; SEI, solid electrolyte interface; SNR, signal to noise ratio; SOC, state of charge; SOH, state of health; SUT, structure under test; TD, transversal direction; TM, transfer measurement

* Corresponding author.
E-mail address: philipp.berg@tum.de (P. Berg).

https://doi.org/10.1016/j.est.2019.100916
Received 18 June 2019; Received in revised form 29 August 2019; Accepted 29 August 2019

[16,18].

Secondly, quasi-static or low dynamic loading appear during regular operation due to lithium intercalation and de-intercalation during charge and discharge with respective electrode swelling [26–32], and due to thermal swelling [33–35]. The influence of external stress due to e.g. the bracing of the cell and its influence on aging and performance has been researched as well [36–40]. For example, high and inhomogeneous external pressure can cause increased and inhomogeneous plating [40].

Thirdly, during regular operation in mobile or portable applications, vibrations pose a highly dynamic load. This can be for example:

- Stochastically distributed random vibration – most important in the automotive sector representing rough surface or ground conditions [41–43].
- Deterministic sine vibration, which can be a single sine or multi sine due to periodic movements as they appear in power tools but also in helicopters driven by a propeller with a specific frequency [44].
- A mix of both.

To ensure safe operation, vibration testing is an important part of many safety-testing standards, which have been already analyzed and compared by other research groups with respect to the automotive sector [42,43,45–47]. They revealed significant differences amongst the testing standards in duration, state of charge during testing, amplitude level or ambient temperature [47]. Ruiz et al. therefore questioned if the testing conditions are developed and validated enough [47]. If such a variety amongst the different standards exists, it raises suspicion that the tests could be insufficient or may require over-testing.

Several publications report about vibration durability testing of cells and packs. They were tested for application in aviation [48], space [49–52], telecommunications [53], electric buses [54], electric vehicles [55–57] and heavy-duty vehicles [58]. None of these publications found, reported or proved any cell intrinsic failure as they focused on qualification testing with a pass or fail evaluation and were not dedicated to a scientific understanding of possible failure mechanisms inside the cells.

Hooper et al. and Zhang et al. tested the durability of 18650 cells under the load of electric vehicle random vibration by shaker testing [59–61] and multi-axis shaker table testing [62]. The cells in [60,62] did not show significant degradation, while for the Samsung ICR18650-22F cells in [59], the most significant change was reported for the inner resistance. In [61], 32 18650 cells were tested and a degradation of the cell capacities could be observed, but as no control cells were used the degradation can also be due to calendric aging.

The influence of sine vibrations was tested with 18650 cells [63,64] and pouch cells [64]. The measured cell capacities showed some variation in [63], but no clear tendency of degradation.

Brand et al. revealed failure due to a local internal short circuit because of a loose inner mandrel inside the jellyroll of an 18650 cell. The moving mandrel damaged the negative current collector and the separator in case of long-term vibration testing for 186 days. In addition, the inner mandrel deformed the current interrupt device (CID) in case of repeated shock loading according to UN 38.3 T4. Comparison with reference cells, computer tomography (CT) imaging and post-mortem analysis revealed and proved the failure mechanism of a moving mandrel causing reduced safety and performance [64].

Remaining questions to be answered with regard to the influence of vibrations are, for example, if or how the tests can be accelerated by amplitude scaling, if further failure mechanisms exist and how different state of charge (SOC), state of health (SOH) or temperature influence the vibration durability. It is further unclear if e.g. acceleration, displacement, stress or strain governs the failure and the time to failure. As most of the vibration research is about safety testing, the question of possible accelerated degradation received even less attention.

To understand how vibrations influence a structure (here: lithium-ion pouch cell) and if stress-related fatigue by repetitive loading can occur, it is required to understand the structural dynamics of the structure [65,66]. The natural frequencies (also called eigen-frequencies), damping ratios and mode shapes of a structure describe the structural dynamics. The common method to capture the structural dynamics is EMA [67]. As a lithium-ion cell is a complex, dynamic and nonlinear system, permanently influenced by its SOC, SOH, and temperature, it is further required to understand the sensitivity of the structural dynamics to these parameters.

EMA has been already used by some researchers for structural response analysis of pouch cells [68–71], composites with embedded pouch cells [72] and prismatic cell packs [73]. Choi et al. [68] performed the first attempt to investigate the natural frequencies of lithium-ion pouch cells for one SOC by EMA with impact testing and shaker testing with a fixed boundary condition. Hooper et al. investigated pouch cells for different SOC by impact testing and obtained natural frequencies, damping and mode shapes with little sensitivity to the SOC [70]. Popp et al. used a miniature shaker and an impedance head upside down for different SOC, two SOH (one new and one cycled cell) and three distinct temperatures with sensitivity of natural frequencies and damping from both SOC and SOH [69,71]. Galos et al. found that EMA and finite-element-based modal analysis can be used to improve vibration damping properties of structural batteries through beneficial placement of the pouch cells [72].

Volk et al. performed EMA on 14 cell packs composed of prismatic lithium-ion cells with different SOC and different SOH and investigated the first two bending modes. The variations of the natural frequencies did not reveal a statistically significant dependence from either SOC or SOH and were assumed to be due to cell-to-cell variations because of production tolerances [73].

Finite-element-based modal analysis on the pack level for a pouch cell pack [74] and for a prismatic cell pack [75] was performed to investigate the influence of e.g. pre-stress and cell-to-cell variation and the possibility of using the natural frequencies for health monitoring. The simulations were built on parameter assumptions; no measurements were done or used for parameterization or validation.

The presented method and results in this publication are part of our approach to systematically understand and reveal the impact of vibrations on the safety and lifetime of lithium-ion cells.

The approach consists of three steps:

1. The structural dynamics of different lithium-ion cells are examined under varying conditions to reveal the sensitivity of the structural response to SOC, SOH, temperature and excitation level. If relative displacements occur, the mode shapes can deliver valuable insights into critical movements.
2. The obtained data is used for the setup of finite element models (FEM) to obtain mechanical properties, comparable to [76] and to calculate stress and strain concentrations, comparable to [74,75] for different loading conditions.
3. Based on the experimental data and the simulation results, systematic design of experiment for vibrational testing is possible to achieve maximum stress and to validate if periodic loading can cause fatigue of the cell or any of its components. By this, the question whether resonances are critical for lithium-ion pouch cells (as they are for other systems [67]) can be answered.

This failure mechanism-oriented approach is assumed to reveal more information than an application-oriented approach, which is often limited to a pass or fail statement.

This publication focuses on the first step of the explained approach. A newly designed test bench with the validated free-free condition is introduced and validated and a consumer pouch cell is investigated. The sensitivities of the structural dynamics to SOC, SOH, temperature and excitation amplitude are shown and the nonlinear characteristics are analyzed. The free-free condition, as well as the understanding of

nonlinear behavior, is mandatory for any further analysis by finite element modeling, fatigue calculation or damage accumulation to name only a few examples.

The EMA presented in this work is the first one in literature with a validated shaker-based test bench with the free-free condition for cell-level testing and the first one applying a multi-degree of freedom (MDOF) fit. Furthermore, it is the first EMA based investigation of the nonlinear dynamics, and the measurement of more than one cycle-aged cell.

2. Experimental

Beginning with a brief introduction of EMA, the developed test bench and the structure under test (SUT) are introduced.

2.1. Experimental modal analysis (EMA)

The modal analysis is very important in vibration testing. Mechanical malfunction or failure can be caused by the excitation of the preferred motion of the system, in other terms by resonance excitation. The modal analysis enables the understanding of the extent and location of severe vibration and is, therefore, a useful tool for diagnostics and prediction [67].

In EMA, a force $F(\omega)$ excites the SUT and the response acceleration $a(\omega)$ is measured with an accelerometer. The measured force excitation and acceleration response are used to calculate the frequency response function FRF(ω) according to Eq. (1).

$$\mathrm{FRF}(\omega) = \frac{a(\omega)}{F(\omega)} \tag{1}$$

Measurement of the FRF for one position on the structure is sufficient to calculate natural frequencies and modal damping [77,78] if nodal points are avoided. If excitation or response is located on a nodal point of the respective mode shape, the resonance remains undetected [77].

Damping is usually described as damping ratio ζ according to Eq. (2) [79].

$$\zeta = \frac{c}{c_0} \tag{2}$$

Hereby, c is the actual damping and c_0 is the critical damping (damping threshold for which and above no oscillation occurs) [79].

If the characteristic mode shapes for each resonance are required, the FRF has to be measured at different locations on the structure by roving excitation or roving response [67,77]. Each combination of position and respective orientation, e.g. x, y or z (if the rotational movement is neglected), is called a degree of freedom (DOF). Generally speaking, the DOF is the number of independent incremental coordinates to represent the general incremental motion of a system [67]. If a structure or system consists of only one concentrated mass and is constrained in all but one directions, than the system is called a single degree of freedom (SDOF) system. If the system consists of distributed masses with several DOF, the system is called a multi degree of freedom (MDOF) system. The measurement matrix in this work consists of 25 DOF, defined as *pXX(z)*, equally distributed over the surface of the pouch cell, shown in Fig. 1 b). *XX* are placeholders for the respective matrix locations. The cell under test is excited at the two DOF *p22(z)* and *p33(z)* from the bottom side of the cell. Direction for both excitation and response is always *z* (through plane) in this work. In the event that the DOF for force and acceleration is the same, the measurement is called a driving point measurement (DPM), otherwise it is called transfer measurement (TM) [77]. All results in this study, besides the mode shapes, are measured with DPM.

Mode indicator function (MIF) and stability diagrams are used to extract modes with frequency and damping values in a MDOF fit [77,80]. It is required to use MDOF instead of the more simple single degree of freedom (SDOF) fit, as the modes overlap due to high modal density and high damping [77,80]. The fitting algorithm is a poly-reference least squares Complex Frequency Domain (p-LSCF) fit from [81], which is recommended for highly damped structures [82].

To check the quality of the measurement the coherence function [83], which gives the degree of linearity between input and output, is used (1 for perfect linear correlation of input and output, 0 for no correlation). Additionally, the FRF is checked in both bode and Nyquist plots as distortions of the FRF e.g. can be more clearly seen in the Nyquist plane.

The advantage of the modal analysis procedure is that a complex structural system with coupled differential equations can be transformed into a set of uncoupled equations with easy-handle mass, stiffness and damping matrices [77]. The obtained data can be used to build models, e.g. by the finite element method, which can be incorporated into a higher order system model [67].

2.2. Test bench and measurement setup

Fig. 1 depicts the test bench and respective setup. The test bench consists of a TIRA S51140 force exciter (TIRA GmbH, Germany), also called a shaker, with a maximum force of 400 N and the amplifier BAA 1000 (TIRA GmbH, Germany) with a nominal power of 1200 V A. An eight-channel m + p vibPilot (m + p international, Germany) serves as data acquisition and control unit. A Bio-Logic VSP-300 (Bio-Logic Science Instruments, France) with impedance capability and 10 A booster is available for SOC adjustment of the cells and other electric tests. m + p Analyzer 5.1 (m + p international, Germany) is the software for measurement, data acquisition, and post-processing. The shaker is placed below a self-built safety chamber with temperature control. The armature of the shaker is therefore extended into the chamber with a rubber membrane to seal the chamber. The safety chamber is equipped with gas detection, temperature, and voltage observation capabilities and an automatic shutdown of the exciter in case of safety values out of bounds. The safety system is controlled with a PXI System from NI (National Instruments, USA). The temperature of the SUT can be measured contactless with an infrared (IR) sensor optris CS (Optris GmbH, Germany) without any interference with the measurement. Force transducer and accelerometer are selected with respect to size and weight to minimize the influence on the measurement. The excitation force is measured by a Kistler 9712B5 force transducer (Kistler Group, Switzerland) with a measurement range of 22 N for both compression and tension, a sensitivity of 180 mV/N and low weight of 19 grams. The accelerometer is a PCB 352A73 sensor (PCB Piezotronics Inc., USA) with a measurement range of ± 1000 g, a sensitivity of 5 mV/g and a weight of only 0.3 g (< 1% of the mass of the SUT m_{SUT}). Sensors and SUT are joined with a thin layer of petro wax 080A109 (PCB Piezotronics Inc., USA). The accelerometer has two 30 cm long thin twisted cables with 10–32 plug at the end to connect the vibPilot with coaxial cable. The thin and lightweight cable reduces possible negative consequences on measurement accuracy.

To uncouple the SUT from the test bench, the force transducer is mounted on a stinger made from stainless steel with a diameter of 1.5 mm and adjustable length. The SUT is supported by two metallic springs with a wire diameter of 0.2 mm, a length of 30 mm, low suspension rate of 0.02 N/mm, a preload of 0.13 N, a maximum displacement of 28.5 mm and a maximum load of 0.69 N. This results in an initial displacement of 4.12 mm for the pouch cell of 43 g. Therefore, in both tension and compression, the suspension is in the linear elastic range for all measurements.

2.3. Samples under test

In this work, five new and five aged pouch cells of the type SLPB356495 from Kokam with a nominal capacity of C_{nom} = 2.1 Ah and a weight of 43 g with Nickel Manganese Cobalt Oxide (NMC)

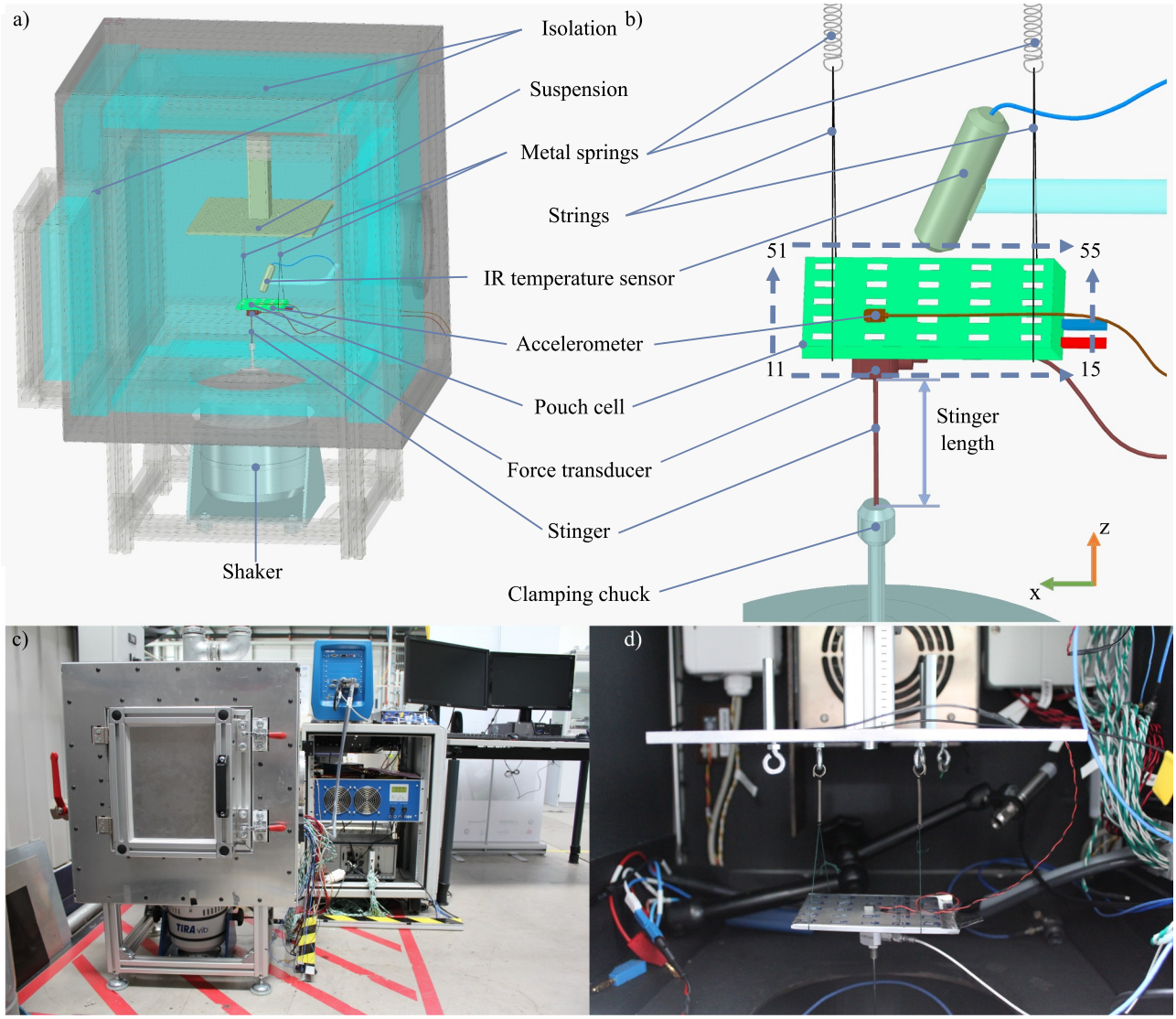

Fig. 1. Schematic and depictions of the test bench and setup: a) temperature-controlled safety chamber with shaker and measurement setup, b) zoom on measurement setup with the cell as SUT and DOF location matrix, c) complete test bench setup photography, d) photography of the cell under test inside the safety chamber.

cathode and graphite anode are selected as SUT. The cut-off voltage is 4.2 V for charge and 3 V for discharge. The dimensions of the cells are 64 mm × 95 mm in width and length and 3.5 mm in thickness.

The aged cells have been cycled with a C-rate of 0.9 C in another study, published by Ebert et al. [38]. The cells have been aged under various pressure with flexible or solid bracing and three different pressure levels of 0.05, 0.25 and 0.45 MPa for both types of bracing (0.05 MPa cell with rigid bracing not included in this work). Capacities of the cells are determined by a constant current (CC) discharge with $I_{discharge}$ = 0.9 C according to the test regime in [38]. Measured capacities of the five aged cells are in the range of 2.018–2.056 Ah with a mean capacity of 2.038 Ah showing little variation although being cycled under different pressure levels. The five new cells have actual capacities from 2.181–2.194 Ah with a mean capacity of 2.187 Ah.

A dummy cell made of aluminum EN AW 5083 (density ρ = 2660 kg/m^3, Young's modulus E = 70 GPa and Poisson's ratio ϑ = 0.33) with the same dimensions than the pouch cell and a resulting weight of 56.6 g is used to validate the test bench in advance to ensure high measurement quality without systematic errors.

2.4. SOC adjustment

SOC adjustment in the experiments is required to evaluate the influence of the SOC on the structural dynamics. Before these tests, one of the five new cells is charged to 100% SOC with CC–CV (constant current–constant voltage) profile with a C-rate of $C/2$ until a voltage of 4.2 V and a C-rate of $C/50$ is reached. From this fully charged state, the cell is discharged with $C/5$ to vary the SOC for the EMA. Ampere-hour counting is used to drain 20% of C_{nom} in five steps. In the end, the cell is discharged with CC–CV with constant current of $C/5$ and termination criterion of 3 V and $C/200$ for CV, draining the remaining 6.5% of capacity beyond the nominal capacity from the cell. After each SOC adjustment, the cell is allowed to relax for at least 30 min and until the voltage relaxation is less than 0.2 mV/min. The SOC levels given for analysis in this work are calculated with respect to the available capacity.

3. Test bench validation

As the EMA is a linear method [84], special care shall be taken to ensure linear measurement. In addition, several other factors can

influence the quality of the measurement. These have to be considered and are addressed below.

3.1. Potential error sources

Potential sources for errors or low-quality measurements may result from [85]:

- Mechanical setup
  - shaker-stinger-structure interaction
  - bad attachment or support, e.g. support too stiff
  - mass loading effects due to the roving accelerometer
  - insufficient force transducer joint or accelerator attachment
  - limited reproducibility for above reasons and operator errors
- Measurement and signal processing
  - excitation of nonlinear response
  - measurement noise
  - leakage effect
  - aliasing

Furthermore, sufficient and suitable locations for excitation and measurement must be chosen to avoid nodal points [85]. The following section refers to each potential error source category named above and describes the chosen countermeasures and the resulting setup. In the end, the test bench and the setup is validated with the aluminum dummy.

3.2. Countermeasures and chosen setup

3.2.1. Mechanical setup

The stinger shall be designed to be stiff in the axial direction to transfer the force to the SUT and to avoid bending and to be as flexible as possible in all other DOF to allow the SUT to move freely [77]. If the stinger is to stiff, the rigid body modes, which describe the three translational and three rotational movements of a structure, will increase in frequency and will, therefore, influence the flexible modes. If the stinger is too flexible insufficient force is transmitted to the structure in direction of the DOF (z in this work) and the flexible modes are insufficiently excited [77]. Upfront an ideal choice for the stinger length cannot be given [77,85] and has to be identified in an iterative procedure. Several stinger lengths have been tested and the length of 50 mm has emerged as a valid choice for both pouch cell and aluminum dummy.

To achieve reproducible and linear results, metallic springs of well-defined stiffness are chosen as described in the experimental section. Previous experiments with elastic rubber bands introduced errors due to the nonlinear characteristic of the rubber. The metallic springs are chosen so that in both tension and compression only the linear range of the spring is in use. The validity of both support and stinger is shown with the aluminum dummy.

The presented approach with flexible support and stinger is different from the approach by Popp et al. [69,71], who used a miniature shaker with an impedance head. The shaker and impedance head were put upside down on the cell and therefore the weight of the shaker lasted on the cell. This can be a valid method to detect changes as it is the purpose in [69,71] as a prerequisite for e.g. mechanical SOH determination. At the same time this method has limitations in characterization of a cell without any shaker-structure interactions in free-free conditions since even much lower sensor masses influence the FRF [77,85].

The influence of the accelerometer and its cable due to its mass loading effect on the measurement results is minimized by minimizing the size and weight of the accelerometer in this work. The remaining influence is determined by piling up two identical accelerometers, thus doubling the weight as proposed in [85]. No difference can be observed, so mass loading effects or cable rattle effects can be neglected.

Sufficient attachment between transducer or accelerometer and SUT is achieved by a very thin layer of petro wax, which gives the best results for both force transducer and accelerometer. After three or four shifts of the accelerometer, the petro wax layer has to be renewed to avoid increased noise in the measurement.

Shaker testing is usually favored to impact testing with regard to reproducible measurements and minimized operator errors. However, reproducibility might be an issue if the SUT must be removed from the test setup as must be done especially for SOC variation to charge or discharge the cell, but also in case of the SOH investigation where different cells are compared. Therefore, if re-assembly is required in between the tests, three repetitions with full dis- and reassembling for each measurement are performed. If reproducibility measurements are performed, it is mentioned at the respective place in this work.

3.2.2. Measurement and signal processing

Different excitations have been tested prior to this work. As lithium-ion cells are expected to show strong nonlinear behavior, a random excitation shall be preferred. Random signals can average out nonlinearities and can give a linear approximation [84]. In contrast, a fast sine sweep, called sine chirp (used in [71]) or impact hammer measurements (used in [70]), tend to excite the nonlinear characteristics of the structure under test [84]. Especially impact excitation can overdrive the SUT due to its high crest factor (ratio of peak to root mean square (RMS) value). As the signal is of deterministic nature and therefore, the coherence cannot indicate signal distortion due to the leakage effect or nonlinear behavior [84].

In this work, burst random is chosen over random testing to avoid the leakage effect [77]. A burst rate of 90% allows the signal 10% of the excitation duration to return to zero. This is sufficient as pouch cells exhibit strong damping and the oscillation therefore quickly levels off. The force level or excitation amplitude can be chosen in steps of 0.01 in the Analyzer software as a dimensionless non-physical quantity. The force level is therefore calculated in terms of RMS values afterwards if required.

In the case of random testing, several measurements need to be averaged to achieve a sufficient signal-to-noise ratio (SNR). 50 averages have shown to be a good choice for the investigated pouch cells. To average the complex FRF, an estimator has to be used. Estimators use cross- and auto-spectra to average multiple measurements of the complex FRF. Different estimators can be used depending on whether noise is dominant at the input or the output [77]. The H1 estimator is chosen in this study. Comparison of H1 and H2 estimators prior to this work did not reveal significant differences.

Signal acquisition parameters as frequency range, block size or sample rate were varied without any significant effect. The frequency range is therefore chosen from 20 to 6500 Hz with a block size of 32 768 samples, a sample rate of 16 384 Hz and a frequency spacing of Δf_{line} of 0.5 Hz.

3.3. Validation with an aluminum dummy and parameter optimization

To ensure valid measurement results, a validation test with an aluminum cell dummy is established. The expected structural response of the aluminum dummy can be easily and reliably calculated in the FEM software ANSYS 18.2. The material parameters from Section 2.3 are used as initial values. The modal analysis function of ANSYS Mechanical is used with the free-free condition and suppressed damping to obtain the natural frequencies.

For measurement, the two DOF $p22(z)$ and $p33(z)$, similar to Fig. 1b) for the pouch cell, are used for both excitation and response to obtain the respective DPM.

The aluminum dummy is measured three times for each DOF with complete reassembly of the test setup in between to prove reproducibility. One exemplary measured and fitted FRF, as well as the simulated natural frequencies, are depicted in Fig. 2a) for $p22(z)$ and Fig. 2b) for

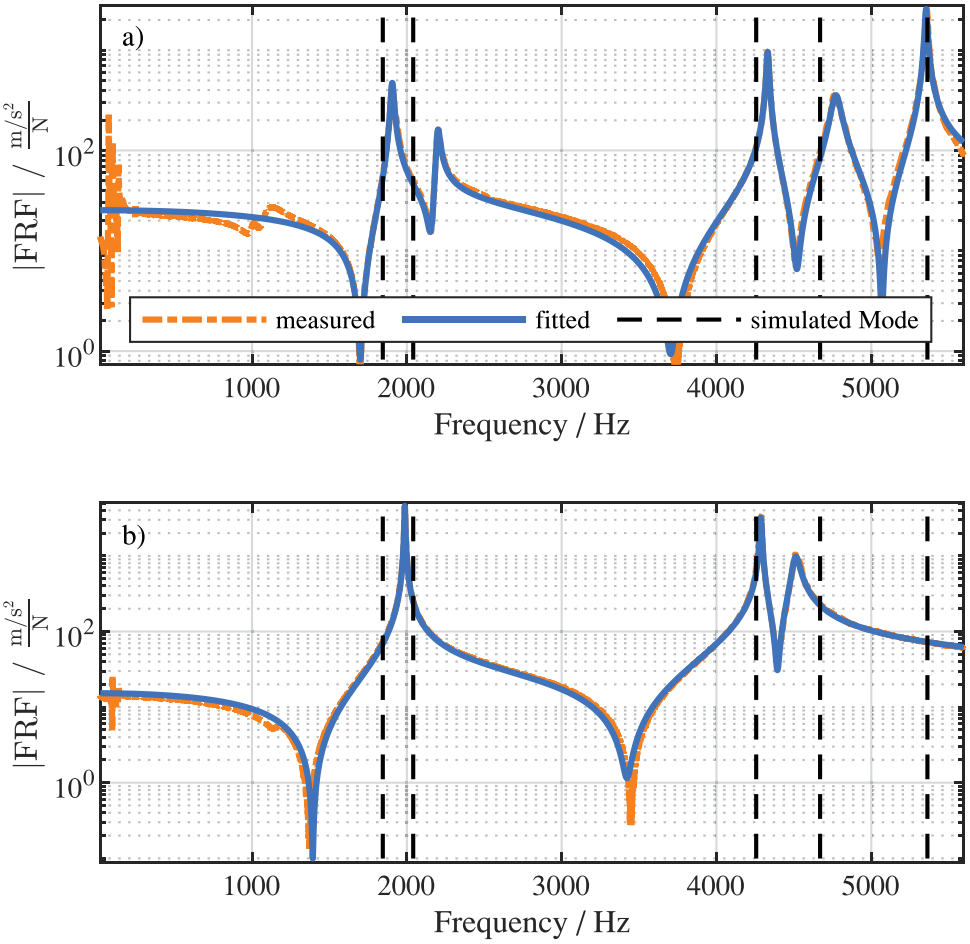

Fig. 2. FRF of measurement and MDOF fit and natural frequencies $f_{nat,ANSYS,n}$ from ANSYS calculation depicted as vertical scattered lines for a) excitation at *p22(z)* and b) excitation at *p33(z)*.

p33(*z*). Peaks in the magnitude of the FRF mark a resonance. The alternating order of resonances (maximum peaks) and anti-resonances (minimum peaks) indicates successful DPM [77].

Fig. 2 shows that MDOF fit and measurement are in good accordance for both DOF (least square error (LSE) in the range of 1.1–3.4% for all six measurements and respective MDOF fits). Rigid body modes can interfere with the elastic modes if the support is too rigid [77,78]. In this validation, they are well separated and can be seen as peaks in the measurement in the low frequency range less than 200 Hz. Small deviations at approx. 1000 Hz are due to the asymmetric setup in case of DOF *p22*(*z*), especially significant for very small structures. The deviations for *p33*(*z*) are smaller due to symmetry, but while *p33*(*z*) is easier to measure not every resonance mode can be detected due to nodal areas in the middle of the cell for several mode shapes. Due to nodal areas, modes 1 and 5 are not visible in Fig. 2b), while mode 2 can be determined more precisely from Fig. 2b) and excitation at *p33*(*z*), because *p22*(*z*) is not exactly, but already very close, to a nodal area for mode 2. In other words if all resonances shall be detected with one single measurement, *p22*(*z*) would be preferable, but measurements at several positions can enhance the accuracy and reduces the risk of missing one resonance.

The peaks in both measured and fitted (MDOF fit) FRF are in good accordance with the frequencies of the simulation (dashed vertical lines in Fig. 2). In addition, measurement of the FRF at all 25 DOF is done to assure that measured and simulated mode shapes match.

The relative deviation $\varepsilon_{f,n}$ for each mode n is calculated for each measurement repetition according to Eq. (3) with the natural frequencies from MDOF fit $f_{nat,MDOF,n}$ and from the FEM simulation $f_{nat,ANSYS,n}$.

$$\varepsilon_{f,n} = \frac{f_{nat,MDOF,n} - f_{nat,ANSYS,n}}{f_{nat,ANSYS,n}} \tag{3}$$

If modes 1, 4 and 5 are determined from Fig. 2a) and modes 2 and 3 from Fig. 2b), the maximum deviation $\varepsilon_{f,n}$ is 3.3% or less, as listed in Table 1.

Mean values are calculated according to Eq. (4) for each mode n and given in Table 1.

$$f_{nat,mean,n} = \frac{1}{k}\sum_{1}^{k}\left(f_{nat,MDOF,n}(k)\right) \tag{4}$$

The value k represents the number of repetitions. A similar calculation is done for damping ratios $\zeta_{mean,n}$ and the results are also shown in Table 1.

Table 1
Data from the validation test with an aluminum dummy for comparison of fitted measurement and simulation results for each mode n with the respective DOF for DPM.

Mode n	MDOF fit $f_{nat,mean,n}$/Hz	MDOF fit Damp. $\zeta_{mean,n}$	ANSYS $f_{nat,ANSYS,n}$/Hz	Max. dev. $\varepsilon_{f,n}$	Exc. DOF
1	1898	0.47%	1845	3.3%	*p22(z)*
2	1987	0.15%	2041	2.7%	*p33(z)*
3	4284	0.53%	4257	0.7%	*P33(z)*
4	4785	0.64%	4669	2.2%	*p22(z)*
5	5351	0.19%	5363	0.3%	*p22(z)*

The damping ratio ζ_n cannot be calculated for several reasons, e.g. insufficient knowledge of the mode, the effective mass, the stiffness friction at the connections and more [79]. Instead, it has to be measured and compared with results from other investigations. The experimentally determined average damping ratio $\zeta_{mean,n}$ in this work is in the range of 0.15–0.64% for all five modes and therefore in very good correlation with other investigations of aluminum bodies [86,87].

The variation in between the three measurements for each DOF is also low for both natural frequencies and damping ratios, indicating high reproducibility. Spreads for each mode n are defined according to Eqs. (5) and (6).

$$\Delta f_n = \max(f_{nat,n,1}, f_{nat,n,2}, f_{nat,n,3}) - \min(f_{nat,n,1}, f_{nat,n,2}, f_{nat,n,3}) \quad (5)$$

$$\Delta \zeta_n = \max(\zeta_{n,1}, \zeta_{n,2}, \zeta_{n,3}) - \min(\zeta_{n,1}, \zeta_{n,2}, \zeta_{n,3}) \quad (6)$$

The highest absolute spread for natural frequencies occurred for mode 4, with $\Delta f_4 = 27$ Hz (0.6% of $f_{nat,mean,4}$) and the highest relative spread for mode 1 0.7% $f_{nat,mean,1}$ ($\Delta f_1 = 14$ Hz). In case of damping ratio ζ_n for example for mode 1, a small variation in the range of 0.42–0.51% ($\Delta\zeta_1 = 0.09\%$) could be ensured.

In summary, both natural frequencies and damping ratios can be reliably determined with the presented test bench setup even for small and lightweight structures. The free-free condition is proven because the simulation has been performed without any constraints and the conformity with the measurement results can be seen. Additionally, little variation in between the measurement repetitions proves high reproducibility.

4. Results & discussion of pouch cell characterization

In this section, measurement results on the pouch cells are presented and discussed. Table 2 gives an overview of all of the following investigations and the chosen parameters.

For the investigation of the SOC and SOH sensitivity, three measurements are performed and averaged to ensure the high accuracy of the results. While reproducibility is proven for the test bench in Section 3.3, this is done to ensure accurate results also in case of the more complex structure of the pouch cell with e.g. imperfect surface. In case of temperature and nonlinearity investigation, only one measurement and MDOF fit are performed because no reassembly is required to change the temperature or the excitation amplitude. In general, this work concentrates on the method and the observable sensitivities while absolute values depend on the specific cell under investigation and are therefore less important.

4.1. Natural frequencies and mode shapes

To identify resonances, nodal points have to be avoided. For the pouch cell, two excitation positions are required. The same positions as in Section 3.3, in the middle of the cell *p33*(z) and closer to one of the corners *p22*(z) are chosen. As at least coarse symmetry can be assumed and measurement closer to the edge (*p1x, p5x, px1, px5*) would be difficult to measure reliably due to asymmetry as discussed in Section 3.3, the two proposed DOFs *p22*(z) and *p33*(z) are the best choice. All expected mode shapes can be revealed. The pouch cell is excited by force at the two DOF *p22*(z) and *p33*(z) and all 25 chosen response DOFs are measured by roving the accelerometer. In this manner, the mode shapes of the pouch cells can be captured. The mode shape analysis is done for both a new and an aged cell to ensure that if new and aged cells are compared, the respective modes coincide.

Table 2
Overview of the investigations done in this work and the respective chosen parameter settings.

Purpose	Excitation	SOC/%	Temp./°C	SOH	Chapter
Mode shapes	0.01	0	25	1 New/1 Aged	4.1
Nonlinearities	0.01-0.07	0	25	1 New	4.2
SOC	0.01	0-100	25	1 New	4.3
Temperature	0.01	0	17-34	1 New	4.4
SOH	0.01	0	25	4 New/5 Aged	4.5

Exemplary FRF for one new cell and two DOFs are shown in Fig. 3a. Five modes can be identified. Higher order modes cannot be reliably detected, as they become too complex to be described with only 25 DOFs. In addition, high modal density and high damping in the high-frequency range further complicate mode identification. The incorporation of residual terms into the MDOF fit accounts for the higher order modes.

In Fig. 3a, the markers are located at the estimated natural frequencies from the MDOF fit. The modes 1 and 2 as well as the modes 3 and 4 are very close to each other and can only be clearly distinguished because each excitation DOF mostly drives only one mode at the time. The principle of nodal lines can be thus useful to eliminate modes to get a clearer look at another mode of interest.

Fig. 3b shows the detected mode shapes for each natural frequency, e.g. mode 1 is the first bending mode along the longer side of the pouch cell, and mode 2 is the first torsional mode. Mode 4 is the second bending mode along the longer side with a little asymmetry. Mode 3 and mode 5 show the characteristic mode shapes according to Fig. 3b. Animated videos of the mode shapes are provided as supplementary material.

The mode shapes are essential to understand which movements happen during vibration excitation and to understand and identify locations with severe stress. This knowledge, can help in the design of battery systems. Additionally, they are required to reliably distinguish the different modes.

The established order of the modes 1–5 remains through the paper, so that e.g. mode 2 always refers to the first torsion, even when the modes change their order as happens for example in the case of cyclic aging.

4.2. Origin and influence of nonlinearities

The EMA is a linear method as it is based on the principle of mode superposition. Hence, a check of the linearity is a very important factor in structural analysis. Also, it can have a very strong impact on response and fatigue in later application [84].

For this investigation, the excitation force is increased from the lowest level that can be chosen in the Analyzer software (level 0.01) by the smallest possible step size (0.01). The FRF is tested for homogeneity to check for nonlinearity [84].

The results of the measurement are depicted in Fig. 4. Each row of subplots represents one of the modes (1–5) and the respective extract from the complete FRF. The dots represent the values from the measurement, while the solid lines represent the corresponding MDOF fit. The FRF is shown both in a magnitude plot (column a) and a Nyquist representation (column c) as each representation has its own advantages to see different effects. Additionally, the coherence is shown (column b) to evaluate the linearity [84].

To survey each mode separately, an extract is shown for each mode. The frequency range for each extract is chosen as follows. For an SDOF system, the half-power bandwidth method is common to calculate the damping ratio ζ or the quality factor Q according to Eq. (7) with the natural frequency f_{nat} and the half power bandwidth Δf_{-3dB}. Equations are adopted from [67].

$$Q = \frac{1}{2\zeta} = \frac{f_{nat}}{\Delta f_{-3dB}} \quad (7)$$

Δf_{-3dB} is defined as the half-power bandwidth, the frequency interval from f_a to f_b. The frequencies f_a and f_b are the frequencies on both sides of the resonance peak where the signal magnitude has dropped by half

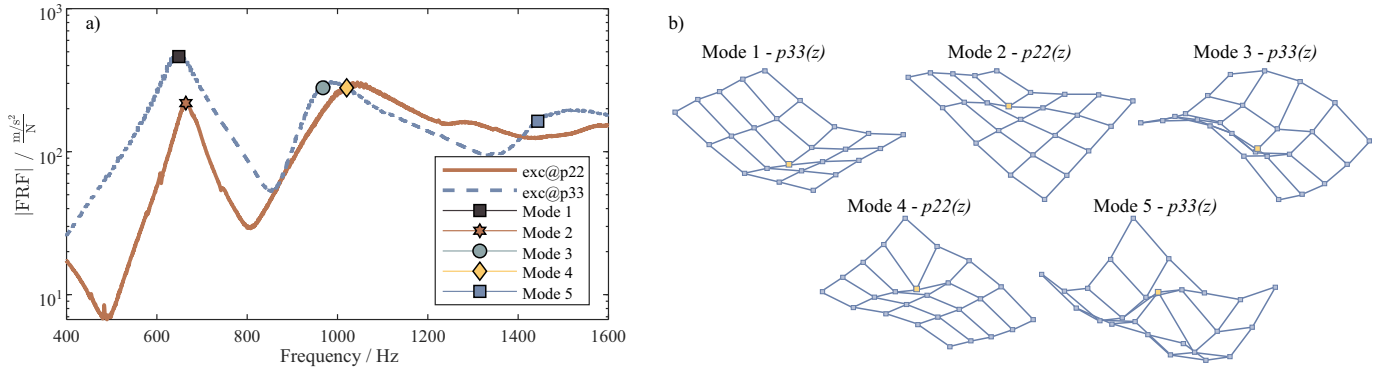

Fig. 3. (a) FRF for both excitation positions with natural frequencies (depicted as square markers); b) Mode shapes of the pouch cell, respective DOF for excitation and response in DPM are marked with yellow squares.

or −3dB. The half-power frequency bandwidth $\Delta f_{-3\mathrm{dB}}$ of an SDOF system is therefore defined according to Eq. (8).

$$\Delta f_{-3dB} = f_b - f_a \tag{8}$$

As f_a and f_b cannot always be directly determined in an MDOF system due to mode overlap, $\Delta f_{-3\ \mathrm{dB}}$ must be approximated differently. Eq. (7) can be converted to Eq. (9) with indexes n to account for the different modes in an MDOF system.

$$\widetilde{\Delta f}_{-3dB,n} = 2\zeta_n f_{nat,n} \tag{9}$$

Solving Eq. (9) with the values, for damping ratio ζ_n and natural frequency $f_{\mathrm{nat},n}$ obtained from the MDOF fit gives a bandwidth approximation $\widetilde{\Delta f}_{-3\ dB,n}$, which can be used to obtain a representative extract from each measurement for each mode n.

Each measurement extract of every mode n is depicted in Fig. 4 in the respective interval according to Eq. (10).

$$\left[f_{nat,n} - 1.75\frac{\widetilde{\Delta f}_{-3dB,n}}{2},\ f_{nat,n} + 1.75\frac{\widetilde{\Delta f}_{-3dB,n}}{2} \right] \tag{10}$$

Several observations can be made from Fig. 4. For every mode, an increased excitation causes a decreased peak in the magnitude representation (column a) and a reduced circle diameter in the Nyquist representation (column c). For the highest tested excitation, the magnitude of the FRF is flattened, especially for modes 1, 3 and 5. The deviations from the MDOF fit to the measurement increase with increased excitation, again mostly for modes 1, 3 and 5. As the MDOF fit is valid for linear systems, this is an expectable observation.

In the Nyquist plot for mode 1, a flattening of the measured FRF circle in comparison to the best fit is visible. This behavior can be described as nonlinear quadratic damping according to [84]. The decrease of the natural frequencies (marked as squares) and the flattening of the FRF is known as softening cubic stiffness [84].

Looking on the coherence plots (column b), it is visible that the coherence is a useful, but not a sufficient tool to indicate or investigate the nonlinear structural response of lithium-ion pouch cells. While all modes or resonances show strong nonlinearity the coherence only gives a strong indication for mode 1 with a sharp drop of the coherence, while there is nearly no indication example in case of mode 5. Therefore, the definition of a fixed coherence limit to check for valid data is impossible in case of lithium-ion pouch cells and burst random excitation. In the case of other excitation signals, the usage of coherence limits has to be carefully investigated.

An identical investigation is also made for the aluminum dummy to exclude the possibility that the observed nonlinearities have the origin in the measurement chain. As the homogeneity of the FRF has been nearly uninfluenced (except a slight increase in damping for mode 1) by the same increase of excitation, the nonlinear effects only occur due to the lithium-ion pouch cell itself.

In addition to the evaluation of the FRF and coherence, the results of the MDOF fit are evaluated in Fig. 5 to take a closer look at the natural frequencies and damping ratios with regard to excitation force. As the proportion of the excitation force in the frequency range of each resonance or mode is primarily relevant for the respective resonance [79], the RMS value of the excitation of each mode n is calculated by the root sum square of all the spectral lines by Eq. (12) after transformation from peak to RMS values by Eq. (11).

$$F_{RMS}(\omega) = \frac{1}{\sqrt{2}} F(\omega) \tag{11}$$

$$F_{RMS,n} = \sqrt{\frac{1}{2}F_{RMS}(\omega_{1,n})^2 + \sum_i F_{RMS}(\omega_{i,n})^2 + \frac{1}{2}F_{RMS}(\omega_{end,n})^2} \tag{12}$$

The respective frequency range is defined according to Eqs. (13) − (17) with the width of the spectral lines Δf_{line}. The width of the spectral lines Δf_{line} shall not be confused with the half-power frequency bandwidth $\Delta f_{\text{-}3dB,n}$ for each mode n. the counter variable i is increased with a step size of 1 till $f_{i,n} = f_{end,n} - \Delta f_{line}$.

$$[f_{1,n},\ f_{end,n}] = \left[f_{nat,n} - \frac{\widetilde{\Delta f}_{-3dB,n}}{2},\ f_{nat,n} + \frac{\widetilde{\Delta f}_{-3dB,n}}{2} \right] \tag{13}$$

$$\omega_{1,n} = 2\Pi f_{1,n} \tag{14}$$

$$\omega_{end,n} = 2\Pi f_{end,n} \tag{15}$$

$$\omega_{i,n} = 2\Pi f_{i,n} \tag{16}$$

$$f_{i,n} = f_{1,n} + (i-1)\Delta f_{line} \tag{17}$$

By this procedure, potential problems due to force drop-out [84] can be neglected and each resonance is assigned to a reproducible measure of excitation. The results of the MDOF fit are plotted in Fig. 5 with respect to the calculated excitation. The natural frequencies and damping values are obtained by the MDOF fit with a max. LSE of 2.40% for excitation at $p33(z)$ (modes 1, 3 and 5) and a max. LSE of 0.29% for $p22(z)$ (mode 2 and mode 4). It can be seen that for values in the range of 5 mN or lower, natural frequencies and damping ratios already change and therefore the FRF is slightly inhomogeneous. With respect to linearity, an even lower excitation force would be beneficial, but this would cause an unacceptable SNR at the same time. The lowest excitation force in this work has the lowest LSE of 0.70% and 0.13% and the highest coherence for both excitation positions and is chosen for all further investigations.

Not for every mode, the same number of values is plotted. All fitted values with a respective LSE > 3% of the MDOF fit in the range according to Eq. (13) for each respective resonance have been excluded from this investigation as no sufficient linearity can be guaranteed.

The natural frequencies are decreasing for four of five modes in

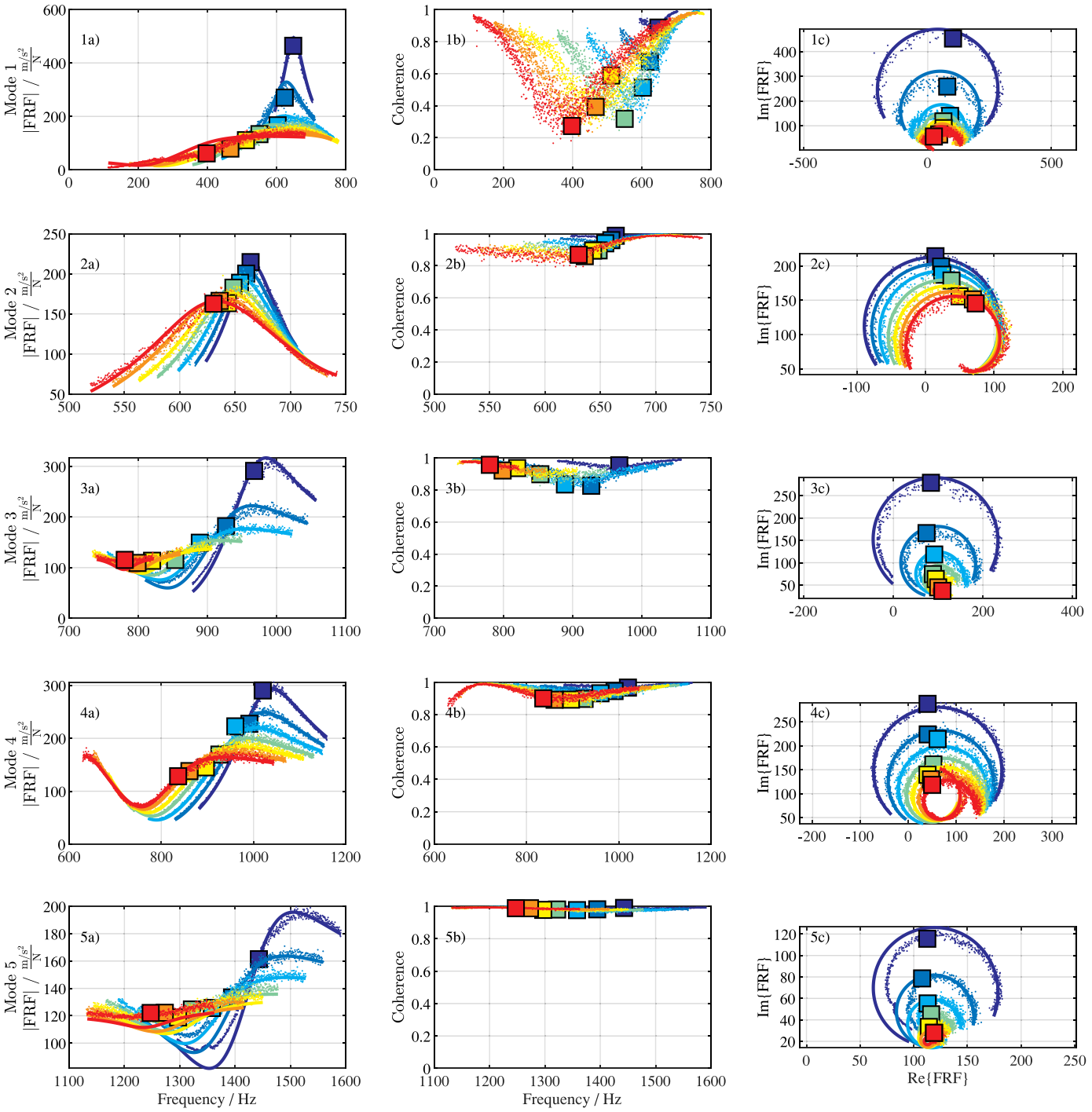

Fig. 4. Measured FRF with respective MDOF fits, shown in both magnitude (column a) and Nyquist representation (column c) and coherence (column b) for each mode and the respective frequency range with varied excitation level (blue – low, red – high), squares indicate the estimated natural frequencies $f_{nat,n}$ from the MDOF fit. (For interpretation of the references to color in this figure legend, the reader is referred to the web version of this article.)

Fig. 5a. Mode 2, first torsion, is only little affected by the increased excitation level. Mode 3 shows some uncertain behavior for the three highest excitation levels for an unclear reason, which would need further investigation if needed to be clarified.

The damping increases steepest for mode 1 in Fig. 5b. Mode 2, mode 3 for the lower excitation levels and mode 4 also increase significantly. Mode 5 remains comparably stable, mode 3 shows uncertain damping ratio values in case of higher excitation level, too.

With the results shown here, it is possible that sine sweep, sine chirp or impact testing [68–71] can easily drive the lithium-ion pouch cells into nonlinear regimes and therefore sufficient linear behavior should be carefully controlled.

If the damping values in this work are compared with other publications, strong differences can be found. While the values obtained by impact testing in [70] are lower than the values in this work (mostly below 2%), the values obtained by sine chirp testing in [71] are much higher (up to 20% for a new cell). As three different setups, three different cells and three different excitation signals have been used in the different publications; a conclusion about the origin is difficult. In addition, this work is the first one using an MDOF fit instead of an SDOF fit [70,71]. An SDOF fit caused errors in our study and was not able to capture the FRF due to the high modal density. The high damping ratios

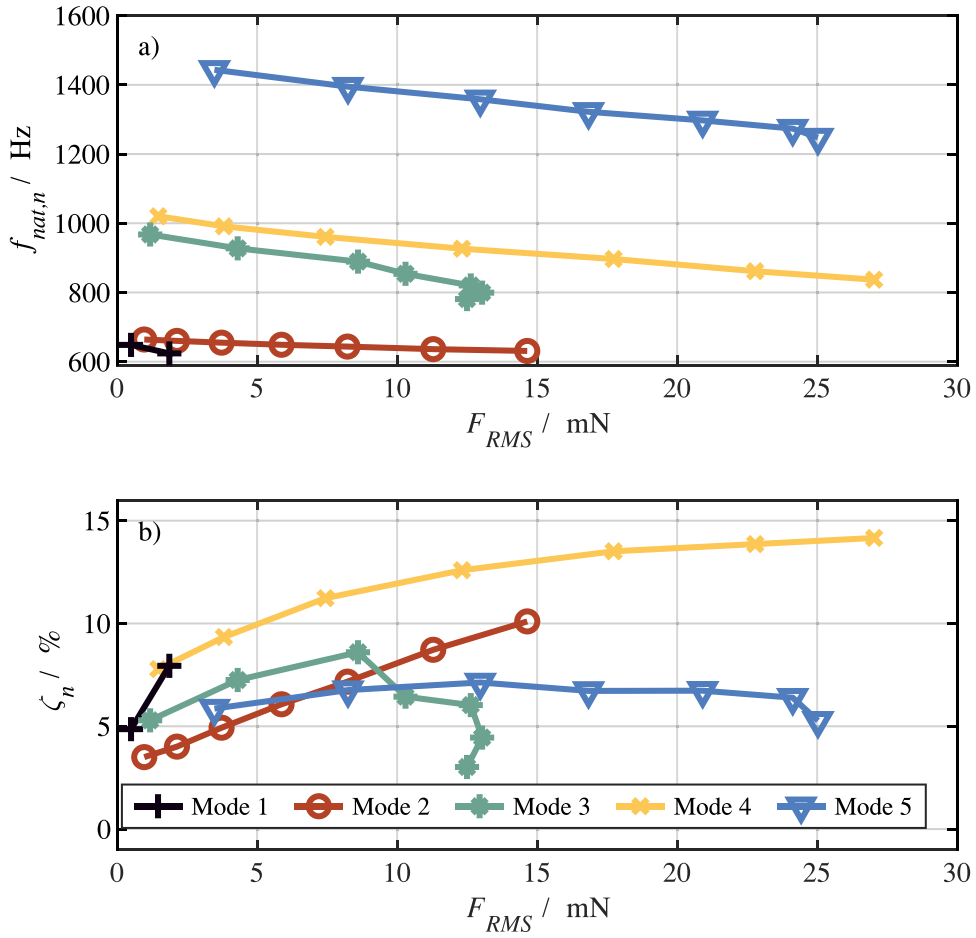

Fig. 5. Variation of excitation force showing nonlinear structural dynamics of the investigated lithium-ion pouch cells for a) natural frequencies $f_{nat,n}$ and b) damping ratios ζ_n.

in [71] might have the origin in the nonlinear behavior with increased nonlinear damping excited by sine chirp excitation or in the different cell design.

According to the literature, excitation by a signal of random nature is the best way to get a linear approximation of a nonlinear system [84]. The results in this work are an indication for very strong nonlinearity as even with the burst random excitation in this work linear behavior and the respective homogeneity of the FRF is already difficult to achieve. Any impact or sine-based technique might show increased nonlinearity [84] and the results have to be always carefully checked. At the same time, a well-defined experiment with sine sweep excitation can give a more precise picture of the nonlinear effects. The authors think that a detailed understanding of the softening and damping inside a lithium-ion pouch cell and its effect on fatigue is a very interesting topic for follow up studies.

Vibration or shock testing of lithium-ion pouch cells should be carefully adapted to the experienced load levels in the respective application later to achieve reliable results as fatigue and damage depend on natural frequencies and damping values [65,66].

4.3. Influence of SOC

As the cell has to be remounted after each SOC adjustment, for each SOC value three measurements are performed with a complete remounting in between the modal analyses. The mean value of each measurement triplet is depicted in Fig. 6 with error bars showing the maximum spread from minimum to maximum value of the three measurements for both natural frequencies and damping values of each mode n.

The obtained spreads Δf_n and $\Delta\zeta_n$ are additionally listed in Table 3 for each mode n. The spreads for natural frequencies are low especially for modes 1, 2 and 4 with $\max(\Delta f_2) < \max(\Delta f_1) < \max(\Delta f_4) < 30$ Hz. For modes 3 and 5 in the case of some specific SOC, the spread is larger up to 93 Hz for Δf_3 and up to 64 Hz for Δf_5, indicating a weaker, but still sufficient reproducibility in the respective condition. For damping ratios it is $\Delta\zeta_n < 0.7\%$.

Both natural frequencies $f_{nat,n}$ (Fig. 6a) and damping values ζ_n (Fig. 6b) are not significantly influenced by changes in SOC. This is in good correlation with the results by Hooper et al. with impact testing [70] and in contrast to the results by Popp et al. [71], who found increasing stiffness with increasing SOC till approx. 75% SOC. This difference might originate from the different measurement setups. In the free-free condition in this work, the cells freely swell or shrink. Volume change probably mostly causes a change in the density; however, the natural frequency of a structure is less sensitive to the density than to the elastic modulus. The measurement setup by Popp et al. [71] includes a miniature shaker pressing with its own weight on top of the pouch cell. Therefore, an additional mass is added to the whole setup. The cell is under compression of approx. 0.02 MPa (calculated with the weight of the combination of the used shaker and impedance head of approx. 274 g and a circular contact surface with a diameter of 13.5 mm) at this position with an increased stress level when the cell swells. This might cause increased stiffness with increasing natural frequencies. The measurements in this work show that a measurement of the elastic modulus of a graphite anode, for example, has to be always considered with regard to the surrounding environment. While in other studies a threefold increase in Young's Modulus of graphite electrodes during lithium intercalation was reported [88], it can be seen

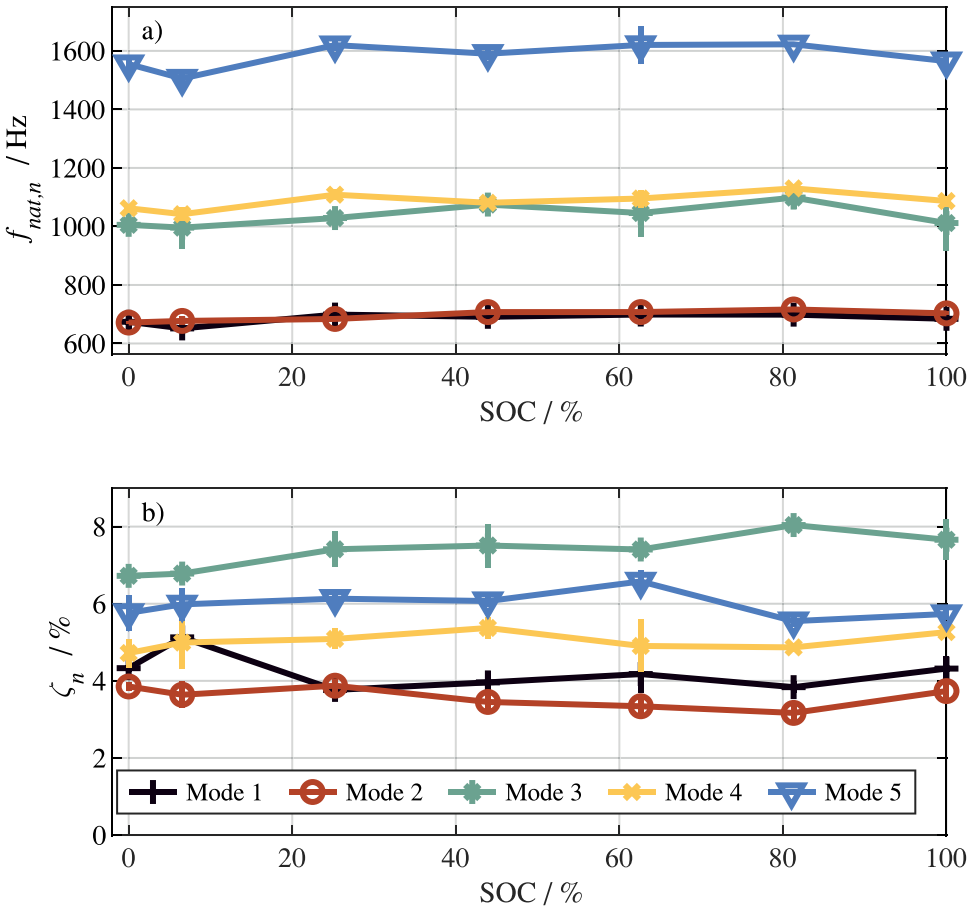

Fig. 6. Variation of SOC showing little sensitivity of both a) natural frequencies $f_{nat,n}$ and b) damping ratios ζ_n with error bars indicating the maximum spread of the measurements.

Table 3
Maximum absolute spread for each measurement triplet at each SOC.

SOC /%	Mode 1		Mode 2		Mode 3		Mode 4		Mode 5	
	Δf_1/Hz	$\Delta\zeta_1$	Δf_2/Hz	$\Delta\zeta_2$	Δf_3/Hz	$\Delta\zeta_3$	Δf_4/Hz	$\Delta\zeta_4$	Δf_5/Hz	$\Delta\zeta_5$
100	9.7	0.32%	6.4	0.18%	92.6	0.53%	17.4	0.05%	23.3	0.15%
81	0.4	0.15%	6.1	0.24%	37.6	0.17%	6.6	0.10%	7.5	0.13%
63	14.9	0.47%	3.6	0.21%	79.7	0.22%	29.4	0.69%	63.8	0.28%
44	15.2	0.28%	1.6	0.20%	23.0	0.56%	10.9	0.28%	21.1	0.14%
25	5.1	0.20%	4.2	0.17%	3.2	0.46%	18.3	0.26%	18.9	0.23%
6,5	15.0	0.57%	13.8	0.34%	70.9	0.23%	22.3	0.68%	33.0	0.42%
0	22.8	0.09%	4.5	0.11%	21.8	0.04%	8.6	0.37%	23.2	0.45%

with the measurement of full cells, that this does not have to transfer to the overall structural dynamics of the pouch cell. This effect has to be considered if e.g. models for simulation are parameterized based on single component measurement as for example available for electrodes [88,89]. If structural dynamics shall be captured it is very important to adopt the measurement setup to the desired output, e.g. if the cell shall be characterized as in this work or if structural health monitoring is the goal [71].

As the SOC has comparably little influence in our setup, it was decided not to consider possible hysteresis effects for lithium-ion pouch cells as has been investigated before [71].

In the case of vibration durability testing of single lithium-ion pouch cells in free-free condition, SOC is not the most important parameter to consider and cells can be tested at low SOC with a reduced risk in case of short circuit failure. In the case of testing with a somewhat constrained cell, the situation might be different due to the constraints and the different stress levels.

4.4. Influence of temperature

The investigations for temperature variation in this work reveal high sensitivity of the structural dynamics from temperature. The temperature has been varied in the range of 17–34 °C. When the climate chamber reached its target temperature, an equalization time of at least 30 min was given to allow the cell to reach thermal equilibrium. The surface temperature of the cell is measured with the IR sensor and is depicted on the horizontal axes in Fig. 7, showing the values of the MDOF fit for natural frequencies $f_{nat,n}$ (Fig. 7a) and damping ζ_n (Fig. 7b).

All natural frequencies in Fig. 7a show a linear decrease with rates of −11.9 Hz/K for mode 1, −7.4 Hz/K for mode 2, −20.6 Hz/K for mode 3, −26.2 Hz/K for mode 4 and −32.9 Hz/K for mode 5 with a

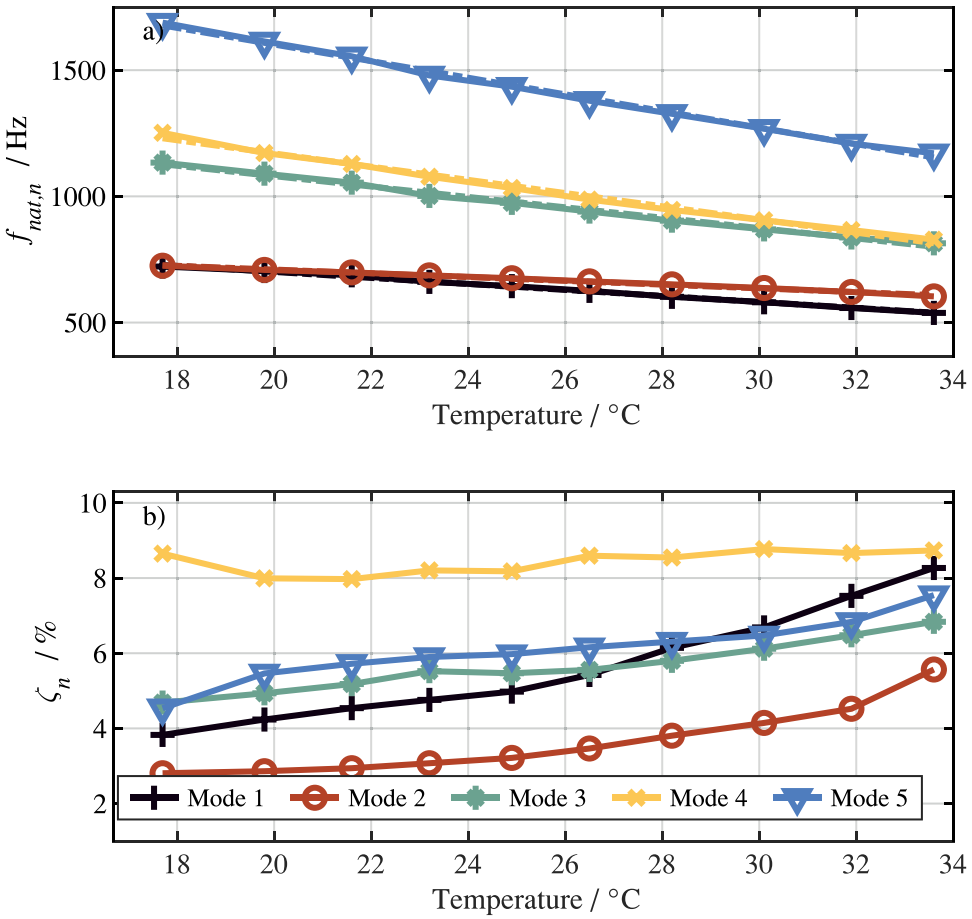

Fig. 7. Variation of temperature showing a high sensitivity of both a) natural frequencies $f_{nat,n}$ with linear fits (dashed line) and b) damping ratios ζ_n.

linear correlation coefficient ρ of −0.99 for each mode. Due to the different slopes of the natural frequencies, mode separation and the order of the modes can change. Therefore, temperature control can be used for better separation of single modes e.g. for better mode shape analysis.

The damping in Fig. 7b increases with increasing temperature in a nonlinear regime for all the modes, except mode 4, which remains nearly constant. The other modes show an increase of the damping ratio of 116% for mode 1, 98% for mode 2, 46% for mode 3 and 66% for mode 5, referred to the results at the minimum temperature.

If temperature is varied in an experiment, not only the effect on the SUT, but also on the measurement setup must be considered. The steel springs have sufficient reserve for both compression and tension to stay linear and can be used up to 40 °C according to manufacturer information without changing their specifications. The temperature sensitivity of the force transducer and the accelerometer according to chapter 2.2 are −0.009%/K and −0.1125%/K respectively. As acceleration is numerator and force is denominator and both sensitivities are negative, the sensitivity of the force transducer partly compensates the deviation of the accelerometer. The nominal sensitivity from calibration applies for room temperature, which is defined as 25 °C in this work. Therefore, the maximum deviation of the FRF for the maximum temperature of 34°C is 1% and 0.9% for the minimum temperature of 17 °C. The maximum possible deviation due to the measurement setup is therefore much smaller than the observed change for both natural frequencies and damping and can be neglected. Additionally small deviation of the FRF magnitude does not change the natural frequency values at all, as the peak positions remain if the FRF magnitude is slightly reduced.

Popp et al. [69,71], who have been the only ones up to now showing dependence of structural dynamics from temperature for lithium-ion pouch cells also found decreasing natural frequencies for increasing temperature. Three distinct temperature values in another range (0 °C, 25 °C and 45 °C) have been reported in [69,71] and no mode shapes have been correlated. Hence, a more detailed comparison is not possible. As no further modal analysis data is available, other areas of research have been considered.

Avdeev et al. [90] investigated the rate- and temperature dependent material behavior of multilayer polymer separators. They observed a strong dependence of the separator's elastic behavior in both machine direction (MD) and transverse direction (TD) on temperature. Young's modulus and the yield stress decreased for increased temperature. The Young's modulus for electrolyte-wetted separators in MD decreased from 1123 ± 169 MPa at 28.5 °C to 289 ± 11 at 80 °C. For TD the decrease was from 310 ± 8 to 129 ± 15 MPa [90].

The temperature dependence of separators with similar results was also reported in [18,91].

The thermal swelling of lithium-ion cells was investigated by Oh et al. [34]. The thermal expansion was much larger than for each electrode only, so the separator was identified as a critical element inside the cell. The thermal swelling followed a quadratic form at low temperatures ($T < 25$ °C) and linear characteristic at high temperatures ($T > 25$ °C) [34].

The fracture mechanics and mechanical strength of lithium-ion batteries under the pinch torsion test were investigated in [92] and a linearly decreasing mechanical strength for increasing temperature from 20 °C to 50 °C was observed.

The natural frequencies decrease due to a softening or, in other words, a reduction in stiffness. The temperature dependence of natural frequencies of the cells observed in our work and the temperature-

dependent elasticity or stiffness of separators and the thermal swelling and mechanical strength in other work shows similar linear trends at temperatures above 20–25 °C. Therefore, it can be assumed that the structural response of the lithium-ion pouch cell is strongly determined by the separator. This is also a probable assumption, as a stronger dependence from the electrodes shall cause higher sensitivity to SOC variation.

The steeper slope of the natural frequency vs. temperature curve for higher order modes could originate from the strain rate sensitivity of separators [90,93–96], but strain rate sensitivity can be only found up to a strain rate of 50/s [96] and therefore much slower than the lowest frequency in this work. In the reported literature, higher strain rates usually cause elastic modulus to increase, which is in contrast to the results in this work with a quicker decrease for higher frequencies. While in [90] temperature and rate dependence were investigated separately for dry and wet separators, no publication testing the strain rate sensitivity under varied temperature, which might explain our results, could be identified.

The high sensitivity of the structural dynamics from temperature makes it questionable, that temperature is often neglected in vibration testing. The results in this work show that different temperature conditions can have a significant influence on the vibrational response of lithium-ion pouch cells due to reduced damping at lower temperatures or due to reduced stiffness at higher temperatures. The temperature should therefore always be considered in vibration fatigue testing of lithium-ion pouch cells. As the temperature sensitivity is caused by the inner components, it further applies to other cell types and geometries as well.

4.5. Influence of SOH

To investigate the influence of cycling on the structural response of lithium-ion cells, the EMA for four of the five new cells and five cells, aged in [38], were measured and the results of the MDOF fit are presented as box plots in Fig. 8.

In these box plots, the box marks the 25th ($q1$) and 75th percentile ($q3$) of the data, the line in the box marks the median. The whiskers outside of the box mark the span of the data ($\pm$ 2.7σ for normally distributed data). Red crosses mark outliers greater than $q3 + 1.5(q3 - q1)$ or smaller as $q1 - 1.5(q3 - q1)$.

To account for measurement uncertainties three measurements with complete disassembly and reassembly of the measurement setup in between are taken. The mean values of each measurement triplet are depicted in the box plot. The box plots are therefore a representation of the cell-to-cell variation, and not of the reproducibility for each cell. The authors of this work are aware of the fact, that four measurements (new cells) and five measurements (aged cells) are low numbers for box plots. Nevertheless, this representation is the best to their knowledge to get a quick visual overview of the cell-to-cell variation and the difference between aged and new cells. Of course, the absolute value of the median shall be treated with care, but is also not the goal of this work because absolute values are specific for one cell, while the authors concentrate on the method and the general trends in case of e.g. cyclic aging. The issue of reproducibility is discussed in the Appendix.

The lithium-ion pouch cells in this work get stiffer due to cyclic aging in comparison to the new ones as the natural frequencies in Fig. 8 1a–5a for all five modes are significantly increased. A check of a potential correlation of the natural frequency to the cycle history (varied rigid or flexible bracing and stress level in [38]) has been done. No correlation or dependence from history is observable. As also the capacities have been in a very narrow range the simple classification of “new” and “aged” has been most useful, while “aged” stands for approx. 90% SOH for all aged cells in this work. Further correlation, e.g. natural frequencies with the impedance, would require further investigations.

For damping in Fig. 8 1b–5b no clear trend can be observed. The median value increases for modes 1, mode 4 and 5, while it stays nearly constant for mode 2 and decreases for mode 3.

While the electrical parameters of lithium-ion cells usually show increased parameter variation due to aging [97–100], this cannot be seen for natural frequencies and damping ratios. However, for an evaluation of the distribution, of course, a larger sample size needed to be measured.

Popp et al. [71] compared a new pouch cell with a cycled pouch cell of ~75% SOH and reported slight changes in natural frequencies: 387.58–406.27 Hz (natural frequency 1), 724.42–710.88 Hz (2) and 1071.18–1041.62 Hz (3). These changes are (1) much smaller as the observations in this work and (2) the cell in [71] got softer (lower natural frequencies) for two of three natural frequencies, what is in contrast to the observations in this work.

Furthermore, Popp et al. [71] reported strongly decreased damping for the cycled cells, e.g. from 20.83% to 11.13% for the first resonance at 0% SOC, which is different from the results in this work. The same reasons as already discussed in the section about nonlinearity also apply here.

An interesting outcome can be obtained by comparison with the studies of Dai et al. [101]. They found decreased elastic modulus and fracture strength of copper foils and decreased adhesive strength of electrodes as an effect of cycling of a commercial $LiCoO_2$ lithium-ion cell [101]. In contrast, the increased stiffness of the cells in this work indicates an increased elastic modulus of the lithium-ion pouch cell. Therefore, it is very important to understand which component determines the structural dynamics and how the different components behave as a compound as the dynamic mechanical behavior of lithium-ion cells is strongly determined by the interfaces and the boundary conditions [102].

While the separator, as could be seen in the temperature sensitivity (Section 4.4), significantly dominates the structural response of the investigated new pouch cells, other effects might dominate the sensitivity from the SOH. During aging, passive layers as the solid electrolyte interface (SEI) are formed in the cell [103,104]. This causes a volume expansion of the electrode stack inside the pouch foil. Consequently, the pressure might rise inside in the cell due to the outer constraints given by the pouch foil, e.g., changing the porosity of the separator. This could cause an increased stiffness of the cell due to outer constraints. Other possible explanations are the changed electrode-separator interfaces because of passive layers on the electrode surfaces as well as changes in the structure of the porous electrode itself due to the repeated volumetric changes caused by aging. If the underlying mechanisms for the sensitivity of the structural dynamics from aging shall be understood in detail, we recommend to perform the procedure of experimental modal analysis, as presented in this work, at various points in time during an aging experiment. As the method in this publication is non-destructive, the experiment can be done on the same cell for many different state of healths. With a well-designed aging experiment, e.g., promoting lithium-plating or SEI growth through the right combination and variation of conditions, as temperature, charge and discharge current, SOC range and cell bracing, the effect of different aging mechanisms on the stiffness of the cell might be explored.

Our study in this publication, reveals several sensitivities of the structural dynamics. While many studies in the literature are concentrated on the influence of different SOC levels, we emphasize an additional focus on the influence of temperature and aging and the effect of the excitation level due to nonlinear effects. The obtained information, including mode shapes, can be used to investigate possible failure mechanisms caused by vibration, according to the approach given in the introduction. This shall help to, for example, understand if a possible failure depends on stress or strain, if the acceleration of tests is possible or which cell deformation pattern has to be avoided through pack design, to name only a few examples.

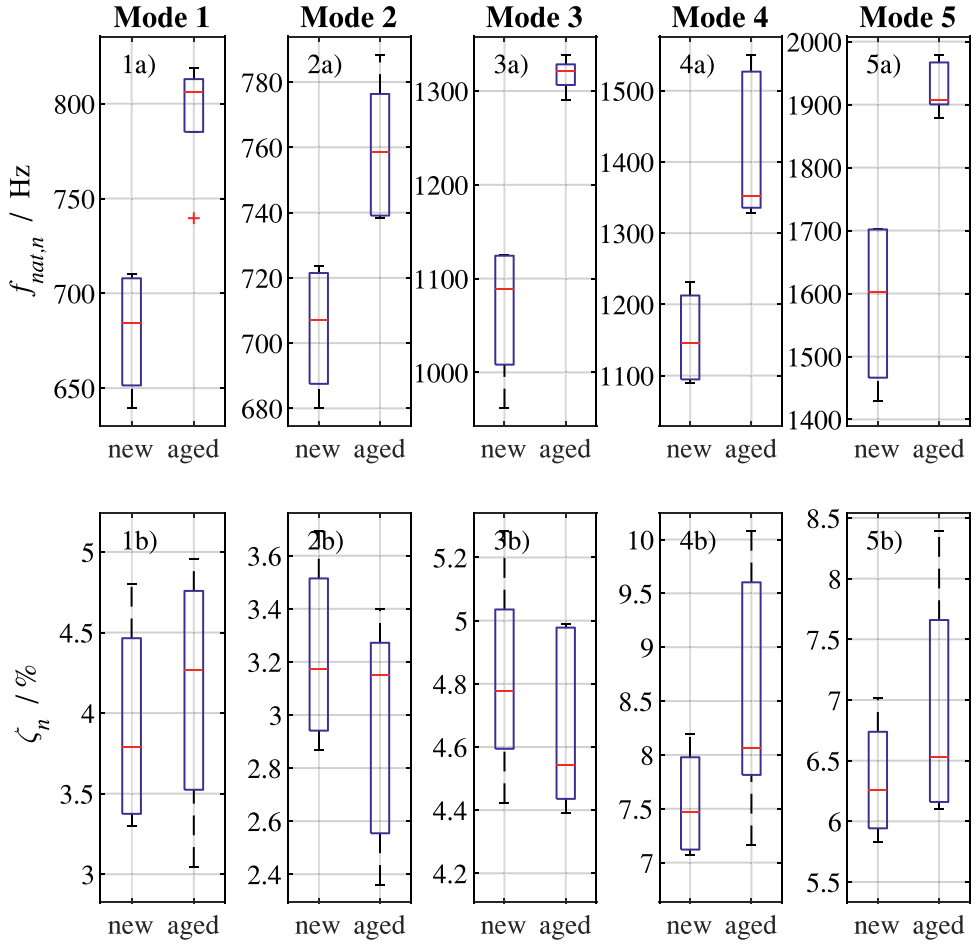

Fig. 8. Variation of SOH showing high sensitivity to the SOH especially for a) natural frequencies $f_{nat,n}$ with increased stiffness for aged cells and b) damping ratios ζ_n.

5. Conclusion

In this work, the structural response of lithium-ion pouch cells was investigated. The structural dynamics were measured including the characteristic mode shapes. The sensitivities on excitation level, temperature, SOC and SOH were shown.

Therefore the test bench has been enabled to measure cells of different weight and size, proven with consumer cells of 2.1 Ah. The test bench can be adapted to larger and heavier cell types and sizes by the adoption of the support springs and if required an adjustment of the stinger length.

This work revealed the following key takeaways. They are structured into method-related conclusions (with respect to EMA) and findings-related conclusions.

Method-related conclusions:

1. Lithium-ion pouch cells have shown strong nonlinear dynamics; therefore, the concept of modal analysis has to be used with care. Sine sweep can be used for further analysis. Signals of random nature are preferable if a linear approximation is desired.
2. Lithium-ion pouch cells show high modal density and high damping values compared to an aluminum dummy for example. Therefore, the usage of an MDOF-fitting procedure in contrast to an SDOF-fitting procedure is emphasized.
3. The obtained data can be used to parameterize FEM models of the cells and to calculate stress and strain distributions as a prerequisite to understand potential fatigue or to obtain elastic parameters of a full cell, including all interfaces through fitting of a proper model.

Findings-related conclusions:

1. The effects of nonlinear stiffness and damping of lithium-ion pouch cells in the case of vibration excitation have been underrepresented in the available literature up until now. Nonlinear cubic softening as well as nonlinear quadratic damping could be shown. The effect of nonlinearity has to be considered in safety testing and whether tests should be accelerated by amplitude scaling.
2. The sensitivity analysis of SOC, temperature, and SOH showed that thermal expansion and cyclic aging have significantly higher influence on the structural response of lithium-ion pouch cells than lithium intercalation and the respective change in the SOC.
3. The mechanical behavior of single components (e.g. electrodes or separators), obtained by component testing can significantly differ from the behavior of these components as part of a full cell.

Declaration of Competing Interest

None.

Acknowledgments

This work was supported by the German Federal Ministry for Economic Affairs and Energy (BMWi) [03ETE004B]. Funding by the German Federal Ministry for Economic Affairs and Energy (BMWi) and the management of the project ReViSEDBatt by the Project Management Juelich (PTJ) are gratefully acknowledged.

Furthermore, we want to thank the Institute for Machine Tools and Industrial Management (*iwb*) for space and support to run our test

bench. We also thank Fabian Ebert from Fraunhofer ISC for providing the aged cells. Special thanks by Philipp Berg goes to his mentor Jan Philipp Schmidt for valuable discussions, ideas and reviews.

Supplementary material

Supplementary material associated with this article can be found, in the online version, at doi:10.1016/j.est.2019.100916.

Appendix A

Table A.1 shows the reproducibility of the SOH-related measurements by means of the spread of each measurement triplet. The reproducibility is again best for mode 1 and mode 2, same as for SOC investigation. Mode 3 shows better reproducibility as in SOC variation. Mode 4 has higher reproducibility for the new cells (spreads Δf_4 of 19.4 Hz up to 43.7 Hz) as for aged cells (spreads Δf_4 of 44.9 Hz up to 132.4 Hz). Mode 5, in contrast, shows the opposite behavior with spreads Δf_5 of 7.6 Hz up to 44.7 Hz for aged cells and spreads Δf_5 up to 101.7 Hz for new cells.

Table A.1
Maximum absolute spread for each measurement triplet of each cell in SOH investigation.

SOH	Mode 1		Mode 2		Mode 3		Mode 4		Mode 5	
	Δf_1/Hz	$\Delta\zeta_1$	Δf_2/Hz	$\Delta\zeta_2$	Δf_3/Hz	$\Delta\zeta_3$	Δf_4/Hz	$\Delta\zeta_4$	Δf_5/Hz	$\Delta\zeta_5$
New 1	6.8	0.36%	12.8	0.20%	40.1	0.65%	19.4	0.04%	42.5	0.92%
New 2	2.6	0.02%	2.7	0.08%	8.8	0.02%	35.0	0.32%	101.7	3.43%
New 3	5.5	0.29%	8.8	0.64%	15.3	0.30%	25.8	0.63%	80.6	1.92%
New 4	1.7	0.34%	3.3	0.14%	6.0	0.25%	43.7	0.24%	19.3	0.55%
Aged 1	2.4	0.18%	14.7	0.26%	27.7	0.23%	111.6	0.18%	44.7	0.63%
Aged 2	8.8	0.19%	14.8	0.10%	5.3	0.11%	94.6	1.22%	7.6	0.31%
Aged 3	5.3	0.15%	12.8	0.17%	23.8	0.35%	65.2	0.61%	34.7	1.36%
Aged 4	2.7	0.08%	4.1	0.84%	10.0	0.27%	44.9	0.87%	23.6	1.83%
Aged 5	6.2	0.17%	13.0	0.29%	30.0	0.60%	132.4	1.10%	43.8	0.21%

References

[1] E. Helmers, P. Marx, Electric cars: technical characteristics and environmental impacts, Environ. Sci. Eur. 24 (2012) 564, https://doi.org/10.1186/2190-4715-24-14.

[2] R. Jansen, C. Bowman, A. Jankovsky, R. Dyson, J. Felder, Overview of NASA Electrified Aircraft Propulsion (EAP) research for large subsonic transports, 53rd AIAA/SAE/ASEE Joint Propulsion Conference 2017, Atlanta, GA, Curran Associates Inc, Red Hook, NY, 2017, p. 2202.

[3] B. Liu, Y. Jia, J. Li, S. Yin, C. Yuan, Z. Hu, L. Wang, Y. Li, J. Xu, Safety issues caused by internal short circuits in lithium-ion batteries, J. Mater. Chem. A 6 (2018) 21475–21484, https://doi.org/10.1039/C8TA08997C.

[4] B. Scrosati, J. Garche, Lithium batteries: Status, prospects and future, J. Power Sources 195 (2010) 2419–2430, https://doi.org/10.1016/j.jpowsour.2009.11.048.

[5] S. Abada, G. Marlair, A. Lecocq, M. Petit, V. Sauvant-Moynot, F. Huet, Safety focused modeling of lithium-ion batteries: a review, J. Power Sources 306 (2016) 178–192, https://doi.org/10.1016/j.jpowsour.2015.11.100.

[6] FAA Office of Security and Hazardous Materials Safety, Aviation cargo and passenger baggage events involving smoke, fire, extreme heat or explosion involving lithium batteries or unknown battery types, 2018. https://www.faa.gov/hazmat/resources/lithium_batteries/media/Battery_incident_chart.pdf (accessed 1 September 2019).

[7] C. Mikolajczak, M. Kahn, K. White, Lithium-ion batteries hazard and use assessment, Springer, New York, 2012.

[8] National Highway Traffic Safety Administration, Chevrolet Volt Battery Incident Overview Report, Washington DC, 2012.

[9] Q. Wang, P. Ping, X. Zhao, G. Chu, J. Sun, C. Chen, Thermal runaway caused fire and explosion of lithium ion battery, J. Power Sources 208 (2012) 210–224, https://doi.org/10.1016/j.jpowsour.2012.02.038.

[10] Samsung confirms battery faults as cause of Note 7 fires, 2018. https://www.bbc.com/news/business-38714461(accessed 8 January 2019).

[11] X. Feng, M. Ouyang, X. Liu, L. Lu, Y. Xia, X. He, Thermal runaway mechanism of lithium ion battery for electric vehicles: a review, Energy Storage Mater. 10 (2018) 246–267, https://doi.org/10.1016/j.ensm.2017.05.013.

[12] D.P. Finegan, E. Darcy, M. Keyser, B. Tjaden, T.M.M. Heenan, R. Jervis, J.J. Bailey, N.T. Vo, O.V. Magdysyuk, M. Drakopoulos, M. Di Michiel, A. Rack, G. Hinds, D.J.L. Brett, P.R. Shearing, Identifying the cause of rupture of Li-ion batteries during thermal runaway, Adv. Sci. 5 (2017) 1700369, , https://doi.org/10.1002/advs.201700369.

[13] J. Lamb, C.J. Orendorff, L.A.M. Steele, S.W. Spangler, Failure propagation in multi-cell lithium ion batteries, J. Power Sources 283 (2015) 517–523, https://doi.org/10.1016/j.jpowsour.2014.10.081.

[14] J. Sun, J. Li, T. Zhou, K. Yang, S. Wei, N. Tang, N. Dang, H. Li, X. Qiu, L. Chen, Toxicity, a serious concern of thermal runaway from commercial Li-ion battery, Nano Energy 27 (2016) 313–319, https://doi.org/10.1016/j.nanoen.2016.06.031.

[15] S. Koch, A. Fill, K.P. Birke, Comprehensive gas analysis on large scale automotive lithium-ion cells in thermal runaway, J. Power Sources 398 (2018) 106–112, https://doi.org/10.1016/j.jpowsour.2018.07.051.

[16] G. Kermani, E. Sahraei, Review: characterization and modeling of the mechanical properties of lithium-ion batteries, Energies 10 (2017) 1730, https://doi.org/10.3390/en10111730.

[17] J.A. Turner, S. Allu, S.B. Gorti, S. Kalnaus, A. Kumar, D.T. Lebrun-Grandie, S. Pannala, S. Simunovic, S.R. Slattery, H. Wang, Crash models for advanced automotive batteries: a review of the current state of the art, 2015. doi:10.2172/1302885.

[18] J. Zhu, T. Wierzbicki, W. Li, A review of safety-focused mechanical modeling of commercial lithium-ion batteries, J. Power Sources 378 (2018) 153–168, https://doi.org/10.1016/j.jpowsour.2017.12.034.

[19] M.Y. Ali, W.-J. Lai, J. Pan, Computational models for simulations of lithium-ion battery cells under constrained compression tests, J. Power Sources 242 (2013) 325–340, https://doi.org/10.1016/j.jpowsour.2013.05.022.

[20] L. Greve, C. Fehrenbach, Mechanical testing and macro-mechanical finite element simulation of the deformation, fracture, and short circuit initiation of cylindrical Lithium ion battery cells, J. Power Sources 214 (2012) 377–385, https://doi.org/10.1016/j.jpowsour.2012.04.055.

[21] H. Wang, A. Kumar, S. Simunovic, S. Allu, S. Kalnaus, J.A. Turner, J.C. Helmers, E.T. Rules, C.S. Winchester, P. Gorney, Progressive mechanical indentation of large-format Li-ion cells, J. Power Sources 341 (2017) 156–164, https://doi.org/10.1016/j.jpowsour.2016.11.094.

[22] E. Sahraei, J. Meier, T. Wierzbicki, Characterizing and modeling mechanical properties and onset of short circuit for three types of lithium-ion pouch cells, J. Power Sources 247 (2014) 503–516, https://doi.org/10.1016/j.jpowsour.2013.08.056.

[23] H. Wang, S. Simunovic, H. Maleki, J.N. Howard, J.A. Hallmark, Internal configuration of prismatic lithium-ion cells at the onset of mechanically induced short circuit, J. Power Sources 306 (2016) 424–430, https://doi.org/10.1016/j.jpowsour.2015.12.026.

[24] W. Cai, H. Wang, H. Maleki, J. Howard, E. Lara-Curzio, Experimental simulation of internal short circuit in Li-ion and Li-ion-polymer cells, J. Power Sources 196 (2011) 7779–7783, https://doi.org/10.1016/j.jpowsour.2011.04.024.

[25] X. Zhang, T. Wierzbicki, Characterization of plasticity and fracture of shell casing of lithium-ion cylindrical battery, J. Power Sources 280 (2015) 47–56, https://doi.org/10.1016/j.jpowsour.2015.01.077.

[26] J. Cannarella, C.B. Arnold, State of health and charge measurements in lithium-ion batteries using mechanical stress, J. Power Sources 269 (2014) 7–14, https://doi.org/10.1016/j.jpowsour.2014.07.003.

[27] F. Ebert, G. Sextl, J. Adermann, C. Reiter, M. Lienkamp, Detection of cell-stack inhomogeneities via mechanical SOC and SOH measurement, 2017 IEEE Transportation Electrification Conference and Expo (ITEC), IEEE, Chicago, IL, USA, 2017, pp. 545–549.

[28] J. Luo, C.Y. Dai, Z. Wang, K. Liu, W.G. Mao, D.N. Fang, X. Chen, In-situ measurements of mechanical and volume change of LiCoO 2 lithium-ion batteries

during repeated charge–discharge cycling by using digital image correlation, Measurement 94 (2016) 759–770, https://doi.org/10.1016/j.measurement.2016.09.023.
[29] S.P.V. Nadimpalli, V.A. Sethuraman, D.P. Abraham, A.F. Bower, P.R. Guduru, Stress evolution in lithium-ion composite electrodes during electrochemical cycling and resulting internal pressures on the cell casing, J. Electrochem. Soc. 162 (2015) A2656–A2663, https://doi.org/10.1149/2.0341514jes.
[30] K.-Y. Oh, B.I. Epureanu, J.B. Siegel, A.G. Stefanopoulou, Phenomenological force and swelling models for rechargeable lithium-ion battery cells, J. Power Sources 310 (2016) 118–129, https://doi.org/10.1016/j.jpowsour.2016.01.103.
[31] B. Rieger, S. Schlueter, S.V. Erhard, A. Jossen, Strain propagation in lithium-ion batteries from the crystal structure to the electrode level, J. Electrochem. Soc. 163 (2016) A1595–A1606, https://doi.org/10.1149/2.0431608jes.
[32] D. Sauerteig, N. Hanselmann, A. Arzberger, H. Reinshagen, S. Ivanov, A. Bund, Electrochemical-mechanical coupled modeling and parameterization of swelling and ionic transport in lithium-ion batteries, J. Power Sources 378 (2018) 235–247, https://doi.org/10.1016/j.jpowsour.2017.12.044.
[33] O. Valentin, P.-X. Thivel, T. Kareemulla, F. Cadiou, Y. Bultel, Modeling of thermo-mechanical stresses in Li-ion battery, J. Energy Storage 13 (2017) 184–192, https://doi.org/10.1016/j.est.2017.07.018.
[34] K.-Y. Oh, B.I. Epureanu, A novel thermal swelling model for a rechargeable lithium-ion battery cell, J. Power Sources 303 (2016) 86–96, https://doi.org/10.1016/j.jpowsour.2015.10.085.
[35] K.-Y. Oh, B.I. Epureanu, Characterization and modeling of the thermal mechanics of lithium-ion battery cells, Appl. Energy 178 (2016) 633–646, https://doi.org/10.1016/j.apenergy.2016.06.069.
[36] A. Barai, R. Tangirala, K. Uddin, J. Chevalier, Y. Guo, A. McGordon, P. Jennings, The effect of external compressive loads on the cycle lifetime of lithium-ion pouch cells, J. Energy Storage 13 (2017) 211–219, https://doi.org/10.1016/j.est.2017.07.021.
[37] J. Cannarella, C.B. Arnold, Stress evolution and capacity fade in constrained lithium-ion pouch cells, J. Power Sources 245 (2014) 745–751, https://doi.org/10.1016/j.jpowsour.2013.06.165.
[38] F. Ebert, G. Sextl, M. Lienkamp, Effect of a flexible battery module bracing on cell aging, 2017 Twelfth International Conference on Ecological Vehicles and Renewable Energies (EVER), IEEE, Monte-Carlo, Monaco, 2017, pp. 1–5.
[39] X.M. Liu, C.B. Arnold, Effects of cycling ranges on stress and capacity fade in lithium-ion pouch cells, J. Electrochem. Soc. 163 (2016) A2501–A2507, https://doi.org/10.1149/2.1131610jes.
[40] T.C. Bach, S.F. Schuster, E. Fleder, J. Müller, M.J. Brand, H. Lorrmann, A. Jossen, G. Sextl, Nonlinear aging of cylindrical lithium-ion cells linked to heterogeneous compression, J. Energy Storage (2016), https://doi.org/10.1016/j.est.2016.01.003.
[41] J.M. Hooper, J. Marco, Understanding vibration frequencies experienced by electric vehicle batteries, IET Hybrid and Electric Vehicles Conference 2013 (HEVC 2013), IEEE, Piscataway, NJ, 2013, , https://doi.org/10.1049/cp.2013.1908.
[42] G. Kjell, J.F. Lang, Comparing different vibration tests proposed for li-ion batteries with vibration measurement in an electric vehicle, 2013 World Electric Vehicle Symposium and Exhibition (EVS27), IEEE, Barcelona, Spain, 2013, pp. 1–11, , https://doi.org/10.1109/EVS.2013.6914869.
[43] J. Marco, J.M. Hooper, Defining a representative vibration durability test for electric vehicle (EV) rechargeable energy storage systems (RESS), Electric Vehicle Symposium (EVS 29), Montréal, Québec, 2016, pp. 1–12.
[44] C. Lalanne, Mechanical Vibration and Shock Analysis, Volume 1 - Sinusoidal Vibration (3rd Edition), John Wiley & Sons.
[45] J. Frodelius Lang, G. Kjell, Comparing vibration measurements in an electric vehicle with standard vibration requirements for Li-ion batteries using power spectral density analysis, Int. J. Electr. Hybrid Veh. (2015) 7, https://doi.org/10.1504/IJEHV.2015.071640.
[46] J.M. Hooper, J. Marco, Characterising the in-vehicle vibration inputs to the high voltage battery of an electric vehicle, J. Power Sources 245 (2014) 510–519, https://doi.org/10.1016/j.jpowsour.2013.06.150.
[47] V. Ruiz, A. Pfrang, A. Kriston, N. Omar, P. van den Bossche, L. Boon-Brett, A review of international abuse testing standards and regulations for lithium ion batteries in electric and hybrid electric vehicles, Renew. Sustain. Energy Rev. (2017), https://doi.org/10.1016/j.rser.2017.05.195.
[48] P.J. Swornowski, Destruction mechanism of the internal structure in Lithium-ion batteries used in aviation industry, Energy (2017), https://doi.org/10.1016/j.energy.2017.01.121.
[49] J. Kim, W. Na, S. Lee, M. Jang, C. Lim, Cell failure evaluations under environmental and safety tests of multiple 18650 Li-Ion NCA and NMC cells for space cell's qualification estabilishment, 2018 IEEE Energy Conversion Congress and Exposition (ECCE), IEEE, Portland, OR, USA, 2018, pp. 2033–2038.
[50] M.G. Darvish, Vibration and functional tests on a new designed battery pack of a micro-satellite, 10.5267/j.esm (2018) 129–134. https://doi.org/10.5267/j.esm.2018.3.001.
[51] C.-O. Yoon, P.-Y. Lee, M. Jang, K. Yoo, J. Kim, Comparison of internal parameters varied by environmental tests between high-power series/parallel battery packs with different shapes, J. Indus. Eng. Chem. 71 (2019) 260–269, https://doi.org/10.1016/j.jiec.2018.11.034.
[52] X. Wang, M. Kato, H. Naito, C. Yamada, G. Segami, K. Kibe, A feasibility study of commercial laminated lithium-ion polymer cells for space applications, J. Electrochem. Soc. 153 (2006) A89, https://doi.org/10.1149/1.2131825.
[53] T. Tsujikawa, K. Yabuta, M. Arakawa, K. Hayashi, Safety of large-capacity lithium-ion battery and evaluation of battery system for telecommunications, 16th International Meeting on Lithium Batteries (IMLB) 244 (2013) 11–16, https://doi.org/10.1016/j.jpowsour.2013.01.155.
[54] L. Shuyan, C. Yan, J. Fachao, Z. Jianzhu, W. Guoye, Research on the finite element analysis and failure strengthening test of electric bus quick-change battery box, 2015 8th International Conference on Intelligent Computation Technology and Automation (ICICTA), IEEE, Nanchang, China, 2015, pp. 771–775.
[55] J. Li, H. Tian, P. Wu, Analysis of random vibration of power battery box in electric vehicles, 2014 IEEE Conference and Expo Transportation Electrification Asia-Pacific (ITEC Asia-Pacific), IEEE, Beijing, China, 2014, pp. 1–5.
[56] Y. Choi, D. Jung, K. Ham, S. Bae, A study on the accelerated vibration endurance tests for battery fixing bracket in electrically driven vehicles, Procedia Eng. 10 (2011) 851–856, https://doi.org/10.1016/j.proeng.2011.04.140.
[57] J.-K. Lee, J.-S. Yeo, M.-C. Jang, J.-M. Yoon, D.M. Kang, Mechanical durability and electrical durability of an aluminium-laminated lithium-ion polymer battery pack for a hybrid electric vehicle, Proc. Inst. Mech. Eng. 224 (2010) 765–773, https://doi.org/10.1243/09544070JAUTO1388.
[58] P. Svens, Methods for Testing and Analyzing Lithium-Ion Battery Cells Intended for Heavy-Duty Hybrid Electric Vehicles, Doctoral thesis Chemical Science and Engineering, KTH Royal Institute of Technology, Stockholm, 2014.
[59] J. Hooper, J. Marco, G. Chouchelamane, C. Lyness, Vibration durability testing of nickel manganese cobalt oxide (NMC) lithium-ion 18,650 battery cells, Energies 9 (2016) 52, https://doi.org/10.3390/en9010052.
[60] J. Hooper, J. Marco, G. Chouchelamane, C. Lyness, J. Taylor, Vibration durability testing of nickel cobalt aluminum oxide (NCA) lithium-ion 18650 battery cells, Energies 9 (2016) 281, https://doi.org/10.3390/en9040281.
[61] L. Zhang, Z. Ning, H. Peng, Z. Mu, C. Sun, Effects of vibration on the electrical performance of lithium-ion cells based on mathematical statistics, Applied Sciences 7 (2017) 802, https://doi.org/10.3390/app7080802.
[62] J.M. Hooper, J. Marco, G.H. Chouchelamane, J.S. Chevalier, D. Williams, Multi-axis vibration durability testing of lithium ion 18650 NCA cylindrical cells, J. Energy Storage 15 (2018) 103–123, https://doi.org/10.1016/j.est.2017.11.006.
[63] L. Zhang, Z. Mu, X. Gao, Coupling analysis and performance study of commercial 18650 lithium-ion batteries under conditions of temperature and vibration, Energies 11 (2018) 2856, https://doi.org/10.3390/en11102856.
[64] M.J. Brand, S.F. Schuster, T. Bach, E. Fleder, M. Stelz, S. Gläser, J. Müller, G. Sextl, A. Jossen, Effects of vibrations and shocks on lithium-ion cells, J. Power Sources 288 (2015) 62–69, https://doi.org/10.1016/j.jpowsour.2015.04.107.
[65] C. Lalanne, Mechanical Vibration and Shock Analysis, Volume 2: Mechanical shock, Wiley, Hoboken, NJ, 2014.
[66] C. Lalanne, Mechanical Vibration and Shock Analysis, Volume 4: Fatigue damage, Wiley, Hoboken, NJ, 2014.
[67] C.W. de Silva (Ed.), Vibration and Shock Handbook, Taylor & Francis, Boca Raton, 2005.
[68] H.Y. Choi, I. Lee, J.S. Lee, Y.M. Kim, H.K. Kim, A study on mechanical characteristics of lithium-polymer pouch cell battery for electric vehicle, 23rd International Technical Conference on the Enhanced Safety of Vehicles (ESV), Seoul, Republic of Korea, 2013.
[69] H. Popp, M. Luthfi, J.-H. Han, R. Klambauer, A. Bergmann, In-Situ investigation of lithium-ion batteries by combined mechanical FRF and dilatometer measurements, 2018 E-MRS Fall Meeting and Exhibit, Warsaw, 2018.
[70] J.M. Hooper, J. Marco, Experimental modal analysis of lithium-ion pouch cells, J. Power Sources 285 (2015) 247–259, https://doi.org/10.1016/j.jpowsour.2015.03.098.
[71] H. Popp, G. Glanz, K. Alten, I. Gocheva, W. Berghold, A. Bergmann, Mechanical frequency response analysis of lithium-ion batteries to disclose operational parameters, Energies 11 (2018) 541, https://doi.org/10.3390/en11030541.
[72] J. Galos, A.A. Khatibi, A.P. Mouritz, Vibration and acoustic properties of composites with embedded lithium-ion polymer batteries, Compos. Struct. 220 (2019) 677–686, https://doi.org/10.1016/j.compstruct.2019.04.013.
[73] F.-M. Volk, M. Winkler, B. Hermann, A. Hiebl, T. Idikurt, H. Rapp, T. Kuttner, Influence of state of charge and state of health on the vibrational behavior of lithium-ion cell packs, 23rd International Congress on Sound & Vibration (ICSV23), Athen, Greece, 2016.
[74] S.-K. Hong, B.I. Epureanu, M.P. Castanier, Parametric reduced-order models of battery pack vibration including structural variation and prestress effects, J. Power Sources 261 (2014) 101–111, https://doi.org/10.1016/j.jpowsour.2014.03.008.
[75] W. Nam, J.-Y. Kim, K.-Y. Oh, The characterization of dynamic behavior of Li-ion battery packs for enhanced design and states identification, Energy Convers. Manag. 162 (2018) 264–275, https://doi.org/10.1016/j.enconman.2018.02.022.
[76] K.L. Dallon, J. Yao, D.R. Wheeler, B.A. Mazzeo, Characterization of mechanical properties of battery electrode films from acoustic resonance measurements, J. Appl. Phys. 123 (2018) 135102, , https://doi.org/10.1063/1.5021809.
[77] P. Avitabile, Modal Space (in our own little world), 2014.
[78] D.J. Ewins, Modal Testing: Theory and Practice, Research Studies press, Taunton, 1995.
[79] C. Lalanne, Mechanical Vibration and Shock Analysis, Volume 1: Sinusoidal Vibration, John Wiley & Sons, New York, NY, 2014.
[80] E.C. Stasiunas, T.G. Carne, T.D. Hinnerichs, B.R. Rogillio, Modal parameter estimation techniques, in: P. Avitabile (Ed.), Modal Testing: A Practitioner's Guide, John Wiley & Sons Ltd, Chichester, UK, 2017, pp. 189–219.
[81] P. Guillaume, P. Verboven, S. Vanlanduit, H. van der Auweraer, B. Peeters, A poly-reference implementation of the least-squares complex frequency-domain estimator, Proceedings of IMAC, 2003, p. 21.
[82] m + p international, m + p Analyzer: User Manual Revision 5.1, Hannover (2017).
[83] O. Døssing, Structural Testing: Part II: Modal Analysis and Simulation, 1988.

[84] K. Worden, G.R. Tomlinson, Nonlinearity in Structural Dynamics: Detection, Identification and Modelling, Institute of Physics, Bristol, 2001.
[85] M.R. Ashory, High Quality Modal Testing Methods. Dissertation, London, 1999.
[86] N. Granick, J.E. Stern, Material Damping of Aluminum by a Resonant-Dwell Technique: NASA Technical Note TN D-2893, Washington DC, 1965.
[87] H. Mevada, D. Patel, Experimental determination of structural damping of different materials, Procedia Eng. 144 (2016) 110–115, https://doi.org/10.1016/j.proeng.2016.05.013.
[88] Y. Qi, H. Guo, L.G. Hector, A. Timmons, Threefold Increase in the Young's modulus of graphite negative electrode during lithium intercalation, J. Electrochem. Soc. 157 (2010) A558, https://doi.org/10.1149/1.3327913.
[89] Y. Qi, L.G. Hector, C. James, K.J. Kim, Lithium concentration dependent elastic properties of battery electrode materials from first principles calculations, J. Electrochem. Soc. 161 (2014) F3010–F3018, https://doi.org/10.1149/2.0031411jes.
[90] I. Avdeev, M. Martinsen, A. Francis, Rate- and temperature-dependent material behavior of a multilayer polymer battery separator, J. Materi. Eng. Perform. 23 (2014) 315–325, https://doi.org/10.1007/s11665-013-0743-4.
[91] X. Zhang, Mechanical Behavior of Shell Casing and Separator of Lithium-ion Battery. Dissertation, Massachusetts, 2017.
[92] V. Vijayaraghavan, A. Garg, L. Gao, Fracture mechanics modelling of lithium-ion batteries under pinch torsion test, Measurement 114 (2018) 382–389, https://doi.org/10.1016/j.measurement.2017.10.008.
[93] J. Cannarella, X. Liu, C.Z. Leng, P.D. Sinko, G.Y. Gor, C.B. Arnold, Mechanical properties of a battery separator under compression and tension, J. Electrochem. Soc. 161 (2014) F3117–F3122, https://doi.org/10.1149/2.0191411jes.
[94] G.Y. Gor, J. Cannarella, J.H. Prevost, C.B. Arnold, A model for the behavior of battery separators in compression at different strain/charge rates, J. Electrochem. Soc. 161 (2014) F3065–F3071, https://doi.org/10.1149/2.0111411jes.
[95] S. Kalnaus, Y. Wang, J.A. Turner, Mechanical behavior and failure mechanisms of Li-ion battery separators, J. Power Sources 348 (2017) 255–263, https://doi.org/10.1016/j.jpowsour.2017.03.003.
[96] J. Xu, L. Wang, J. Guan, S. Yin, Coupled effect of strain rate and solvent on dynamic mechanical behaviors of separators in lithium ion batteries, Mater. Des. 95 (2016) 319–328, https://doi.org/10.1016/j.matdes.2016.01.082.
[97] T. Baumhöfer, M. Brühl, S. Rothgang, D.U. Sauer, Production caused variation in capacity aging trend and correlation to initial cell performance, J. Power Sources 247 (2014) 332–338, https://doi.org/10.1016/j.jpowsour.2013.08.108.
[98] S.J. Harris, D.J. Harris, C. Li, Failure statistics for commercial lithium ion batteries: a study of 24 pouch cells, J. Power Sources 342 (2017) 589–597, https://doi.org/10.1016/j.jpowsour.2016.12.083.
[99] S. Paul, C. Diegelmann, H. Kabza, W. Tillmetz, Analysis of ageing inhomogeneities in lithium-ion battery systems, J. Power Sources 239 (2013) 642–650, https://doi.org/10.1016/j.jpowsour.2013.01.068.
[100] S.F. Schuster, M.J. Brand, P. Berg, M. Gleissenberger, A. Jossen, Lithium-ion cell-to-cell variation during battery electric vehicle operation, J. Power Sources 297 (2015) 242–251, https://doi.org/10.1016/j.jpowsour.2015.08.001.
[101] C. Dai, Z. Wang, K. Liu, X. Zhu, X. Liao, X. Chen, Y. Pan, Effects of cycle times and C-rate on mechanical properties of copper foil and adhesive strength of electrodes in commercial LiCoO2 LIBs, Eng. Fail. Anal. 101 (2019) 193–205, https://doi.org/10.1016/j.engfailanal.2019.03.015.
[102] Y. Chen, S. Santhanagopalan, V. Babu, Y. Ding, Dynamic mechanical behavior of lithium-ion pouch cells subjected to high-velocity impact, Compos. Struct. 218 (2019) 50–59, https://doi.org/10.1016/j.compstruct.2019.03.046.
[103] A. Barré, B. Deguilhem, S. Grolleau, M. Gérard, F. Suard, D. Riu, A review on lithium-ion battery ageing mechanisms and estimations for automotive applications, J. Power Sources 241 (2013) 680–689, https://doi.org/10.1016/j.jpowsour.2013.05.040.
[104] J. Vetter, P. Novák, M.R. Wagner, C. Veit, K.-C. Möller, J.O. Besenhard, M. Winter, M. Wohlfahrt-Mehrens, C. Vogler, A. Hammouche, Ageing mechanisms in lithium-ion batteries, J. Power Sources 147 (2005) 269–281, https://doi.org/10.1016/j.jpowsour.2005.01.006.

7 Structural dynamics of lithium-ion cells – Part II: Investigation of large-format lithium-ion prismatic cells and method evaluation

In the following, the third core-publication [110] is briefly introduced.

Introduction and motivation

This chapter and the respective publication [110] are based on the test bench developed in Chapter 6 and [109]. A large-format lithium-ion prismatic cell is under test to investigate the influence of the constraints due to the hard case cell and to see if any harmful displacements inside the cell occur. This could be possible as a result of initial gaps between the four jelly rolls and the casing, as it was detected with force measurements and for another prismatic cell in [69]. Less tight cell packaging in comparison to, for example, 18650 cells is also mentioned in literature [128,129]. This is especially interesting, since the negative effects of insufficiently constrained cell components with respect to vibration durability have been already proven in the case of 18650 cells [84,99]. As cells with a nominal capacity of 94 Ah pose a significant safety threat, costly and sophisticated measurement setups are required for durability tests. For that reason, a characterization beforehand makes sense to narrow down the required variation of parameters as SOC, SOH and temperature.

Addressed objectives

This chapter and the respective publication [110] are the basis for the evaluation of several failure mechanisms, e.g., the possible mechanism of abrasion of the jelly rolls due to relative displacement, and therefore addresses Objective 1 (failure mechanisms) and Objective 2 (failure modes). Objective 3 (influencing factors) is in the center of the investigation through the sensitivity analysis for variation in SOC, SOH and temperature. Objective 4 (methods) is briefly investigated because nonlinearity is considered but with lower importance and depth than in Chapter 6. Since the direct comparability of the results for pouch cells and prismatic hard-case cells delivered interesting results, the publication [110] contains an evaluation of the EMA, directly answering to Objective 5 (EMA potential).

Key results

The investigated large-format prismatic cells show sensitivity to SOC, temperature and aging for both natural frequencies (stiffness) and damping ratios. Interestingly, as depicted in Fig. 20 and Fig. 22 thermal swelling causes the cell to soften and to become less damped, while intercalation-induced swelling causes the cell to harden and to become more damped. This is an interesting outcome, since both mechanisms cause the jelly rolls to swell inside the hard casing. This is an indication for the complex interdependencies of interfaces and boundary conditions, making the cell more than a simple sum of its components. This notion is further supported by the comparison of pouch cells and prismatic cells. While the temperature sensitivities of the natural frequencies for the pouch cells in

Fig. 19a and Fig. 20a are similar – softening for higher temperatures, Fig. 19b and Fig. 20b show contrary behavior for the damping ratios. As discussed in [110], this is assumed to happen due to the constraints through the casing and the respective interdependencies.

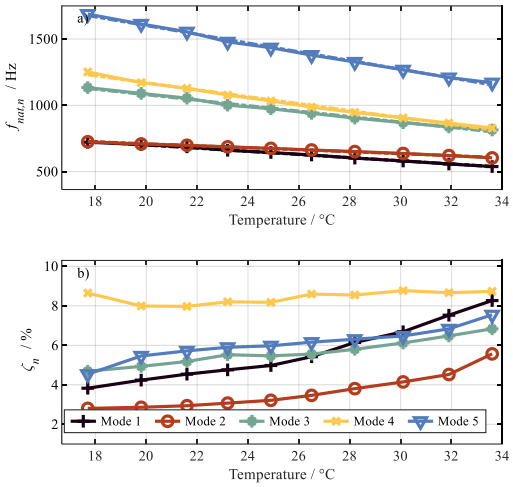

Fig. 19: Sensitivity of a) natural frequencies $f_{nat,n}$ and b) damping ratios ζ_n for each mode n of the lithium-ion pouch cells for varying temperatures [109]

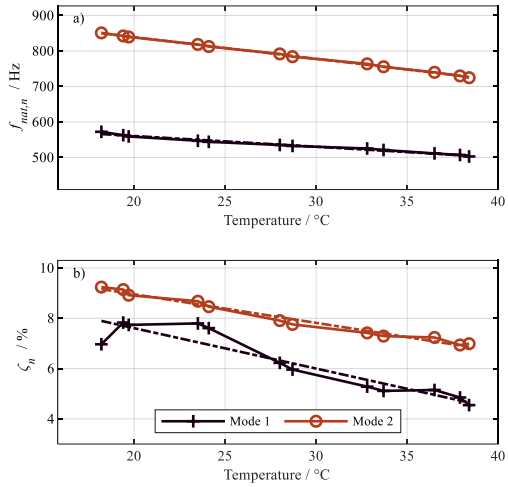

Fig. 20: Sensitivity of a) natural frequencies $f_{nat,n}$ and b) damping ratios ζ_n for each mode n of the lithium-ion large-format prismatic cells for varying temperatures [110]

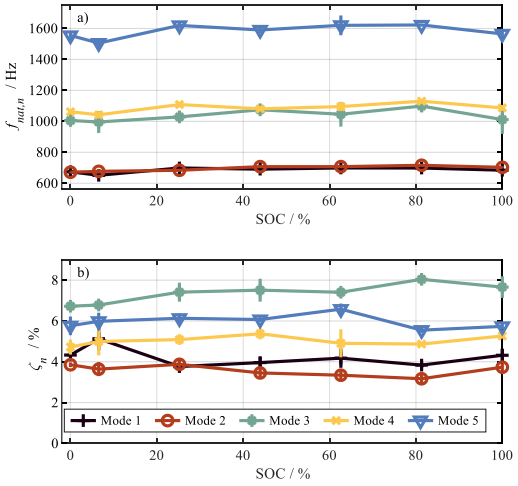

Fig. 21: Sensitivity of a) natural frequencies $f_{nat,n}$ and b) damping ratios ζ_n for each mode n of the lithium-ion pouch cells for varying SOC [109]

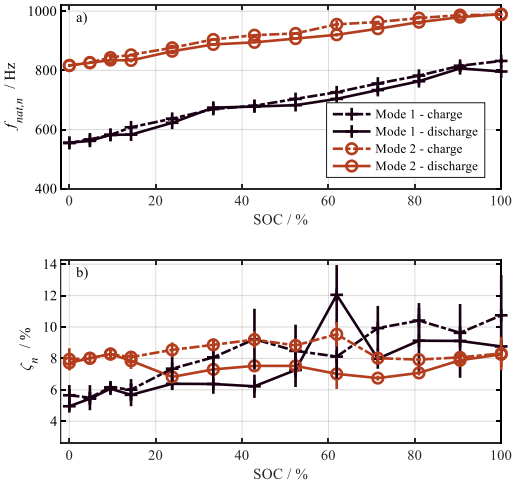

Fig. 22: Sensitivity of a) natural frequencies $f_{nat,n}$ and b) damping ratios ζ_n for each mode n of the lithium-ion large-format prismatic cells for varying SOC [110]

In the case of SOC variation, there is also a significant difference. While there is nearly no sensitivity in the case of the pouch cells for both natural frequencies and damping ratios in Fig. 21, the prismatic cell in Fig. 22 exhibits significant sensitivity with hysteresis behavior and a slope, like prior reported graphite swelling behavior. The deviating damping behavior of mode 1 in Fig. 20b for temperatures

below 24 °C and the missing hysteresis for SOC below 15% in Fig. 22 have been attributed to a possible gap between jelly roll and casing if both intercalation-induced swelling and thermal swelling are low.

Results with regard to the objectives

This chapter and the respective publication [110] delivered interesting insights into the effect of the inner cell design and the parameters SOC, SOH and temperature according to Objective 3 (influencing factors). Identified gaps between jelly rolls and casing might influence the vibration durability, addressing the topic of the inner cell design. In addition, the sensitivities revealed that a cold cell with a high SOC is both stiffer and more damped than a heated cell with a low SOC (e.g., at the beginning and end of an EV-ride in winter). This could have an impact on the failure mechanisms and their frequency of occurrence. This phenomenon pertains to Objective 1 (failure mechanisms) and Objective 2 (failure modes). Clarification if, or which, failure mechanism can occur is part of the Outlook in the next paragraph. It could not be included in this thesis in detail. Regarding Objective 5 (EMA potential), EMA is considered as a method with potential for the future, e.g., to parameterize FE models, to estimate elasticity of a cell in its entirety comprising all interfaces and boundaries or to be used as a method for diagnosis in the laboratory.

Outlook

EMA has a high sensitivity and can be valuable for future laboratory experiments. It might be used, for example, to detect gaps inside lithium-ion cells [110]. This possibility could be the motivation for more detailed investigations, e.g., if the structural response is sensitive to interesting and important effects such as lithium plating. Of course, the results for the prismatic cell can be also used for parameterization of an FE model in a similar manner as in Chapter 8 for the pouch cells from Chapter 6. Then the vibration durability of the investigated cell could be addressed with specialized experiments, e.g., to cause the jelly rolls to move inside the cell in a specific manner. Initial attempts at resonance excitation have been already performed and caused a cell casing failure, but further research is required here (see Appendix A.2).

Contributions

The conceptualization of the idea to use the EMA for mechanical characterization of lithium-ion cells was initiated, developed, and evaluated by the author of this thesis. He also formulated the overarching research goals and aims and defined the methodology. The author made the design of experiment and was responsible for the test bench design, conceptualization, construction, and validation as well as the funding acquisition and the project administration of the ReViSEDBatt project at the Institute for Electrical Energy Storage Technology. The author of this thesis was further responsible for analysis and validation of the results. The author of this thesis wrote the complete manuscript for this publication.

Jonas Soellner performed most of the experiments at the test bench and the subsequent MDOF fits according to the DOE by the author of this thesis. Furthermore, he visualized the data in the figures of this publication according to the ideas and instructions of the author of this thesis. Matthias Herrmann was responsible for the aging experiments. Andreas Jossen supervised the work, was

involved in the research conceptualization and in the discussion of the results. All co-authors did proofread of this publication.

Structural dynamics of lithium-ion cells – Part II: Investigation of large-format lithium-ion prismatic cells and method evaluation

Philipp Berg, Jonas Soellner, Matthias Herrmann, Andreas Jossen

Journal of Energy Storage 28 (2020) 101246

Permanent weblink: https://doi.org/10.1016/j.est.2020.101246

Journal of Energy Storage 28 (2020) 101246

Contents lists available at ScienceDirect

Journal of Energy Storage

journal homepage: www.elsevier.com/locate/est

Structural dynamics of lithium-ion cells—part II: Investigation of large-format prismatic cells and method evaluation

Philipp Berg[a,*], Jonas Soellner[a], Matthias Herrmann[b], Andreas Jossen[a]

[a] Technical University of Munich (TUM), Institute for Electrical Energy Storage Technology, Arcisstrasse 21, 80333 Munich, Germany
[b] Intilion GmbH, Dr.-Sinsteden-Strasse 8, 08056 Zwickau, Germany

ARTICLE INFO

Keywords:
Lithium-ion cell
Experimental modal analysis
Lithium-ion safety
Structural dynamics
Vibration durability
Aging

ABSTRACT

A recently introduced test bench for experimental modal analysis of lithium-ion cells is used to investigate the structural dynamics of large-format prismatic cells for battery electric vehicles. To our knowledge, it is the first experimental investigation of the structural dynamics of a single lithium-ion prismatic cell in literature. Significant differences in the sensitivity of the natural frequencies on the state of charge (SOC), compared with previous pouch cell investigations, can be observed, likely due to different boundary conditions through the cell casing. The natural frequencies follow the staged characteristic of anode swelling due to lithium-intercalation with an hysteresis behavior. Linear characteristic is seen in the temperature sensitivity, which is known from thermal swelling of the separator. Mode shape analysis indicates displacement of the jelly roll inside the new cells due to an initially present gap, while aged cells show significantly changed dynamics. Mode shapes and SOC sensitivity indicate a potentially stressful situation for the jelly rolls in the case of vibrational load, especially for new and unconstrained cells. The obtained natural frequencies and mode shapes can be used to design vibrational abuse experiments for maximum stress, so as to better understand if vibration can be harmful to lifetime and safety.

1. Introduction

Lithium-ion cells are one of the key components in the evolution of environmentally friendly and sustainable technologies to limit the emission of greenhouse gases [1], because the battery significantly influences performance, cost and safety of e.g. hybrid electric vehicles (HEV) or battery electric vehicles (BEV) [2]. Lithium-ion batteries are preferred due to their advantageous specific energy and energy density, low self-discharge, high energy efficiency and long lifetime [3]. Lithium-ion cells exist in three main shapes and kinds of casing: cylindrical hard-case cells (most of the 18,650 type and, recently, the new 21,700 type), pouch or coffee bag cells with a soft casing and prismatic hard-case cells [3,4].

Prismatic hard-case cells are used nowadays for example in HEVs (e.g. Ford Fusion Hybrid) [5] and in BEVs (e.g. BMW i3) [6]. Their advantages are the simple and dense packaging of the cells due to their prismatic shape and the lower number of cells and cell connections required, due to the higher cell capacity, thus reducing assembly effort [6]. At the same time, the jelly rolls of a prismatic cell are less constrained inside the cell case in contrast to cylindrical 18,650 cells [7,8]. This less rigid packing could pose a risk in the event of vibration if a critical relative displacement of inner components occurs. In the case of 18,650 cells, it is already proven that loose inner components, such as the inner mandrel in the middle of the jelly roll, can cause internal short circuits and the destruction of safety devices in the case of dynamic loading, e.g. vibrations or shock [9]. Although there are some publications available which examine the influence of vibrations on 18,650 cells [9–15] and pouch cells [9,16], there is no robust research regarding the influence of vibrations on safety and lifetime of prismatic cells.

In general, literature about the mechanical impact on lithium-ion prismatic cells is limited, as can be seen in the overviews given in two

Abbreviations: BEV, battery electric vehicle; CC, constant current; CC-CV, constant current-constant voltage; CV, constant voltage; DOF, degree of freedom; DPM, driving point measurement; EMA, experimental modal analysis; FEM, finite element model; FRF, frequency response functions; HEV, hybrid electric vehicle; IR, infrared; LSE, least square error; LSCF, least square complex frequency; MAC, modal assurance criterion; MDOF, multi degree of freedom; MIF, mode indicator function; MOV, modal overcomplexity value; NVH, noise vibration harshness; RMS, root mean square; SDOF, single degree of freedom; SNR, signal to noise ratio; SOC, state of charge; SOH, state of health; SUT, system under test; TM, transfer measurement

* Corresponding author:
E-mail address: philipp.berg@tum.de (P. Berg).

https://doi.org/10.1016/j.est.2020.101246
Received 6 November 2019; Received in revised form 25 January 2020; Accepted 25 January 2020

reviews [17,18], listing the fewest of all for prismatic cells in comparison with pouch and cylindrical cells. Oh et al. undertook pioneering research in the field of prismatic cells [5,19–22]. They reported their results regarding the swelling of a lithium-ion prismatic HEV cell with regard to C-rate dependence [5] as well as temperature and SOC [19], identified and compared two swelling mechanisms – lithium-ion intercalation-induced swelling and thermal swelling [5,20] - together with the respective swelling shapes [5,20] and thickness expansion [5]. Furthermore, they developed force and swelling models for prediction and health management [21,22] based on their previous findings.

One important parameter, related to swelling, is the stress generated inside the lithium-ion cell, since this stress can influence lifetime and performance [23–31]. The effects of stresses on electrodes have been investigated on the micro-scale inside electrodes [32,33]. Wu et al. investigated the stress in the separator due to intercalation, temperature and the mismatching of thermal expansion coefficients in a cell, and found that the effects are not a simple summation, but that boundaries play an important role [34]. Valentin et al. investigated the interface stress due to thermal swelling with a linear isotropic approach [35]. Stress-strain behavior and the failure of a wide range of different separators has been measured to investigate, for example, sensitivity to electrolyte wetting [36–39], temperature and strain rate [36,40,41], strain levels [42], the type of separator [43] and the effect of ceramic coating [38]. Shi et al. found the corners to be the area with highest stress levels in the separator [44]. Stress-strain relationship has been also measured for electrodes [42,45,46] and cell casing material [47]. A decreased fracture strength of lithium-ion cell components (foils and electrode coatings) for cycled cells was reported by Dai et al. [48]. The failure of lithium-ion cells due to indentation or mechanical abuse has been reported such as to identify the levels of force load, stress or strain, at which failure occurs, given a wide range of parameters [17,46,49–55]. Adams et al., used a nano-impactor to investigate the effect of dynamic impacts on lithium-ion cobalt oxide ($LiCoO_2$) cathodes with up to 1000 repetitions and reported, for example, accelerated capacity fading [56]. Chen et al. reported on the high-speed impact on lithium-ion cells and revealed a higher relevance of the cell design in comparison to quasi-static loading conditions [57]. Zhu et al. reported about the strengthening of battery cells under dynamic loading compared to quasi-static loading and found that the electrolyte increased the battery's mechanical resistance [58].

The presented literature above, which is only an excerpt as the complete extent of the literature on mechanical abuse and component characterization is far too numerous, shows that much research work has been undertaken to understand stress and strain inside lithium-ion cells under static, quasi-static and dynamic abuse conditions. There are also reviews available for the interested reader [17,18]. At the same time, there has been relatively little investigations into low stress and strain levels with a high number of repetitions, which can be caused, for example, by vibration during operation. This paper and the preceding part I [59] are intended to set the foundation for a detailed investigation of the stress which occurs during vibration. Stress is important since it is the cause of fatigue as a possible failure mechanism in the course of repetitive loading [60]. Since stress inside a lithium-ion battery is a quantity which is difficult to measure, especially under a free-free condition in vibration testing, finite element models must accompany the research. For the successful parameterization of these models, information about the structural dynamics of the lithium-ion cells is mandatory.

In order to obtain these parameters, the chosen method in this series of papers is the experimental modal analysis (EMA). Modal analysis is an important method to understand the extent and location of severe vibration stress [61]. The structural dynamics of a system under test (SUT) can be captured by means of natural frequencies (also called eigenfrequencies), damping ratios and characteristic mode shapes of each natural frequency of the SUT [62,63].

The knowledge about natural frequencies and damping ratios is required if a thorough understanding of vibration-caused stress and potential fatigue shall be established as they strongly depend on these parameters. Excitation at a natural frequency can in particular cause high levels of mechanical stress on the system under test. Mechanical failure can therefore sometimes be attributed to the excitation of the preferred motion of the system. [60,64]

The knowledge about the structural dynamics of the cell can be used to define new experiments, by applying periodic stress to reveal potential failure mechanisms, e.g. due to relative displacements with subsequent stress localizations and fatigue. The approach is comparable to a number of test procedures aimed at triggering a short circuit of lithium-ion cells on purpose, e.g. [65,66]. In addition, the sensitivities from load parameters (e.g. vibration amplitude), cell state parameters (e.g. state of charge (SOC) and state of health (SOH)), and ambiance parameters (e.g. temperature) are identified in order to reveal possible operational points with the higher risk level.

The structural parameters are also required to use common damage evaluation methods, such as fatigue damage spectrum (FDS) [60] and shock response spectrum (SRS) [64]. Additionally, the nonlinear effects and therefore the sensitivity to the excitation must be understood since nonlinear effects can significantly influence damage and fatigue [67]. It is hence useful to understand the structural dynamics, to also better understand the application and results of FDS and SRS for comparison of load profiles, as it has been done in [68,69].

The presented research aims to reveal possible failure mechanisms for different cell formats, in order to understand possible impact of vibrations on the safety and lifetime of lithium-ion cells. If specific failure mechanisms are revealed and - only at that point - the applicability of methods as SRS and FDS, damage accumulation models or test acceleration methods can be investigated for their usefulness and applicability in battery research.

To the authors' knowledge, no publication exists, which investigates single prismatic or, in general, hard-case cells without module constraints, using EMA. Volk et al. [70] used the EMA on prismatic cells in a pack configuration with a focus on the influence of SOC and SOH variation. No statistically significant influences of SOC and SOH were reported, structural variations due to manufacturing tolerances were reported to be more significant [70]. Finite-element-based modal analysis for prismatic cell packs was performed in [71] to investigate the influence of SOC, aging, cell-to-cell variation and design modifications of the pack, with the goal of an enhanced design and states identification. A similar approach for a lithium-ion pouch cell pack was performed in [72], considering pre-stress effects and cell-to-cell variations with respect to stress localization. Both approaches are purely simulative, and without experimental background. While in [70], no sensitivity to the SOC on pack level was found, a dependence of the elastic modulus from SOC has been included in [71]. Considering these discrepancies, there is a need for further investigation to increase knowledge about what really happens inside a lithium-ion cell during vibration and how this is influenced by boundaries, e.g. due to the module design.

Experimental investigations have been performed on single lithium-ion pouch cells by experimental modal analysis in several publications [59,73–76] with significant differences in the measurement setups [59].

In this work, we investigate for the first time the structural dynamics of 94 Ah large format prismatic lithium-ion cells under free-free condition and linear excitation, investigate the sensitivities to SOC, temperature and aging history and conditions, and show the characteristic mode shapes of both new and aged cells. All results are compared to the findings for lithium-ion pouch cells [59], so as to understand the impact of cell packaging and respective constraints. Finally, the possible implications with regard to safety and lifetime, as well as with regard to vibration testing, are given. Since this paper is part II of the series about the structural dynamics of lithium-ion cells, this paper contains a critical evaluation of the potentials and limitations

of EMA for lithium-ion battery research. The main novelties of this work are therefore: The first in-depth analysis of large-format prismatic cells regarding structural dynamics; the comparison of different cell formats to each other, which could be tested with an identical setup and procedure because of the novel test bench and the critical discussion of the future usefulness for EMA in lithium-ion cell research. It is further novel, that swelling effects such as intercalation induced anode-swelling and thermally induced separator swelling can be investigated from a new perspective in terms of natural frequencies and damping ratios.

2. Experimental

This section includes an introduction to:

- the EMA, the modal assurance criterion (MAC) and the modal overcomplexity value (MOV), in Section 2.1
- the test bench, in Section 2.2
- the cells which serve as SUT and their current capacity and aging history, in Section 2.3
- the measurement procedure, in Section 2.4
- the SOC adjustment procedure, in Section 2.5 and
- the mathematical background for linearity investigation, in Section 2.6

The topics of EMA, test bench and mathematical background, have already been covered in more detail in [59].

2.1. Experimental modal analysis (EMA) and modal assurance criterion (MAC)

The modal analysis gives information about natural frequencies, damping ratios and the respective mode shapes for each resonance mode. Therefore, the so-called frequency response function (FRF) according to Eq. (1) is measured. There are several representations for the FRF, depending on whether displacement, velocity or acceleration are the measured response to the force excitation $F(\omega)$ [61,63]. Natural frequencies and damping ratios can be calculated from one single measurement of the FRF, if both excitation and response are not located on a nodal point (motionless) for the respective resonance [62,77].

To get the characteristic mode shapes for each natural frequency or resonance, the FRF has to be measured at different locations and orientations on the structure. The mode shapes are typical patterns of deformation, which occur if the SUT is excited at the respective natural frequency. Roving excitation or roving response can be used. Each measured position, in combination with the orientation, represents a degree of freedom (DOF). If the DOF for both force and acceleration are the same, it is a driving point measurement (DPM), while cross measurements of different DOF are transfer measurements (TM). [61,62]

The possible types of obtained FRF are: receptance for displacement response; mobility for velocity response; and accelerance or inertance for acceleration response [78]. While accelerance is used in this work, and is common for measurements [77], most basic literature uses receptance for the theory. In addition, through integration or differentiation, each version of the FRF can be calculated. If the FRF in terms of receptance is measured or calculated at several locations, the receptance matrix is gained. One element of this matrix $\alpha(\omega)$ is defined according to Eq. (1) [61,62].

$$\alpha_{jk}(\omega) = \frac{x_j}{F_k} = \sum_{r=1}^{N} \frac{\phi_j^n \times \phi_k^n}{{\lambda_n}^2 - \omega^2} \tag{1}$$

Where:

- λ_n is the complex eigenvalue or modal frequency of the n^{th} mode (in basic literature about EMA r is often used instead of n, but since we used n in the first part of the paper, n is also used throughout this publication).
- ϕ^n is the normalized mode shape vector of the n^{th} mode (equal to the n^{th} column in the modal matrix [Φ]).
- j and k are points on the structure, with F_k being the force acting at location k, and x_j being the relative displacement response measured at location j, therefore representing a DOF,
- N is the number of modes.
- and ω is the circular frequency.

Mode shapes are dimensionless and arbitrarily scaled if not normalized. The modal assurance criterion (MAC) is a mathematical method to compare mode shapes with each other, e.g. if the EMA has been performed with two different measurement techniques, such as shaker testing and impact testing, or if experimental results and the results of a finite element simulation are to be compared. The MAC value is always in a range from 0–100%. A value of 0% indicates no correlation of the two mode shapes, while 100% indicates perfect correlation of the two mode shapes. [62]

Eq. (2) gives the mathematical formula to calculate the MAC value for the two mode shapes or modal vectors $\{\phi_a\}$ and $\{\phi_b\}$ with n being the number of elements in the modal vector. These are called modal coefficients. The number of modal coefficients is equal to the number of measured responses. [78,79]

$$\mathrm{MAC}(\{\phi_a\}, \{\phi_b\}) = \frac{|\{\phi_a\}^*\{\phi_b\}|^2}{(\{\phi_a\}^*\{\phi_a\}) \times (\{\phi_b\}^*\{\phi_b\})} \tag{2}$$

In this work, the MAC is used to compare the different cells and therefore, to have a mathematical quantity in order to be able to investigate the influence of aging on the cells under test and their structural dynamics. This is done, because it is expected that the swelling of the jelly rolls due to aging with a higher internal pressure inside the cell can cause higher constraints with changed shapes of the modes. The shapes can for example change, such that less relative displacements near to the edges compared to the center of the cell occurs. The MAC value can give a quantitative criterion of these changes, since only optical investigation of the shape might lack of objectivity.

The mode overcomplexity value (MOV) is based on the theory that an added mass causes the natural frequency to decrease. Therefore, for each measured node or DOF, a value is calculated, which is set to 0 if the natural frequency increases due to the addition of a virtual mass, while it is set to 1 if the frequency decreases or stays constant. The sum of all these values weighted with the magnitude of the mode shape is the MOV. A high value close to 100% indicates a physical mode, while a low value indicates noise or computational nodes. [79]

2.2. Test bench and measurement setup

The test bench was introduced and validated in our preceding work [59] and is depicted with the setup for this part of the work in Fig. 1. The most important components are the TIRA S51140 force exciter (TIRA GmbH, Germany) with maximum force F_{max} = 400 N, the amplifier BAA 1000 (TIRA GmbH, Germany), the $m + p$ vibPilot eight-channel controller ($m + p$ international, Germany) for data acquisition and control and a Bio-Logic VSP-300 (Bio-Logic Science Instruments, France) with EIS module, 10 A booster and the software EC-Lab. The shaker is incorporated into a safety chamber with webcam monitoring, temperature regulation, gas detection and safety-relief valve. Temperatures and cell voltages can be monitored using a PXI system from NI (National Instruments, USA). In addition, an infrared (IR) sensor optris CS (Optris GmbH, Germany) enables contactless temperature measurements.

The software $m + p$ Analyzer 5.1 ($m + p$ international, Germany) is used for the measurement and post-processing of the EMA. LabView by NI (National Instruments, USA) is used for the control of the PXI system.

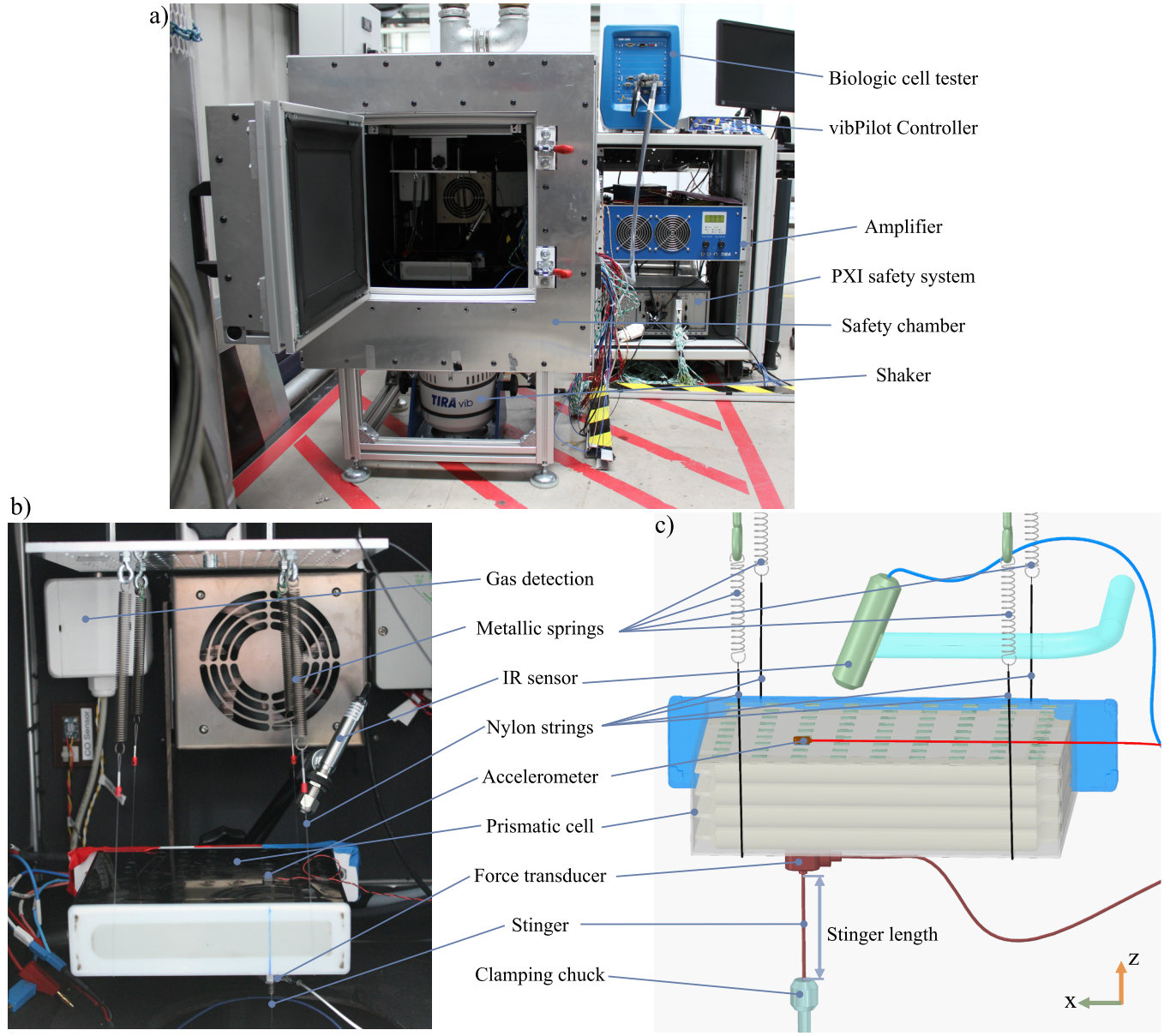

Fig. 1. Depictions of the test bench and measurement setup with labeling of the most important parts, (a) safety chamber with shaker and measurement setup, (b) measurement setup inside the safety chamber with the cell as SUT supported with springs and nylon strings in free-free-condition, (c) same as in b as a schematic for an easier and quicker view.

The same force transducer and accelerometer as in [59] are selected due to their low influence on the measurement, thanks to their small size and weight, and their flexible cable connections. The force transducer used, is the Kistler 9712B5 (Kistler Group, Switzerland) weighing 19 grams with a measurement range of ± 22 N and a sensitivity of 180 mV/N at room temperature (−0.009%/K temperature dependence). The accelerometer is a PCB 352A73 sensor (PCB Piezotronics Inc., USA) at only 0.3 grams with a measurement range of ± 1000 g and a sensitivity of 5 mV/g (−0.1125%/K approximated temperature dependence [59]). Petro wax 080A109 (PCB Piezotronics Inc., USA) is used for the sensor attachment.

A possible shaker-stinger-structure interaction is minimized by the usage of the same stinger with a diameter of 1.5 mm and adjustable length as in [59]. 50 mm has proven to be a good choice for the investigation of the prismatic cell, too. In terms of support for the SUT, four linear elastic springs made of high strength cold drawn spring steel with the following parameters are used:

- wire diameter d_{wire} of 0.7 mm
- length l_{spring} of 60 mm
- suspension rate k_{spring} of 0.093 N/mm
- preload F_{init} of 1.08 N
- maximum displacement s_{max} of 80 mm
- maximum load F_{max} of 8.53 N

The static displacement s_0 can be calculated according to Eq. (3)

$$s_0 = \left(\frac{m_{SUT}}{n_{springs}} \times 9.81\text{ms}^{-2} - F_{init} \right) \times k_{spring} \tag{3}$$

Hereby m_{SUT} is the mass of the cell and $n_{springs}$ is the number of springs used for support.

Two nylon threads are connected with two springs each and the SUT is bedded on the nylon threads. For the SUT in this work with m_{SUT} = 2.1 kg, the load per spring is 5.15 N (60.4% utilization capacity), and the static displacement s_0 is 43.71 mm (54.6% of s_{max}).

Table 1
Parameters of the prismatic cell which serves as the SUT.

Chemistry	Graphite/NMC
Number of jelly rolls	4
Nom. capacity C_{nom} /Ah	94
Cell length l_{cell}/mm	174
Cell height $h_{cellw\backslash oT}$/mm	126 (without terminals)
Cell height $h_{cellw\backslash T}$/mm	133 (with terminals)
Cell thickness t_{cell}/mm	45
Mass m_{cell} /kg	Approx. 2.1
Charge cut-off U_{max}/V	4.15
Discharge cut-off U_{min}/V	2.7

Therefore, sufficient reserve for displacement in terms of both tension and compression, is provided.

By this setup, the cell is suspended as free as possible, because of the thin stinger and the soft and linear springs. The thing stinger ensures good force transmission to the SUT and at the same time allows free perpendicular movement. The soft springs decouple the SUT as good as possible from gravimetric influences while being linear at all time and as soft as possible.

2.3. Cell samples under test

Four prismatic cells, designed for application in BEVs, are tested in this work. Table 1 gives information about the cell. A schematic of the cell is depicted in Fig. 2. The casing of the cell is covered with a thin polyethylene terephthalate (PET) layer as standard to protect against external short circuits. Additionally, a 3D-printed connector unit is placed on top of the cell, to enable easy linkage of the cell with a four-wire measurement system.

Two of the cells are new and electrically uncycled, while the other two cells have been aged through electrical cycling, using 1C charge and 2C discharge, prior to the investigations in this paper. One of them has been electrically cycled under unconstrained conditions, while the other one has been electrically cycled under constrained conditions. The constraints during electrical cycling have been achieved with two form-fit metal plates with an undefined pressure at the beginning of the electrical cycling. The pressure then has risen during the electrical cycling due to the respective swelling with possible effects on, for example, lifetime of the lithium-ion cells [23,29]. Information regarding the history of the four cells is given in Table 2. During EMA and the final capacity check-up prior to the EMA, all cells were unconstrained, meaning that the only constraints are posed by the cell housing itself.

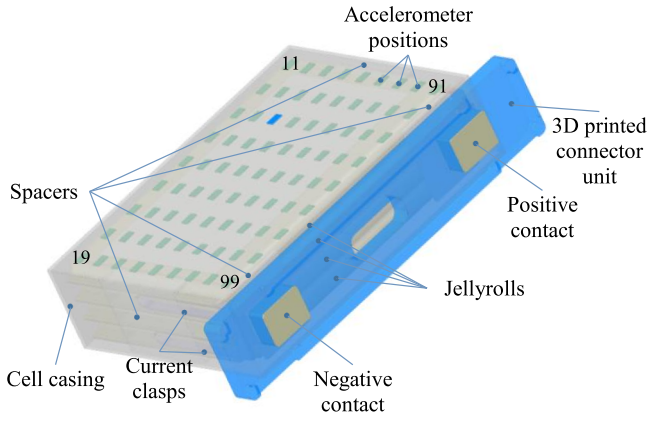

Fig. 2. Schematic of the prismatic cell, is shown. The cell casing is illustrated such that is somewhat transparent in order to show the internal construction, with four jelly rolls, current clasps and four spacers. The 9 × 9 DOF matrix chosen for mode shape investigation is depicted on the surface of the cell with the respective accelerometer positions; the DOF of the main driving point *p33(z)* is highlighted in blue. On top of the cell, an additional 3D printed connector unit is attached for simple electrical connectivity.

Table 2
Information regarding the electric cycling history and current state of the four cells under test. In the case of the aged cells, the boundary conditions describe only the state during electric cycling prior to the application of EMA.

Cell ID	CN1	CN2	CA1	CA2
State	New	New	Aged	Aged
Actual C/20 capacity C_{20}/Ah	98.3	98.1	77.1	69.6
$SOH_{C20} = C_{20}/C_{nom}$ /%	104.6	104.4	82.0	74.0
Aging protocol (Charge/discharge rates)	none	none	1C/2C	1C/2C
Electric cycles	none	none	7250	7500
Boundary conditions during electric cyclic aging	–	–	constrained	unconstrained

2.4. Measurement procedure and parameters

The authors of this publication validated and optimized the proposed test bench in preceding work [59]. Therefore, the adjustment of the parameters is only covered in a brief manner here.

To capture the mode shapes of the prismatic cells, 9 × 9 equally distributed DOFs (81 in total) are measured on the cells surface by a roving accelerometer. The 81 DOFs are marked as accelerometer positions in Fig. 2. All DOFs are in through-plane direction (z). One single excitation at *p33(z)* has shown to be a good choice for the new cells under test in this paper (highlighted in Fig. 2). For the aged cells, *p33(z)* has been less suitable, since mode 1 changes its shape because of the aging process, which is further discussed in Section 3.5. For this reason, all three cells in Section 3.5 have been also measured at DOF *p55(z)* for the analysis of aging. The preceding sections are based on measurements with an excitation at *p33(z)* solely.

The mode shape comparison, using MAC, is performed using 9 × 9 FRF matrices, with the exception of the MAC analysis for the two new cells. The latter is based on 5 × 5 FRF matrices, since these were available and are sufficient to show the similarity of the cells CN1 and CN2. For this, only measurements corresponding to the rows and columns 1,3,5,7 and 9 of the measurement matrix in Fig. 2 were recorded. One new cell is also measured using the 9 × 9 DOF matrix, for the sake of comparison with the aged cells. The sensitivity studies, regarding the variation of excitation force, SOC and temperature in the Sections 3.2, 3.3 and 3.4 use a single DPM at *p33(z)*.

The cells under test in this work have shown significant damping ratios and high modal density, which means that many natural frequencies occur within a small frequency range [62,80]. Therefore, a multi-degree of freedom (MDOF) fit with residual terms to account for modes outside the region of interest is used. Burst random excitation with a burst rate of 90% is used for linear approximation [67,81] of the nonlinear dynamics and to avoid leakage effects [62]. Both excitation and fitting procedure are therefore identical to part I [59].

The FRF of a damped system is always a complex function and must be estimated [62]. The H1 estimator [62] is in use in this work and 50 or 25 (for the mode shapes analysis) measurements are averaged to achieve sufficient signal to noise ratio (SNR). The frequency range for the measurement is 20–6500 Hz with a block size of 32,768 samples, a sample rate of 16,384 Hz and a frequency spacing of Δf_{line} = 0.5 Hz. For the investigation of the sensitivity to SOC and aging history, the EMA is performed three times for each operation point and respective SOC level. This accounts for possible reproducibility limitations due to the required remounting at SOC adjustment or change of the cells.

2.5. SOC adjustment

To check the sensitivity of the structural dynamics on SOC, one of the new cells (CN2) is charged to 100% SOC with constant current (CC) I_{charge} of 9.4 A (C-rate 1/10 C_{nom}) and subsequent constant voltage (CV) phase of 4.15 V with charge termination at a minimum C-rate of C/20 C_{nom}. In the following, CC discharge with $|I_{discharge}|$ of 9.4 A (C-rate 1/10 C_{nom}) and sequential ampere-hour counting is used to adjust the desired SOC steps (5% or 10% of C_{nom}). After draining 100% of C_{nom} the cell is fully discharged with CC–CV (CC discharge with $|I_{discharge}|$ of 9.4 A, CV at 2.7 V with the termination criterion of $|I_{discharge}| < C/50$).

After the full stepwise discharge, the cell is charged again with a CC current I_{charge} of 9.4 A and ampere-hour counting, to measure the hysteresis behavior. The previously discharged ampere-hour steps are charged backwards to achieve identical SOC levels in both charge and discharge directions for each measurement point.

After each step, the cell is allowed to relax for at least 30 min and until the voltage relaxation is at least less than 1 mV/min, before the EMA is performed. The SOC levels given for analysis in this work are calculated afterwards with respect to the actual measured capacity for all steps of discharge.

2.6. Half-power bandwidth calculations

If the SUT shows nonlinear dynamics, the homogeneity of the FRF is distorted. This means that the FRFs are different for different excitation levels, while for a perfectly linear system all FRFs shall be exactly the same, no matter the level of excitation [67]. In order to check the homogeneity of the obtained FRFs for varied excitation forces in detail, the half-power bandwidth method [61] was adopted in [59] to calculate the respective share of excitation force for each resonance mode. The relevant RMS value of the force is calculated in the range according to Eqs. (4) and (5) with natural frequencies $f_{nat,n}$ and damping ratios ζ_n for each mode n according to the procedure described in [59].

$$[f_{a,n},\ f_{b,n}] = \left[f_n - \frac{\Delta f_{-3dB,n}}{2},\ f_n + \frac{\Delta f_{-3dB,n}}{2} \right] \tag{4}$$

$$\Delta f_{-3dB,n} = 2\zeta_n f_{nat,n} \tag{5}$$

3. Results and discussion

Table 3 provides an overview of all investigations in this paper.

3.1. Natural frequencies and mode shapes

The measurement of the mode shapes with 81 DOFs in the through-plane direction and excitation at *p33(z)*, according to Fig. 2, revealed two clearly identifiable mode shapes on the upper surface of one of the new cells. Mode shapes are also obtained for the aged cells, but this is dealt with in Section 3.5, where the sensitivity of the cell's structural dynamics to aging and the respective aging conditions are investigated. The two obtained mode shapes for the new cell are depicted in Fig. 3b, next to the DPM-FRF, and the natural frequencies in Fig. 3a.

Table 3
Overview of the investigations performed in this work and the chosen parameter settings (* Excitation level is a software value; resulting force level is calculated afterwards).

Purpose/Sensitivity	Cells	Excitation*	SOC /%	Temp. / °C	Section
Mode shapes	*1 new*	0.01	0	25	3.1
Excitation level	*1 new*	0.01–0.1	0	25	3.2
SOC	*1 new*	0.01	0–100	25	3.3
Temperature	*1 new*	0.01	0	17–38	3.4
Aging and aging conditions	*2 new / 2 aged*	0.01 (new) 0.04 (aged)	0	25	3.5

A mode shape analysis covering all surfaces of the cell delivered no beneficial information, because the main displacement occurs at the biggest surface of the cell first. To measure the first natural frequencies and the respective mode shapes, the big surface is the relevant one. The alternating order of resonances (peaks) and anti-resonances (valleys) in Fig. 3b indicates DPM and therefore the validity of this approach. If higher order modes than in this paper, were to be investigated, then a more complete geometric model of the cell would be beneficial, of course. However, the investigations in this work revealed already that higher-order modes overlap significantly due to high damping ratios and especially due to a high modal density. The mode indicator function (MIF) could not reliably indicate further modes. A system with distinct modes and light damping shows sharp drops in the MIF, while the MIF for the investigated cells gets blurred for higher frequencies. Additionally a poor SNR at higher frequencies makes a reliable mode estimation impossible in that frequency range. Therefore, in this paper, additional modes are neglected for the mode shape analysis of the new cells.

The first resonance mode shape in Fig. 3 is very similar in its shape to the swelling shape reported by Oh et al. [20,22]. The significant movement, therefore, occurs in the area of the jelly roll and may show a displacement of the jelly roll at this resonance. An interesting observation, which can be best seen in the videos of the supplementary material, is that the maximum displacement is higher on the bottom side of the cell, compared to the top of the cell. This could be caused by the connection of the jelly roll with the poles on the cover of the cell and a higher resulting stiffness.

The second mode shape has bi-directional phases for the two halves of the cell, forming two “valleys”. The movement of the jelly rolls in the case of resonance excitation may pose a possible risk for safety and lifetime of the prismatic cells, if the displacement of the jelly roll package causes a high stress level, e.g. at the welding joints of the jelly rolls with the current clasps. According to literature, it is also recommended to avoid mode shapes that are similar to deformation patterns caused by static loading conditions [61]. This makes the first mode shape of the prismatic cell especially interesting, as it has a similar deformation pattern to the quasi-static loadings due to lithium-intercalation [22] and thermal swelling [19,20]. To determine if a possible risk exists, further investigations based on finite element calculations and load experiments with resonance excitation are required. A more detailed investigation of the mode shapes is given in Section 3.5, discussing both new and aged cells. The mode shapes are introduced here, since these two modes are used for the sensitivity to excitation force, SOC and temperature in the next two sections.

3.2. Investigation of potential nonlinearities

Previous investigations of lithium-ion pouch cells [59] showed significant nonlinear effects with regard to stiffness, reflected in natural frequency values, and damping ratios. Nonlinear cubic softening and nonlinear quadratic damping were identified for different modes according to the types of damping defined in [67].

Nonlinear structural dynamics are very important with respect to damage and fatigue [60,67] because the severity of vibration or shock depends on natural frequencies, and on the quality factor or damping [60,64]. Both parameters can change significantly depending on the excitation level, in the case of nonlinear behavior.

The excitation has been increased stepwise using the smallest available step size in the Analyzer Software. The respective relevant share of excitation force for each resonance mode is then calculated according to the procedure explained in Section 2.6 since only force excitation in the frequency region of interest is of relevance. The MDOF fitting procedure is used to extract natural frequencies and damping ratios.

Fig. 4 depicts the obtained results for natural frequencies $f_{nat,n}$ and

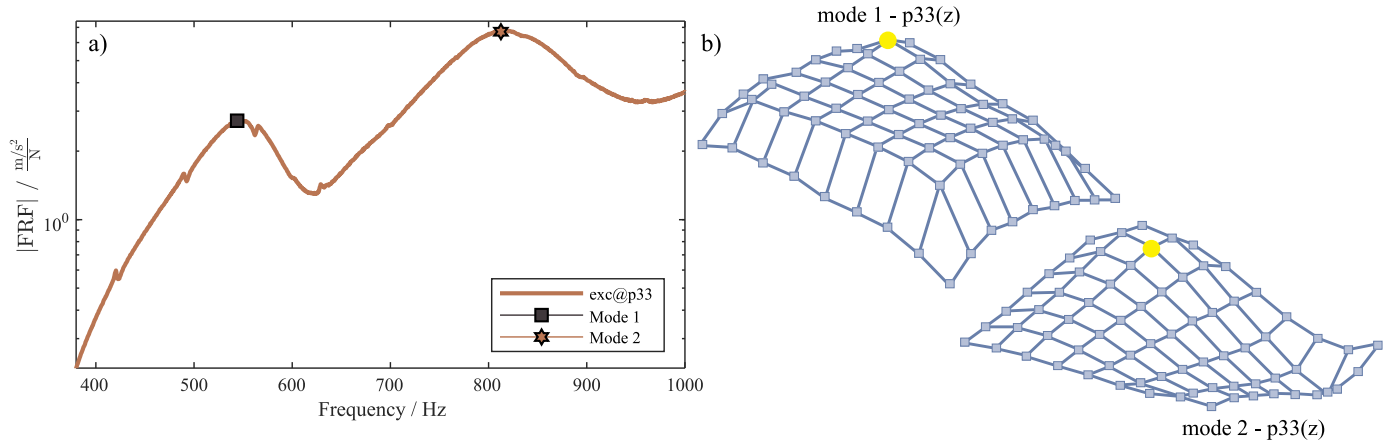

Fig. 3. (a) Exemplary FRF magnitude from DPM with respective natural frequencies $f_{nat,n}$ and (b) the two identified mode shapes of the upper surface measured on one of the two new cells. Animated videos of the mode shapes are available as supplementary material.

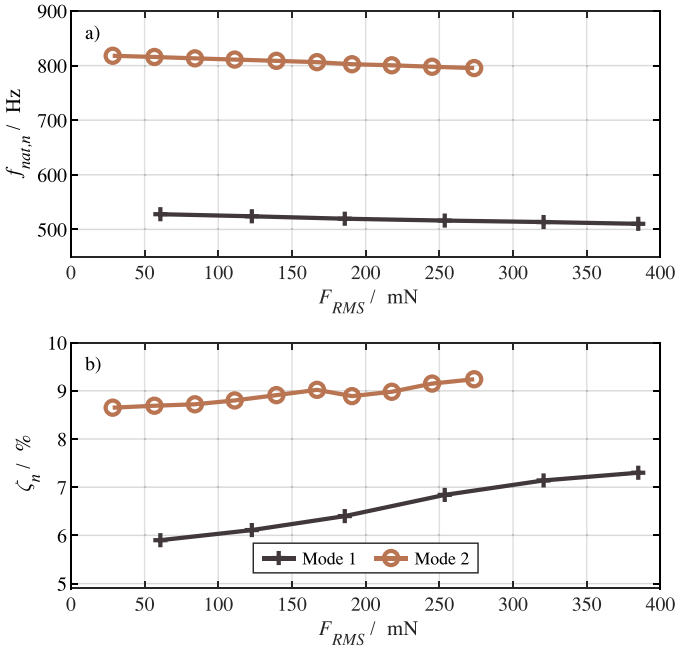

Fig. 4. Variation of excitation force and the effect on the results of the MDOF fit in terms of (a) natural frequencies $f_{nat,n}$ and (b) damping ratios ζ_n for the two modes $n = 1$ and $n = 2$. Only fits with an LSE $< 5\%$ in the respective frequency range according to Eq. (4) are depicted.

damping ratios ζ_n for the two modes 1 and 2 of the cell CN2. CN1 showed similar results and is therefore of little further interest. It is obvious that for mode 2, fewer values are plotted. This is because only fit results with a least-square error (LSE) $< 5\%$ in the region of interest according to Eq. (4) are considered. In the case of mode 1, the fit delivered degraded results more quickly than for mode 2. This is an indication that mode 1 has a stronger nonlinear characteristic than mode 2.

The positive outcome of this investigation is that the low excitation levels do not significantly show nonlinear effects, which means that reliable linear measurements can be made at low excitation levels. Since excitation with a level of 0.01 caused the lowest overall LSE (e.g., 1.00% for CN1 and 0.84% for CN2), this level has been chosen for the new cells in the upcoming investigations. The LSE values for the fittings are further given in the Appendix in Table A.1.

The natural frequencies $f_{nat,n}$ in Fig. 4a are only slightly influenced by the excitation level in the given frequency range. The damping ratios ζ_n also have much lower sensitivity to the excitation level, compared to the observations for pouch cells. For example, for the small pouch cells, the increase in damping for mode 2 was nearly threefold in the investigated range. [59]

It must be said that a direct comparison is difficult, due to the very different masses of the two cells (43 grams for the pouch cells [59] and approx. 2100 grams for the prismatic cells in this work). The maximum achieved RMS force level with the current transducer setup is only approximately 10 times higher for the prismatic cell, while the cell weight is approximately 50 times higher. Therefore, a force transducer with a higher measurement range would be required, but since the MDOF already showed a degraded LSE, this has not been included in this work.

3.3. Influence of SOC

One of the two new cells (CN2) was investigated for its sensitivity to the SOC according to the procedure described in Section 2.5. Fig. 5 depicts the results of the MDOF fit for both natural frequencies $f_{nat,n}$ and damping ratios ζ_n of the two first modes in the case of SOC variation for the new cell CN2. Three measurements were taken at each

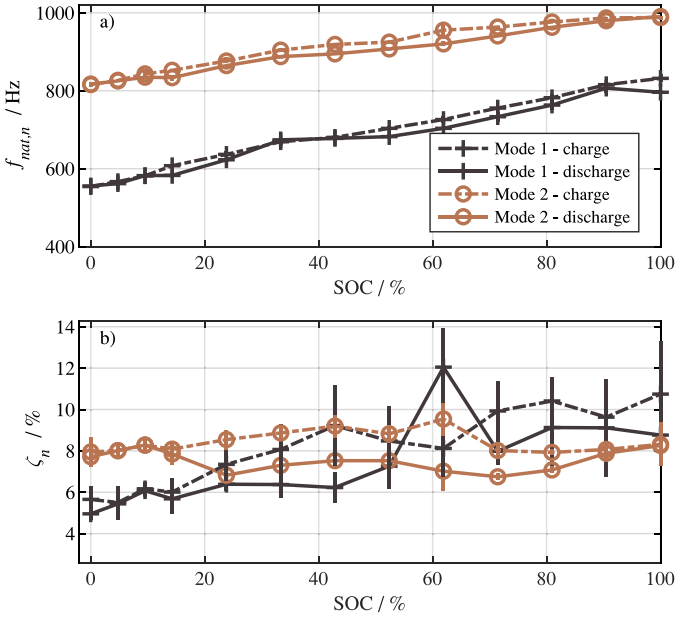

Fig. 5. Variation of SOC and the effect on (a) natural frequencies $f_{nat,n}$ and (b) damping ratios ζ_n, both showing hysteresis behavior with charge curves above discharge curves.

measurement point, with a reassembly of the test setup prior to each measurement, in order to account for measurement uncertainties. The markers represent the mean value from each measurement triplet for each measurement point. The spreads due to reproducibility limitations are included with bars, stretching from the minimum to the maximum measured value of the three repetitions.

Natural frequencies can be measured in a very reproducible manner with low spreads. The spread is defined as the absolute difference between the maximum measured value and the minimum measured value in each triplet for both natural frequencies and damping ratios according to Eqs. (6) and (7).

$$\Delta f_n = \max(f_{nat,n,1}, f_{nat,n,2}, f_{nat,n,3}) - \min(f_{nat,n,1}, f_{nat,n,2}, f_{nat,n,3}) \quad (6)$$

$$\Delta \zeta_n = \max(\zeta_{n,1}, \zeta_{n,2}, \zeta_{n,3}) - \min(\zeta_{n,1}, \zeta_{n,2}, \zeta_{n,3}) \quad (7)$$

The mean value of all natural frequency spreads Δf_n for all measurement triplets is 4.8 Hz for mode 1 and 3.1 Hz for mode 2. The damping ratio shows mean spreads $\Delta \zeta_n$ of 1 percentage point for mode 1 and 0.4 percentage points for mode 2. The maximum spread is 2.6 percentage points and 1.1 percentage points respectively. The quantitative spreads are also depicted in detail in the appendix in Table A.2.

One visible main characteristic of SOC sensitivity is that both natural frequencies and damping ratios show hysteresis behavior for charge and discharge. Aside from one outlier for the damping ratio at 60% SOC and the low SOC range at SOC < 15%, the values obtained during discharge are lower than the values during ~~the~~ charge. This applies for both natural frequencies and damping ratios. In the range of SOC lower than 15%, the hysteresis is negligible.

During charge, the graphite anode is lithiated, while during discharge the graphite anode is subject to delithiation. Hysteresis behavior for the thickness change of graphite anodes due to lithium-intercalation and -deintercalation has been reported before using dilatometry measurements. The thickness during lithiation was below the thickness during delithiation. [82]

One possible explanation for the non-existent hysteresis for low SOC, is that the jelly rolls in such a new cell (less than 3 charge-discharge cycles) have enough space for volume expansion inside the casing, up to 15% SOC from where it might then reach the inner surface of the housing.

Rieger et al. reported a reversible thickness change of 7% for the graphite anode and an overall thickness change of 2.4% of the pouch cell including all components during a full discharge. The pouch cell had a thickness of 6.5 mm. Statistical analysis of the 1D through-plane displacement fields revealed a 1D displacement of 120 µm when the pouch cell was charged from 0–79% SOC. They also reported a mean displacement of approx. 32 µm for one pouch cell, obtained using laser scanning, for an SOC of 17%, which is close to the above mentioned 15% SOC, at which the jelly rolls might fill the gap between the jelly rolls and the cell housing. [82]

Given a thickness of 45 mm of the cells in this work, minus two times an approximated wall thickness of 1 mm for the casing the thickness change $\Delta t_{jellyrolls,int}$ of the prismatic cell from 0–15% SOC, can be therefore roughly approximated according to Eq. (8).

$$\Delta t_{jellyrolls,int} = \frac{(45 - 2)\ \text{mm}}{6.5\ \text{mm}} \times 0.032\ \text{mm} = 0.212\ \text{mm} \quad (8)$$

According to this rough estimation, the fully discharged new cell has an approximated initial total gap of around 212 µm. This is further cross-checked with the temperature sensitivity in the next section.

The natural frequencies increase for both modes for higher SOCs. In the case of mode 1, the natural frequency $f_{nat,1}$ is decreased by 241 Hz for full discharge and increased by 278 Hz for charge from 0–100% SOC. The difference at 100% SOC at the beginning and the end of the test can be existent due to a settling behavior of the cell and its components. During initial SOC adjustment and storage, the cell was standing upright, while during the EMA the cell was lying horizontally. The discharge value for mode 1 at 100% SOC could therefore differ a little and the value from charge is more reliable. For mode 2, the total change due to discharge and charge are 174 Hz and 172 Hz respectively.

The gap between the two modes hence becomes smaller when the SOC is increased during charge. The difference between the first and second natural frequency is 262 Hz at 0% SOC and 156 Hz at 100% SOC. For both modes, the slope of the natural frequencies can be subdivided into three areas: one in the range of approx. 0–35% SOC; one in the range of 35–55% SOC; and the third one in the range of 55–100% SOC. The same characteristic slope, in a qualitative manner, with similar SOC ranges has been reported for the intercalation-induced swelling of lithium-ion cells with graphite anodes [19] and for the graphite anode itself [82]. The characteristic slopes have been attributed to the phase transitions of the graphite anode [19]. Therefore, the structural dynamics of the investigated prismatic cell is strongly determined by the intercalation-induced swelling and the respective change in the elasticity of the graphite anode, and shows high sensitivity to the SOC.

This is in contrast to the observations for pouch cells, performed on the same test bench. The structural dynamics of the investigated pouch cells did not show identifiable sensitivity to the SOC. [59]. Since both cells contain graphite anodes, it is thus shown that the behavior of one component as the anode cannot be treated in an isolated manner.

A lithium-ion cell is not only the simple sum of its elastic components and their elasticity parameters, but ~~that~~ the overall structural dynamics is strongly influenced by the structural interfaces and the boundary conditions, e.g. when comparing a soft pouch cell vs. a rigid aluminum case and the respective differences in stress and strain. Therefore, experiments to measure the elastic properties of single components must be performed, evaluated and applied with care. The electrochemically active materials cause the structural dynamics to change, but in conjunction with the somehow rigid casing.

With regard to the damping ratio, increased hysteresis in the medium SOC range can be seen, in contrast to SOCs below 15% and higher than 90%. Both stiffness and damping ratios therefore show the most pronounced hysteresis for similar SOC values. Mode 1 shows an increased damping ratio due to the intercalation and the subsequent swelling with what is probably an increased quasi-static stress level inside the hard case for higher SOC. Mode 2 has comparable damping for both fully charged (100% SOC) and fully discharged (0% SOC) states.

The different sensitivities of the damping ratios of both modes to SOC can occur due to different damping effects. While for mode 1 all jelly rolls move in phase towards the casing, in the case of mode 2 a torsional behavior of the jelly roll occurs. This can cause different normal and shear stresses with other damping effects coming into play, e.g. more friction between jelly roll and casing in the case of mode 1 and higher layer-to-layer friction in the case of mode 2. It is interesting to perform the same measurement for the pouch cells from [59] too, in order to see if the damping ratio hysteresis is related to the interdependency with the casing or not.

The high sensitivity of both natural frequencies and damping ratio to the SOC as well as the current direction (charge or discharge) can have an impact on the vibration testing of prismatic cells. Testing at different SOCs is recommended. A lower SOC is expected to be more critical for mode 1 with respect to mechanical stability, because the damping ratio for the first mode is reduced, which is likely due to the smaller volume of the jelly roll in its discharged condition. The lower damping ratio is similar to a higher Q-factor, which is usually more critical with respect to fatigue [60]. In addition, the reduced stiffness for lower SOCs with lower natural frequencies make critical resonance excitation in the automotive application more likely, since the power spectral density of automotive vibrations is higher for lower frequencies than for higher frequencies in most cases [83,84].

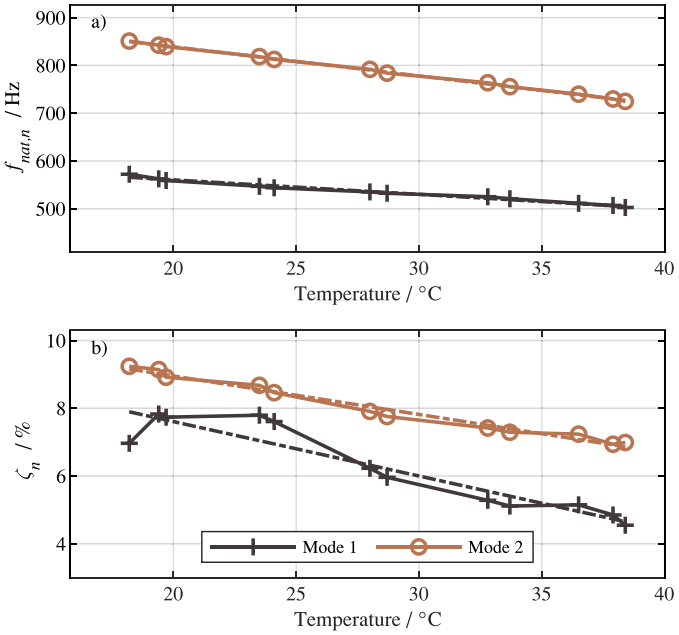

Fig. 6. Variation of temperature (measured on the cell surface with the IR sensor) and the effect on (a) natural frequencies $f_{nat,n}$ and (b) damping ratios ζ_n. Both natural frequencies and damping ratios are reduced for higher temperatures. Scattered lines are linear fits to the plotted MDOF fit data value.

3.4. Influence of temperature

To understand the sensitivity of the structural dynamics of lithium-ion prismatic cells to cell temperature, the EMA of the cell was measured at different temperature levels with DPM at *p33(z)*. To ensure the reliable characterization of the temperature sensitivity of the SUT, a significant influence of the measurement equipment used, must be avoided. The negligible influence of the measurement setup and the sensors (force transducer and accelerometer) on the accuracy of the results was proven in [59].

The temperature was varied from low to high values. After the temperature-controlled safety chamber reached each target temperature, the cell was allowed to obtain thermal equilibrium for 30 min and the first FRF was measured. The FRF measurement was repeated after an additional 15 min (45 min for equilibrium in total). The surface temperature of the cell was measured with the IR sensor at the upper cell surface. This surface temperature is depicted in Fig. 6 with the results of the MDOF fit. The two circles appearing as a pair for both natural frequencies $f_{nat,n}$, and damping ratios ζ_n are the respective measurements after the aforementioned 30 and 45 min.

Both natural frequencies decrease with a linear negative slope. The slope of $f_{nat,1}$ is -3.0 Hz/K with a correlation coefficient of -0.99. The slope of $f_{nat,2}$ is -6.1 Hz/K, also with a correlation coefficient of -0.99.

The softening behavior of the cell (softening is associated with a decrease in the natural frequency) for increased temperature could be caused by thermal swelling, which is published to have a linear characteristic in the investigated temperature range [19,20]. Furthermore, it has been suggested in literature that the separator and the complex shape of the cell play a critical role in thermal expansion [19].

Considering that the separator might be important for the structural dynamics' sensitivity to temperature, as was already discussed for pouch cells in [59], the thermal expansion coefficients of the different components in the cell are compared. Since no thermal expansion coefficients are available for the specific cell in this work, values from literature are taken into account. The separator has been reported to have the highest thermal expansion coefficient α of the cell components, with $\alpha_{sep} = 133.2 \times 10^{-6}$/K compared to 4.06×10^{-6}/K for the negative electrode, 8.62×10^{-6}/K for the positive electrode, 17×10^{-6}/K for Cu foil, 23.6×10^{-6}/K for the aluminum foil and 12.4×10^{-6}/K for the electrolyte [34,44]. This correlates well with the observation of the importance of the separator for the thermal swelling, as made by Oh et al. [19].

While both intercalation-induced swelling and thermal swelling cause an expansion of the jelly roll(s) and the cell [20], there is a difference between these two effects in terms of the structural dynamics of the investigated lithium-ion prismatic cell. The intercalation-induced swelling of the anode during SOC variation in Section 3.3 causes an increase in stiffness for higher lithiation, whilst increased thermal swelling causes the cell to soften. This may be due to changes in the microstructure of the electrodes and the separator or may depend on whether the separator or the electrodes swell and therefore occupy a higher share of the cell volume.

Comparison of the results in this work with the previous work for unconstrained pouch cells reveal a similar trend for the natural frequencies with regard to temperature sensitivity, while the damping ratios behave completely differently for the two different cell types.

The natural frequencies of the lithium-ion pouch cells in the unconstrained condition have ~~a~~ similar correlation coefficients and negative slopes, with -11.9 Hz/K (−3.0 Hz/K for the prismatic cell) for mode 1 and -7.4 Hz/K (−6.1 Hz/K for the prismatic cell) for mode 2. [59]

In contrast, while the damping ratios in this work also have a linear (mode 2) or approximately linear (mode 1 above 25 °C) characteristic with a negative slope, the damping ratios of the pouch cells showed an increase in a nonlinear manner, with a positive slope for increased temperature [59]. An interesting comparison is possible with the work by Oh et al., who reported zero or little nonlinear expansion of a cell due to thermal swelling below 20 °C, while above 25 °C the expansion is linear [19]. This behavior has been attributed to small initial gaps between the jelly roll and the can at low temperatures [19]. This initial gap might be apparent in our investigated cell as well, causing nonlinear behavior of the damping ratio at low temperatures. Interestingly, if this is the case, this gap does not have a similar impact on the stiffness, since the natural frequencies show linear sensitivity to temperature across the entire investigated temperature range.

To further investigate the thesis of a possible gap between the jelly roll and the casing, a coarse approximation for the expansion due to thermal swelling is performed. To calculate the overall thermal swelling, an effective thermal expansion coefficient of the cell is first calculated by a rule of mixture, taking approximated thicknesses t_i of the different layers i for a unit cell into account according to Eq. (9) and Table 4. The separator must be counted twice for one unit cell.

Table 4
Approximated values for the calculation of an effective cell thermal expansion coefficient from the coefficients of all components i (electrolyte neglected); expansion coefficients are taken from [34,44].

Component per unit cell	Approx. thickness t_i/µm	Approx. therm. exp. coeff. α_i /10^{-6} K^{-1}
Anode active layer (two-sided)	330	4.06
Cu foil	15	17
Cathode active layer (two-sided)	200	8.62
Al foil	30	23.6
Separator (2x)	2 × 20 = 40	133.2

$$\alpha_{cell} = \frac{1}{\sum_{i=1}^{5} t_i} \sum_{i=1}^{5} t_i \times \alpha_i = 15.21 \times 10^{-6}/\mathrm{K} \tag{9}$$

In the preceding section about the sensitivity to SOC, an initial gap of 200 µm was approximated. Taking the value of $\alpha_{cell} = 15.21 \times 10^{-6}$/K for the unit cell into account, an approximated jelly roll expansion $\Delta t_{jellyrolls,th}$, using the temperature difference ΔT = 24 °C-18 °C = 6 K with non-decreasing damping for mode 1 in Fig. 1, can be calculated with Eq. (10).

$$\Delta t_{jellyrolls,th} = \alpha_{cell} \times \Delta T \times t_{cell,\ inner} = 15.21 \times \frac{10^{-6}}{\mathrm{K}} \times 6\mathrm{K} \times 43\mathrm{mm} = 3.924\mu\mathrm{m} \tag{10}$$

The term $t_{cell,inner}$ describes the total initial thickness of the inner cell components, respectively the jelly rolls. According to this approximation, a significant difference between the effective thickness change due to intercalation $\Delta t_{jellyrolls,int}$ and thermal swelling $\Delta t_{jellyrolls,th}$ is obtained. While the aforementioned values are calculated from component values, Oh et al. reported an experimentally determined thermal swelling coefficient for a prismatic cell in the range of approx. 8×10^{-4}–13×10^{-4}/K depending on the measurement location for a prismatic cell [19]. Rieger et al. reported a thermal expansion coefficient of the 6.4 mm thick pouch cell (same cell type as discussed in Section 3.3 for the SOC sensitivity) of 1.1 µm/K, which equals to 1.72×10^{-4}/K when normalized to the cell thickness [85]. It becomes obvious, that there is a wide range of reported thermal expansion coefficients. Using a value of 10×10^{-4}/K in Eq. (10), since this is in the range of the values reported for a prismatic cell [19], the thickness change due to thermal swelling would be approximately 258 µm, which is close to the approximated 212 µm swelling due to intercalation, until the gap inside the cell is closed. Oh et al. also stated that the effective thermal swelling is not the pure thermal swelling, but reflects all the mechanical constraints and interfaces inside the cell [19]. The presented rough approximations provide for a gap between the jelly roll and the casing as a possible important factor in the consideration of the structural dynamics of large-format prismatic cells.

The variation in reported values in literature highlights a need for further research to improve the understanding of the thermal swelling phenomenon and its interaction in between the components, the interfaces and the boundary conditions. A more detailed investigation should incorporate the disassembly of the prismatic cell with an exact measurement of all components and the determination of specific thermal expansion coefficients, which is beyond the scope of this paper.

Considering the effect of boundary conditions due to mechanical constraints with or without a gap and interfaces and varying temperature, it appears that the damping ratios are more influenced by the boundaries than the natural frequencies. For both pouch cells [59] and prismatic cells, the natural frequencies decrease with increased temperature, due to softening. In contrast, the damping ratio (at least for mode 1), seems to be significantly affected by the boundary conditions provided by the cell casing. The pouch cell showed a nonlinear increase in the damping ratio upon an increase in temperature [59]. The prismatic cell shows an increase at the beginning in the range 18 °C to 20 °C, followed by a plateau and then a subsequent decrease of the damping ratio. If there were a gap between the jelly roll and the casing at low temperatures, the boundary conditions of the jelly roll in the prismatic cell would be similar to the boundary conditions of a z-folded electrode stack in a pouch cell with a soft casing, until such time as the gap were filled. This similarity with little constraints, before the casing ~~can~~ gets in contact with the jelly roll, would therefore mean that the casing causes the sensitivity of the damping ratio to change from a positive slope to a negative slope.

Summarizing the observations regarding temperature sensitivity and SOC sensitivity from both prismatic cells and pouch cells [59] the following observations can be stated:

- The effect of swelling (both intercalation and thermal) on structural dynamics depends on the mechanical constraints provided by the cell housing.
- While both cell types show softening due to thermal swelling, only the hard case cell with higher constraints shows hardening due to intercalation.
- Whether swelling causes the investigated prismatic hard case cell to soften ($f_{nat,n}$ decreasing) or to harden ($f_{nat,n}$ increasing) depends on the physical origin of the swelling (thermal- or intercalation-induced).
- The sensitivities of the damping ratios are significantly different for the two investigated cell types, since it mostly increases for a temperature increase for a pouch cell, while mostly decreases for the prismatic hard case cell.

Therefore, the different cell designs with different interfaces and boundaries seem to cause very different dynamic behavior and different sensitivities to the parameters of the cell or the ambiance. This is more proof that the interfaces and boundaries are at least as important as the components itself [57,59] and might be underrepresented in the literature.

Unfortunately, the current climate chamber setup does not reach higher or lower temperatures due to limited insulation. Therefore, the sensitivity of both natural frequencies and damping ratios cannot be investigated for temperatures outside of the depicted range at the moment. If the temperature sensitivity continues in the same linear manner for higher temperatures, high temperatures in operation could significantly alter the structural dynamics and therefore the structural durability of the lithium-ion prismatic cells.

With respect to vibration durability testing, the investigated prismatic cell should be tested at different conditions. A cell charged to 100% SOC at a temperature of 17 °C is much stiffer and more damped, than a cell discharged to 0% SOC at an elevated temperature of 38 °C. The natural frequency of mode 1 $f_{nat,1}$ for example changes from approx. 800 Hz to 500 Hz when discharged from 100% SOC to 0% SOC and warmed up from 25 °C to 38 °C due to, e.g., ohmic losses. In addition, the damping ratio ζ_1 decreases from approximately 9% to 5%, which means higher relative displacement and higher potential for fatigue [60]. Testing or operation at temperature levels of 0 °C or 50 °C might render this effect even more pronounced.

It would be interesting to repeat this sensitivity study with a wider temperature range and with measurements at different locations on the cell, as it was done by Oh et al. [19], so as to further investigate the relevance of the jelly rolls, the boundaries through the housing, the initial gaps inside the cell and the thermal swelling.

3.5. Influence of aging

In this section, two cyclically aged cells are investigated with respect to natural frequencies, damping ratios and mode shapes and are compared with the new and uncycled cell CN1. To make reliable and meaningful comparisons between cells, the first step always has to be the identification of the different modes, since the first mode of one cell not necessarily is the first mode of another cell, too [59]. While the driving point FRFs at *p33(z)* of the aged cells seem to have the same characteristic - albeit frequency-shifted - shape as the new cells, mode shape analysis revealed that two similar peaks in the two respective FRFs can represent completely different modes. Another significant difference between the new and aged cells is that the mode 1 from the preceding sections could not be detected for the aged cell CA1 using excitation at *p33(z)*. This is probably caused by changes in the mechanical structure during aging.

The following procedure has been therefore defined to systematically compare the new cells and the aged cells:

1 The two new cells CN1 and CN2 were compared using MDOF fit and

MAC analysis for existent 5 × 5-FRF measurements. Due to high similarity, only CN1 is used for further comparison with the aged cells.
2 The cells CN1, CA1 and CA2 were investigated with 9 × 9-FRF for both excitation positions *p33(z)* and *p55(z)*.
3 MDOF fits of both 9 × 9 modal analyses were done subsequently. Multi-reference fits, using both sets of results in one fitting procedure did not reveal any advantages.
4 Poles of the FRF and the respective modes were identified using the MIF and MOV values, as well as engineering judgment, in order to differentiate between real physical modes and the effects of noise. The high modal density, depicted through a very flat MIF curve (clearly distinct modes are represented by distinct drops in the MIF, which is not the case for the investigated prismatic cells) and complex modes with non-proportional damping, make the identification of the modes a non-trivial task. Adjustment of the region of interest in the frequency range and the choice of the correct identified poles must be carefully done.
5 If a mode shape was found for both excitation positions, both optical comparison and MAC analysis is used to check the correlation or similarity of the modes. If the modes are assumed to be identical, the mode obtained through the excitation position with the higher MOV is retained for further comparison. This kind of MAC analysis is called "auto-MAC" in this paper, calculating the MAC table for the cell with itself.
6 Throughout these steps, four modes for each cell were identified, which were investigated by "cross-MAC" and optical investigation to identify correlating shapes. Cross-MAC is performed for each possible combination of cells. This permitted an evaluation of the similarity of the different mode shapes in between different cells.
7 The shapes of the modes are used to investigate the influence of aging under constrained and unconstrained conditions.
8 Natural frequencies and damping ratios of correlating modes are compared to investigate the effect of aging on stiffness and damping. Please note that the present results with the limited number of tested cells is the first investigation of this kind at all and therefore not meant to provide statistical significance. This can be done in upcoming studies.

Table 5 depicts the cross-MAC table for the comparison of the two new cells (step 1) with values above 90% and 71% on the diagonal and values below 2.3% in the other fields. This shows a high similarity of the two new cells, and at the same time sets the benchmark for the comparison with the aged cells, since the correlation between new and aged cells can be expected to be lower than for two new cells. If measuring an aluminum dummy for example, this second value might already be considered an indication of an error, but since the prismatic cells are much more complex, these values are used as a benchmark for the further investigations. Videos of the superimposed mode shapes from Table 5 are provided in the supplementary materials.

Due to the high similarity of CN1 and CN2, only CN1 is used in the following. The results for the MDOF fits and the MAC calculation, as described in the steps 2–5, are given in Table 6 for the new cell CN1 with 9 × 9 FRF. MAC analysis reveals a high correlation of the first identified modes from both *p33(z)* and *p55(z)* in the first two rows, with a MAC value of 82%. Therefore, the two results are both identified as being the 1st mode. It should be noted that the term "1st mode" is used instead of "mode 1", since similarity of the modes with the used modes 1 and 2 throughout Sections 3.1–3.4 is not proven at this stage. Of course, in the case of CN1, the first and second modes are equal to mode 1 and mode 2, but this does not necessarily apply for the aged cells. All other MAC values outside the diagonal are very low from 0–11%, indicating different modes.

Table 6
Results from MDOF fit and auto-MAC for cell CN1 based on 9 × 9 FRF measurements at both *p33(z)* and *p55(z)*; modes with an asterisk (*) are retained.

Mode	Exc.	$f_{nat,n}$/Hz	ζ_n	MOV	Auto-MAC				
					1st *	1st	2nd *	3rd *	4th *
1st *	*p55(z)*	565	5.6%	99.8%	100%	82%	1%	4%	3%
1st	*p33(z)*	609	6.4%	98.2%	82%	100%	0%	2%	11%
2nd *	*p33(z)*	854	6.9%	98.8%	1%	0%	100%	3%	1%
3rd *	*p55(z)*	877	6.2%	99.4%	4%	2%	3%	100%	0%
4th *	*p33(z)*	1067	6.9%	96.6%	3%	11%	1%	0%	100%

It can also be seen that both the natural frequencies and the damping ratios for the 1st mode of CN1 differ from each other depending on the chosen excitation position, e.g., a difference of 44 Hz of $f_{nat,1}$ for *p55(z)* in comparison to *p33(z)*. Therefore, there seems to be a certain impact of the measurement setup on the results. Nevertheless, since the sensitivity and therefore the variation of the structural dynamics to the variation of cell parameters is the main aspect of interest, the deviation in absolute values does not negatively influence the results in the preceding sections.

Table 7 depicts the results for the auto-MAC of cell CA1, which has been aged under constrained conditions. The 1st mode could not be identified with excitation at *p33(z)* in contrast to the new cell CN1. The second interesting observation is that the MAC table has values of 50% and 37% outside of the diagonal, indicating a higher similarity of different modes than for the new cell, which complicates mode identification.

Table 8 depicts the results for cell CA2, which was aged under unconstrained condition. This cell is rather difficult to interpret, since MAC values of up to 59% are observable between different mode assignments (1st mode to 2nd mode).

Based on an optical interpretation of the mode shapes and on a consideration of natural frequency and damping, the first and second row are both assumed to be the first mode. Row four and five are also assumed to be identical in terms of both the MAC table and optical comparison, but the MAC value, at 33%, is no strong indication. The second mode in the third row has a comparably low MOV and also a high MAC value of 59% with regard to the first row of the MAC table and is therefore difficult to interpret. It could not be excluded from the MDOF fit to achieve a low LSE of the fit, therefore a physical origin is assumed. The first mode, with estimation at *p33(z)* (second row), probably suffers from mode overlap, since the natural frequencies of estimated mode 1 and 2 are very close to each other for cell CA2 ($f_{nat,1}$ = 1040 Hz and $f_{nat,2}$ = 1126 Hz).

The two first modes are separated more clearly for the new cells, with more than 200 Hz difference for an SOC = 0% and T = 25 °C (see Section 3.3), making mode-identification easier. The overlap of 1st and 2nd mode for CA2 is a good reason for the high MAC values in the first three rows and columns in Table 8. Generally, the mode separation is

Table 5
MDOF fit results and MAC table for the two new cells showing a high correlation of the modes on the diagonal, and therefore comparable mode shapes of the two new cells. The values $f_{nat,mean,n}$ and $\zeta_{mean,n}$ for the modes n = 1 and n = 2 on the left side of the table are the average values of three DPM measurements at *p33(z)*. The MAC values are based on the 5 × 5 FRF with excitation at *p33(z)* as described in Section 2.4.

Cell	$f_{nat,mean,1}$/Hz	$f_{nat,mean,2}$/Hz	$\zeta_{mean,1}$	$\zeta_{mean,2}$	Cross-MAC	CN2 mode 1	CN2 mode 2
CN1	558	827	5.6%	8.0%	CN1 mode 1	91%	2%
CN2	528	819	5.6%	8.9%	CN1 mode 2	1%	71%

Table 7
Results from MDOF fit and auto-MAC for cell CA1 based on 9 × 9 FRF measurements at both *p33(z)* and *p55(z)*; modes with an asterisk (*) are retained.

Mode	Exc.	$f_{nat,n}$/Hz	ζ_n	MOV	Auto-MAC 1st *	2nd *	3rd *	4th *
1st *	*p55(z)*	942	6.0%	100.0%	100%	50%	0%	3%
2nd *	*p55(z)*	1180	6.0%	99.0%	50%	100%	13%	37%
3rd *	*p33(z)*	1246	5.0%	99.9%	0%	13%	100%	5%
4th *	*p55(z)*	1305	5.2%	99.9%	3%	37%	5%	100%

the weakest for CA2 with approximated four modes in the range from 1039–1387 Hz (Δf_{CA2} = 348 Hz), while the new cell CN1 shows four modes in the range from 564–1067 Hz (Δf_{CN1} = 503 Hz) and the aged cell CA1 has four modes between 942–1305 Hz (Δf_{CA1} = 363 Hz). It is therefore obvious that the aging of the cell increases the modal density in the investigated frequency range. Mode 4 of CA2 is very different from all other shapes of CA2 with auto-MAC values of less than 10% outside of the diagonal.

Tables 9–11 give the cross-MAC results for the four retained modes of each cell according to step 6. MAC values which are assumed to show a correlation are written in bold. Taking all three MAC tables into account, the 2nd mode of the aged cells cannot be assigned to any other mode, including the MAC analysis of the two aged cells in Table 11. Further optimization of the DOF for excitation could be an option for obtaining a clearer picture, since significant mode overlap is likely. Another interesting observation is that CN1 and CA1 have higher MAC values (65–73%) for the three identified correlations, compared to CN1/CA2 (44–61%). This is likely to be caused by the mechanical constraints throughout aging for cell CA1, which kept the geometry of the cell closer to the geometry of the new cell, while the cell, which has been cycled without constraints, experienced significant swelling. The measured thicknesses are 45.5 mm for the new cells, 46.2 mm and 46.5 mm at *p33(z)* and *p55(z)* respectively for the aged cell CA1 (constrained) and 50.8 mm/50.5 mm at *p33(z)/p55(z)* for cell CA2 (unconstrained). The cell CA2 therefore experienced a thickness increase of 11% and the cell CA1 of only 2%.

It is further obvious that the MAC tables generally contain values which are below the recommended values for mode identification (close to 1). Since lithium-ion cells are complex structures with well-known parameter variations [86–89] and the cells in this study have different histories, the MAC analysis must be used with reduced demands regarding obtained maximum values.

The modes which are analyzed in the cross-MAC tables (Tables 9–11) are also given in Fig. 7 as static pictures, and as animated videos in the supplementary materials. Since the cell is a complex geometry, which appears to have non-proportional damping, the nodal lines are not completely static. Therefore, it is recommended to take the animated videos into account, since they provide better information as to the occurring deformation patterns. Modes, which are correlated according to the cross-MAC, are framed in the same color and line-style. It can be seen that the modes which are most similar do not necessarily occur in the same order. Due to the high modal density, it can happen that modes switch their order.

Table 9
Cross-MAC analysis of new cell CN1 and aged cell CA1 (constrained aging); assumed correlations of modes are printed in bold.

CN1/CA1 Cross-MAC	CA1 1st (942 Hz)	CA1 2nd (1180 Hz)	CA1 3rd (1246 Hz)	CA1 4th (1305 Hz)
CN1 1st (565 Hz)	73%	49%	2%	5%
CN1 2nd (854 Hz)	1%	8%	66%	1%
CN1 3rd (877 Hz)	2%	41%	3%	65%
CN1 4th (1067 Hz)	5%	1%	1%	2%

Table 10
Cross-MAC analysis of new cell CN1 and aged cell CA2 (unconstrained aging); assumed correlations of modes are printed in bold.

CN1/CA2 Cross-MAC	CA2 1st (1039 Hz)	CA2 2nd (1125 Hz)	CA2 3rd (1262 Hz)	CA2 4th (1387 Hz)
CN1 1st (565 Hz)	**44%**	30%	8%	0%
CN1 2nd (854 Hz)	1%	5%	3%	**49%**
CN1 3rd (877 Hz)	3%	3%	**61%**	0%
CN1 4th (1067 Hz)	7%	2%	8%	1%

Table 11
Cross-MAC analysis of aged cell CA1 (constrained aging) and aged cell CA2 (unconstrained aging); assumed correlations of modes are printed in bold.

CA1/CA2 Cross-MAC	CA2 1st (1040 Hz)	CA2 2nd (1126 Hz)	CA2 3rd (1262 Hz)	CA2 4th (1387 Hz)
CA1 1st (942 Hz)	64%	39%	7%	0%
CA1 2nd (1180 Hz)	46%	18%	47%	3%
CA1 3rd (1246 Hz)	10%	1%	0%	89%
CA1 4th (1305 Hz)	10%	21%	44%	3%

It can be concluded that in the course of aging, the cells get stiffer, since the lowest identified natural frequency is 565 Hz for the new cell, 942 Hz for the aged cell CA1 and 1040 Hz for the aged cell CA2. While all modes are shifted to higher frequencies, the modal density is also increased, whereby Δf_{CN1} = 503 Hz, Δf_{CA1} = 363 Hz and Δf_{CA2} = 348 Hz.

Mode 1 shows a very regular and equal relative displacement of the surface for the new cell according to its mode shape, while for the two aged cells, the bulge is more concentrated close to the tabs (DOF 91–99) in comparison to the bottom of the cell (DOF 11–19). With regard to mode shapes, aging has shown stronger effects on the prismatic cells than for the pouch cells in part I [59], which showed higher stiffness but similar mode shapes. A very detailed comparison cannot be made, since the average SOH of the pouch cells was about 90%, while the SOH of the prismatic cells is below 80% for both cells.

Since the mode identification is difficult, a detailed quantitative look on the single natural frequencies and damping ratios is limited to the first mode here. Table 12 shows that the aged cells are stiffer with increased natural frequencies, while for the damping ratios, no clear picture occurs. Since, our paper series is the first one investigating more

Table 8
Results from MDOF fit and auto-MAC for cell CA2 based on 9 × 9 FRF measurements at both *p33(z)* and *p55(z)*; modes with an asterisk (*) are retained.

Mode	Exc.	$f_{nat,n}$/Hz	ζ_n	MOV	Auto-MAC 1st	1st	2nd	3rd	3rd	4th
1st *	*p55(z)*	1040	4.9%	98.9%	100%	59%	59%	8%	4%	6%
1st	*p33(z)*	1085	4.7%	96.3%	59%	100%	37%	15%	13%	8%
2nd *	*p55(z)*	1126	3.4%	89.7%	59%	37%	100%	26%	0%	2%
3rd	*p33(z)*	1234	3.4%	91.0%	8%	15%	26%	100%	33%	1%
3rd *	*p55(z)*	1262	4.3%	98.6%	4%	13%	0%	33%	100%	2%
4th *	*p33(z)*	1387	3.4%	99.8%	6%	8%	2%	1%	2%	100%

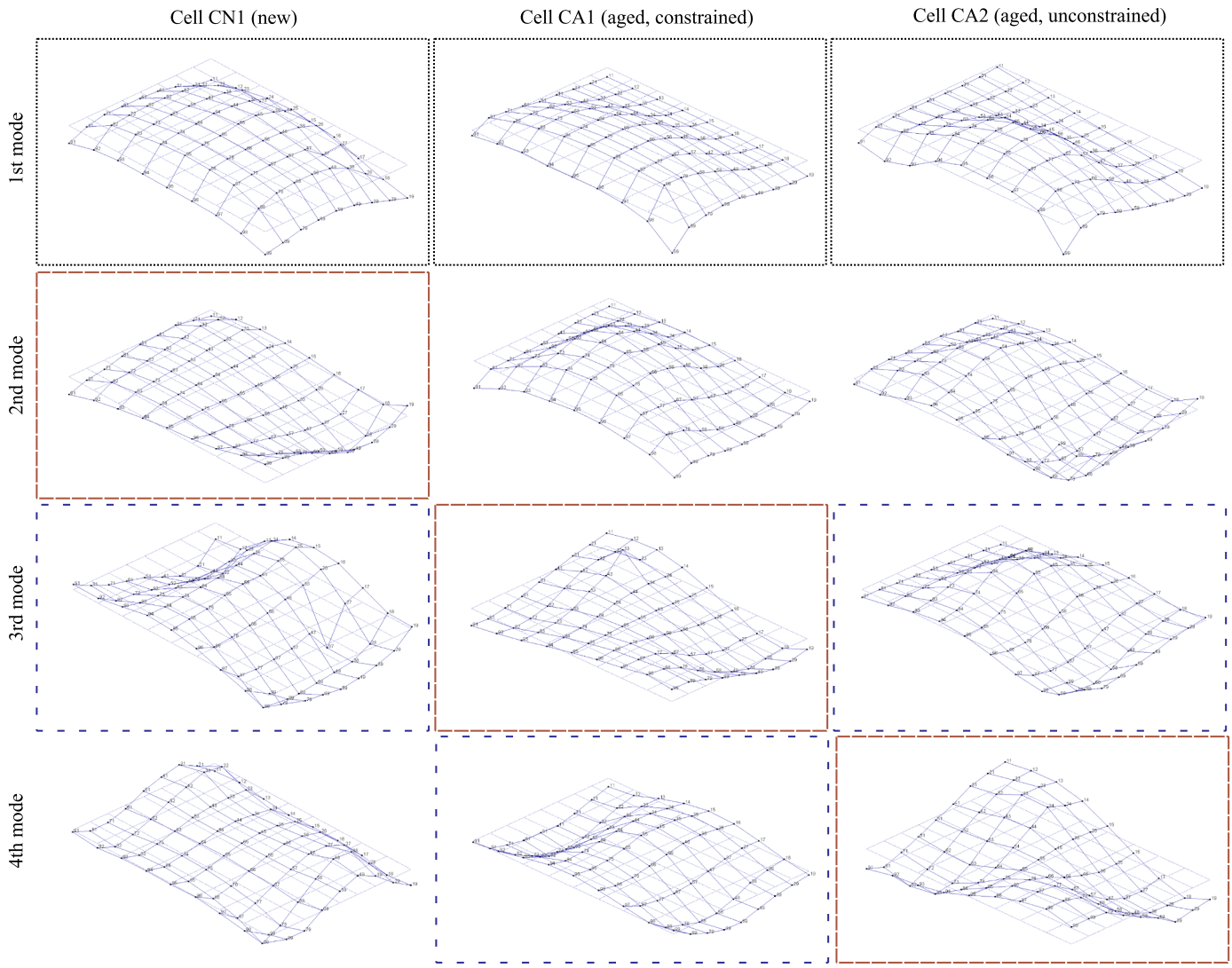

Fig. 7. Mode shapes from the MAC analyses in Table 9–11. Modes for which MAC analysis indicates mode correlation have identical frames. Variation in the order of modes is visible.

Table 12
Natural frequencies and damping ratios of mode 1 for the three investigated cells.

	CN1	CA1	CA2
$f_{nat,1}$/Hz	565	942	1040
ζ_1	5.6%	6.0%	4.9%

than one aged pouch cell and an aged prismatic cell at all with regard to its structural dynamics, already available aged cells have been used. If the progress of aging is to be investigated in a detailed quantitative manner, it is recommended that several cells are cycled at the same time with intermitting EMA analysis, e.g., each 250 cycles or each 2% loss of capacity. Small steps will improve the identification and tracking of the different modes.

4. Evaluation of experimental modal analysis as a method for lithium-ion cell research

EMA has been used for two different cell types in this paper series. Since, it is a less usual method for lithium-ion cell research nowadays; this section shall provide an evaluation of this method in terms of its applicability and probable usefulness in the future.

The original idea, which is also described in the introduction, was to use the EMA for the characterization of lithium-ion cells in order to parameterize finite element models and to design fatigue experiments to improve the understanding of possible failure mechanisms caused by vibration. The method has shown itself to be very useful to understand the occurring displacements (through mode shape analysis) and to understand the various sensitivities which might promote fatigue. There is also the general option of parameterizing FEM models based on the obtained data.

At the same time, it must be stated that the experimental estimation of higher order modes has shown to be difficult for both cell types due to several reasons, for example the high modal density and complex non-proportional damping. If the fitting procedure for the parameterization of a finite element model of a cell is to be based on the results of the modal analysis, the number of unknown parameters shall be limited. In an optimization with a finite element modal analysis tool, for example, unknown material properties are varied to calculate the desired natural frequencies, which serve as target values in the optimization procedure. If only two natural frequencies are known, while e.g. nine material parameters have to be determined, the optimization problem is likely to be under-constrained, depending on the sensitivity of the natural frequencies from each material parameter. The aforementioned nine parameters may occur as three elastic moduli E_x,E_y,E_z,

three shear moduli G_{xy}, G_{xz}, G_{yz} and three Poisson values ϑ_{xy}, ϑ_{yz}, ϑ_{yz} for an homogenized orthotropic material. In case of an isotropic behavior of the cell, the finite element software needs only values for the density, the isotropic elastic modulus and the Poisson value or shear modulus. If density is calculated from mass and volume, only two parameters remain, which have to be estimated. Therefore, the applicability of the EMA for the parameterization of FEM models of the structural dynamics depends on the required complexity of the model, and on whether the measurement may be further optimized to extract modes of higher order. The final evaluation of this is the subject of further research, since the sensitivity of the modal results from the material parameters has to be investigated.

In addition, a more sophisticated selection of excitation positions through parallel application of finite element models has the potential to improve the mode determination through an iterative procedure.

While the failure mechanism-driven approach was the original idea, other observations came along the way. The EMA has shown to be sensitive to changes in several parameters and for example allow one to distinguish between thermal swelling and intercalation-based swelling, for example through the damping behavior of the investigated prismatic hard case cell. In this publication, it is for example stated that the damping behavior of mode 1 could be an indicator for the existence or the filling of an initially existing gap inside the cell. In this case, the EMA could be a helpful addition to other measurements, e.g. with strain gauges, so as to obtain more information about the mechanical behavior of the cell and the mechanical effects.

A general advantage of the EMA is that it is a non-destructive method, and that it includes all boundary conditions and interfaces inside the cell. In addition, with a well-designed free-free condition, the cell can be tested in a manner, which is relatively unaffected from outer constraints (especially for heavier and larger cells for which, for example, the weight of the accelerometers becomes negligible). Throughout the two parts of this series of papers, it has been shown several times that a lithium-ion cell as a mechanical system is much more than the simple sum of its components. Considering this, the EMA could be a useful addition to component tests, if these are used for the parameterization of models, and/or for a cross-check, if the chosen model structure, material parameters, interfaces and boundary conditions reflect the overall elastic behavior of the cell in a correct manner.

While we see its potential as a method for laboratory investigations, the monitoring and tracking of resonance frequencies as a tool for structural health monitoring in an application, as proposed earlier [71,76], is assumed to be difficult considering the many sensitivities which would have to be considered in an online-model for state estimation. Outer boundaries due to pack design further complicate such an approach.

One disadvantage of the method is the non-negligible effort and experience, e.g., required to achieve the free-free condition, to choose the correct DOF for excitation or to attach the sensors reliably. In addition, experience and knowledge in the MDOF fitting procedure is required. Also the non-linear effects have to be carefully considered and a wrong choice of excitation can significantly alter the quality of the results. This of course, gives further limitations, if the lithium-ion cell shall be examined with regard to more severe mechanical loading conditions. Nevertheless, the electrochemical impedance spectroscopy (EIS) has become one of the most important methods in lithium-ion cell research, although it has the same requirements regarding linearity, time-invariance, causality and reciprocity.

5. Conclusion

In this work, a recently introduced test bench [59] was used to investigate the structural dynamics of a large-format lithium-ion prismatic cell for the first time. The structural dynamics were identified in terms of natural frequencies, damping ratios, and mode shapes. Significant sensitivity to both SOC and temperature were found. In the case of SOC variation, pronounced hysteresis behavior for both natural frequency and damping was observed. Stiffening of the cell, shown by increased natural frequencies, was observed for increased SOC and decreased temperature. Increased temperature caused a linear decrease of natural frequencies, and at the same time an approximately linear decrease in the damping ratio, with the exception of mode 1 in the low temperature range. The decreasing damping ratio for elevated temperatures stands in strong contrast to the increasing damping ratio for elevated temperatures for pouch cells in the preceding part I [59]. The different boundary conditions and constraints, provided through the cell casing were identified as a possible explanation for this observation. This theory has been supported by the possible effect of an initial gap inside the cell between the jelly rolls and the housing, which might cause the damping ratio of the first mode to be non-decreasing below 24 °C.

The results for natural frequencies and damping ratios showed high similarity to results in the literature for intercalation-induced swelling and thermal swelling. In addition, the first mode shape in the case of resonance excitation was a similar shape to the swelling-induced shapes in other work, a factor which could simultaneously pose a risk to safety and cell lifetime, especially in an unconstrained condition.

This work therefore revealed several novelties in comparison to existing literature: Physical processes such as the intercalation induced swelling of the anode and the cell can cause the stiffness and damping behavior of a lithium-ion cell to change significantly, but all interfaces and boundary conditions must be considered. EMA and the proposed testing setup gives the possibility to investigate and compare different cells in a new manner. This paper series is therefore also the first one, which compares two very different cells and is therefore able to derive assumptions, such as an initially existing gap inside the cell.

The detailed investigation of different boundary conditions, especially through external bracing, could be an interesting topic for further research. The observed structural dynamics in this work could show potential risks in the case of a light-weight battery pack design, which for example could be of interest for the application in the aeronautics industry on its path to sustainable air transportation. The question if failure can occur due to relative displacement of inner components must be focus of upcoming research, using both finite element tools and resonance testing experiments.

With respect to vibration durability, the cell used in this work should be tested under different conditions, to ensure safe and long operation. Both stiffness and damping differ significantly between a fully charged cell at low temperatures and a fully discharged cell at high temperatures, which is a possible scenario for a vehicle journey in winter, when the cells are both discharged and heated during the ride.

CRediT authorship contribution statement

Philipp Berg: Conceptualization, Data curation, Formal analysis, Funding acquisition, Investigation, Methodology, Project administration, Resources, Software, Supervision, Validation, Visualization, Writing - original draft. **Jonas Soellner:** Data curation, Formal analysis, Investigation, Software, Visualization, Writing - review & editing. **Matthias Herrmann:** Investigation, Resources, Writing - review & editing. **Andreas Jossen:** Conceptualization, Writing - review & editing.

Declaration of Competing Interest

None.

Acknowledgments

Funding from the German Federal Ministry for Economic Affairs and Energy (BMWi) of the project ReViSEDBatt [grant number 03ETE004B] and management by Project Management Juelich (PtJ) are gratefully

acknowledged.

Furthermore, we would like to thank the Institute for Machine Tools and Industrial Management (*iwb*) for the space and support to run our test bench. A special thanks from Philipp Berg goes to his mentor Jan Philipp Schmidt for valuable discussions, inspiring ideas and reviews.

Supplementary materials

Supplementary material associated with this article can be found, in the online version, at doi:10.1016/j.est.2020.101246.

Appendix

Tables A.1–A2.

Table A.1
Overview of the obtained LSE levels during the investigation of nonlinear dynamics for the new cells CN1 and CN2. The LSE is calculated in the overall frequency range of the MDOF fit including both modes. The excitation level is a software value without physical meaning and the lowest level has the lowest LSE for both new cells (belongs to Fig. 4).

Excitation level	LSE CN1 /%	LSE CN2 /%
0.01	1.00	0.84
0.02	1.04	0.91
0.03	1.11	0.99
0.04	1.18	1.03
0.05	1.22	1.09
0.06	1.33	1.17
0.07	1.32	1.53
0.08	1.37	1.63
0.09	1.47	1.79
0.1	1.39	1.90

Table A.2
Maximum absolute spreads Δf_n and $\Delta\zeta_n$ for each measurement triplet and both modes $n = 1$ and $n = 2$ for the investigation of SOC sensitivity in the case of charge and discharge direction (belongs to Fig. 5).

SOC	Mode 1 discharge Δf_1 /Hz	$\Delta\zeta_1$	Mode 1 charge Δf_1 /Hz	$\Delta\zeta_1$	Mode 2 discharge Δf_2 /Hz	$\Delta\zeta_2$	Mode 2 charge Δf_2 /Hz	$\Delta\zeta_2$
100.0	2.5	0.2%	9.8	2.6%	2.4	0.8%	4.4	1.1%
90.5	11.5	2.3%	0.5	0.2%	3.8	0.4%	2.0	0.3%
81.0	12.3	2.1%	8.3	1.1%	0.8	0.2%	1.5	0.1%
71.4	12.6	0.6%	5.0	1.4%	0.4	0.2%	3.3	0.3%
61.9	3.1	1.9%	8.1	1.4%	6.0	1.0%	13.1	0.8%
52.4	5.4	1.1%	4.3	1.7%	1.5	0.3%	1.5	0.4%
42.9	4.8	0.7%	5.8	1.9%	1.3	0.2%	2.6	0.5%
33.3	1.2	0.6%	6.5	1.2%	0.5	0.2%	2.1	0.3%
23.8	2.5	0.3%	7.1	0.8%	0.7	0.2%	4.2	0.5%
14.3	2.1	0.7%	2.9	0.7%	6.6	0.5%	0.2	0.2%
9.5	1.2	0.2%	2.3	0.3%	1.4	0.3%	5.5	0.4%
4.8	0.8	0.2%	2.1	0.8%	2.7	0.2%	3.4	0.4%
0.0	0.6	0.3%	1.4	0.7%	4.5	0.5%	4.0	0.7%

References

[1] E. Helmers, P. Marx, Electric cars: technical characteristics and environmental impacts, Environ. Sci. Eur. 24 (2012) 564 https://doi.org/10.1186/2190-4715-24-14.
[2] B. Scrosati, J. Garche, Lithium batteries: status, prospects and future, J. Power Sources 195 (2010) 2419–2430 https://doi.org/10.1016/j.jpowsour.2009.11.048.
[3] D. Linden, T.B. Reddy, Handbook of Batteries, 3rd ed., McGraw-Hill, New York, 2002.
[4] R. Korthauer, Handbuch Lithium-Ionen-Batterien, Imprint, Springer Vieweg, Berlin, Heidelberg, 2013.
[5] K.-Y. Oh, J.B. Siegel, L. Secondo, S.U. Kim, N.A. Samad, J. Qin, D. Anderson, K. Garikipati, A. Knobloch, B.I. Epureanu, C.W. Monroe, A. Stefanopoulou, Rate dependence of swelling in lithium-ion cells, J. Power Sources 267 (2014) 197–202 https://doi.org/10.1016/j.jpowsour.2014.05.039.
[6] D. Andre, S.-.J. Kim, P. Lamp, S.F. Lux, F. Maglia, O. Paschos, B. Stiaszny, Future generations of cathode materials: an automotive industry perspective, J. Mater. Chem. A 3 (2015) 6709–6732 https://doi.org/10.1039/C5TA00361J.
[7] R.S. Rubino, H. Gan, E.S. Takeuchi, A study of capacity fade in cylindrical and prismatic lithium-ion batteries, J. Electrochem. Soc. 148 (2001) A1029 https://doi.org/10.1149/1.1390344.
[8] A.S. Mussa, M. Klett, G. Lindbergh, R.W. Lindström, Effects of external pressure on the performance and ageing of single-layer lithium-ion pouch cells, J. Power Sources 385 (2018) 18–26 https://doi.org/10.1016/j.jpowsour.2018.03.020.
[9] M.J. Brand, S.F. Schuster, T. Bach, E. Fleder, M. Stelz, S. Gläser, J. Müller, G. Sextl, A. Jossen, Effects of vibrations and shocks on lithium-ion cells, J. Power Sources 288 (2015) 62–69 https://doi.org/10.1016/j.jpowsour.2015.04.107.
[10] J. Hooper, J. Marco, G. Chouchelamane, C. Lyness, Vibration durability testing of nickel manganese cobalt oxide (NMC) lithium-ion 18,650 battery cells, Energies 9 (2016) 52 https://doi.org/10.3390/en9010052.
[11] J. Hooper, J. Marco, G. Chouchelamane, C. Lyness, J. Taylor, Vibration durability testing of Nickel Cobalt Aluminum oxide (NCA) lithium-ion 18650 battery cells, Energies 9 (2016) 281 https://doi.org/10.3390/en9040281.
[12] J.M. Hooper, J. Marco, G.H. Chouchelamane, J.S. Chevalier, D. Williams, Multi-axis vibration durability testing of lithium ion 18650 NCA cylindrical cells, J. Energy Storage 15 (2018) 103–123 https://doi.org/10.1016/j.est.2017.11.006.
[13] L. Somerville, J. Hooper, J. Marco, A. McGordon, C. Lyness, M. Walker, P. Jennings,

Impact of vibration on the surface film of lithium-ion cells, Energies 10 (2017) 741 https://doi.org/10.3390/en10060741.
[14] L. Zhang, Z. Mu, X. Gao, Coupling analysis and performance study of commercial 18650 lithium-ion batteries under conditions of temperature and vibration, Energies 11 (2018) 2856 https://doi.org/10.3390/en11102856.
[15] L. Zhang, Z. Ning, H. Peng, Z. Mu, C. Sun, Effects of vibration on the electrical performance of lithium-ion cells based on mathematical statistics, Appl. Sci. 7 (2017) 802 https://doi.org/10.3390/app7080802.
[16] X. Wang, M. Kato, H. Naito, C. Yamada, G. Segami, K. Kibe, A feasibility study of commercial laminated lithium-ion polymer cells for space applications, J. Electrochem. Soc. 153 (2006) A89 https://doi.org/10.1149/1.2131825.
[17] J. Zhu, T. Wierzbicki, W. Li, A review of safety-focused mechanical modeling of commercial lithium-ion batteries, J. Power Sources 378 (2018) 153–168 https://doi.org/10.1016/j.jpowsour.2017.12.034.
[18] G. Kermani, E. Sahraei, Review: characterization and modeling of the mechanical properties of lithium-ion batteries, Energies 10 (2017) 1730 https://doi.org/10.3390/en10111730.
[19] K.-Y. Oh, B.I. Epureanu, A novel thermal swelling model for a rechargeable lithium-ion battery cell, J. Power Sources 303 (2016) 86–96 https://doi.org/10.1016/j.jpowsour.2015.10.085.
[20] K.-Y. Oh, B.I. Epureanu, Characterization and modeling of the thermal mechanics of lithium-ion battery cells, Appl. Energy 178 (2016) 633–646 https://doi.org/10.1016/j.apenergy.2016.06.069.
[21] K.-Y. Oh, B.I. Epureanu, A phenomenological force model of Li-ion battery packs for enhanced performance and health management, J. Power Sources 365 (2017) 220–229 https://doi.org/10.1016/j.jpowsour.2017.08.058.
[22] K.-Y. Oh, B.I. Epureanu, J.B. Siegel, A.G. Stefanopoulou, Phenomenological force and swelling models for rechargeable lithium-ion battery cells, J. Power Sources 310 (2016) 118–129 https://doi.org/10.1016/j.jpowsour.2016.01.103.
[23] A. Barai, R. Tangirala, K. Uddin, J. Chevalier, Y. Guo, A. McGordon, P. Jennings, The effect of external compressive loads on the cycle lifetime of lithium-ion pouch cells, J. Energy Storage 13 (2017) 211–219 https://doi.org/10.1016/j.est.2017.07.021.
[24] F. Ebert, G. Sextl, M. Lienkamp, Effect of a flexible battery module bracing on cell aging, 2017 Twelfth International Conference on Ecological Vehicles and Renewable Energies (EVER), Monte-Carlo, Monaco, IEEE, 2017, pp. 1–5.
[25] X.M. Liu, C.B. Arnold, Effects of cycling ranges on stress and capacity fade in lithium-ion pouch cells, J. Electrochem. Soc. 163 (2016) A2501–A2507 https://doi.org/10.1149/2.1131610jes.
[26] M. Wünsch, J. Kaufman, D.U. Sauer, Investigation of the influence of different bracing of automotive pouch cells on cyclic liefetime and impedance spectra, J. Energy Storage 21 (2019) 149–155 https://doi.org/10.1016/j.est.2018.11.019.
[27] D. Grazioli, O. Verners, V. Zadin, D. Brandell, A. Simone, Electrochemical-mechanical modeling of solid polymer electrolytes: Impact of mechanical stresses on Li-ion battery performance, Electrochem. Impedance Spectroscopy 296 (2019) 1122–1141 https://doi.org/10.1016/j.electacta.2018.07.234.
[28] C. Peabody, C.B. Arnold, The role of mechanically induced separator creep in lithium-ion battery capacity fade, J. Power Sources 196 (2011) 8147–8153 https://doi.org/10.1016/j.jpowsour.2011.05.023.
[29] T.C. Bach, S.F. Schuster, E. Fleder, J. Müller, M.J. Brand, H. Lorrmann, A. Jossen, G. Sextl, Nonlinear aging of cylindrical lithium-ion cells linked to heterogeneous compression, J. Energy Storage (2016), https://doi.org/10.1016/j.est.2016.01.003.
[30] Y. Zhao, Y. Patel, I.A. Hunt, K.M. Kareh, A.A. Holland, C. Korte, J.P. Dear, Y. Yue, G.J. Offer, Preventing lithium ion battery failure during high temperatures by externally applied compression, J. Energy Storage 13 (2017) 296–303 https://doi.org/10.1016/j.est.2017.08.001.
[31] A.S. Mussa, G. Lindbergh, M. Klett, P. Gudmundson, P. Svens, R.W. Lindström, Inhomogeneous active layer contact loss in a cycled prismatic lithium-ion cell caused by the jelly-roll curvature, J. Energy Storage 20 (2018) 213–217 https://doi.org/10.1016/j.est.2018.09.012.
[32] H. Xie, H. Song, J.-g. Guo, Y. Kang, W. Yang, Q. Zhang, In situ measurement of rate-dependent strain/stress evolution and mechanism exploration in graphene electrodes during electrochemical process, Carbon 144 (2019) 342–350 https://doi.org/10.1016/j.carbon.2018.12.033.
[33] R. Fu, M. Xiao, S.-Y. Choe, Modeling, validation and analysis of mechanical stress generation and dimension changes of a pouch type high power Li-ion battery, J. Power Sources 224 (2013) 211–224 https://doi.org/10.1016/j.jpowsour.2012.09.096.
[34] W. Wu, X. Xiao, X. Huang, S. Yan, A multiphysics model for the in situ stress analysis of the separator in a lithium-ion battery cell, Comput. Mater. Sci. 83 (2014) 127–136 https://doi.org/10.1016/j.commatsci.2013.10.002.
[35] O. Valentin, P.-X. Thivel, T. Kareemulla, F. Cadiou, Y. Bultel, Modeling of thermo-mechanical stresses in Li-ion battery, J. Energy Storage 13 (2017) 184–192 https://doi.org/10.1016/j.est.2017.07.018.
[36] J. Cannarella, X. Liu, C.Z. Leng, P.D. Sinko, G.Y. Gor, C.B. Arnold, Mechanical properties of a battery separator under compression and tension, J. Electrochem. Soc. 161 (2014) F3117–F3122 https://doi.org/10.1149/2.0191411jes.
[37] G.Y. Gor, J. Cannarella, C.Z. Leng, A. Vishnyakov, C.B. Arnold, Swelling and softening of lithium-ion battery separators in electrolyte solvents, J. Power Sources 294 (2015) 167–172 https://doi.org/10.1016/j.jpowsour.2015.06.028.
[38] I.C. Halalay, M.J. Lukitsch, M.P. Balogh, C.A. Wong, Nanoindentation testing of separators for lithium-ion batteries, J. Power Sources 238 (2013) 469–477 https://doi.org/10.1016/j.jpowsour.2013.04.036.
[39] A. Sheidaei, X. Xiao, X. Huang, J. Hitt, Mechanical behavior of a battery separator in electrolyte solutions, J. Power Sources 196 (2011) 8728–8734 https://doi.org/10.1016/j.jpowsour.2011.06.026.
[40] I. Avdeev, M. Martinsen, A. Francis, Rate- and temperature-dependent material behavior of a multilayer polymer battery separator, J. Mater. Eng. Perform. 23 (2014) 315–325 https://doi.org/10.1007/s11665-013-0743-4.
[41] S. Kalnaus, Y. Wang, J.A. Turner, Mechanical behavior and failure mechanisms of Li-ion battery separators, J. Power Sources 348 (2017) 255–263 https://doi.org/10.1016/j.jpowsour.2017.03.003.
[42] J. Zhu, X. Zhang, H. Luo, E. Sahraei, Investigation of the deformation mechanisms of lithium-ion battery components using in-situ micro tests, Appl. Energy 224 (2018) 251–266 https://doi.org/10.1016/j.apenergy.2018.05.007.
[43] X. Zhang, E. Sahraei, K. Wang, Deformation and failure characteristics of four types of lithium-ion battery separators, J. Power Sources 327 (2016) 693–701 https://doi.org/10.1016/j.jpowsour.2016.07.078.
[44] D. Shi, X. Xiao, X. Huang, H. Kia, Modeling stresses in the separator of a pouch lithium-ion cell, J. Power Sources 196 (2011) 8129–8139 https://doi.org/10.1016/j.jpowsour.2011.05.026.
[45] L. Wang, S. Yin, C. Zhang, Y. Huan, J. Xu, Mechanical characterization and modeling for anodes and cathodes in lithium-ion batteries, J. Power Sources 392 (2018) 265–273 https://doi.org/10.1016/j.jpowsour.2018.05.007.
[46] J. Xu, B. Liu, D. Hu, State of charge dependent mechanical integrity behavior of 18650 lithium-ion batteries, Sci. Rep. 6 (2016) 21829 https://doi.org/10.1038/srep21829.
[47] L. Wang, S. Yin, Z. Yu, Y. Wang, T.X. Yu, J. Zhao, Z. Xie, Y. Li, J. Xu, Unlocking the significant role of shell material for lithium-ion battery safety, Mater. Des. 160 (2018) 601–610 https://doi.org/10.1016/j.matdes.2018.10.002.
[48] C. Dai, Z. Wang, K. Liu, X. Zhu, X. Liao, X. Chen, Y. Pan, Effects of cycle times and C-rate on mechanical properties of copper foil and adhesive strength of electrodes in commercial LiCoO2 LIBs, Eng. Fail. Anal. 101 (2019) 193–205 https://doi.org/10.1016/j.engfailanal.2019.03.015.
[49] S.H. Chung, T. Tancogne-Dejean, J. Zhu, H. Luo, T. Wierzbicki, Failure in lithium-ion batteries under transverse indentation loading, J. Power Sources 389 (2018) 148–159 https://doi.org/10.1016/j.jpowsour.2018.04.003.
[50] B. Dixon, A. Mason, E. Sahraei, Effects of electrolyte, loading rate and location of indentation on mechanical integrity of li-ion pouch cells, J. Power Sources 396 (2018) 412–420 https://doi.org/10.1016/j.jpowsour.2018.06.042.
[51] Y. Jia, S. Yin, B. Liu, H. Zhao, H. Yu, J. Li, J. Xu, Unlocking the coupling mechanical-electrochemical behavior of lithium-ion battery upon dynamic mechanical loading, Energy 166 (2019) 951–960 https://doi.org/10.1016/j.energy.2018.10.142.
[52] Z. Gao, X. Zhang, Y. Xiao, H. Wang, N. Li, Influence of coupling of overcharge state and short-term cycle on the mechanical integrity behavior of 18650 Li-ion batteries subject to lateral compression, Int. J. Hydrogen Energy (2018), https://doi.org/10.1016/j.ijhydene.2018.01.150.
[53] L. Wang, S. Yin, J. Xu, A detailed computational model for cylindrical lithium-ion batteries under mechanical loading: from cell deformation to short-circuit onset, Selected Papers Presented at the 12th Ulm ElectroChemical Talks (UECT):2015 Technologies on Batteries and Fuel Cells, 413 2019, pp. 284–292 https://doi.org/10.1016/j.jpowsour.2018.12.059.
[54] W. Wenwei, L. Yiding, L. Cheng, S. Yuefeng, Y. Sheng, State of charge-dependent failure prediction model for cylindrical lithium-ion batteries under mechanical abuse, Appl. Energy 251 (2019) 113365https://doi.org/10.1016/j.apenergy.2019.113365.
[55] J. Xu, B. Liu, L. Wang, S. Shang, Dynamic mechanical integrity of cylindrical lithium-ion battery cell upon crushing, Eng. Fail. Anal. 53 (2015) 97–110 https://doi.org/10.1016/j.engfailanal.2015.03.025.
[56] R.A. Adams, B. Li, J. Kazmi, T.E. Adams, V. Tomar, V.G. Pol, Dynamic impact of LiCoO2 electrodes for Li-ion battery aging evaluation, Electrochem. Impedance Spectroscopy 292 (2018) 586–593 https://doi.org/10.1016/j.electacta.2018.08.101.
[57] Y. Chen, S. Santhanagopalan, V. Babu, Y. Ding, Dynamic mechanical behavior of lithium-ion pouch cells subjected to high-velocity impact, Compos. Struct. 218 (2019) 50–59 https://doi.org/10.1016/j.compstruct.2019.03.046.
[58] J. Zhu, H. Luo, W. Li, T. Gao, Y. Xia, T. Wierzbicki, Mechanism of strengthening of battery resistance under dynamic loading, Int. J. Impact Eng. 131 (2019) 78–84 https://doi.org/10.1016/j.ijimpeng.2019.05.003.
[59] P. Berg, J. Soellner, A. Jossen, Structural dynamics of lithium-ion cells - Part I: method, test bench validation and investigation of lithium-ion pouch cells, J. Energy Storage 26 (2019) 100916https://doi.org/10.1016/j.est.2019.100916.
[60] C. Lalanne, Mechanical Vibration and Shock Analysis, Volume 4: Fatigue Damage, Wiley, Hoboken, NJ, 2014.
[61] C.W. de Silva (Ed.), Vibration and Shock Handbook, Taylor & Francis, Boca Raton, 2005.
[62] P. Avitabile, Modal space (in our own little world), 2014. https://www.uml.edu/docs/Modal_Space_Articles_1998-2014_17years_MACL_tcm18-189938.pdf (accessed 15 February 2017).
[63] D.J. Ewins, Modal Testing: Theory and Practice, Research Studies Press, Taunton, 1995.
[64] C. Lalanne, Mechanical Vibration and Shock Analysis, Volume 2: Mechanical Shock, Wiley, Hoboken, NJ, 2014.
[65] D.P. Finegan, J. Darst, W. Walker, Q. Li, C. Yang, R. Jervis, T.M.M. Heenan, J. Hack, J.C. Thomas, A. Rack, D.J.L. Brett, P.R. Shearing, M. Keyser, E. Darcy, Modelling and experiments to identify high-risk failure scenarios for testing the safety of lithium-ion cells, J. Power Sources 417 (2019) 29–41 https://doi.org/10.1016/j.jpowsour.2019.01.077.
[66] W. Cai, H. Wang, H. Maleki, J. Howard, E. Lara-Curzio, Experimental simulation of internal short circuit in Li-ion and Li-ion-polymer cells, J. Power Sources 196 (2011) 7779–7783 https://doi.org/10.1016/j.jpowsour.2011.04.024.

[67] K. Worden, G.R. Tomlinson, Nonlinearity in Structural Dynamics: Detection, Identification and Modelling, Institute of Physics, Bristol, 2001.
[68] G. Kjell, J.F. Lang, Comparing different vibration tests proposed for li-ion batteries with vibration measurement in an electric vehicle, 2013 World Electric Vehicle Symposium and Exhibition (EVS27), Barcelona, Spain, IEEE, 2013, pp. 1–11.
[69] J. Marco, J.M. Hooper, Defining a representative vibration durability test for electric vehicle (EV) rechargeable energy storage systems (RESS), Electric Vehicle Symposium (EVS 29), Montréal, Québec, 2016, pp. 1–12.
[70] F.-M. Volk, M. Winkler, B. Hermann, A. Hiebl, T. Idikurt, H. Rapp, T. Kuttner, Influence of state of charge and state of health on the vibrational behavior of lithium-ion cell packs, 23rd International Congress on Sound & Vibration (ICSV23), Athen, Greece, 2016.
[71] W. Nam, J.-.Y. Kim, K.-Y. Oh, The characterization of dynamic behavior of Li-ion battery packs for enhanced design and states identification, Energy Convers. Manage. 162 (2018) 264–275 https://doi.org/10.1016/j.enconman.2018.02.022.
[72] S.-K. Hong, B.I. Epureanu, M.P. Castanier, Parametric reduced-order models of battery pack vibration including structural variation and prestress effects, J. Power Sources 261 (2014) 101–111 https://doi.org/10.1016/j.jpowsour.2014.03.008.
[73] H.Y. Choi, I. Lee, J.S. Lee, Y.M. Kim, H.K. Kim, A study on mechanical characteristics of lithium-polymer pouch cell battery for electric vehicle, 23rd International Technical Conference on the Enhanced Safety of Vehicles (ESV), Seoul, Republic of Korea, 2013.
[74] H. Popp, M. Luthfi, J.-H. Han, R. Klambauer, A. Bergmann, In-Situ investigation of lithium-ion batteries by combined mechanical FRF and dilatometer measurements, 2018 E-MRS Fall Meeting and Exhibit, Warsaw, 2018.
[75] J.M. Hooper, J. Marco, Experimental modal analysis of lithium-ion pouch cells, J. Power Sources 285 (2015) 247–259 https://doi.org/10.1016/j.jpowsour.2015.03.098.
[76] H. Popp, G. Glanz, K. Alten, I. Gocheva, W. Berghold, A. Bergmann, Mechanical frequency response analysis of lithium-ion batteries to disclose operational parameters, Energies 11 (2018) 541 https://doi.org/10.3390/en11030541.
[77] O. Døssing, Structural testing: part II: modal analysis and simulation, 1988.
[78] A. Bilosova, Modal testing, ostrava, 2011.
[79] m + p international, m + p analyzer: user manual revision 5.1, Hannover, 2017.
[80] E.C. Stasiunas, T.G. Carne, T.D. Hinnerichs, B.R. Rogillio, Modal parameter estimation techniques, in: P. Avitabile (Ed.), Modal Testing: A Practitioner's Guide, John Wiley & Sons Ltd, Chichester, UK, 2017, pp. 189–219.
[81] O. Døssing, Structural testing: part I: mechanical mobility measurements, 1988.
[82] B. Rieger, S. Schlueter, S.V. Erhard, J. Schmalz, G. Reinhart, A. Jossen, Multi-scale investigation of thickness changes in a commercial pouch type lithium-ion battery, J. Energy Storage 6 (2016) 213–221 https://doi.org/10.1016/j.est.2016.01.006.
[83] J. Frodelius Lang, G. Kjell, Comparing vibration measurements in an electric vehicle with standard vibration requirements for Li-ion batteries using power spectral density analysis, Int. J. Electr. Hybrid Veh. 7 (2015), https://doi.org/10.1504/IJEHV.2015.071640.
[84] J.M. Hooper, J. Marco, Characterising the in-vehicle vibration inputs to the high voltage battery of an electric vehicle, J. Power Sources 245 (2014) 510–519 https://doi.org/10.1016/j.jpowsour.2013.06.150.
[85] B. Rieger, S.V. Erhard, K. Rumpf, A. Jossen, A new method to model the thickness change of a commercial pouch cell during discharge, J. Electrochem. Soc. 163 (2016) A1566–A1575 https://doi.org/10.1149/2.0441608jes.
[86] M. Baumann, L. Wildfeuer, S. Rohr, M. Lienkamp, Parameter variations within Li-ion battery packs – Theoretical investigations and experimental quantification, J. Energy Storage 18 (2018) 295–307 https://doi.org/10.1016/j.est.2018.04.031.
[87] T. Baumhöfer, M. Brühl, S. Rothgang, D.U. Sauer, Production caused variation in capacity aging trend and correlation to initial cell performance, J. Power Sources 247 (2014) 332–338 https://doi.org/10.1016/j.jpowsour.2013.08.108.
[88] S.F. Schuster, M.J. Brand, P. Berg, M. Gleissenberger, A. Jossen, Lithium-ion cell-to-cell variation during battery electric vehicle operation, J. Power Sources 297 (2015) 242–251 https://doi.org/10.1016/j.jpowsour.2015.08.001.
[89] K. Rumpf, M. Naumann, A. Jossen, Experimental investigation of parametric cell-to-cell variation and correlation based on 1100 commercial lithium-ion cells, J. Energy Storage 14 (2017) 224–243 https://doi.org/10.1016/j.est.2017.09.010.

8 Finite element model of a lithium-ion pouch cell based on experimental modal analysis data

8.1 Introduction

In this Chapter 8, the data obtained through EMA in Chapter 6 for a lithium-ion pouch cell are used to parameterize a model in the FEM-tool ANSYS Workbench. This tool is used to simulate the structural dynamics of a lithium-ion pouch cell. This effort is motivated by limitations 19 and 20 listed in Section 3.4. Two FE modeling approaches to describe structural dynamics of lithium-ion packs in literature are available based on theoretical values and not on experimental results [163,164]. Galos et al. reported on an investigation of the integration of LiPo-cells into composite structures. This approach would allow cells to be integrated directly into the structure of a vehicle or an airplane to reduce the weight of the battery. Their investigations are based on both experiments and FEM and aim to improve the damping behavior of the composites with integrated cells by careful placement of the LiPo cells. [167]

Therefore, no publication describing the structural dynamics of a single cell could be found. In this work, this model is an indispensable step to understanding and investigating in the future if fatigue mechanisms can damage a lithium-ion cell or any of its components (see Section 4.4). In addition, a fully parameterized model can be used to obtain values of, e.g., the elastic modulus. Due to the sensitivity of the elastic behavior to the interfaces and boundary conditions, as extensively discussed in [110], this is a non-trivial task. It has been shown that a cell cannot be described as a simple sum of its components and that several measurements probably interact with the cell under test. For the method which is developed and presented in this thesis, the independence from the measurement setup is evaluated and proven in Chapter 6 and the respective publication [109]. Therefore, the obtained measurement data will describe only the lithium-ion cell under test. If a model is successfully optimized, the real elastic parameters, comprising all interfaces and boundary conditions inside the cell are gained. Such a combined experimental-simulative approach was used in [198] to characterize battery electrode films using the acoustic resonance measurements of circular clamped samples.

A good set of starting values to initialize the model is required for the successful optimization of model parameters. This requirement justifies a parameter study regarding available values of elastic moduli and Poisson's ratios for lithium-ion cells in advance. Ali et al. reported values for the compressive modulus of 188 MPa (experimental result) or 190 MPa (based on a composite rule of mixture) for dry lithium-ion pouch cells and in-plane constrained compression tests [29]. The tensile modulus, also called Young’s Modulus, is required to describe the structural dynamics. The tensile and compressive behaviors of lithium-ion cells differ. For example, in the case of an anode with copper current collector foil the compressive modulus is published as 83 MPa, while the tensile

modulus is reported to be 4,700 MPa [29]. The same applies for all other components, e.g., for a separator with 500 MPa in the tensile direction and 90 MPa in the compressive direction [29]. Generally, the choice or selection of parameters must be done carefully. It has already been discussed that tests under constrained conditions probably reveal other results than tests under unconstrained conditions [110]. In addition, further parameters including strain rate or temperature [199–201], electrolyte wetting [199,202–204], the kind of the separator [205] or the coating of a separator [203] have a significant impact on the elastic behavior.

To give only one example, the Young's modulus E of a separator has been reported to be 843±20 MPa in the machine direction (MD) and dry condition, while values of 430±23 MPa are given in the transversal direction (TD) and dry condition. If the separator is immersed in dimethyl carbonate (DMC) (wetted condition), the values are reduced to 409±28 MPa in MD and 377±10 in TD. [204]

The paragraphs above are only a small digression to give an impression of the complex behavior of lithium-ion cells and their components without the respective interfaces. The differences in TD and MD give an indication that an isotropic approach is insufficient to describe the structural dynamics in a reliable manner. The strain rate dependability also aligns with the observation of nonlinear behavior made in Chapter 6 and [109].

Gibellini et al. reported a Young's modulus for an active pouch cell varying over a wide range during cycling with a behavior matching closer to the natural frequencies of the prismatic cell investigation in Chapter 7 and a dependence on the charge rate, indicating the influence of the external measurement setup and the resulting pressure. A value of 3,200 MPa was assigned as the Young's modulus value for equilibrium in the fully charged state. [53]

Kumar et al. reported an effective homogenized Young's modulus E for a pouch cell of 495 MPa and an effective Poisson's ratio of 0.01, calculated from values for the different layers using a Voigt average technique [39]. Sahraei et al. reported E = 500 MPa and a Poisson's ratio ν = 0.01 [206]. This low Poisson's ratio is assigned because of the porosity of the components [206]. Dixon et al. calculated a value of E = 4,200 MPa for a homogenized pouch cell [207].

Kermani et al. published a review summarizing various mechanical tests and constructed FE models in their Appendix. They found nine modeling approaches with three approaches discussed in two publications. Seven of these nine approaches are isotropic, and two models are anisotropic. Neither of the two anisotropic models provided values for the baseline of the model in this work. [208]

Tang et al. published elasticity parameters for an orthotropic model of a single lithium-ion cell, but for an 18650 cell (Young's modulus: $E_{\text{radial/in-plane}}$ = 260 MPa, $E_{\text{axial/transversal}}$ = 1,200 MPa, shear modulus $G_{\text{radial/in-plane}}$ = 118 MPa, $G_{\text{axial/transversal}}$ = 500 MPa) [19].

The Poisson's ratios of jelly rolls or pouch cells in the literature varies significantly, with values such as 0.01 [56,206], 0.08 (axial) and 0.1 (radial) [19], 0.15 [49] or 0.3 [209]. Orthotropic elasticity parameters for a lithium-ion pouch cell could not be found in the literature.

The apparent variation in reported elasticity parameters and the limited availability of orthotropic material parameters show the need to find new approaches to determine orthotropic material

parameters for lithium-ion cells. The proposed approach in this thesis is a combination of the experimental and simulative modal analysis and harmonic response analysis in the Sections 8.2-8.5.

8.2 Cell model and parameter optimization

The investigated lithium-ion pouch cell in this work (Kokam SLPB356495, 2.1 Ah) is modeled according to its true geometric geometry and mass. Density ρ_{cell} = 2.235 g/cm³ is calculated according to the estimated mass and volume and is fixed in the optimization. The overlapping fold on three edges of the pouch cell is disregarded, since otherwise the ANSYS Mechanical module for modal analysis would calculate a huge number of natural frequencies for the fold, which are not of interest. The cell is modeled as a homogeneous and orthotropic material. An isotropic modeling approach beforehand could not replicate the measured results. In an isotropic model, the variation of the material parameters changes the natural frequencies of bending modes and torsion modes only in parallel with a certain distance. This approach does not yield experimentally determined results. Due to this finding, a homogeneous model with an orthotropic material is used. The starting values of the material parameters are chosen to $E_x = E_y = E_z$ = 500 MPa, $G_{xy} = G_{xz} = G_{yz}$ = 170 MPa and $\nu_{xy} = \nu_{xz} = \nu_{yz}$ = 0.01. These values are equal to an isotropic model which can be adjusted for each dimension separately. Manual adjustment of the nine elastic material parameters reveals sensitivities of the different single modes to different single material parameters, which offer the possibility of adjusting the parameters in a stepwise and iterative manner. The parameters are adjusted manually until the calculated natural frequencies are close to a set of natural frequencies $f_{nat,n}$ for the first four modes, taken from Chapter 6 and [109], chosen as optimization target values and given in Table 5.

Table 5: Overview of the data from EMA and MDOF fit, taken from [109] *and the respective results from the simulation with optimized parameters in ANSYS. The DOFs p33(z) and p22(z) are equal to the definitions for the DOFs in Chapter 6.*

Mode n	MDOF fit $f_{nat,n}$/Hz	FEM $f_{nat,ANSYS,n}$/Hz	Rel. Dev. $\varepsilon_{f,n}$	MDOF fit ζ_n	FEM $\zeta_{ANSYS,n}$	Abs. Dev. $\varepsilon_{\zeta,n}$	Exc. DOF
1	644.3	624.8	-3.0%	4.98%	3.81%	-1.18%	*p33(z)*
2	675.6	648.0	-4.1%	3.22%	4.12%	0.90%	*p22(z)*
3	974.3	939.3	-3.6%	5.47%	5.94%	0.47%	*p33(z)*
4	1033.1	1026.5	-0.6%	8.18%	6.30%	-1.88%	*p22(z)*

After coarse manual adjustment, the ANSYS optimization toolbox is used for an automatized fine-tuning in a narrow band between upper and lower limit. This optimization is a simple candidate search via variation of the material parameters to fit the natural frequencies of the model to the measured ones. The values for the obtained natural frequencies $f_{nat,ANSYS,n}$ are given in Table 5 together with a relative deviation $\varepsilon_{f,n}$ to the MDOF fitting. The highest deviation is -4.1%, which is already close and can be further optimized in the future. The Rayleigh damping is calculated with $c_m = \alpha = 0$ and $c_k = \beta = 1.94e^{-5}$. The fit of the complete Rayleigh damping according to Eq. (24) did not cause significant improvement and, therefore, the mass-proportional part is disregarded. The resulting damping ratios $\zeta_{ANSYS,n}$ for each simulated mode n can be calculated according to Eq. (26) for each

estimated natural frequency $f_{nat,ANSYS,n}$. The results are given in Table 5, showing a sufficient approximation of the damping ratio.

$$\zeta_{ANSYS,n} = \frac{1}{2} c_k \omega_{nat,ANSYS,n} = c_k \Pi f_{nat,ANSYS,n} \tag{26}$$

The orthotropic material properties obtained after optimization are E_x = 11,608 MPa, E_y = 2,212 MPa and E_z = 4.12e^5 MPa in the case of Young's Modulus. The dimensions *x*, *y* and *z* are chosen according to [109] with x as long side of the cell (longitudinal), *y* as short side of the cell (transversal) and *z* as thickness of the cell (through-plane). The values seem high, but values, for example, up to 4,200 MPa have been reported [207] as also listed in Section 8.1. Regarding the very high value of E_z, it is shown later in Section 8.4 that this value is arbitrary. The Poisson values are $\nu_{xy} = \nu_{xz} = \nu_{yz} = 0.01$. The values for the shear moduli are G_{xy} = 9,146 MPa, G_{xz} = 10 MPa and G_{yz} = 2,038 MPa. These values are discussed later, since beforehand the sensitivity of the natural frequencies and the harmonic response to each parameter must be carefully investigated. This is done in Section 8.4 and Section 8.5.

8.3 Analysis of mode shapes and operational deflection shapes

Besides the natural frequencies, the model must also give the same mode shapes as derived using EMA. Fig. 23 depicts the measured mode shapes for $n = 1–4$ in the first row for the natural frequencies $f_{nat,n}$, the mode shapes from the FEM simulation for the $f_{nat,ANSYS,n}$ in the second row and the operational deflection shape measurements (ODS), calculated at $f_{nat,n}$. It must be noted that the measured mode shapes are shown upside down in contrast to the simulated mode shapes and ODS. Since mode shapes are theoretically symmetric, this is acceptable. The same applies for phase differences of 180°.

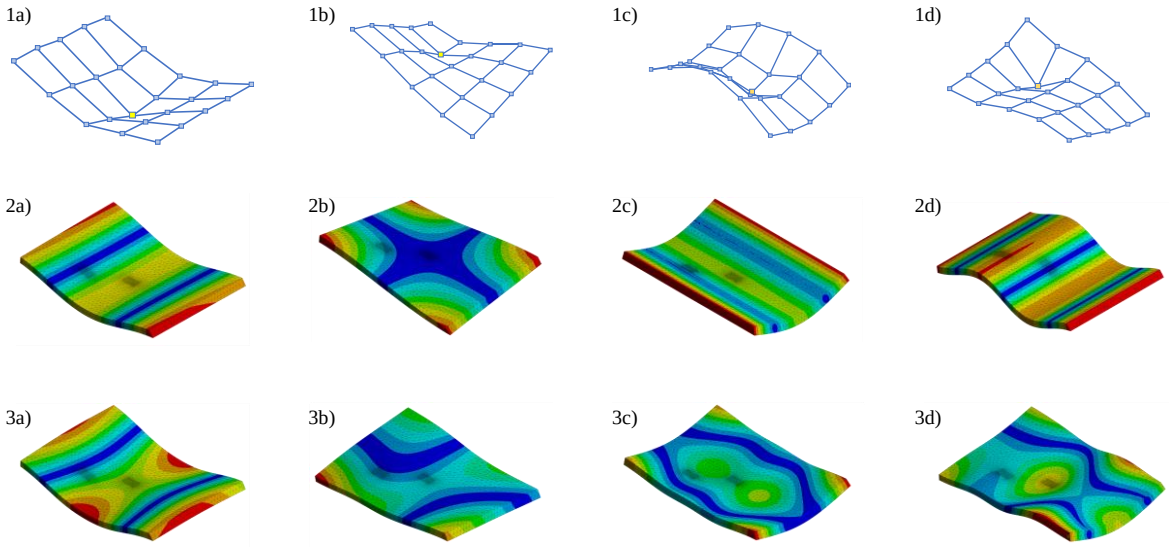

Fig. 23: The first row (1a-1d) depicts the measured mode shapes from [109] and Chapter 6, the second row (2a-2d) depicts the mode shapes out of the ANSYS modal analysis and the third row (3a-3d) depicts the ODS out of the ANSYS harmonic response analysis. The driving point DOFs p22(z) and p33(z) can be recognized by the small yellow squares (row a) and the higher net density (row 2 and 3). Red indicates strong displacement and blue no displacement (nodal areas).

It becomes also apparent that the simulated mode shapes in the second row show clearer shapes than the measured ones. Mode 1 is the first longitudinal bending, mode 2 is the first torsion, mode 3 is the first transversal bending and mode 4 is the second longitudinal bending. This became obvious right from the beginning of the FEM analysis. Therefore, the assumption and simplification were made that the most-closely shaped modes can be expected in a similar frequency range and the target frequency in the optimization was set to the respective $f_{nat,n}$. After optimization, the harmonic response toolbox from ANSYS was used to calculate the ODS at the respective $f_{nat,n}$. The ODS are very similar to the mode shapes from the EMA. The MDOF fit in Chapter 6 and [109] is hence not completely capable of distinguishing the different modes because of the high modal density and the high damping ratios. These two effects cause overlaps of the different modes. Simulative modal analysis can be a valuable companion for the EMA of lithium-ion cells to improve the results.

8.4 Sensitivity analysis of natural frequencies

Fig. 24 depicts the results of the sensitivity analysis. All vertical axes have the same limits for easy comparison of the different sensitivities. The Poisson's values are varied in a wider range because the initial value of 0.01 is already at the lower limit of a reasonable range from 0 to 0.5. Therefore, a similar variation in both directions provides limited insights. In the case of ν_{yz}, ANSYS did not allow calculation for higher values, likely due to an invalid combination of all nine elasticity parameters.

The sensitivity analysis shows that the values of E_z (Fig. 24c), G_{yz} (Fig. 24h) and ν_{xz} (Fig. 24f) can be disregarded for this particular optimization, because they do not influence the natural frequencies. This also means that this approach cannot be used to estimate these parameters. The Poisson's ratios ν_{xy} (Fig. 24d) and ν_{yz} (Fig. 24e) do not have an influence at values below 0.05. An influence is possible for higher values, especially in the case of mode 3 for the Poisson's ratio in the *XY*-plane ν_{xy} in Fig. 24d. The value 0.01 is a common value in literature [39,56,206]. All three Poisson values for the model are set to 0.01 at the beginning of this investigation, accordingly. The validity of this assumption is addressed again in Section 8.5 regarding the harmonic response.

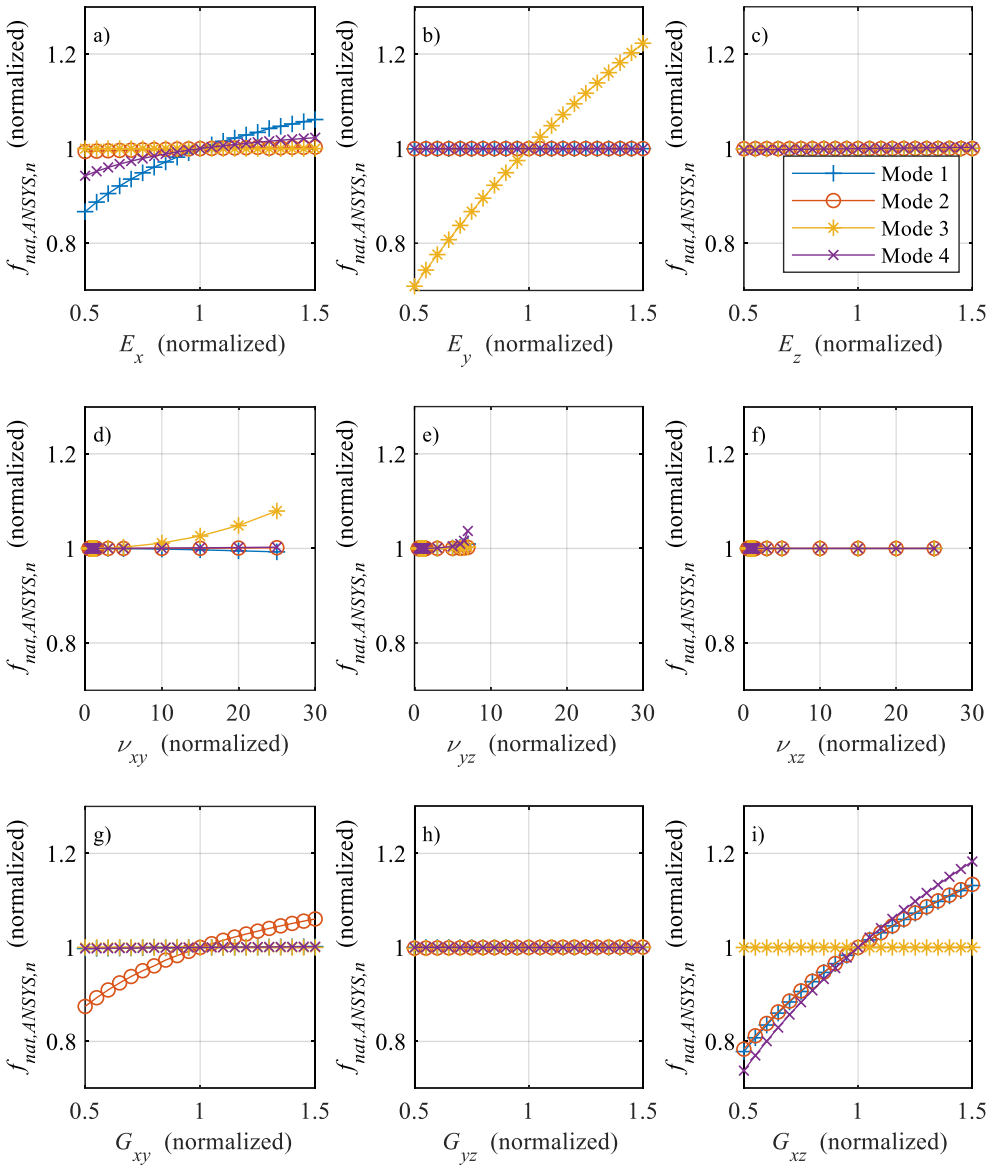

Fig. 24: Sensitivity study for all nine parameters of an orthotropic material with the dimensions x (longitudinal), y (transversal) and z (through-plane) and the respective planes xy, yz and xz

The Young's modulus E_y influences only mode 3 in Fig. 24b, G_{xy} influences only mode 2 in Fig. 24g. Therefore, E_y and G_{xy} can be estimated through the optimization of $f_{nat,ANSYS,2}$ and $f_{nat,ANSYS,3}$. Mode 1 and mode 4 are the first and second longitudinal (x) bending modes. Therefore, $f_{nat,ANSYS,1}$ and $f_{nat,ANSYS,4}$ are both sensitive to E_x and G_{xz} (see Fig. 24a and Fig. 24i). A good fit of experimentally and mathematically determined natural frequencies is one criterion for the successful parameterization of a model based on EMA data. A second is that the order of the modes be correct and that no other modes appear in the frequency range of the modes under consideration. Both requirements are fulfilled. For the optimization up to this point, only the natural frequencies are used as target values and only the results from the two driving point measurements (DPM) are used as an input. Therefore, in the next Section 8.5 the experimental and simulative harmonic response or FRF is compared, including all frequencies and with an outlook to the use of the remaining 48 transfer point measurement (TPM) FRFs [109].

8.5 Harmonic acceleration and stress response

Fig. 25 depicts a comparison of measured and simulated DPM-FRF for both *p33(z)* and *p22(z)* according to the locations given in Fig. 23 with the optimized parameter set.

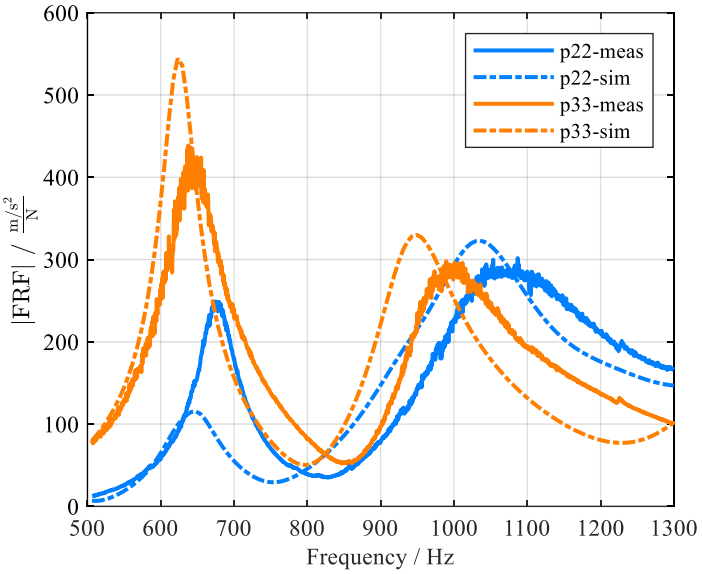

Fig. 25: Measured and FEM-based FRF (acceleration response / force excitation) for both driving points at p22(z) and p33(z)

It is apparent that there is a difference left due to slightly too low natural frequencies and a certain mismatch of the damping ratios in ANSYS as seen in Table 5. Nevertheless, this is already a good approximation.

One goal of the FE modeling of the lithium-ion cells is to obtain better knowledge of stress and strains that occur inside the cell when vibrated. This is the prerequisite for the analysis of fatigue. The parameters E_z, G_{yz} and ν_{xz} cannot be estimated with optimization and natural frequencies as target values because of their insensitivity. The arbitrarily chosen values might be wrong. For this reason, the influence of these material parameters on the model output must be checked. As an example, the Poisson's ratio ν_{xz} is changed from 0.01 to 0.3 and the Young's modulus E_z is divided by 100. The natural frequencies are insensitive to both parameters as depicted in Fig. 24. In contrast, Fig. 26 depicts the calculated normal stress σ_x in longitudinal direction x for the reference case and the two variations of ν_{xz} and E_z. The reference case is based on the parameter set, given in Section 8.2 after optimization.

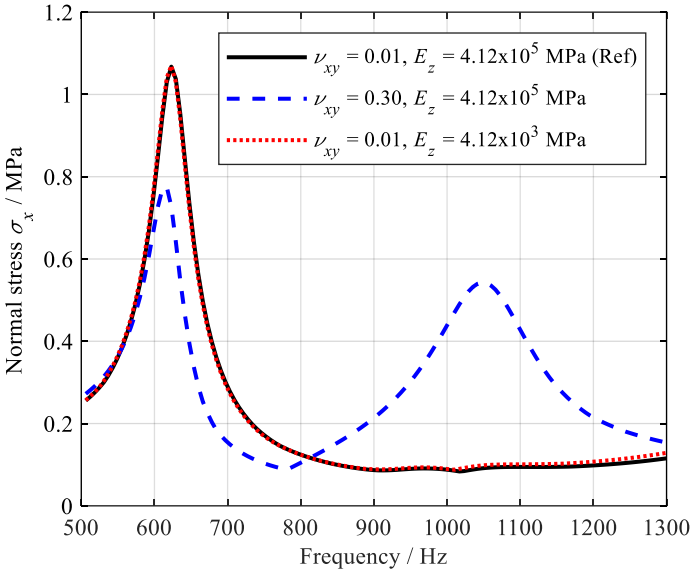

Fig. 26: Simulated normal stress frequency response in the case of harmonic force excitation with 1 N *at p33(z) for two exemplarily varied parameters*

The highest stress in the longitudinal direction is expected to appear at the two longitudinal bending modes. These are mode 1 – first longitudinal bending and mode 4 – second longitudinal bending. In the case of ν_{xz} = 0.3 both expected modes are visible as peaks in the stress response (blue scattered line), while for ν_{xz} = 0.01 (black solid and red dotted lines), the stress is higher for the first longitudinal bending mode (mode 1) and completely vanishes for the second longitudinal bending mode (mode 4).

This means that more than just natural frequencies and DPM are required to build a suitable FE model of a lithium-ion pouch cell. In a next step, the remaining 48 TPM-FRF – 24 for excitation at *p33(z)* and 24 for excitation at *p22(z)* – can be used to further optimize the model. Future optimization should be based on the harmonic response analysis toolbox in ANSYS instead of the modal analysis toolbox. Taking 50 FRF with the various acceleration responses into account gives more information, as it includes a spatial resolution. These calculations are more time-consuming and are out of the scope of this thesis, but are part of the outlook. With the variation of reported elasticity parameters in the literature in mind, it is interesting to continue this approach. This variation certainly also depends on different load conditions and load levels, but it is worthwhile to evaluate further how much modal analysis and harmonic response analysis, especially in combination with other methods, can help to achieve a better understanding of the mechanical behavior of lithium-ion cells.

9 Conclusions and outlook

Chapter 9 summarizes the results of this thesis with respect to the objectives from Section 3.4 and the identified possible failure mechanisms in Section 4.4. Conclusions and outlook are given together for all the objectives.

9.1 Failure mechanisms and failure modes of lithium-ion cells

The investigated lithium-ion cells in this work showed a high durability in the case of vibration. Nevertheless, important conclusions can be drawn. Objective 1 deals with the question which failure mechanisms can occur inside a lithium-ion cell because of vibrations. Objective 2 is about the respective failure modes. A theoretical risk assessment based on the available scientific publications and an incident analysis resulted in Fig. 17, which depicts the possible combinations of vulnerable components, failure mechanisms and failure modes. Fig. 27 is identical to Fig. 17, but with results and outlook being highlighted. Already obtained results are depicted with a blue background, while fields with grey background give an outlook on possible future research tasks.

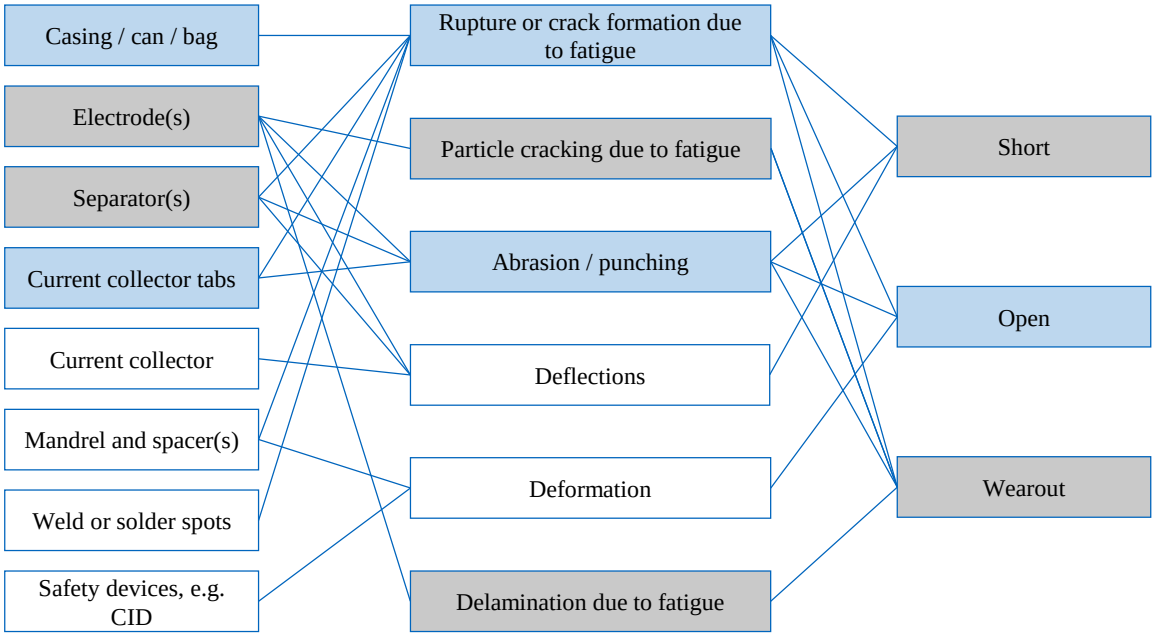

Fig. 27: Depiction of the possible combinations of vulnerable components, failure mechanisms and failure modes. Paths with blue fields can be observed, while paths with grey fields depict the outlook for further research.

The durability tests of 18 different 18650 cells in Chapter 5 showed that the abrasion or punching of the current collector tabs by an insufficiently constrained mandrel is the most relevant failure mechanism for 18650 cells and vibrations. Due to sufficiently large welding areas between current

collector tabs and cell cans, no failure mode occurred for the cells under test. In case of failure, an open (or intermittent) failure mode would have been the most likely consequence of a fully disconnected current collector tab. Cells that have been preloaded with several drops before vibration showed the rupture of the current collector tabs with a subsequent open (or intermittent) failure (see Appendix A.1). The possibility of a short failure due to the generation of electrically conductive particles could be part of further research and is depicted as outlook. A more detailed look on vibration durability of pre-dropped cells is another possible future research topic.

Rupture due to fatigue of the casings during resonance excitation could be observed (see Appendix A.2). The electrodes or separators showed no sign of fatigue in any investigation. Failure mechanisms such as particle cracking, rupture or delamination of electrodes and separators are therefore also depicted as part of the outlook. On the basis of the characterization in Chapter 6 and the simulation results in Chapter 8, the resonance excitation of the lithium-ion pouch cell can be used to induce certain stresses in the cells. Then it can be determined if fatigue occurs in the materials of electrodes and separators, as it sometimes happened for the casings of cylindrical and prismatic cells, as is apparent in Appendix A.2. If fatigue would occur, different failure modes would be possible, e.g., wear out due to the deactivation of electrode particles or shorts due to failures of the separator. The obtained model in Chapter 8 can be further investigated in the future with focus on the sensitivities of the stresses to the material parameters. Measurement with additional strain gauges could give valuable additional information to optimize the fit of the material parameters.

At the beginning of this thesis, there was also the question if a non-instantaneous failure can occur, e.g., if vibration can cause any creeping wear out of the cells. According to the current knowledge, no creeping wear out failure can be expected, and a cell is more likely to have an instantaneous failure.

9.2 Influencing factors

Objective 3 addresses the question what influence the inner cell design and common parameters as SOC, SOH and temperature has on the vibration durability of lithium-ion cells. The comparison of 18 different 18650 cells in Chapter 5 showed the importance of the inner cell design. An insufficiently constrained mandrel can cause serious damage to the current collector tabs inside the cell, which is even more serious if a small welding area is used to connect tab and can to each other. If a cylindrical cell must be used in a harsh environment with severe vibration, the use of a tightly packed cell without inner mandrel and with big welding area is recommended.

The structural response in terms of the natural frequencies and damping ratios of the cells to dynamic excitation, shown for pouch cells in Chapter 6 and for prismatic cells in Chapter 7, revealed high sensitivity to SOC, SOH and temperature. Very interesting observations, e.g., a contrary sensitivity of the damping ratios to the temperature, depending on the cell type, were made. There is a strong indication that the chosen approach to use EMA for the mechanical characterization can capture the effects of interfaces and boundary conditions and is usable, e.g., to detect gaps inside a hard case cell. Regarding the Outlook, it could be investigated if effects such as lithium plating have an observable effect on the structural response.

9.3 Nonlinear behavior of lithium-ion cells and application of fatigue damage spectrum

The investigation of the nonlinearity of lithium-ion cells in the structural response and the evaluation of FDS as a method, e.g., to compare different vibrations regarding their severity for the durability of lithium-ion cells is the focus of Objective 4. Fatigue depends significantly on both the load and the structural response of the structure. The damping ratio, for example, is an important factor with respect to possible fatigue. The application of EMA in Chapter 6 and Chapter 7 showed that the structural dynamics of lithium-ion cells are nonlinear. Besides nonlinearity, the natural frequencies and damping ratios significantly depend on the other parameters, such as SOC, SOH or temperature. Since the characteristic parameters of a lithium-ion cell, therefore, constantly change during operation, the application of methods such as FDS cannot be advised. In addition, FDS is meant to describe classic fatigue, which is a failure mechanism, which could yet not be proven.

9.4 The potential of experimental modal analysis in lithium-ion cell research

The EMA revealed interesting results during this thesis, which are in focus of Objective 5 (EMA potential). The experimental investigations in Chapter 6 and Chapter 7 uncovered the influence of boundary conditions and interfaces, revealed sensitivities to SOC, SOH and temperature and gave indication of the possibility e.g., to detect gaps inside a lithium-ion cell. Chapter 8 investigates the possibility of and limitations to parameterization of FE models with the obtained data. Through this combination of experimental and simulative methods, it might be possible to parameterize parameters which are rare in literature, such as shear moduli, in the future. The fact that a cell on the one hand can be described including all its interfaces and on the other hand is only slightly influenced by the measurement setup, makes EMA a useful addition to other methods such as, tensile component tests, nano-indentation, stress measurements under constrained conditions, etc. The further investigation of the potential of EMA is the most promising continuation of the research included in this thesis in the opinion of the author.

Appendix

This Appendix gives additional information, especially about unpublished results, which offer potential future research questions.

A.1 Combined drop and vibration testing of lithium-ion 18650 cells

Combined loads, which in this case are combined drops with subsequent vibrations according to the procedure described in Subsection 2.2.4, were tested as a pre-study in the course of the master thesis of Christian Schenk [100] supervised by the author of the present thesis. This investigation is briefly included here in the Appendix, because it is one of the possible future research topics in the Outlook of this thesis. The cells were dropped in the axial direction with their minus pole on an aluminum plate after a 2 m long downpipe.

Six cells of the type A123 18650M1A and six cells of the type Molicel IHR18650A with an SOC of 0% were tested. Four cells of each type were dropped, while two cells were kept un-dropped as reference. One of the Molicel IHR18650A failed suddenly with a high ohmic failure (open) at drop number 7. Therefore, the drops for the remaining Molicel IHR18650A were terminated after 7 drops. None of the A123 18650M1A failed because of the drops. After 21 drops, drop testing for the A123 18650M1A was also terminated. The cells were still functioning well and did not show significant signs of degradation prior to vibration. For the vibration testing, a single-sine excitation with an amplitude of 30 g and a frequency of 100 Hz was applied. The cells were connected to the shaker with two-component adhesive. The damping of this connection can be disregarded.

Four out of four dropped A123 18650M1A and two out of four dropped Molicel IHR18650A were vibrated according to the procedure described above. Two of the four A123 18650M1A cells and one of the two Molicel IHR18650A cells failed with an intermittent failure during testing in a time frame of up to three hours. The other cells survived 10 hours of vibration without a sign of failure. Several other 18650 cells of the same or other type were also tested only with vibration and without drops. These cells did not show any sign of degradation. [100]

The failure mode is assumed to be intermittent, because EIS becomes unstable and irreproducible. QEIS during vibration was completely inoperable, while SPEIS could be measured, but showed a high variance of inner resistance R_i. Reproducible measurements were impossible. These are indications for an intermittent failure mode. Since the ohmic part of the impedance is the most affected part, a failure of the current collectors or current collector tabs is likely. This can be finally proven using CT-analysis. Fig. 28 shows a broken current collector tab at the positive tab of one of the failed cells. The result is that dropping a lithium-ion 18650 cell can pre-damage the cell in such a manner that subsequently during vibration, damage of the current collector tabs can occur. This could happen

because of a jelly roll loosened by the drops and the subsequent fatigue of the current collector tabs resulting from the displacement of the jelly roll.

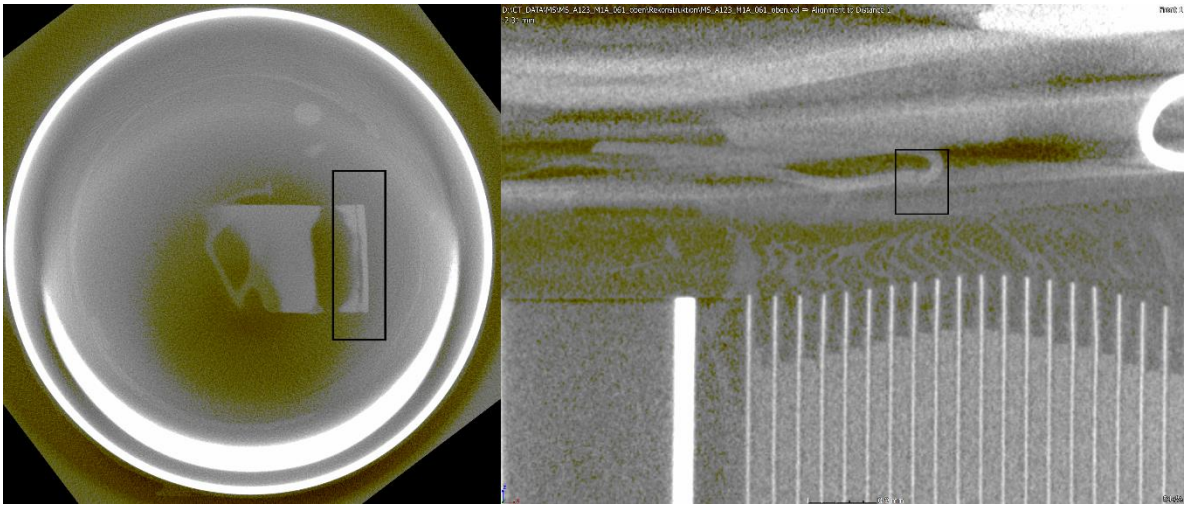

Fig. 28: CT depictions of one tested cell (type A123 18650M1A) with a broken current collector tab at the positive tab of the cell after a combined drop and vibration test

This study is not included in the thesis itself, and details such as exact vibration cycle numbers are disregarded here since it was only a pre-study to evaluate if drops have an impact on vibration durability. For more detailed analysis, the tests must be repeated in a more structured manner.

In future studies, different cell designs should be considered according to the example given in Chapter 5. Other required variations would include both the number of drops and the characteristics of the vibration load profile. Especially interesting are the variation and reduction of drops, since in real-world conditions, the number of drops is limited. Therefore, the estimation of a threshold of critical drops would be of great interest, especially for the purpose of, for example, predictive maintenance of power tools. Another interesting research question would be the diagnosis or prediction of such failures.

A.2 Casing failures due to resonance excitation

The impact of resonance excitation on lithium-ion cells has been tested in two master theses, supervised by the author. Tillinger excited the prismatic lithium-ion cells that are investigated in Chapter 7 at their resonance with varying excitation levels and cell support on three edges for the connection with the shaker. The resulting failure of the cell casing, probably due to fatigue is depicted in Fig. 29. [197]

Fig. 29: Broken casing probably due to resonances excited during a sine sweep test from 50–1000 Hz (sweep rate 0.1 oct/min) with stepwise increased amplitude from 1–15 g (1 g increment) with fixation at three edges [197]

Schenk used resonance excitation for the testing of cylindrical lithium-ion cells. A Molicel IHR18650A glued with two component adhesives to the shaker at its positive pole also caused the cell to open. This casing failure is depicted in Fig. 30. [100]

Fig. 30: 18650 cell Molicel IHR18650C with broken casing after resonance excitation. During the test the positive pole of the cell was glued to the shaker adapter, and the resonance caused the cell to break at the connection of the can and the positive cell cap [100].

A.3 List of lithium-ion cell related recalls

Table 6 depicts all the recalls, which are investigated in Section 4.1.

Table 6: List of analyzed recalls with the respective web reference and the number of failed items k_{fail} and the number of sold items n_{sold}. This list does not include the eliminated recalls according to Section 4.1.

Recall date	Web reference	Company	Product	Product category	Cell type	k_{fail}	n_{sold}
2000/10/13	http://www.cpsc.gov/en/Recalls/2001/CPSC-Dell-Announce-Recall-of-Batteries-for-Notebook-Computers/	Dell	DELL Battery Module Rechargeable Li-Ion Battery	Laptop	Lithium -ion	1	27,000
2001/05/03	http://www.cpsc.gov/en/Recalls/2001/CPSC-Dell-Computer-Corp-Announce-Recall-of-Notebook-Computer-Batteries/	Dell	Notebook Computer Batteries	Laptop	Lithium -ion	1	284,000
2001/11/13	http://www.cpsc.gov/en/Recalls/2002/CPSC-Computer-Distributors-Announce-Recall-of-Batteries-for-Notebook-Computers/	Computer Distributors	Batteries for Notebook Computers	Laptop	Lithium -ion	2	13,000
2004/01/23	http://www.cpsc.gov/en/Recalls/2004/CPSC-Kyocera-Wireless-Corp-Announce-Recall-of-Batteries-in-Smartphone-Cell-Phones-/	Kyocera Wireless	Batteries in Kyocera Cell Phones (Model 7135 Smartphones)	Electronics: Cell phones	Lithium -ion	4	140,000
2004/08/19	http://www.cpsc.gov/en/Recalls/2004/CPSC-Apple-Announce-Recall-of-PowerBook-Computer-Batteries-/	Apple	Rechargeable batteries used in 15-inch PowerBook G4 computers	Laptop	Lithium -ion	4	28,000
2005/05/20	http://www.cpsc.gov/en/Recalls/2005/CPSC-Apple-Announce-Recall-of-iBook-and-PowerBook-Computer-Batteries/	Apple	Rechargeable batteries for iBook G4 and PowerBook G4 computers	Laptop	Lithium -ion	6	128,000
2005/06/21	http://www.cpsc.gov/en/Recalls/2005/CPSC-Belkin-Announce-Recall-of-Batteries-Sold-with-Bluetooth-GPS-Navigation-System/	Belkin	Li-Polymer battery pack sold with Bluetooth™ Global Positioning System (GPS) Navigation System	Electronics: Navigation	LiPo	15	10,300
2005/06/22	http://www.cpsc.gov/en/Recalls/2005/CPSC-Battery-Biz-Announce-Recall-of-Notebook-Computer-Batteries/	Battery-Biz	Hi-Capacity® rechargeable notebook computer batteries	Laptop	Lithium -ion	6	10,000
2005/10/14	http://www.cpsc.gov/en/Recalls/2006/CPSC-Hewlett-Packard-Company-Announce-Recall-of-Notebook-Computer-Batteries/	HP	HP and Compaq Notebook Computer Battery Packs	Laptop	Lithium -ion	16	135,000
2005/11/08	http://www.cpsc.gov/en/Recalls/2006/CPSC-Nikon-Inc-Announce-Recall-to-Replace-Rechargeable-Battery-Packs-Sold-with-Digital-SLR-Cameras/	Nikon Inc.	Nikon Rechargeable Battery Packs with Model Number EN-EL3	Electronics: Digicam	Lithium -ion	4	710,000
2005/12/16	http://www.cpsc.gov/en/Recalls/2006/CPSC-Dell-Announce-Recall-of-Notebook-Computer-Batteries/	Dell	Dell Notebook Computer Batteries	Laptop	Lithium -ion	3	22,000
2005/12/22	http://www.cpsc.gov/en/Recalls/2006/CPSC-Petters-Consumer-Brands-LLC-Announce-Recall-of-Batteries-Found-In-Polaroid-Portable-DVD-Players/	Petters Consumer Brands LLC	Battery packs used with Polaroid-brand portable DVD players	Electronics: DVD player	Lithium -ion	8	165,000
2006/02/17	http://www.cpsc.gov/en/Recalls/2006/Polycom-Inc-Recalls-Conference-Phone-Batteries-for-Fire-Hazard/	Polycom Inc.	Lithium-Ion batteries in SoundStation2W wireless conference phone	Electronics: Wireless phone	Lithium -ion	2	27,700
2006/04/20	http://www.cpsc.gov/en/Recalls/2006/HP-Recalls-Notebook-Computer-Batteries-Due-to-Fire-Hazard/	HP	HP and Compaq Notebook Computer Batteries	Laptop	Lithium -ion	20	15,700
2006/08/15	http://www.cpsc.gov/en/recalls/2006/dell-announces-recall-of-notebook-computer-batteries-due-to-fire-hazard/	Dell	Dell-branded lithium-ion batteries made with cells manufactured by Sony	Laptop	Lithium -ion	6	4,200,000

2006/08/24	http://www.cpsc.gov/en/recalls/2006/apple-announces-recall-of-batteries-used-in-previous-ibook-and-powerbook-computers-due-to-fire-hazard/	Apple	Rechargeable, lithium-ion batteries with cells manufactured by Sony for certain previous iBook G4 and PowerBook G4 notebook computers only	Laptop	Lithium -ion	9	1,800,000
2006/09/28	http://www.cpsc.gov/en/Recalls/2006/Lenovo-and-IBM-Announce-Recall-of-ThinkPad-Notebook-Computer-Batteries-Due-to-Fire-Hazard/	Lenovo & IBM	Rechargeable, lithium-ion batteries used in ThinkPad notebook computers	Laptop	Lithium -ion	1	526,000
2006/10/23	http://www.cpsc.gov/en/Recalls/2007/Sony-Recalls-Notebook-Computer-Batteries-Due-to-Previous-Fires/	Sony	Rechargeable, lithium-ion batteries containing Sony cells used in Fujitsu Computer Systems Corporation, Gateway Inc., Sony Electronics Inc., and Toshiba America Information Systems Inc. notebook computers.	Laptop	Lithium -ion	16	3,420,000
2007/02/13	http://www.cpsc.gov/en/Recalls/2007/Battery-Packs-for-Toy-Vehicles-Recalled-by-JAKKS-Pacific-Due-to-Fire-Hazard/	JAKKS	Battery Packs for Toy Vehicles	Toys	LiPo	33	245,000
2007/03/01	http://www.cpsc.gov/en/Recalls/2007/Lenovo-Recalls-ThinkPad-Notebook-PC-Extended-Life-Batteries-Due-to-Fire-Hazard/	Lenovo	Lithium-ion extended-life batteries used in ThinkPad notebook computers	Laptop	Lithium -ion	4	205,000
2007/03/27	http://www.cpsc.gov/en/Recalls/2007/Estes-Cox-Radio-Control-Airplanes-with-Lithium-Polymer-Batteries-Recalled-for-Fire-Hazard/	Estes-Cox	Radio Control Model Airplanes (Models 4153 and 4161) with Lithium Polymer Batteries	Toys	LiPo	9	66,000
2007/04/25	http://www.cpsc.gov/en/Recalls/2007/Acer-America-Corporation-Recalls-Notebook-Computer-Batteries-Due-to-Previous-Fires/	Acer	Rechargeable lithium-ion batteries containing Sony-made cells used in Acer notebook computers.	Laptop	Lithium -ion	16	27,000
2007/06/19	http://www.cpsc.gov/en/Recalls/2007/Gateway-Inc-Recalls-Notebook-Computer-Batteries-Due-to-Fire-Hazard/	Gateway Inc.	Gateway Lithium-Ion Battery Packs	Laptop	Lithium -ion	4	14,000
2007/10/23	http://www.cpsc.gov/en/Recalls/2005/CPSC-Mintek-Digital-Inc-Announce-Recall-of-Portable-DVD-Player-Batteries/	Mintek Digital Inc.	Portable DVD player battery packs	Electronics: DVD player	LiPo	10	116,000
2008/07/24	http://www.cpsc.gov/en/Recalls/2008/Remote-Controlled-Helicopter-Toys-Recalled-by-Innovage-Due-to-Fire-and-Burn-Hazards/	Innovage	"Sky Scrambler" and "The Sharper Image" Wireless Indoor Helicopters	Toys	Lithium -ion	2	685,000
2008/08/19	http://www.cpsc.gov/en/Recalls/2008/Hobbico-Inc-Recalls-Batteries-Used-In-Radio-Controlled-Helicopters-Due-to-Fire-Hazard/	Hobbico Inc.	Batteries Used in Radio-Controlled Helicopter Kits	Toys	LiPo	28	11,000
2008/09/03	http://www.cpsc.gov/en/Recalls/2008/Cordless-Screwdrivers-Recalled-by-Menards-Due-to-Fire-and-Burn-Hazards/	Menards	MasterForce 3.6-volt Cordless Screwdrivers	Misc: Screwdriver	Lithium -ion	3	42,000
2008/09/04	http://www.cpsc.gov/en/Recalls/2008/Sony-Recalls-Notebook-Computers-Due-to-Burn-Hazard/	Sony	Certain VAIO TZ-series Notebook Computers	Laptop	Lithium -ion	15	73,000
2008/10/14	http://www.cpsc.gov/en/Recalls/2009/Wireless-Headset-Batteries-Recalled-by-GN-Netcom-Due-to-Fire-Hazard/	GN Netcom	GN9120 Wireless Headsets	Electronics: Headset	Lithium -ion	47	1,200,000
2008/10/30	http://www.cpsc.gov/en/Recalls/2009/PC-Notebook-Computer-Batteries-Recalled-Due-to-Fire-and-Burn-Hazard/	HP, Toshiba, Dell	Lithium-Ion Batteries used in Hewlett-Packard, Toshiba, and Dell	Laptop	Lithium -ion	19	100,000

			Notebook Computers				
2009/10/15	http://www.cpsc.gov/en/Recalls/2009/HP-Recalls-Notebook-Computer-Batteries-Due-to-Fire-Hazard/	HP	Lithium-Ion batteries used in Hewlett-Packard and Compaq notebook computers	Laptop	Lithium -ion	2	70,000
2010/05/21	http://www.cpsc.gov/en/recalls/2010/hp-expands-recall-of-notebook-computer-batteries-due-to-fire-hazard/	HP	Lithium-Ion batteries used in Hewlett-Packard and Compaq notebook computers	Laptop	Lithium -ion	38	54,000
2010/06/30	http://www.cpsc.gov/en/Recalls/2010/Sony-Recalls-VAIO-Laptop-Computers-Due-to-Burn-Hazard/	Sony	Notebook computers	Laptop	Lithium -ion	30	233,000
2011/04/19	http://www.cpsc.gov/en/Recalls/2011/Lithium-Ion-Batteries-Used-with-Bicycle-Lights-Recalled-by-GeoManGear-Due-to-Fire-Hazard/	GeoManGear	Lithium-Ion batteries used with Magicshine bicycle lights	Lights	Lithium -ion	3	18,100
2011/05/27	http://www.cpsc.gov/en/Recalls/2011/HP-Expands-Recall-of-Notebook-Computer-Batteries-Due-to-Fire-Hazard/	HP	Lithium-ion batteries used in HP and Compaq notebook computers	Laptop	Lithium -ion	40	162,600
2011/11/30	http://www.cpsc.gov/en/Recalls/2012/Rocketfish-Battery-Case-for-iPhone-3G3GS-Recalled-by-Best-Buy-Due-to-Fire-Hazard/	Rocketfish	Rocketfish™ Model RF-KL12 Mobile Battery Cases for iPhone 3G and 3GS	Pack: Battery power	Lithium -ion	14	32,000
2012/07/11	http://www.cpsc.gov/en/Recalls/2012/Nikon-Recalls-Rechargeable-Battery-Packs-Sold-with-Digital-SLR-Cameras-Due-to-Burn-Hazard/	Nikon	Nikon digital SLR camera battery packs	Electronics: Digicam	Lithium -ion	7	201,200
2013/02/26	http://www.cpsc.gov/en/Recalls/2013/One-World-Technologies-Recalls-Ryobi-Cordless-Tool-Battery-Pack/	Ryobi	Ryobi Lithium 18 V 4Ah Battery Pack	Pack: Battery power	Lithium -ion	4	56,400
2014/03/27	http://www.cpsc.gov/en/Recalls/2014/Lenovo-Recalls-Battery-Packs-for-ThinkPad-Notebook-Computers/	Lenovo	ThinkPad notebook computer battery packs	Laptop	Lithium -ion	2	37,400
2014/04/29	http://www.cpsc.gov/en/Recalls/2014/DGL-Group-Recalls-Vibe-USB-Mobile-Power-Bars/	DGL Group	Vibe USB Mobile Power Bar	Pack: Battery power	Lithium -ion	6	99,000
2014/11/25	http://www.cpsc.gov/en/Recalls/2015/Goal-Zero-Recalls-Battery-Packs/	Goal Zero	Goal Zero Sherpa brand 50 and 120 rechargeable battery packs	Pack: Battery power	Lithium -ion	1	10,110
2015/04/21	http://www.cpsc.gov/en/Recalls/2015/Lenovo-Expands-Recall-of-Battery-Packs-for-ThinkPad-Notebook-Computers/	Lenovo	ThinkPad notebook computer battery packs	Laptop	Lithium -ion	4	166,500
2015/04/28	http://www.cpsc.gov/en/Recalls/2015/Whistler-Recalls-Jump-and-Go-Portable-Jumpstart-and-Power-Supply-Units/	Whistler	Portable jumpstart power supplies	Pack: Battery power	Lithium -ion	45	10,400
2015/06/03	http://www.cpsc.gov/en/Recalls/2015/Apple-Recalls-Beats-Pill-XL-Portable-Wireless-Speakers/	Apple	Beats Pill XL speaker	Electronics: Speaker	Lithium -ion	8	233,000
2015/07/31	http://www.cpsc.gov/en/recalls/2015/nvidia-recalls-tablet-computers/	Nvidia	NVIDIA SHIELD tablet computers	Electronics: Tablet	Lithium -ion	4	88,000
2015/11/12	http://www.cpsc.gov/en/recalls/2016/pny-recalls-portable-lithium-polymer-battery-packs/	PNY	Portable Lithium Polymer Battery Packs	Pack: Battery power	LiPo	1	56,800
2016/06/06	http://www.cpsc.gov/en/Recalls/2016/Self-Balancing-Scooters-Hoverboards-Recalled-by-10-Firms/	10 companies	Self-Balancing Scooters/Hoverboards Recalled by 10 Firms	Mobility: Hoverboards	Lithium -ion	99	501,000
2016/10/13	https://www.cpsc.gov/Recalls/2017/samsung-Expands-Recall-of-Galaxy-Note7-Smartphones-Based-on-Additional-Incidents-with-Replacement-Phones	Samsung	Galaxy Note7	Electronics: Smartphone	Lithium -ion	96	1,900,000

List of Figures

List of Tables

References

[1] B. Scrosati, J. Garche, Lithium batteries: Status, prospects and future, Journal of Power Sources 195 (2010) 2419–2430. https://doi.org/10.1016/j.jpowsour.2009.11.048.

[2] B. Liu, Y. Jia, J. Li, S. Yin, C. Yuan, Z. Hu, L. Wang, Y. Li, J. Xu, Safety issues caused by internal short circuits in lithium-ion batteries, J. Mater. Chem. A 6 (2018) 21475–21484. https://doi.org/10.1039/C8TA08997C.

[3] UNFCCC, Paris Agreement, 2015.

[4] L.W. Traub, Range and Endurance Estimates for Battery-Powered Aircraft, Journal of Aircraft 48 (2011) 703–707. https://doi.org/10.2514/1.C031027.

[5] A. Muetze, S.R. Durkee, Conceptual design of an electric helicopter powertrain, in: PEMD 2010, Brighton, UK, IET, Stevenage, 2010, p. 353.

[6] C.M. Reid, M.A. Manzo, M.J. Logan, Performance Characterization of a Lithium-Ion Gel Polymer Battery Power Supply System for an Unmanned Aerial Vehicle: SAE Transactions, 0096736X 113 (2004) 1793–1800.

[7] Europäische Kommission, Flightpath 2050: Europe's vision for aviation ; maintaining global leadership and serving society's needs ; report of the High-Level Group on Aviation Research, Publ. Off. of the Europ. Union, Luxembourg, 2011.

[8] Guidelines and Methods for Conducting the Safety Assessment Process on Civil Airborne Systems and Equipment, SAE International, 400 Commonwealth Drive, Warrendale, PA, United States, 1996.

[9] National Highway Traffic Safety Administration, Chevrolet Volt Battery Incident Overview Report, Washington DC, 2012.

[10] NTSB, Auxiliary Power Unit Battery Fire Japan Airlines Boeing 787-8, Boston, MA January 7, 2013, 2014.

[11] Q. Wang, P. Ping, X. Zhao, G. Chu, J. Sun, C. Chen, Thermal runaway caused fire and explosion of lithium ion battery, Journal of Power Sources 208 (2012) 210–224. https://doi.org/10.1016/j.jpowsour.2012.02.038.

[12] N. Williard, W. He, C. Hendricks, M. Pecht, Lessons Learned from the 787 Dreamliner Issue on Lithium-Ion Battery Reliability, Energies 6 (2013) 4682–4695. https://doi.org/10.3390/en6094682.

[13] J. Xuan, X.-H. Wang, L.-Z. Wang, Safety Assesment of Lithium-Ion Battery based on FMEA Method, in: 13th International Conference on Probabilistic Safety Assesment and

Management (PSAM 13), Seoul, Korea, John Wiley & Sons, Inc, Hoboken, NJ, USA, 2016, pp. 1–22.

[14] Samsung confirms battery faults as cause of Note 7 fires, 2018. https://www.bbc.com/news/business-38714461 (accessed 8 January 2019).

[15] X. Feng, M. Ouyang, X. Liu, L. Lu, Y. Xia, X. He, Thermal runaway mechanism of lithium ion battery for electric vehicles: A review, Energy Storage Materials 10 (2018) 246–267. https://doi.org/10.1016/j.ensm.2017.05.013.

[16] X. Kong, Y. Zheng, M. Ouyang, L. Lu, J. Li, Z. Zhang, Fault diagnosis and quantitative analysis of micro-short circuits for lithium-ion batteries in battery packs, Journal of Power Sources 395 (2018) 358–368. https://doi.org/10.1016/j.jpowsour.2018.05.097.

[17] A. Barai, K. Uddin, J. Chevalier, G.H. Chouchelamane, A. McGordon, J. Low, P. Jennings, Transportation Safety of Lithium Iron Phosphate Batteries - A Feasibility Study of Storing at Very Low States of Charge, Sci. Rep. 7 (2017) 5128. https://doi.org/10.1038/s41598-017-05438-2.

[18] M. Sheikh, A. Elmarakbi, M. Elkady, Thermal runaway detection of cylindrical 18650 lithium-ion battery under quasi-static loading conditions, Journal of Power Sources 370 (2017) 61–70. https://doi.org/10.1016/j.jpowsour.2017.10.013.

[19] L. Tang, J. Zhang, P. Cheng, Homogenized modeling methodology for 18650 lithium-ion battery module under large deformation, PLoS ONE 12 (2017) e0181882. https://doi.org/10.1371/journal.pone.0181882.

[20] H. Wang, E. Lara-Curzio, E.T. Rule, C.S. Winchester, Mechanical abuse simulation and thermal runaway risks of large-format Li-ion batteries, Journal of Power Sources 342 (2017) 913–920. https://doi.org/10.1016/j.jpowsour.2016.12.111.

[21] C. Zhang, J. Xu, L. Cao, Z. Wu, S. Santhanagopalan, Constitutive behavior and progressive mechanical failure of electrodes in lithium-ion batteries, Journal of Power Sources 357 (2017) 126–137. https://doi.org/10.1016/j.jpowsour.2017.04.103.

[22] M. Gilaki, I. Avdeev, Impact modeling of cylindrical lithium-ion battery cells: A heterogeneous approach, Journal of Power Sources 328 (2016) 443–451. https://doi.org/10.1016/j.jpowsour.2016.08.034.

[23] W. Wang, S. Yang, F. Sun, Q. Yu, The Clay-like Mechanics Model of Cylindrical Lithium-Ion Battery Cells under Radial Compression, Energy Procedia 88 (2016) 652–655. https://doi.org/10.1016/j.egypro.2016.06.093.

[24] J. Xu, B. Liu, X. Wang, D. Hu, Computational model of 18650 lithium-ion battery with coupled strain rate and SOC dependencies, Applied Energy 172 (2016) 180–189. https://doi.org/10.1016/j.apenergy.2016.03.108.

[25] X. Zhang, E. Sahraei, K. Wang, Deformation and failure characteristics of four types of lithium-ion battery separators, Journal of Power Sources 327 (2016) 693–701. https://doi.org/10.1016/j.jpowsour.2016.07.078.

[26] J. Zhu, X. Zhang, E. Sahraei, T. Wierzbicki, Deformation and failure mechanisms of 18650 battery cells under axial compression, Journal of Power Sources 336 (2016) 332–340. https://doi.org/10.1016/j.jpowsour.2016.10.064.

[27] W.-J. Lai, M.Y. Ali, J. Pan, Mechanical behavior of representative volume elements of lithium-ion battery modules under various loading conditions, Journal of Power Sources 248 (2014) 789–808. https://doi.org/10.1016/j.jpowsour.2013.09.128.

[28] E. Sahraei, J. Meier, T. Wierzbicki, Characterizing and modeling mechanical properties and onset of short circuit for three types of lithium-ion pouch cells, Journal of Power Sources 247 (2014) 503–516. https://doi.org/10.1016/j.jpowsour.2013.08.056.

[29] M.Y. Ali, W.-J. Lai, J. Pan, Computational models for simulations of lithium-ion battery cells under constrained compression tests, Journal of Power Sources 242 (2013) 325–340. https://doi.org/10.1016/j.jpowsour.2013.05.022.

[30] T. Wierzbicki, E. Sahraei, Homogenized mechanical properties for the jellyroll of cylindrical Lithium-ion cells, Journal of Power Sources 241 (2013) 467–476. https://doi.org/10.1016/j.jpowsour.2013.04.135.

[31] E. Sahraei, J. Campbell, T. Wierzbicki, Modeling and short circuit detection of 18650 Li-ion cells under mechanical abuse conditions, Journal of Power Sources 220 (2012) 360–372. https://doi.org/10.1016/j.jpowsour.2012.07.057.

[32] S. Kalnaus, H. Wang, T.R. Watkins, A. Kumar, S. Simunovic, J.A. Turner, P. Gorney, Effect of packaging and cooling plates on mechanical response and failure characteristics of automotive Li-ion battery modules, Journal of Power Sources 403 (2018) 20–26. https://doi.org/10.1016/j.jpowsour.2018.09.071.

[33] V. Vijayaraghavan, A. Garg, L. Gao, Fracture mechanics modelling of lithium-ion batteries under pinch torsion test, Measurement 114 (2018) 382–389. https://doi.org/10.1016/j.measurement.2017.10.008.

[34] B. Liu, H. Zhao, H. Yu, J. Li, J. Xu, Multiphysics computational framework for cylindrical lithium-ion batteries under mechanical abusive loading, Electrochimica Acta 256 (2017) 172–184. https://doi.org/10.1016/j.electacta.2017.10.045.

[35] H. Luo, Y. Xia, Q. Zhou, Mechanical damage in a lithium-ion pouch cell under indentation loads, Journal of Power Sources 357 (2017) 61–70. https://doi.org/10.1016/j.jpowsour.2017.04.101.

[36] J. Marcicki, M. Zhu, A. Bartlett, X.G. Yang, Y. Chen, T. Miller, P. L'Eplattenier, I. Caldichoury, A Simulation Framework for Battery Cell Impact Safety Modeling Using LS-DYNA, J. Electrochem. Soc. 164 (2017) A6440-A6448. https://doi.org/10.1149/2.0661701jes.

[37] M. Raffler, A. Sevarin, C. Ellersdorfer, S.F. Heindl, C. Breitfuss, W. Sinz, Finite element model approach of a cylindrical lithium ion battery cell with a focus on minimization of the computational effort and short circuit prediction, Journal of Power Sources 360 (2017) 605–617. https://doi.org/10.1016/j.jpowsour.2017.06.028.

[38] H. Wang, T.R. Watkins, S. Simunovic, P.R. Bingham, S. Allu, J.A. Turner, Fragmentation of copper current collectors in Li-ion batteries during spherical indentation, Journal of Power Sources 364 (2017) 432–436. https://doi.org/10.1016/j.jpowsour.2017.08.068.

[39] A. Kumar, S. Kalnaus, S. Simunovic, S. Gorti, S. Allu, J.A. Turner, Communication—Indentation of Li-Ion Pouch Cell: Effect of Material Homogenization on Prediction of Internal Short Circuit, J. Electrochem. Soc. 163 (2016) A2494-A2496. https://doi.org/10.1149/2.0151613jes.

[40] B. Liu, S. Yin, J. Xu, Integrated computation model of lithium-ion battery subject to nail penetration, Applied Energy 183 (2016) 278–289. https://doi.org/10.1016/j.apenergy.2016.08.101.

[41] E. Sahraei, E. Bosco, B. Dixon, B. Lai, Microscale failure mechanisms leading to internal short circuit in Li-ion batteries under complex loading scenarios, Journal of Power Sources 319 (2016) 56–65. https://doi.org/10.1016/j.jpowsour.2016.04.005.

[42] H. Wang, S. Simunovic, H. Maleki, J.N. Howard, J.A. Hallmark, Internal configuration of prismatic lithium-ion cells at the onset of mechanically induced short circuit, Journal of Power Sources 306 (2016) 424–430. https://doi.org/10.1016/j.jpowsour.2015.12.026.

[43] M.Y. Ali, W.-J. Lai, J. Pan, Computational models for simulation of a lithium-ion battery module specimen under punch indentation, Journal of Power Sources 273 (2015) 448–459. https://doi.org/10.1016/j.jpowsour.2014.09.072.

[44] E. Sahraei, M. Kahn, J. Meier, T. Wierzbicki, Modelling of cracks developed in lithium-ion cells under mechanical loading, RSC Adv 5 (2015) 80369–80380. https://doi.org/10.1039/C5RA17865G.

[45] C. Zhang, S. Santhanagopalan, M.A. Sprague, A.A. Pesaran, Coupled mechanical-electrical-thermal modeling for short-circuit prediction in a lithium-ion cell under mechanical abuse, Journal of Power Sources 290 (2015) 102–113. https://doi.org/10.1016/j.jpowsour.2015.04.162.

[46] I. Avdeev, M. Gilaki, Structural analysis and experimental characterization of cylindrical lithium-ion battery cells subject to lateral impact, Journal of Power Sources 271 (2014) 382–391. https://doi.org/10.1016/j.jpowsour.2014.08.014.

[47] J. Lamb, C.J. Orendorff, Evaluation of mechanical abuse techniques in lithium ion batteries, Journal of Power Sources 247 (2014) 189–196. https://doi.org/10.1016/j.jpowsour.2013.08.066.

[48] Y. Xia, T. Wierzbicki, E. Sahraei, X. Zhang, Damage of cells and battery packs due to ground impact, Journal of Power Sources 267 (2014) 78–97. https://doi.org/10.1016/j.jpowsour.2014.05.078.

[49] L. Greve, C. Fehrenbach, Mechanical testing and macro-mechanical finite element simulation of the deformation, fracture, and short circuit initiation of cylindrical Lithium ion battery cells,

Journal of Power Sources 214 (2012) 377–385.
https://doi.org/10.1016/j.jpowsour.2012.04.055.

[50] D. Sauerteig, N. Hanselmann, A. Arzberger, H. Reinshagen, S. Ivanov, A. Bund, Electrochemical-mechanical coupled modeling and parameterization of swelling and ionic transport in lithium-ion batteries, Journal of Power Sources 378 (2018) 235–247. https://doi.org/10.1016/j.jpowsour.2017.12.044.

[51] H. Dai, C. Yu, X. Wei, Z. Sun, State of charge estimation for lithium-ion pouch batteries based on stress measurement, Energy 129 (2017) 16–27. https://doi.org/10.1016/j.energy.2017.04.099.

[52] K.-Y. Oh, B.I. Epureanu, A phenomenological force model of Li-ion battery packs for enhanced performance and health management, Journal of Power Sources 365 (2017) 220–229. https://doi.org/10.1016/j.jpowsour.2017.08.058.

[53] E. Gibellini, C. Lanciotti, R. Giovanardi, M. Bononi, G. Davolio, A. Marchetti, C. Fontanesi, Dimensional Changes in Automotive Pouch Li-Ion Cells: A Combined Thermo-Mechanical/Electrochemical Study, J. Electrochem. Soc. 163 (2016) A2304-A2311. https://doi.org/10.1149/2.0831610jes.

[54] X.M. Liu, C.B. Arnold, Effects of Cycling Ranges on Stress and Capacity Fade in Lithium-Ion Pouch Cells, J. Electrochem. Soc. 163 (2016) A2501-A2507. https://doi.org/10.1149/2.1131610jes.

[55] J. Luo, C.Y. Dai, Z. Wang, K. Liu, W.G. Mao, D.N. Fang, X. Chen, In-situ measurements of mechanical and volume change of LiCoO 2 lithium-ion batteries during repeated charge–discharge cycling by using digital image correlation, Measurement 94 (2016) 759–770. https://doi.org/10.1016/j.measurement.2016.09.023.

[56] K.-Y. Oh, B.I. Epureanu, J.B. Siegel, A.G. Stefanopoulou, Phenomenological force and swelling models for rechargeable lithium-ion battery cells, Journal of Power Sources 310 (2016) 118–129. https://doi.org/10.1016/j.jpowsour.2016.01.103.

[57] B. Rieger, S. Schlueter, S.V. Erhard, J. Schmalz, G. Reinhart, A. Jossen, Multi-scale investigation of thickness changes in a commercial pouch type lithium-ion battery, Journal of Energy Storage 6 (2016) 213–221. https://doi.org/10.1016/j.est.2016.01.006.

[58] B. Rieger, S.V. Erhard, K. Rumpf, A. Jossen, A New Method to Model the Thickness Change of a Commercial Pouch Cell during Discharge, J. Electrochem. Soc. 163 (2016) A1566-A1575. https://doi.org/10.1149/2.0441608jes.

[59] S.P. Nadimpalli, V.A. Sethuraman, D.P. Abraham, A.F. Bower, P.R. Guduru, Stress Evolution in Lithium-Ion Composite Electrodes during Electrochemical Cycling and Resulting Internal Pressures on the Cell Casing, J. Electrochem. Soc. 162 (2015) A2656-A2663. https://doi.org/10.1149/2.0341514jes.

[60] J. Cannarella, C.B. Arnold, State of health and charge measurements in lithium-ion batteries using mechanical stress, Journal of Power Sources 269 (2014) 7–14. https://doi.org/10.1016/j.jpowsour.2014.07.003.

[61] J. Cannarella, C.B. Arnold, Stress evolution and capacity fade in constrained lithium-ion pouch cells, Journal of Power Sources 245 (2014) 745–751. https://doi.org/10.1016/j.jpowsour.2013.06.165.

[62] P.K. Leung, C. Moreno, I. Masters, S. Hazra, B. Conde, M.R. Mohamed, R.J. Dashwood, R. Bhagat, Real-time displacement and strain mappings of lithium-ion batteries using three-dimensional digital image correlation, Journal of Power Sources 271 (2014) 82–86. https://doi.org/10.1016/j.jpowsour.2014.07.184.

[63] A. Mukhopadhyay, B.W. Sheldon, Deformation and stress in electrode materials for Li-ion batteries, Progress in Materials Science 63 (2014) 58–116. https://doi.org/10.1016/j.pmatsci.2014.02.001.

[64] K.-Y. Oh, J.B. Siegel, L. Secondo, S.U. Kim, N.A. Samad, J. Qin, D. Anderson, K. Garikipati, A. Knobloch, B.I. Epureanu, C.W. Monroe, A. Stefanopoulou, Rate dependence of swelling in lithium-ion cells, Journal of Power Sources 267 (2014) 197–202. https://doi.org/10.1016/j.jpowsour.2014.05.039.

[65] R. Fu, M. Xiao, S.-Y. Choe, Modeling, validation and analysis of mechanical stress generation and dimension changes of a pouch type high power Li-ion battery, Journal of Power Sources 224 (2013) 211–224. https://doi.org/10.1016/j.jpowsour.2012.09.096.

[66] V.A. Sethuraman, N. van Winkle, D.P. Abraham, A.F. Bower, P.R. Guduru, Real-time stress measurements in lithium-ion battery negative-electrodes, Journal of Power Sources 206 (2012) 334–342. https://doi.org/10.1016/j.jpowsour.2012.01.036.

[67] Y. Qi, H. Guo, L.G. Hector, A. Timmons, Threefold Increase in the Young's Modulus of Graphite Negative Electrode during Lithium Intercalation, J. Electrochem. Soc. 157 (2010) A558. https://doi.org/10.1149/1.3327913.

[68] O. Valentin, P.-X. Thivel, T. Kareemulla, F. Cadiou, Y. Bultel, Modeling of thermo-mechanical stresses in Li-ion battery, Journal of Energy Storage 13 (2017) 184–192. https://doi.org/10.1016/j.est.2017.07.018.

[69] K.-Y. Oh, B.I. Epureanu, A novel thermal swelling model for a rechargeable lithium-ion battery cell, Journal of Power Sources 303 (2016) 86–96. https://doi.org/10.1016/j.jpowsour.2015.10.085.

[70] M. Wünsch, J. Kaufman, D.U. Sauer, Investigation of the influence of different bracing of automotive pouch cells on cyclic liefetime and impedance spectra, Journal of Energy Storage 21 (2019) 149–155. https://doi.org/10.1016/j.est.2018.11.019.

[71] A. Barai, R. Tangirala, K. Uddin, J. Chevalier, Y. Guo, A. McGordon, P. Jennings, The effect of external compressive loads on the cycle lifetime of lithium-ion pouch cells, Journal of Energy Storage 13 (2017) 211–219. https://doi.org/10.1016/j.est.2017.07.021.

[72] F. Ebert, G. Sextl, M. Lienkamp, Effect of a flexible battery module bracing on cell aging, in: 2017 Twelfth International Conference on Ecological Vehicles and Renewable Energies (EVER), Monte-Carlo, Monaco, IEEE, 2017, pp. 1–5.

[73] B. Rieger, S. Schlueter, S.V. Erhard, A. Jossen, Strain Propagation in Lithium-Ion Batteries from the Crystal Structure to the Electrode Level, J. Electrochem. Soc. 163 (2016) A1595-A1606. https://doi.org/10.1149/2.0431608jes.

[74] L. Brassart, K. Zhao, Z. Suo, Cyclic plasticity and shakedown in high-capacity electrodes of lithium-ion batteries, International Journal of Solids and Structures 50 (2013) 1120–1129. https://doi.org/10.1016/j.ijsolstr.2012.12.019.

[75] F. Hao, D. Fang, Reducing diffusion-induced stresses of electrode–collector bilayer in lithium-ion battery by pre-strain, Journal of Power Sources 242 (2013) 415–420. https://doi.org/10.1016/j.jpowsour.2013.05.098.

[76] C. Peabody, C.B. Arnold, The role of mechanically induced separator creep in lithium-ion battery capacity fade, Journal of Power Sources 196 (2011) 8147–8153. https://doi.org/10.1016/j.jpowsour.2011.05.023.

[77] T.C. Bach, S.F. Schuster, E. Fleder, J. Müller, M.J. Brand, H. Lorrmann, A. Jossen, G. Sextl, Nonlinear aging of cylindrical lithium-ion cells linked to heterogeneous compression, Journal of Energy Storage (2016). https://doi.org/10.1016/j.est.2016.01.003.

[78] C.M. Amodeo, M.Y. Ali, J. Pan, Computational models for simulations of lithium-ion battery modules under quasi-static and dynamic constrained compression tests, International Journal of Crashworthiness 22 (2016) 1–14. https://doi.org/10.1080/13588265.2016.1213489.

[79] C. Lalanne, Mechanical vibration and shock Analysis, Volume 1: Sinusoidal vibration, Third edition, John Wiley & Sons, New York, NY, 2014.

[80] B. Deutschland, ReViSEDBatt - Projektdatenbank. https://db.batterieforum-deutschland.de/verbundprojekte/revisedbatt/ (accessed 8 July 2019).

[81] Was Batterien weh tut – Projekt »ReViSEDBatt« soll mechanische Schadensmechanismen aufklären - Fraunhofer ISC. https://www.isc.fraunhofer.de/de/presse-und-medien/presseinformationen/was-batterien-weh-tut-projekt-revisedbatt.html (accessed 5 December 2019).

[82] A. Birolini, Reliability Engineering: Theory and Practice, Springer Berlin Heidelberg, Berlin, Heidelberg, s.l., 2017.

[83] R.J. Sadlon, Mechanical Applications in Reliability Engineering, Reliability Analysis Center, New York, NY, 1993.

[84] P. Berg, M. Spielbauer, M. Tillinger, M. Merkel, M. Schoenfuss, O. Bohlen, A. Jossen, Durability of lithium-ion 18650 cells under random vibration load with respect to the inner cell design, Journal of Energy Storage 31 (2020) 101499. https://doi.org/10.1016/j.est.2020.101499.

[85] A. Birolini, Reliability engineering: Theory and practice; mit … 60 tables, seventh. ed., Springer, Berlin, Heidelberg [u.a.], 2014.

[86] I.A. Ushakov, R.A. Harrison, Reliability handbook, Wiley, New York, 1994.

[87] US Nuclear Regulatory Commission, Fault Tree Handbook NUREG-0492, Washington DC, 1981.

[88] NASA, Fault Tree Handbook with Aerospace Application, Washington DC, 2002.

[89] M. Abele, Modellierung und Bewertung hochzuverlässiger Energiebordnetz-Architekturen für sicherheitsrelevante Verbraucher in Kraftfahrzeugen, Kassel University Press, Kassel, 2008.

[90] DIN Deutsches Institut für Normung e.V., Zuverlässigkeitsmanagement – Teil 3-1: Anwendungsleitfaden – Verfahren zur Analyse der Zuverlässigkeit – Leitfaden zur Methodik (IEC 60300-3-1:2003); Deutsche Fassung EN 60300-3-1:2004, Beuth Verlag GmbH, Berlin 03.120.10; 29.020, 2005 (accessed 22 October 2015).

[91] C. Mikolajczak, M. Kahn, K. White, Lithium-ion batteries hazard and use assessment, Springer, New York, 2012.

[92] V. Ruiz, A. Pfrang, A. Kriston, N. Omar, P. van den Bossche, L. Boon-Brett, A review of international abuse testing standards and regulations for lithium ion batteries in electric and hybrid electric vehicles, Renewable and Sustainable Energy Reviews (2017). https://doi.org/10.1016/j.rser.2017.05.195.

[93] C.W. de Silva (Ed.), Vibration and Shock Handbook, Taylor & Francis, Boca Raton, 2005.

[94] C. Lalanne, Mechanical vibration and shock analysis, Volume 4: Fatigue damage, Third edition, Wiley, Hoboken, NJ, 2014.

[95] C. Lalanne, Mechanical vibration and shock analysis, Volume 2: Mechanical shock, Third edition, Wiley, Hoboken, NJ, 2014.

[96] C. Lalanne, Mechanical vibration and shock analysis, Volume 3: Random vibration, Third edition, Wiley, Hoboken, NJ, 2014.

[97] Vibrationdata. https://vibrationdata.wordpress.com/ (accessed 16 August 2019).

[98] C. Lalanne, Mechanical vibration and shock analysis, Volume 5: Specification development, Third edition, Wiley, Hoboken, NJ, 2014.

[99] M.J. Brand, S.F. Schuster, T. Bach, E. Fleder, M. Stelz, S. Gläser, J. Müller, G. Sextl, A. Jossen, Effects of vibrations and shocks on lithium-ion cells, Journal of Power Sources 288 (2015) 62–69. https://doi.org/10.1016/j.jpowsour.2015.04.107.

[100] C. Schenk, Schädigungsmechanismen in zylindrischen Lithium-Ionen-Zellen unter skalierter Vibrationsbeanspruchung. Masterarbeit, München, 2019.

[101] D.J. Ewins, Modal testing: Theory and practice, Repr. revised., Research Studies press, Taunton, 1995.

[102] A. Bilosova, Modal Testing, Ostrava, 2011.

[103] P. Avitabile, Modal Space (in our own little world), 2014. https://www.uml.edu/docs/Modal_Space_Articles_1998-2014_17years_MACL_tcm18-189938.pdf (accessed 15 February 2017).

[104] Y. Zhu, A.T. Zehnder, J. Harrington, G.S. Schajer (Eds.), Measurement of Structural Stresses by Hole-Drilling and DIC: Experimental and Applied Mechanics, Volume 4, Springer International Publishing, 2017.

[105] Agilent Technologies, The Fundamentals of Modal Testing: Application Note 243-3.

[106] K. Worden, G.R. Tomlinson, Nonlinearity in structural dynamics: Detection, identification and modelling, Institute of Physics, Bristol, 2001.

[107] O. Døssing, Structural Testing: Part II: Modal Analysis and Simulation, 1988.

[108] m+p international, m+p Analyzer: User Manual Revision 5.1, Hannover, 2017.

[109] P. Berg, J. Soellner, A. Jossen, Structural dynamics of lithium-ion cells - Part I: Method, test bench validation and investigation of lithium-ion pouch cells, Journal of Energy Storage 26 (2019) 100916. https://doi.org/10.1016/j.est.2019.100916.

[110] P. Berg, J. Soellner, M. Herrmann, A. Jossen, Structural dynamics of lithium-ion cells—part II: Investigation of large-format prismatic cells and method evaluation, Journal of Energy Storage 28 (2020) 101246. https://doi.org/10.1016/j.est.2020.101246.

[111] E. Barsoukov, J.R. Macdonald (Eds.), Impedance spectroscopy: Theory, experiment, and applications, Wiley, Hoboken, NJ, 2018.

[112] J.R. Macdonald, Impedance spectroscopy, Annals of Biomedical Engineering 20 (1992) 289–305. https://doi.org/10.1007/BF02368532.

[113] J.P. Schmidt, Verfahren zur Charakterisierung und Modellierung von Lithium-Ionen Zellen, Verfahren zur Charakterisierung und Modellierung von Lithium-Ionen Zellen 25 (2013).

[114] M. Schönleber, Verfahren zur Charakterisierung des Niederfrequenzverhaltens von Lithium-Ionen Batterien. Dissertation, Karlsruhe.

[115] J. Illig, J.P. Schmidt, M. Weiss, A. Weber, E. Ivers-Tiffée, Understanding the impedance spectrum of 18650 LiFePO4-cells, Journal of Power Sources 239 (2013) 670–679. https://doi.org/10.1016/j.jpowsour.2012.12.020.

[116] J.P. Schmidt, T. Chrobak, M. Ender, J. Illig, D. Klotz, E. Ivers-Tiffée, Studies on LiFePO4 as cathode material using impedance spectroscopy, Journal of Power Sources 196 (2011) 5342–5348. https://doi.org/10.1016/j.jpowsour.2010.09.121.

[117] S.F. Schuster, T. Bach, E. Fleder, J. Müller, M. Brand, G. Sextl, A. Jossen, Nonlinear aging characteristics of lithium-ion cells under different operational conditions, Journal of Energy Storage 1 (2015) 44–53. https://doi.org/10.1016/j.est.2015.05.003.

[118] P. Keil, Aging of Lithium-Ion Batteries in Electric Vehicles. Dissertation, München, 2017.

[119] A. Jossen, Fundamentals of battery dynamics, Journal of Power Sources 154 (2006) 530–538. https://doi.org/10.1016/j.jpowsour.2005.10.041.

[120] M. Spielbauer, P. Berg, M. Ringat, O. Bohlen, A. Jossen, Experimental study of the impedance behavior of 18650 lithium-ion battery cells under deforming mechanical abuse, Journal of Energy Storage 26 (2019) 101039. https://doi.org/10.1016/j.est.2019.101039.

[121] C.T. Love, M.B. Virji, R.E. Rocheleau, K.E. Swider-Lyons, State-of-health monitoring of 18650 4S packs with a single-point impedance diagnostic, Journal of Power Sources 266 (2014) 512–519. https://doi.org/10.1016/j.jpowsour.2014.05.033.

[122] R. Srinivasan, P.A. Demirev, B.G. Carkhuff, Rapid monitoring of impedance phase shifts in lithium-ion batteries for hazard prevention, Journal of Power Sources 405 (2018) 30–36. https://doi.org/10.1016/j.jpowsour.2018.10.014.

[123] T.M. Heenan, C. Tan, J. Hack, D.J. Brett, P.R. Shearing, Developments in X-ray tomography characterization for electrochemical devices, Materials Today (2019). https://doi.org/10.1016/j.mattod.2019.05.019.

[124] V. Yufit, P. Shearing, R.W. Hamilton, P.D. Lee, M. Wu, N.P. Brandon, Investigation of lithium-ion polymer battery cell failure using X-ray computed tomography, Electrochemistry Communications 13 (2011) 608–610. https://doi.org/10.1016/j.elecom.2011.03.022.

[125] D.P. Finegan, E. Darcy, M. Keyser, B. Tjaden, T.M.M. Heenan, R. Jervis, J.J. Bailey, N.T. Vo, O.V. Magdysyuk, M. Drakopoulos, M. Di Michiel, A. Rack, G. Hinds, D.J.L. Brett, P.R. Shearing, Identifying the Cause of Rupture of Li-Ion Batteries during Thermal Runaway, Adv. Sci. 5 (2017) 1700369. https://doi.org/10.1002/advs.201700369.

[126] D.P. Finegan, X-ray Imaging of Failure and Degradation Mechanisms of Lithium-ion Batteries. Dissertation, London, 2016.

[127] D.P. Finegan, J. Darst, W. Walker, Q. Li, C. Yang, R. Jervis, T.M. Heenan, J. Hack, J.C. Thomas, A. Rack, D.J. Brett, P.R. Shearing, M. Keyser, E. Darcy, Modelling and experiments to identify high-risk failure scenarios for testing the safety of lithium-ion cells, Journal of Power Sources 417 (2019) 29–41. https://doi.org/10.1016/j.jpowsour.2019.01.077.

[128] A.S. Mussa, M. Klett, G. Lindbergh, R.W. Lindström, Effects of external pressure on the performance and ageing of single-layer lithium-ion pouch cells, Journal of Power Sources 385 (2018) 18–26. https://doi.org/10.1016/j.jpowsour.2018.03.020.

[129] R.S. Rubino, H. Gan, E.S. Takeuchi, A Study of Capacity Fade in Cylindrical and Prismatic Lithium-Ion Batteries, J. Electrochem. Soc. 148 (2001) A1029. https://doi.org/10.1149/1.1390344.

[130] M.R. Ashory, High Quality Modal Testing Methods. Dissertation, London, 1999.

[131] Cambridge University Engineering Department, Materials Data Book 2003 Edition, Cambridge, 2003.

[132] L. Florence, H.P. Jones, A. Liang, Safety Issues for Lithium ion Batteries, 2009.

[133] J.M. Hooper, Characterising the Effects of Vibration on the Durability of Electric Vehicle Batteries. Dissertation, Warwick, 2017.

[134] G. Kjell, J.F. Lang, Comparing different vibration tests proposed for li-ion batteries with vibration measurement in an electric vehicle, in: 2013 World Electric Vehicle Symposium and Exhibition (EVS27), Barcelona, Spain, IEEE, 2013, pp. 1–11.

[135] M.D. Farrington, Safety of lithium batteries in transportation, Proceedings of the 22nd International Power Sources Symposium 96 (2001) 260–265. https://doi.org/10.1016/S0378-7753(01)00565-1.

[136] J.M. Hooper, J. Marco, Characterising the in-vehicle vibration inputs to the high voltage battery of an electric vehicle, Journal of Power Sources 245 (2014) 510–519. https://doi.org/10.1016/j.jpowsour.2013.06.150.

[137] J. Frodelius Lang, G. Kjell, Comparing vibration measurements in an electric vehicle with standard vibration requirements for Li-ion batteries using power spectral density analysis, International Journal of Electric and Hybrid Vehicles 7 (2015). https://doi.org/10.1504/IJEHV.2015.071640.

[138] J. Marco, J.M. Hooper, Defining a representative vibration durability test for electric vehicle (EV) rechargeable energy storage systems (RESS), in: Electric Vehicle Symposium (EVS 29), Montréal, Québec, 2016, pp. 1–12.

[139] J2380: Vibration Testing of Electric Vehicle Batteries - SAE International, 2020. https://www.sae.org/standards/content/j2380_200903/ (accessed 28 March 2020).

[140] P.J. Swornowski, Destruction mechanism of the internal structure in Lithium-ion batteries used in aviation industry, Energy (2017). https://doi.org/10.1016/j.energy.2017.01.121.

[141] J. Kim, W. Na, S. Lee, M. Jang, C. Lim, Cell Failure Evaluations under Environmental and Safety Tests of Multiple 18650 Li-Ion NCA and NMC Cells for Space Cell's Qualification Estabilishment, in: 2018 IEEE Energy Conversion Congress and Exposition (ECCE), Portland, OR, USA, IEEE, 2018, pp. 2033–2038.

[142] M.G. Darvish, Vibration and functional tests on a new designed battery pack of a micro-satellite, 10.5267/j.esm (2018) 129–134. https://doi.org/10.5267/j.esm.2018.3.001.

[143] C.-O. Yoon, P.-Y. Lee, M. Jang, K. Yoo, J. Kim, Comparison of internal parameters varied by environmental tests between high-power series/parallel battery packs with different shapes, Journal of Industrial and Engineering Chemistry 71 (2019) 260–269. https://doi.org/10.1016/j.jiec.2018.11.034.

[144] X. Wang, M. Kato, H. Naito, C. Yamada, G. Segami, K. Kibe, A Feasibility Study of Commercial Laminated Lithium-Ion Polymer Cells for Space Applications, J. Electrochem. Soc. 153 (2006) A89. https://doi.org/10.1149/1.2131825.

[145] T. Tsujikawa, K. Yabuta, M. Arakawa, K. Hayashi, Safety of large-capacity lithium-ion battery and evaluation of battery system for telecommunications, 16th International Meeting

on Lithium Batteries (IMLB) 244 (2013) 11–16. https://doi.org/10.1016/j.jpowsour.2013.01.155.

[146] L. Shuyan, C. Yan, J. Fachao, Z. Jianzhu, W. Guoye, Research on the Finite Element Analysis and Failure Strengthening Test of Electric Bus Quick-Change Battery Box, in: 2015 8th International Conference on Intelligent Computation Technology and Automation (ICICTA), Nanchang, China, IEEE, 2015, pp. 771–775.

[147] J. Li, H. Tian, P. Wu, Analysis of random vibration of power battery box in electric vehicles, in: 2014 IEEE Conference and Expo Transportation Electrification Asia-Pacific (ITEC Asia-Pacific), Beijing, China, IEEE, 2014, pp. 1–5.

[148] Y. Choi, D. Jung, K. Ham, S. Bae, A study on the accelerated vibration endurance tests for battery fixing bracket in electrically driven vehicles, Procedia Engineering 10 (2011) 851–856. https://doi.org/10.1016/j.proeng.2011.04.140.

[149] J.-K. Lee, J.-S. Yeo, M.-C. Jang, J.-M. Yoon, D.M. Kang, Mechanical durability and electrical durability of an aluminium-laminated lithium-ion polymer battery pack for a hybrid electric vehicle, Proceedings of the Institution of Mechanical Engineers, Part D: Journal of Automobile Engineering 224 (2010) 765–773. https://doi.org/10.1243/09544070JAUTO1388.

[150] P. Svens, Methods for testing and analyzing lithium-ion battery cells intended for heavy-duty hybrid electric vehicles. Doctoral thesis, Chemical Science and Engineering, KTH Royal Institute of Technology, Stockholm, 2014.

[151] T.J. Chapin, A. Wu, C. Wang, Study of Aging Effects on Safety of 18650-type LiCoOx Cells, 2011.

[152] J. Hooper, J. Marco, G. Chouchelamane, C. Lyness, Vibration Durability Testing of Nickel Manganese Cobalt Oxide (NMC) Lithium-Ion 18,650 Battery Cells, Energies 9 (2016) 52. https://doi.org/10.3390/en9010052.

[153] J. Hooper, J. Marco, G. Chouchelamane, C. Lyness, J. Taylor, Vibration Durability Testing of Nickel Cobalt Aluminum Oxide (NCA) Lithium-Ion 18650 Battery Cells, Energies 9 (2016) 281. https://doi.org/10.3390/en9040281.

[154] L. Somerville, J. Hooper, J. Marco, A. McGordon, C. Lyness, M. Walker, P. Jennings, Impact of Vibration on the Surface Film of Lithium-Ion Cells, Energies 10 (2017) 741. https://doi.org/10.3390/en10060741.

[155] J.M. Hooper, J. Marco, G.H. Chouchelamane, J.S. Chevalier, D. Williams, Multi-axis vibration durability testing of lithium ion 18650 NCA cylindrical cells, Journal of Energy Storage 15 (2018) 103–123. https://doi.org/10.1016/j.est.2017.11.006.

[156] L. Zhang, Z. Ning, H. Peng, Z. Mu, C. Sun, Effects of Vibration on the Electrical Performance of Lithium-Ion Cells Based on Mathematical Statistics, Applied Sciences 7 (2017) 802. https://doi.org/10.3390/app7080802.

[157] L. Zhang, Z. Mu, X. Gao, Coupling Analysis and Performance Study of Commercial 18650 Lithium-Ion Batteries under Conditions of Temperature and Vibration, Energies 11 (2018) 2856. https://doi.org/10.3390/en11102856.

[158] H.Y. Choi, I. Lee, J.S. Lee, Y.M. Kim, H.K. Kim, A study on mechanical characteristics of lithium-polymer pouch cell battery for electric vehicle, in: 23rd International Technical Conference on the Enhanced Safety of Vehicles (ESV), Seoul, Republic of Korea, 2013.

[159] H. Popp, M. Luthfi, Han, R. Klambauer, A. Bergmann, In-Situ Investigation of Lithium-Ion Batteries by Combined Mechanical FRF and Dilatometer Measurements, in: 2018 E-MRS Fall Meeting and Exhibit, Warsaw, 2018.

[160] J.M. Hooper, J. Marco, Experimental modal analysis of lithium-ion pouch cells, Journal of Power Sources 285 (2015) 247–259. https://doi.org/10.1016/j.jpowsour.2015.03.098.

[161] H. Popp, G. Glanz, K. Alten, I. Gocheva, W. Berghold, A. Bergmann, Mechanical Frequency Response Analysis of Lithium-Ion Batteries to Disclose Operational Parameters, Energies 11 (2018) 541. https://doi.org/10.3390/en11030541.

[162] F.-M. Volk, M. Winkler, B. Hermann, A. Hiebl, T. Idikurt, H. Rapp, T. Kuttner, Influence of State of Charge and State of Health on the Vibrational Behavior of Lithium-Ion Cell Packs, in: 23rd International Congress on Sound & Vibration (ICSV23), Athen, Greece, 2016.

[163] S.-K. Hong, B.I. Epureanu, M.P. Castanier, Parametric reduced-order models of battery pack vibration including structural variation and prestress effects, Journal of Power Sources 261 (2014) 101–111. https://doi.org/10.1016/j.jpowsour.2014.03.008.

[164] W. Nam, J.-Y. Kim, K.-Y. Oh, The characterization of dynamic behavior of Li-ion battery packs for enhanced design and states identification, Energy Conversion and Management 162 (2018) 264–275. https://doi.org/10.1016/j.enconman.2018.02.022.

[165] D.H. Doughty, Vehicle Battery Safety Roadmap Guidance, 2012.

[166] E. Darcy, Screening Li-ion batteries for internal shorts, 13th International Meeting on Lithium Batteries 174 (2007) 575–578. https://doi.org/10.1016/j.jpowsour.2007.06.245.

[167] J. Galos, A.A. Khatibi, A.P. Mouritz, Vibration and acoustic properties of composites with embedded lithium-ion polymer batteries, Composite Structures 220 (2019) 677–686. https://doi.org/10.1016/j.compstruct.2019.04.013.

[168] J. Lamb, C.J. Orendorff, L.A.M. Steele, S.W. Spangler, Failure propagation in multi-cell lithium ion batteries, Journal of Power Sources 283 (2015) 517–523. https://doi.org/10.1016/j.jpowsour.2014.10.081.

[169] F. Larsson, J. Anderson, P. Andersson, B.-E. Mellander, Thermal Modelling of Cell-to-Cell Fire Propagation and Cascading Thermal Runaway Failure Effects for Lithium-Ion Battery Cells and Modules Using Fire Walls, J. Electrochem. Soc. 163 (2016) A2854-A2865. https://doi.org/10.1149/2.0131614jes.

[170] S. Koch, A. Fill, K.P. Birke, Comprehensive gas analysis on large scale automotive lithium-ion cells in thermal runaway, Journal of Power Sources 398 (2018) 106–112. https://doi.org/10.1016/j.jpowsour.2018.07.051.

[171] A. Nedjalkov, J. Meyer, M. Köhring, A. Doering, M. Angelmahr, S. Dahle, A. Sander, A. Fischer, W. Schade, Toxic Gas Emissions from Damaged Lithium Ion Batteries—Analysis and Safety Enhancement Solution, Batteries 2 (2016) 5. https://doi.org/10.3390/batteries2010005.

[172] J. Sun, J. Li, T. Zhou, K. Yang, S. Wei, N. Tang, N. Dang, H. Li, X. Qiu, L. Chen, Toxicity, a serious concern of thermal runaway from commercial Li-ion battery, Nano Energy 27 (2016) 313–319. https://doi.org/10.1016/j.nanoen.2016.06.031.

[173] Samsung Galaxy Note 7 recall has explosive impact on company's mobile earnings, 2016. https://www.independent.co.uk/news/business/news/samsung-galaxy-note-7-recall-exploding-phones-profits-a7382786.html (accessed 6 February 2019).

[174] S. Abada, G. Marlair, A. Lecocq, M. Petit, V. Sauvant-Moynot, F. Huet, Safety focused modeling of lithium-ion batteries: A review, Journal of Power Sources 306 (2016) 178–192. https://doi.org/10.1016/j.jpowsour.2015.11.100.

[175] FAA Office of Security and Hazardous Materials Safety, Aviation Cargo and Passenger Baggage Events Involving Smoke, Fire, Extreme Heat or Explosion Involving Lithium Batteries or Unknown Battery Types, 2018. https://https://www.faa.gov/hazmat/resources/lithium_batteries/media/Battery_incident_chart.pdf (accessed 1 September 2019).

[176] C. Kranner, Ausfallratenstudie für Lithium-Ionen-Batteriezellen. Bachlorarbeit, München, 2015.

[177] D.G. Kleinbaum, M. Klein, Survival analysis: A self-learning text, second. ed., [Nachdr.], Springer, New York [u.a.], 2010.

[178] O'Connor, Patrick D. T, A. Kleyner, Practical reliability engineering, fifth. ed, Wiley, Chichester [u.a.], 2012.

[179] U.S. Consumer Product Safety Commission, Samsung Expands Recall of Galaxy Note7 Smartphones Based on Additional Incidents with Replacement Phones; Serious Fire and Burn Hazards, 2016. https://www.cpsc.gov/Recalls/2016/samsung-expands-recall-of-galaxy-note7-smartphones-based-on-additional-incidents-with (accessed 6 February 2019).

[180] Samsung smartphone sales worldwide 2010-2018 | Statistic. https://www.statista.com/statistics/299144/samsung-smartphone-shipments-worldwide/ (accessed 6 February 2019).

[181] S. Amiri, X. Chen, A. Manes, M. Giglio, Investigation of the mechanical behaviour of lithium-ion batteries by an indentation technique, International Journal of Mechanical Sciences 105 (2016) 1–10. https://doi.org/10.1016/j.ijmecsci.2015.10.019.

[182] C. Qi, Y.-L. Zhu, F. Gao, S.-C. Wang, K. Yang, Q.-J. Jiao, Safety analysis of lithium-ion battery by rheology-mutation theory coupling with fault tree method, Journal of Loss

Prevention in the Process Industries 49 (2017) 603–611. https://doi.org/10.1016/j.jlp.2017.06.006.

[183] R. Bubbico, V. Greco, C. Menale, Hazardous scenarios identification for Li-ion secondary batteries, Safety Science 108 (2018) 72–88. https://doi.org/10.1016/j.ssci.2018.04.024.

[184] C. Hendricks, N. Williard, S. Mathew, M. Pecht, A failure modes, mechanisms, and effects analysis (FMMEA) of lithium-ion batteries, Journal of Power Sources 297 (2015) 113–120. https://doi.org/10.1016/j.jpowsour.2015.07.100.

[185] R. Li, J. Wu, H. Wang, J. Guo, G. Li, Reliability assessment and failure analysis of lithium iron phosphate batteries, Information Sciences 259 (2014) 359–368. https://doi.org/10.1016/j.ins.2013.06.038.

[186] C. Schlasza, P. Ostertag, D. Chrenko, R. Kriesten, D. Bouquain (Eds.), Review on the aging mechanisms in Li-ion batteries for electric vehicles based on the FMEA method. Transportation Electrification Conference and Expo (ITEC), 2014 IEEE, 2014.

[187] F.J. Soares, L. Carvalho, I.C. Costa, J.P. Iria, J.-M. Bodet, G. Jacinto, A. Lecocq, J. Roessner, B. Caillard, O. Salvi, The STABALID project: Risk analysis of stationary Li-ion batteries for power system applications, Reliability Engineering & System Safety 140 (2015) 142–175. https://doi.org/10.1016/j.ress.2015.04.004.

[188] M. Held, R. Brönnimann, Safe cell, safe battery? Battery fire investigation using FMEA, FTA and practical experiments, Proceedings of the 27th European Symposium on Reliability of Electron Devices, Failure Physics and AnalysisProceedings of the 27th European Symposium on Reliability of Electron Devices, Failure Physics and Analysis 64 (2016) 705–710. https://doi.org/10.1016/j.microrel.2016.07.051.

[189] S. Arora, W. Shen, A. Kapoor, Review of mechanical design and strategic placement technique of a robust battery pack for electric vehicles, Renewable and Sustainable Energy Reviews 60 (2016) 1319–1331. https://doi.org/10.1016/j.rser.2016.03.013.

[190] S. Arora, A. Kapoor, W. Shen, Application of Robust Design Methodology to Battery Packs for Electric Vehicles: Identification of Critical Technical Requirements for Modular Architecture, Batteries 4 (2018) 30. https://doi.org/10.3390/batteries4030030.

[191] W. Li, Z. Jiao, Q. Xiao, J. Meng, Y. Mu, H. Jia, R. Teodorescu, F. Blaabjerg, A Study on Performance Characterization Considering Six-Degree-of-Freedom Vibration Stress and Aging Stress for Electric Vehicle Battery Under Driving Conditions, IEEE Access 7 (2019) 112180–112190. https://doi.org/10.1109/ACCESS.2019.2935380.

[192] T. Waldmann, S. Gorse, T. Samtleben, G. Schneider, V. Knoblauch, M. Wohlfahrt-Mehrens, A Mechanical Aging Mechanism in Lithium-Ion Batteries, Journal of the Electrochemical Society 161 (2014) A1742-A1747. https://doi.org/10.1149/2.1001410jes.

[193] X. Fleury, M.H. Noh, S. Geniès, P.X. Thivel, C. Lefrou, Y. Bultel, Fast-charging of Lithium Iron Phosphate battery with ohmic-drop compensation method: Ageing study, Journal of Energy Storage 16 (2018) 21–36. https://doi.org/10.1016/j.est.2017.12.015.

[194] A. Pfrang, A. Kersys, A. Kriston, D.U. Sauer, C. Rahe, S. Käbitz, E. Figgemeier, Long-term cycling induced jelly roll deformation in commercial 18650 cells, Journal of Power Sources 392 (2018) 168–175. https://doi.org/10.1016/j.jpowsour.2018.03.065.

[195] M. Merkel, Einfluss von Automotive-Vibrationen auf Lithium-Ionen-Zellen des Typs 18,650. Bachelorarbeit, München, 2018.

[196] M. Schönfuß, Einfluss von Vibrationen auf die elektrischen Performance Parameter von gealterten 18650 Lithium-Ionen-Zellen. Bachelorarbeit, München, 2019.

[197] M. Tillinger, Einfluss von Vibrationsbelastungen auf zylindrische, prismatische und Flachzellen. Masterarbeit, München, 2019.

[198] K.L. Dallon, J. Yao, D.R. Wheeler, B.A. Mazzeo, Characterization of mechanical properties of battery electrode films from acoustic resonance measurements, Journal of Applied Physics 123 (2018) 135102. https://doi.org/10.1063/1.5021809.

[199] J. Cannarella, X. Liu, C.Z. Leng, P.D. Sinko, G.Y. Gor, C.B. Arnold, Mechanical Properties of a Battery Separator under Compression and Tension, J. Electrochem. Soc. 161 (2014) F3117-F3122. https://doi.org/10.1149/2.0191411jes.

[200] I. Avdeev, M. Martinsen, A. Francis, Rate- and Temperature-Dependent Material Behavior of a Multilayer Polymer Battery Separator, J. Materi. Eng. and Perform. (Journal of Materials Engineering and Performance) 23 (2014) 315–325. https://doi.org/10.1007/s11665-013-0743-4.

[201] S. Kalnaus, Y. Wang, J.A. Turner, Mechanical behavior and failure mechanisms of Li-ion battery separators, Journal of Power Sources 348 (2017) 255–263. https://doi.org/10.1016/j.jpowsour.2017.03.003.

[202] G.Y. Gor, J. Cannarella, C.Z. Leng, A. Vishnyakov, C.B. Arnold, Swelling and softening of lithium-ion battery separators in electrolyte solvents, Journal of Power Sources 294 (2015) 167–172. https://doi.org/10.1016/j.jpowsour.2015.06.028.

[203] I.C. Halalay, M.J. Lukitsch, M.P. Balogh, C.A. Wong, Nanoindentation testing of separators for lithium-ion batteries, Journal of Power Sources 238 (2013) 469–477. https://doi.org/10.1016/j.jpowsour.2013.04.036.

[204] A. Sheidaei, X. Xiao, X. Huang, J. Hitt, Mechanical behavior of a battery separator in electrolyte solutions, Journal of Power Sources 196 (2011) 8728–8734. https://doi.org/10.1016/j.jpowsour.2011.06.026.

[205] J. Zhu, X. Zhang, H. Luo, E. Sahraei, Investigation of the deformation mechanisms of lithium-ion battery components using in-situ micro tests, Applied Energy 224 (2018) 251–266. https://doi.org/10.1016/j.apenergy.2018.05.007.

[206] E. Sahraei, R. Hill, T. Wierzbicki, Calibration and finite element simulation of pouch lithium-ion batteries for mechanical integrity, Journal of Power Sources 201 (2012) 307–321. https://doi.org/10.1016/j.jpowsour.2011.10.094.

[207] B. Dixon, A. Mason, E. Sahraei, Effects of electrolyte, loading rate and location of indentation on mechanical integrity of li-ion pouch cells, Journal of Power Sources 396 (2018) 412–420. https://doi.org/10.1016/j.jpowsour.2018.06.042.

[208] G. Kermani, E. Sahraei, Review: Characterization and Modeling of the Mechanical Properties of Lithium-Ion Batteries, Energies 10 (2017) 1730. https://doi.org/10.3390/en10111730.

[209] K.-Y. Oh, B.I. Epureanu, Characterization and modeling of the thermal mechanics of lithium-ion battery cells, Applied Energy 178 (2016) 633–646. https://doi.org/10.1016/j.apenergy.2016.06.069.